VORTEX BURST BEHAVIOR OF A DYNAMICALLY PITCHED DELTA WING UNDER THE INFLUENCE OF A VON KÀRMÀN VORTEX STREET AND UNSTEADY FREESTREAM

A Dissertation by

ISMAEL HERON

M.S.A.E., Wichita State University, 1997

B.S.A.E., Wichita State University, 1995

Submitted to the Department of Aerospace Engineering
and the faculty of the Graduate School of
Wichita State University
in partial fulfillment of
the requirements for the degree of
Doctor of Philosophy

December 2007

© Copyright 2007 by Ismael Heron

All Rights Reserved

VORTEX BURST BEHAVIOR OF A DYNAMICALLY PITCHED DELTA WING UNDER THE INFLUENCE OF A VON KÀRMÀN VORTEX STREET AND UNSTEADY FREESTREAM

The following faculty have examined the final copy of this Dissertation for form and content, and recommend that it be accepted in partial fulfillment of the requirement for the degree of Doctor of Philosophy, with a major in Aerospace Engineering.

_____
Roy Y. Myose, Committee Chair

_____
L. Scott Miller, Committee Member

_____
Kamran Rokhsaz, Committee Member

_____
Klaus A. Hoffmann, Committee Member

_____
Dharam Chopra, Committee Member

Accepted for the College of Engineering

_____
Zulma Toro-Ramos, Dean

Accepted for the Graduate School

_____
Susan Kovar, Dean

DEDICATION

I dedicate this Dissertation to my family,

David Theodore Heron

Martha Esther Ramirez de Heron

Martha Esther Heron

and to my wife and children,

Susan My Heron

Ruben Ismael Heron

Gina Abigail Heron

ACKNOWLEDGEMENTS

I would like to take this opportunity to acknowledge the contributions of several people. First and foremost, I am forever grateful to my dissertation advisor, Dr. Roy Myose. His wisdom and encouragement were instrumental in the successful completion of this long and hard journey.

I am also very grateful to the Committee Members: L. Scott Miller, Kamran Rokhsaz, Klaus Hoffmann, and Dharam Chopra. Without your contributions and suggestions, this work would not have been completed. I also would like to acknowledge the contributions made by Mahesh Greywall at the beginning of the project.

I also need to acknowledge John Laffen and the staff of the Aerodynamic Laboratories at the National Institute for Aviation Research at Wichita State University. They have been kind enough to allow me to work in their facilities, have always been extremely helpful when things did not work as planned, and were interested in the progress of this work.

To two great people, Dale Pittman and Larry Morton, for they took the time to teach me the skills I needed to construct the towing mount used in this work, and allowed me to build it using their tools and equipment.

ABSTRACT

An experimental investigation was undertaken at Wichita State University in order to quantify the vortex burst behavior of a pitching 70-degree sweep delta wing subjected to a variable freestream velocity (accelerating or decelerating flow), as well as to an impinging von Kàrmàn vortex street generated by a cylinder placed ahead of the apex. The experiments were inspired by flow features present in the flow field of an aircraft executing a "Cobra" maneuver. A total of 222 test runs were conducted which resulted in the analysis of 6481 video frames for the von Kàrmàn experiments and 8566 video frames for the variable velocity experiments.

It was found that at different α–ranges and velocity ratios, accelerating the flow produced a mild to strong negative effect (i.e., an acceleration of the forward propagation velocity) on the burst location. This negative effect was almost independent of the actual acceleration or range of α over which it occurred. Deceleration, on the other hand, was found to delay the forward burst movement along the vortex core. This was consistent for the pitch rates tested, and in all cases resulted in a momentary reduction of the forward propagation of the burst location. In the more extreme cases where the velocity ratio was large (V_{start}/V_{final} = 2) a complete stop to the forward burst movement was possible.

The most important result from the von Kàrmàn experiments was that the burst could be observed by the "jumping" of the burst location forward towards the wing's apex in response to the convection of the von Kàrmàn wake filament. This was accomplished at both a regular frequency of approximately 3 Hz, and at higher non-uniform frequency centered around 5 Hz, the only difference between the two being the degree of change in the burst location. The experiments performed here represent an initial step towards a more complex Cobra maneuver experiment.

TABLE OF CONTENTS

Chapter	Page
1. INTRODUCTION	1
1.1- Definition	1
1.2- Lift Production Mechanism	2
1.3- Nomenclature	5
1.4- The Delta Wing Main Vortex	6
1.5- Vortex Burst	8
1.6- Vortex Breakdown Theories	13
1.6.1- Spiral Instability Theory	14
1.6.2- Core Stagnation Theory	15
1.6.3- Conjugate States Theory	15
1.7- Prediction of Vortex Burst Location in Static Flow Conditions	20
1.7.1- Helical Instability Criterion	20
1.7.2- Q-Vortex Model	21
1.7.3- Circulation Criteria	22
1.7.4- Negative Azimuthal Vorticity Onset Criteria	23
2. DYNAMIC DELTA WING	25
2.1- Dynamic Vortex Burst Behavior	25
2.2- Phase Lag Causes	26
2.3- Time Scales Involved in the Dynamic Delta Wing	28
2.4- Other Dynamic Delta Wing Experiments	29
2.5- Dynamic Freestream Effects	30
2.6- The “Cobra” Maneuver	33
2.7- Simulation of the “Cobra” Maneuver	35
2.8- Summary of Findings	38

TABLE OF CONTENTS (continued)

Chapter	Page
3. PROBLEM STATEMENT	39
3.1- Problem	39
3.2- Motivation	42
3.3- Overall Goals and Intermediate Milestones	43
3.4- Circular Cylinder Wakes	45
3.5- von Kàrmàn Vortex Street Collisions	47
4. EXPERIMENTAL METHOD	50
4.1- Facility Description	50
4.1.1- Water Tunnel	50
4.1.2- Towing Mount	50
4.1.3- Data Collection Equipment	54
4.2- Calibration	55
4.2.1- Velocity	55
4.2.2- Cameras	56
4.3- Influence Due to Tunnel	57
4.3.1- Wall Induced Upwash	57
4.3.2- Blockage	57
4.4- Vortex Burst and Track Length	58
4.4.1- Track Length	58
4.4.2- Time Interval Between Runs	58
4.4.3- Flow Quality	59
4.5- VisualBASIC Analysis Software	60
4.5.1- Analysis Process	60
4.5.2- Resolution	61

TABLE OF CONTENTS (continued)

Chapter	Page
4.5.3- Refraction and Perspective Errors	62
4.5.4- User Induced Error	62
4.5.5- Vortex Burst Location Definition	64
4.6- Mount Validation	65
4.6.1- Experimental Set-Up for Validation of Mount	66
4.6.2- Static Results	67
4.6.3- Dynamic Results	68
4.6.4- Stem Results	69
5. VARIABLE VELOCITY EXPERIMENTS	70
5.1- Experimental Set-Up	70
5.1.1- Experimental Similarity	70
5.1.2- Variable Velocity Set-Up	73
5.1.2.1- Capacitor Discharge Method	73
5.1.2.2- Pulse Width Modulated Method	73
5.1.3- Experimental Matrix	74
5.1.4- Experimental Limitations	76
5.2- Results & Discussion	76
5.2.1- Capacitor Discharge Method	76
5.2.2- PWM Method	79
5.2.3- Discussion of Observed Behavior	93

TABLE OF CONTENTS (continued)

Chapter	Page
6. VON KÀRMÀN IMPINGEMENT EXPERIMENTS	95
6.1- The Oscillating Cylinder	95
6.2- Experimental Set-Up	97
6.2.1- Large Cylinder	97
6.2.2- Small Cylinder	98
6.3- Experimental Issues	99
6.4- Thrust Generated by the Oscillating Cylinder	101
6.5- Cylinder Results	102
6.5.1- Experiment Matrix	102
6.5.2- Quantitative Results with Fixed Large Cylinder	105
6.5.3- Qualitative Observations with Fixed Large Cylinder	106
6.5.4- Quantitative Results with Large Oscillating Cylinder	107
6.5.5- Quantitative Results with Small Oscillating Cylinder	111
7. CONCLUSIONS	117
7.1- The Towing Mount Validation	118
7.2- Variable Freestream Velocity Experiments	119
7.3- The von Kàrmàn Impngement Experiments	122
7.4- Recommendations about the Experimental Investigation	124
7.5- Future Work	126
REFERENCES	127
List of References	128

TABLE OF CONTENTS (continued)

Chapter	Page
APPENDICES	135
A. Figures	136
B. Circuit Diagrams	259
C. VisualBASIC® Program Listings	268
D. Lab Notes On Von Kàrmàn Experiments	282

LIST OF TABLES

Table		Page
4.1	Error due to Analysis Process	63
4.2	Overview of Experimental Investigation	66
4.3	Experimental Parameters of Validation Experiment	67
4.4	Test Matrix for Towing Mount Validation	68
5.1	Similarity and Possible Test Parameters	71
5.2	Experimental Matrix for Variable Freestream Experiments	75
5.3	Type of Vortex Burst Encountered During Variable Freestream Experiments	90
6.1	Cylinder Specifications	98
6.2	Experimental Matrix for von Kàrmàn Impingement Experiments	103
6.3	Type of Vortex Burst Encountered during von Kàrmàn Wake Experiments	116
B1	Components Used In Carriage Electronics Layout	260
B2	Components Used In Carriage Power Supply	263
B3	Components Used In PWM Motor Driver	266
D1	Vortex Burst Details On Von Kàrmàn Experiments	282

LIST OF FIGURES

Figure		Page
1.1	The Delta Wing	136
1.2	Delta Wing Flow Field Features	136
1.3	Lift Producing Mechanism of Delta Wing	137
1.4	K_V and K_P Values	137
1.5	Vortex Lift Contribution on a 70-degree Delta	138
1.6	Vortex Lift and Potential Lift in for a Λ=70o Delta Wing	138
1.7	Attachment and Separation Lines on the Delta Wing Surface	139
1.8	Delta Wing Nomenclature	139
1.9	Structure of Main Vortex Core	140
1.10	Typical Axial Velocity Profile	140
1.11	Typical Swirl Velocity Profile	141
1.12	Vortex Burst Classification	141
1.13	Longitudinal and Crossflow Fluctuations in Vortex Burst Position	142
1.14	Two Types of Vortex Tube Generators	142
1.15	The Regions of Swirl and Reynolds Number	143
1.16	Vortex Burst Location in Vane-Type Vortex Tube	143
1.17	Measured Swirl Angle Φ in Vortex-Tubes	144
1.18	VB Position, 70-degree Delta, Static Pitch, Uniform U_∞	144
1.19	Velocity Components on Leading Edge of Delta Wing	145
1.20	Ludweig's Stability Criterion for Spiral Vortex Burst	145
1.21	Ludweig's Stability Criteria, Experimental Results	146
1.22	Q-Vortex Parameters	146
1.23	Q-Vortex Stability Boundaries	147
1.24	VB Location Using Parabolic Axial Circulation Predictor	147
1.25	Azimuthal Vorticity Behavior	148

LIST OF FIGURES (continued)

Figure		Page
2.1	Vortex Burst Behavior During Dynamic Pitching, 70^o Delta Wing	148
2.2	Dynamic Equivalent Steady (DES) Effect of Dynamic Pitching	149
2.3	Group Velocity Change due to Pitching	149
2.4	Convection of Vorticity from Leading Edge	150
2.5	The “Cobra” Maneuver	150
2.6	The Forebody Coning Motion	151
3.1	The Forebody Vortex and the Leading Edge Vortex	152
3.2	Strouhal Number and Vortex Shedding on Long Cylinder	153
3.3	Expected LE Vortex Behavior to von Kàrmàn Vortex Impingement	154
3.4	Görtler Vortex Interacting with a Perpendicular Vortex	154
4.1	2- x 3-Feet Water Tunnel	155
4.2	Schematic of Towing Mount, Tracks	156
4.3	Close-Up of Towing Mount in Water Tunnel	156
4.4	Schematic of Towing Mount, Carriage	157
4.5	Carriage Drive	158
4.6	Tachometer and Floating Roller Detail	158
4.7	Towing Mount Installed in Water Tunnel	159
4.8	Carriage Pitch-Up Mechanism	160
4.9	Angle of Attack Linearity to Motor Rotation	161
4.10	Experimental Set-Up (Mount Validation and Variable Velocity Cases)	162
4.11	Carriage Velocity Behavior	163
4.12	Vortex Burst Behavior as Function of Distance from Standstill	163
4.13	Analysis Process	164

LIST OF FIGURES (continued)

Figure		Page
4.14	Position Error due to Water Refraction	165
4.15	Perspective Error due to Camera Position	165
4.16	Author's Influence on Vortex Burst Analysis Repeatability	166
4.17	Definition of Vortex Burst Point	166
4.18	Schematic of the Delta Wing Used.	167
4.19	Stem Used on Validation Tests	167
4.20	Towing Mount Validation - Static Results	168
4.21	Towing Mount Validation - Dynamic Pitch, κ= 0.1	169
4.22	Towing Mount Validation - Dynamic Pitch, κ= 0.2	169
4.23	Effect due to Stem, κ= 0.1	170
4.24	Effect due to Stem, κ= 0.2	170
5.1	Sample Vortex Burst Behavior, Dynamic Pitch and Variable Velocity ($15 < \alpha < 55$ deg, Slow Down from $30 < \alpha < 55$ deg)	171
5.2	Vortex Burst Time Behavior, Dynamic Pitch and Variable Velocity, κ=0.2 to 0.4 ($15 < \alpha < 55$ deg, Slow Down from $30 < \alpha < 55$ deg)	172
5.3	Vortex Burst Behavior, Dynamic Pitch and Variable Velocity, κ= 0.2 to 0.27 ($15 < \alpha < 55$ deg, Slow Down from $30 < \alpha < 55$ deg)	173
5.4	Vortex Burst Behavior Comparison, Capacitor Slow-Down	174
5.5	Burst Behavior, Pitch Up at κ=0.2, Acceleration from 0.2 ft/s (30 deg) to 0.4 ft/s (50 deg)	175
5.6	Burst Behavior, Pitch Up at κ=0.2, Deceleration from 0.4 ft/s (30 deg) to 0.2 ft/s (50 deg)	176

LIST OF FIGURES (continued)

Figure		Page
5.7	Burst Behavior, Pitch Up at κ=0.2, Acceleration from 0.2 ft/s (45 deg) to 0.4 ft/s (beyond 55 deg)	177
5.8	Burst Behavior, Pitch Up at κ=0.2, Deceleration from 0.4 ft/s (45 deg) to 0.2 ft/s (beyond 55 deg)	178
5.9	Burst Behavior, Pitch Up at κ=0.2, Acceleration from 0.3 ft/s (30 deg) to 0.4 ft/s (40 deg)	179
5.10	Burst Behavior, Pitch Up at κ=0.2, Deceleration from 0.4 ft/s (30 deg) to 0.3 ft/s (40 deg)	180
5.11	Burst Behavior, Pitch Up at κ=0.2, Acceleration from 0.3 ft/s (30 deg) to 0.4 ft/s (50 deg)	181
5.12	Burst Behavior, Pitch Up at κ=0.2, Deceleration from 0.4 ft/s (30 deg) to 0.3 ft/s (50 deg)	182
5.13	Burst Behavior, Pitch Up at κ=0.2, Acceleration from 0.3 ft/s (45 deg) to 0.4 ft/s (beyond 55 deg)	183
5.14	Burst Behavior, Pitch Up at κ=0.2, Deceleration from 0.4 ft/s (45 deg) to 0.3 ft/s (beyond 55 deg)	184
5.15	Burst Behavior, Pitch Up at κ=0.1, Acceleration from 0.2 ft/s (30 deg) to 0.4 ft/s (40 deg)	185
5.16	Burst Behavior, Pitch Up at κ=0.1, Deceleration from 0.4 ft/s (30 deg) to 0.2 ft/s (40 deg)	186
5.17	Burst Behavior, Pitch Up at κ=0.1, Acceleration from 0.2 ft/s (30 deg) to 0.4 ft/s (50 deg)	187
5.18	Burst Behavior, Pitch Up at κ=0.1, Deceleration from 0.4 ft/s (30 deg) to 0.2 ft/s (50 deg)	188

LIST OF FIGURES (continued)

Figure		Page
5.19	Burst Behavior, Pitch Up at κ=0.1, Acceleration from 0.2 ft/s (45 deg) to 0.4 ft/s (beyond 55 deg)	189
5.20	Burst Behavior, Pitch Up at κ=0.1, Deceleration from 0.4 ft/s (45 deg) to 0.2 ft/s (beyond 55 deg)	190
5.21	Burst Behavior, Pitch Up at κ=0.1, Acceleration from 0.3 ft/s (30 deg) to 0.4 ft/s (50 deg)	191
5.22	Burst Behavior, Pitch Up at κ=0.1, Deceleration from 0.4 ft/s (30 deg) to 0.3 ft/s (50 deg)	192
5.23	Burst Behavior, Pitch Up at κ=0.1, Acceleration from 0.3 ft/s (45 deg) to 0.4 ft/s (beyond 55 deg)	193
5.24	Burst Behavior, Pitch Up at κ=0.1, Deceleration from 0.4 ft/s (45 deg) to 0.3 ft/s (beyond 55 deg)	194
5.25	Burst Behavior, Pitch Down at κ=0.1, Acceleration from 0.2 ft/s (50 deg) to 0.4 ft/s (40 deg)	195
5.26	Burst Behavior, Pitch Down at κ=0.1, Deceleration from 0.4 ft/s (50 deg) to 0.2 ft/s (40 deg)	196
5.27	Burst Behavior, Pitch Down at κ=0.1, Acceleration from 0.2 ft/s (50 deg) to 0.4 ft/s (30 deg)	197
5.28	Burst Behavior, Pitch Down at κ=0.1, Deceleration from 0.4 ft/s (50 deg) to 0.2 ft/s (30 deg)	198
5.29	Burst Behavior, Pitch Down at κ=0.1, Acceleration from 0.2 ft/s (45 deg) to 0.4 ft/s (below 30 deg)	199
5.30	Burst Behavior, Pitch Down at κ=0.1, Deceleration from 0.4 ft/s (45 deg) to 0.2 ft/s (below 30 deg)	200

LIST OF FIGURES (continued)

Figure		Page
5.31	Burst Behavior, Pitch Down at κ=0.1, Acceleration from 0.3 ft/s (50 deg) to 0.4 ft/s (30 deg)	201
5.32	Burst Behavior, Pitch Down at κ=0.1, Deceleration from 0.4 ft/s (50 deg) to 0.3 ft/s (30 deg)	202
5.33	Behavior, Pitch Down at κ=0.1, Acceleration from 0.3 ft/s (45 deg) to 0.4 ft/s (below 30 deg)	203
5.34	Burst Behavior, Pitch Down at κ=0.1, Deceleration from 0.4 ft/s (45 deg) to 0.3 ft/s (below 30 deg)	204
5.35	Burst Comparison, Pitch Up at κ=0.2, Acceleration / Deceleration from 0.2 ft/s (30 deg) to 0.4 ft/s (50 deg)	205
5.36	Burst Comparison, Pitch Up at κ=0.2, Acceleration / Deceleration from 0.3 ft/s (30 deg) to 0.4 ft/s (50 deg)	205
5.37	Burst Comparison, Pitch Up at κ=0.2, Acceleration / Deceleration from 0.2 ft/s (45 deg) to 0.4 ft/s (beyond 55 deg)	206
5.38	Burst Comparison, Pitch Up at κ=0.2, Acceleration / Deceleration from 0.3 ft/s (45 deg) to 0.4 ft/s (beyond 55 deg)	206
5.39	Burst Comparison, Pitch Up at κ=0.2, Acceleration / Deceleration from 0.3 ft/s (30 deg) to 0.4 ft/s (40 deg)	207
5.40	Burst Comparison, Pitch Up at κ=0.1, Acceleration / Deceleration from 0.2 ft/s (30 deg) to 0.4 ft/s (50 deg)	207
5.41	Burst Comparison, Pitch Up at κ=0.1, Acceleration / Deceleration from 0.2 ft/s (45 deg) to 0.4 ft/s (beyond 55 deg)	208
5.42	Burst Comparison, Pitch Up at κ=0.1, Acceleration/Deceleration from 0.3 ft/s (30 deg) to 0.4 ft/s (50 deg)	208

LIST OF FIGURES (continued)

Figure		Page
5.43	Burst Comparison, Pitch Up at κ=0.1, Acceleration/Deceleration from 0.3 ft/s (45 deg) to 0.4 ft/s (beyond 55 deg)	209
5.44	Burst Comparison, Pitch Down at κ=0.1, Acceleration/Deceleration from 0.2 ft/s (50 deg) to 0.4 ft/s (40 deg)	209
5.45	Burst Comparison, Pitch Down at κ=0.1, Acceleration/Deceleration from 0.2 ft/s (50 deg) to 0.4 ft/s (30 deg)	210
5.46	Burst Comparison, Pitch Down at κ=0.1, Acceleration/Deceleration from 0.3 ft/s (50 deg) to 0.4 ft/s (30 deg)	210
5.47	Example of Perpendicular Velocity at Leading Edge (Equation (5.2)), Constant Pitch Up Rate, $dU_\infty/dt = 0$	211
5.48	Example of Perpendicular Velocity at Leading Edge, Constant Pitch Up Rate and Deceleration (Ideal Representation of Figure 5.35)	212
5.49	Time Progression of Perpendicular Velocity at Leading Edge into the Vortex Core	213
6.1	von Kàrmàn Wake Locked by Cylinder Oscillation	214
6.2	Simplified Cylinder Set-Up with Synchronization Circuit	215
6.3	Close-Up View of Bottom Cylinder Guide and Skate	215
6.4	Fixed Large Cylinder Vortex Burst Time History, α = 35 deg	216
6.5	Fixed Large Cylinder Vortex Burst Time History, α = 40 deg	217
6.6	Fixed Large Cylinder Vortex Burst Time History, α = 45 deg	218
6.7	Fixed Large Cylinder Vortex Burst Time History, α = 50 deg	219
6.8	Fixed Large Cylinder Angle of Attack Behavior Comparison	220

LIST OF FIGURES (continued)

Figure		Page
6.9	Small Amplitude Wave Distortion of LE Vortex Core, α= 35 deg	221
6.10	Formation of Dye Concentrations on LE vortex core, α= 35 deg	221
6.11	Entrainment of von Kàrmàn vortex filament in shear layer, α= 35 deg	222
6.12	Schematic Explanation of Cylinder Plotting Nomenclature for Figures 6.13 to 6.82	223
6.13	Large Cylinder, Pitch-Up Initiation Synchronized to Cylinder's Port Deflection, 15 < α < 55 degrees, κ = 0.2 (Experiment 1)	224
6.14	Large Cylinder, Pitch-Up Initiation Synchronized to Cylinder's Port Deflection, 15 < α < 55 degrees, κ = 0.2 (Experiment 2)	224
6.15	Large Cylinder, Pitch-Up Initiation Synchronized to Cylinder's Port Deflection, 15 < α < 55 degrees, κ = 0.2 (Experiment 3)	225
6.16	Large Cylinder, Pitch-Up Initiation Synchronized to Cylinder's Starboard Deflection, 15 < α < 55 degrees, κ = 0.2 (Experiment 1)	225
6.17	Large Cylinder, Pitch-Up Initiation Synchronized to Cylinder's to Starboard Deflection, 15 < α < 55 degrees, κ = 0.2 (Experiment 2)	226
6.18	Large Cylinder, Pitch-Up Initiation Synchronized to Cylinder's to Starboard Deflection, 15 < α < 55 degrees, κ = 0.2 (Experiment 3)	226
6.19	Large Cylinder, Pitch-Up Initiation Synchronized to Cylinder's Center to Port Deflection, 15 < α < 55 degrees, κ = 0.2 (Experiment 1)	227
6.20	Large Cylinder, Pitch-Up Initiation Synchronized to Cylinder's Center to Port Deflection, 15 < α < 55 degrees, κ = 0.2 (Experiment 2)	227

LIST OF FIGURES (continued)

Figure		Page
6.21	Large Cylinder, Pitch-Up Initiation Synchronized to Cylinder's Center to Port Deflection, $15 < \alpha < 55$ degrees, $\kappa = 0.2$ (Experiment 3)	228
6.22	Large Cylinder, Pitch-Up Initiation Synchronized to Cylinder's Center to Starboard Deflection, $15 < \alpha < 55$ degrees, $\kappa = 0.2$ (Experiment 1)	228
6.23	Large Cylinder, Pitch-Up Initiation Synchronized to Cylinder's Center to Starboard Deflection, $15 < \alpha < 55$ degrees, $\kappa = 0.2$ (Experiment 2)	229
6.24	Large Cylinder, Pitch-Up Initiation Synchronized to Cylinder's Center to Port Deflection, $35 < \alpha < 55$ degrees, $\kappa = 0.2$ (Experiment 1)	229
6.25	Large Cylinder, Pitch-Up Initiation Synchronized to Cylinder's Center to Port Deflection, $35 < \alpha < 55$ degrees, $\kappa = 0.2$ (Experiment 2)	230
6.26	Large Cylinder, Pitch-Up Initiation Synchronized to Cylinder's Center to Port Deflection, $35 < \alpha < 55$ degrees, $\kappa = 0.2$ (Experiment 3)	230
6.27	Large Cylinder, Pitch-Up Initiation Synchronized to Cylinder's Center to Starboard Deflection, $35 < \alpha < 55$ degrees, $\kappa = 0.2$ (Experiment 1)	231
6.28	Large Cylinder, Pitch-Up Initiation Synchronized to Cylinder's Center to Starboard Deflection, $35 < \alpha < 55$ degrees, $\kappa = 0.2$ (Experiment 2)	231

LIST OF FIGURES (continued)

Figure		Page
6.29	Large Cylinder, Pitch-Up Initiation Synchronized to Cylinder's Center to Starboard Deflection, $35 < \alpha < 55$ degrees, $\kappa = 0.2$ (Experiment 3)	232
6.30	Large Cylinder, Pitch-Up Initiation Synchronized to Cylinder's Starboard Deflection, $35 < \alpha < 55$ degrees, $\kappa = 0.2$ (Experiment 1)	232
6.31	Large Cylinder, Pitch-Up Initiation Synchronized to Cylinder's Starboard Deflection, $35 < \alpha < 55$ degrees, $\kappa = 0.2$ (Experiment 2)	233
6.32	Large Cylinder, Pitch-Up Initiation Synchronized to Cylinder's Starboard Deflection, $35 < \alpha < 55$ degrees, $\kappa = 0.2$ (Experiment 3)	233
6.33	Large Cylinder, Pitch-Up Initiation Synchronized to Cylinder's Port Deflection, $35 < \alpha < 55$ degrees, $\kappa = 0.2$ (Experiment 1)	234
6.34	Large Cylinder, Pitch-Up Initiation Synchronized to Cylinder's Port Deflection, $35 < \alpha < 55$ degrees, $\kappa = 0.2$ (Experiment 2)	234
6.35	Large Cylinder, Pitch-Up Initiation Synchronized to Cylinder's Port Deflection, $35 < \alpha < 55$ degrees, $\kappa = 0.2$ (Experiment 3)	235
6.36	Large Cylinder, Pitch-Up Initiation Synchronized to Cylinder's Center to Starboard Deflection, $35 < \alpha < 55$ degrees, $\kappa = 0.1$ (Experiment 1)	235
6.37	Large Cylinder, Pitch-Up Initiation Synchronized to Cylinder's Center to Starboard Deflection, $35 < \alpha < 55$ degrees, $\kappa = 0.1$ (Experiment 2)	236
6.38	Large Cylinder, Pitch-Up Initiation Synchronized to Cylinder's Center to Starboard Deflection, $35 < \alpha < 55$ degrees, $\kappa = 0.1$ (Experiment 3)	236

LIST OF FIGURES (continued)

Figure		Page
6.39	Large Cylinder, Pitch-Up Initiation Synchronized to Cylinder's Starboard Deflection, $35 < \alpha < 55$ degrees, $\kappa = 0.1$ (Experiment 1)	237
6.40	Large Cylinder, Pitch-Up Initiation Synchronized to Cylinder's Starboard Deflection, $35 < \alpha < 55$ degrees, $\kappa = 0.1$ (Experiment 2)	237
6.41	Large Cylinder, Pitch-Up Initiation Synchronized to Cylinder's Port Deflection, $35 < \alpha < 55$ degrees, $\kappa = 0.1$ (Experiment 1)	238
6.42	Large Cylinder, Pitch-Up Initiation Synchronized to Cylinder's Port Deflection, $35 < \alpha < 55$ degrees, $\kappa = 0.1$ (Experiment 2)	238
6.43	Large Cylinder, Pitch-Up Initiation Synchronized to Cylinder's Port Deflection, $35 < \alpha < 55$ degrees, $\kappa = 0.1$ (Experiment 3)	239
6.44	Large Cylinder, Pitch-Up Initiation Synchronized to Cylinder's Center to Port Deflection, $35 < \alpha < 55$ degrees, $\kappa = 0.1$ (Experiment 1)	239
6.45	Large Cylinder, Pitch-Up Initiation Synchronized to Cylinder's Center to Port Deflection, $35 < \alpha < 55$ degrees, $\kappa = 0.1$ (Experiment 2)	240
6.46	Large Cylinder, Pitch-Up Initiation Synchronized to Cylinder's Center to Port Deflection, $35 < \alpha < 55$ degrees, $\kappa = 0.1$ (Experiment 3)	240
6.47	Small Cylinder, Pitch-Up Initiation Synchronized to Cylinder's Port Deflection, $15 < \alpha < 55$ degrees, $\kappa = 0.2$ (Experiment 1)	241
6.48	Small Cylinder, Pitch-Up Initiation Synchronized to Cylinder's Port Deflection, $15 < \alpha < 55$ degrees, $\kappa = 0.2$ (Experiment 2)	241
6.49	Small Cylinder, Pitch-Up Initiation Synchronized to Cylinder's Port Deflection, $15 < \alpha < 55$ degrees, $\kappa = 0.2$ (Experiment 3)	242

LIST OF FIGURES (continued)

Figure		Page
6.50	Small Cylinder, Pitch-Up Initiation Synchronized to Cylinder's Center to Starboard Deflection, $15 < \alpha < 55$ degrees, $\kappa = 0.2$ (Experiment 1)	242
6.51	Small Cylinder, Pitch-Up Initiation Synchronized to Cylinder's Center to Starboard Deflection, $15 < \alpha < 55$ degrees, $\kappa = 0.2$ (Experiment 2)	243
6.52	Small Cylinder, Pitch-Up Initiation Synchronized to Cylinder's Center to Starboard Deflection, $15 < \alpha < 55$ degrees, $\kappa = 0.2$ (Experiment 3)	243
6.53	Small Cylinder, Pitch-Up Initiation Synchronized to Cylinder's Starboard Deflection, $15 < \alpha < 55$ degrees, $\kappa = 0.2$ (Experiment 1)	244
6.54	Small Cylinder, Pitch-Up Initiation Synchronized to Cylinder's Starboard Deflection, $15 < \alpha < 55$ degrees, $\kappa = 0.2$ (Experiment 2)	244
6.55	Small Cylinder, Pitch-Up Initiation Synchronized to Cylinder's Starboard Deflection, $15 < \alpha < 55$ degrees, $\kappa = 0.2$ (Experiment 3)	245
6.56	Small Cylinder, Pitch-Up Initiation Synchronized to Cylinder's Center to Port Deflection, $15 < \alpha < 55$ degrees, $\kappa = 0.2$ (Experiment 1)	245
6.57	Small Cylinder Pitch-Up Initiation Synchronized to Cylinder's Center to Port Deflection, $15 < \alpha < 55$ degrees, $\kappa = 0.2$ (Experiment 2)	246
6.58	Small Cylinder, Pitch-Up Initiation Synchronized to Cylinder's Center to Port Deflection, $15 < \alpha < 55$ degrees, $\kappa = 0.2$ (Experiment 3)	246

LIST OF FIGURES (continued)

Figure		Page
6.59	Small Cylinder, Pitch-Up Initiation Synchronized to Cylinder's Port Deflection, $35 < \alpha < 55$ degrees, $\kappa = 0.2$ (Experiment 1)	247
6.60	Small Cylinder, Pitch-Up Initiation Synchronized to Cylinder's Port Deflection, $35 < \alpha < 55$ degrees, $\kappa = 0.2$ (Experiment 2)	247
6.61	Small Cylinder, Pitch-Up Initiation Synchronized to Cylinder's Port Deflection, $35 < \alpha < 55$ degrees, $\kappa = 0.2$ (Experiment 3)	248
6.62	Small Cylinder, Pitch-Up Initiation Synchronized to Cylinder's Center to Starboard Deflection, $35 < \alpha < 55$ degrees, $\kappa = 0.2$ (Experiment 1)	248
6.63	Small Cylinder, Pitch-Up Initiation Synchronized to Cylinder's Center to Starboard Deflection, $35 < \alpha < 55$ degrees, $\kappa = 0.2$ (Experiment 2)	249
6.64	Small Cylinder, Pitch-Up Initiation Synchronized to Cylinder's Center to Starboard Deflection, $35 < \alpha < 55$ degrees, $\kappa = 0.2$ (Experiment 3)	249
6.65	Small Cylinder, Pitch-Up Initiation Synchronized to Cylinder's Starboard Deflection, $35 < \alpha < 55$ degrees, $\kappa = 0.2$ (Experiment 1)	250
6.66	Small Cylinder, Pitch-Up Initiation Synchronized to Cylinder's Center to Port Deflection, $35 < \alpha < 55$ degrees, $\kappa = 0.2$ (Experiment 1)	250
6.67	Small Cylinder, Pitch-Up Initiation Synchronized to Cylinder's Center to Port Deflection, $35 < \alpha < 55$ degrees, $\kappa = 0.2$ (Experiment 2)	251

LIST OF FIGURES (continued)

Figure		Page
6.68	Small Cylinder, Pitch-Up Initiation Synchronized to Cylinder's Center to Port Deflection, $35 < \alpha < 55$ degrees, $\kappa = 0.2$ (Experiment 3)	251
6.69	Small Cylinder, Pitch-Up Initiation Synchronized to Cylinder's Port Deflection, $35 < \alpha < 55$ degrees, $\kappa = 0.1$ (Experiment1)	252
6.70	Small Cylinder, Pitch-Up Initiation Synchronized to Cylinder's Port Deflection, $35 < \alpha < 55$ degrees, $\kappa = 0.1$ (Experiment 2)	252
6.71	Small Cylinder, Pitch-Up Initiation Synchronized to Cylinder's Starboard Deflection, $35 < \alpha < 55$ degrees, $\kappa = 0.1$ (Experiment 1)	253
6.72	Small Cylinder, Pitch-Up Initiation Synchronized to Cylinder's Starboard Deflection, $35 < \alpha < 55$ degrees, $\kappa = 0.1$ (Experiment 2)	253
6.73	Small Cylinder, Pitch-Up Initiation Synchronized to Cylinder's Starboard Deflection, $35 < \alpha < 55$ degrees, $\kappa = 0.1$ (Experiment 3)	254
6.74	Small Cylinder, Pitch-Up Initiation Synchronized to Cylinder's Center to Port Deflection, $35 < \alpha < 55$ degrees, $\kappa = 0.1$ (Experiment 1)	254
6.75	Small Cylinder, Pitch-Up Initiation Synchronized to Cylinder's Center to Port Deflection, $35 < \alpha < 55$ degrees, $\kappa = 0.1$ (Experiment 2)	255
6.76	Small Cylinder, Pitch-Up Initiation Synchronized to Cylinder's Center to Port Deflection, $35 < \alpha < 55$ degrees, $\kappa = 0.1$ (Experiment 3)	255
6.77	Large Cylinder Burst Envelope, Sample Experiments, $\kappa = 0.2$, $15 < \alpha < 55$ degrees	256

LIST OF FIGURES (continued)

Figure		Page
6.78	Small Cylinder Burst Envelope, Sample Experiments, $\kappa = 0.2$, $15 < \alpha < 55$ degrees	256
6.79	Large Cylinder Burst Envelope, Sample Experiments, $\kappa = 0.2$, $35 < \alpha < 55$ degrees	257
6.80	Small Cylinder Burst Envelope, Sample Experiments, $\kappa = 0.2$, $35 < \alpha < 55$ degrees	257
6.81	Large Cylinder Burst Envelope, Sample Experiments, $\kappa = 0.1$, $35 < \alpha < 55$ degrees	258
6.82	Small Cylinder Burst Envelope, Sample Experiments, $\kappa = 0.1$, $35 < \alpha < 55$ degrees	258
B1	Carriage Schematic Diagram	261
B2	Towing Mount Power Supply Schematic	264
B3	Pulse-Width Modulated von Kàrmàn Motor Speed Control Schematic	267
C1	User Interface for ASCAN Program	281

LIST OF ABBREVIATIONS

A, B, C, C_o	Constants
A_{Delta}	Projected Frontal Area of Delta Wing
A_{Tunnel}	Water Tunnel Cross-Sectional Area
A/D	Analog-to-Digital Converter
b	Wing Span
BHE	Bragg & Hawthorne Equation
c	Wing root chord
c^+	Wave Velocity Propagating Downstream
c^-	Wave Velocity Propagating Upstream
CCD	Charge-Coupled Device
C_D	Total Drag Coefficient
C_{DO}	Zero-Lift Drag Coefficient
C_g	Wave Group Velocity
C_{go}	Wave Group Velocity, Static Conditions
C_L	Wing Lift Coefficient
C_x	Axial Velocity Gradient
C_θ	Swirl Velocity Gradient
D	Diameter
DMM	Digital Multi-Meter
FOV	Field of View
I	Vortex Impact Parameter
K	Profile Parameter (Ludweig Model)
K_P	Polhamus Potential Lift Coefficient
K_V	Polhamus Vortex Lift Coefficient
K-H	Kelvin-Helmholtz Instability
l/d	Length-Diameter Ratio
L	Length of Entry Slot (Tangential Vortex Tube)

LIST OF ABBREVIATIONS (continued)

LE	Leading Edge
LEX	Leading Edge Extension
L/D	Lift-Drag Ratio
MAV	Micro-Air Vehicle
n_1, n_2	Speed of Light in Transmission Medium 1 and 2, Respectively
N	Criticality Criterion (Squire Model)
NTSC	National Television Standards Committee
P	Pressure
PWM	Pulse-Width Modulation
q	Stability Criterion (Q-Vortex Model)
Q	Volumetric Flow Rate
Q	Velocity Profile Parameter (Q-Vortex Model)
S	Momentum Flux (Benjamin Model)
St	Strouhal Number
r	Radius
r_o	Inviscid outer vortex core diameter
r_v	Viscous inner vortex core diameter
R	Swirl Velocity Ratio (Tangential Vortex Tube)
Re_c	Chord Reynolds Number
Re_d	Diameter Reynolds Number
Re_B	Burst Location Reynolds Number
Re_V	Vortex Reynolds Number
VB	Vortex Burst
u, v, and w	Axial, radial, and angular (or swirl) velocity components, respectively
u_1, u_2	Velocity Constants (Q-Vortex Model)
U_∞	Freestream Velocity
UAV, UCAV	Unmanned (Combat) Air Vehicle

LIST OF ABBREVIATIONS (continued)

x	Streamwise Direction; LE Vortex Axial Direction
x_B	Burst Location
x_{TE}	Trailing Edge x-Location

LIST OF SYMBOLS

α	Angle of Attack
$\mathit{\alpha}$	Velocity Profile Parameter (Q-Vortex Model)
α_{eff}	Effective Angle of Attack
β	Yaw Angle; Vorticity Ratio
Γ	Circulation
$\overline{\Gamma}$	Non-Dimensional Circulation Parameter (Huang Model)
δ	Perturbation
$\mathit{\delta}$	Axial Velocity Profile Parameter (Q-Vortex Model)
$\mathit{\varepsilon}$	Small Amplitude Perturbation
ζ	Half Apex Angle (90 - Λ, degrees)
η	Azimuthal Vorticity
θ_1, θ_2	Light Incident Angle on Surface 1 and on 2
κ	Non-Dimensional Pitch Rate
Λ	Leading Edge Sweepback Angle
ν	Kinematic Viscosity
ρ	Density
τ	Convective Time Constant
Φ	Swirl Angle
$\mathit{\psi}$	Stream Function
ψ	Unperturbed Column Vortex Stream Function
ω	Circular Frequency; Pitching Frequency
Ω	Circulation Number

CHAPTER 1

INTRODUCTION

An experimental investigation was undertaken at Wichita State University in order to quantify the vortex burst behavior of a pitching 70-degree sweep delta wing. The investigation was divided into two main areas. First, the wing was subjected to a variable freestream velocity; second, the wing was subjected to an impinging von Kàrmàn vortex street generated by a cylinder placed ahead of the apex. In order to better understand the flow phenomenon observed in the investigation, as well as its significance, this first chapter will discuss the key concepts and definitions pertaining to the static delta wing flow mechanics.

1.1- Definition

The delta wing (Figure 1.1)* is defined as a thin wing whose triangular planform shape closely resembles the Greek letter Δ [1, 2]. In many cases, the leading edge is beveled to a very small radius (i.e., a "sharp" leading edge). The trailing edge may also be beveled to a sharp edge. It may also be cambered both in the fore-aft direction along the root chord as well as from wing tip to wing tip along the span.

Delta wings have been used on military fighter aircraft and a few commercial transports (e.g., Concorde, Tu-144). Due to the nature of their lift-producing mechanism, delta wings can exhibit very high values of lift coefficient C_L. On the down side, the delta wing is by definition a low aspect-ratio wing, and thus has a lower lift to drag (L/D) ratio than regular wings due to a much shallower lift curve slope. This means that, at low speed, a delta wing must be pitched up higher to attain a given lift, and its drag is much higher. Delta wings are also widely used in

* All Figures are located in Appendix A

fluid dynamics research, in part because they are easily constructed, and because they will readily form vortex structures that are easy to visualize [3].

More recently, very slender delta wings have been used in conjunction with very thin conventional wings on fighter aircraft. These leading edge extensions (LEX) allow combat aircraft enhanced maneuverability and performance when compared to similar designs that do not incorporate an LEX. Research into the phenomena associated with the use of LEX systems has also benefited from delta wing testing.

1.2- Lift Production Mechanism

To illustrate the delta wing's lift-producing mechanism, assume a wing with a 70-degree sweepback is pitched up from an angle of attack, $\alpha = 0$-degrees (i.e., along Line A in Figure 1.2). As α increases, line A crosses four regions, marked I through IV. Each region has distinct flow features. What follows is a general overview of each region and how lift is produced. Detailed discussion of the individual flow features in each region, however, is postponed until later in the chapter.

In region I the delta wing is at low angles of attack ($\alpha < 5$ degrees); the delta wing behaves like a flat plate, and lift production is entirely governed by potential flow. This is the first mechanism [3, 4].

As the angle of attack increases further, it crosses into region II, and the pressure difference between the upper and lower surfaces causes a flow around the leading edge. The flow cannot follow the small radius, and detaches along this leading edge line into a shear layer that curls up into a spiral. The spiral's center is tight enough that it forms, in essence, a pair of strong vortices. These leading edge vortices (or main vortices) induce velocities on the flow field around the delta, which increase the available lift compared to the equivalent flat plate.

As the angle of attack α increases, the greater the pressure difference between upper and lower surfaces, the stronger the main vortices and, hence, the higher the lift. The vortices become the flow field's dominant feature, and form the second mechanism [3, 4] (Figure 1.3).

The additional lift derived from the formation of the main vortices is the result of a vorticity balance condition [5]. At the onset of separation along the delta wing's leading edge, a "local" shear layer between the viscous and inviscid regions forms near the wall. This shear layer is unsteady and, in the process of extracting energy from the freestream flow, generates vorticity [5, 6]. This vorticity is then convected away by the component of the freestream velocity parallel to the leading edge direction. Thus, the main vortices are formed when a balance between the vorticity flux at the wing's surface and the vorticity transport provided by the freestream is reached [5, 7, 8].

To quantify the importance of the main vortices to the generation of lift, the work done by Polhamus to predict the lift of a delta wing will be discussed next. This work [4, 9] is based on the assumption that the main vortices, regardless of their nature, produce suction over the upper surface of the wing. It is restricted to flat delta wings where the initial separation line is fixed at the leading edge. This requires a sharp leading edge. The only other restriction placed on this analogy is that the flow entrained by the main vortices must reattach on the upper surface at some location inboard of the main vortex axis. The total lift and the drag due to lift generated by a flat, non-cambered delta wing is given by

$$C_L = K_P \sin\alpha \cos^2\alpha + K_V \sin^2\alpha \cos\alpha \tag{1.1}$$

$$C_D = C_{DO} + K_P \sin^2\alpha \cos\alpha + K_V \sin^3\alpha \tag{1.2}$$

where K_P is the potential flow coefficient. It is derived from lifting surface theory where the Kutta condition is satisfied at the trailing edge, and K_V is obtained based on the leading edge

suction due to the vortex lift. Typical values for K_P and K_V are illustrated in Figure 1.4. Their interaction and contribution to the total lift produced changes as angle of attack increases. Notice that lift becomes more dependent upon the vortex lift contribution as sweepback angle Λ increases, while at the same time the potential lift term becomes smaller. For a thin delta wing with sharp leading edges and a 70-degree sweepback angle, the Polhamus Vortex-Lift theory predicts that the vortex lift contribution, at angles of attack of interest to aircraft designers, can be as high as 50% of the total lift generated under static conditions (Figure 1.5).

As angle of attack is increased further, the delta wing enters region III (Figure 1.2), and a phenomenon called vortex burst (VB) comes into play. Briefly stated, the vortex burst can be defined as a sudden expansion in radial size of the main vortex, along with an abrupt decrease in the axial velocity of the vortex, and a marked change in the flow's character as it degenerates into a non-coherent, turbulent-like flow. The burst causes a reduction in the lift generated by the delta wing. At angles of attack higher than those where the burst is located above the trailing edge [10] (Figure 1.6), the discrepancy between the Vortex-Lift predictions and the experimental results increases. The vortex burst phenomenon will be discussed in more detail later in the chapter.

If the angle of attack increases further still (region IV in Figure 1.2), the rate of vorticity production outpaces the rate of vorticity convection [5], and the main vortices begin to shed asymmetrically into the flow. The delta wing now behaves like a bluff body in a freestream. The shed vorticity produces fluctuating loads and rolling moments, resulting in a phenomenon [11] called "wing rock." This phenomenon is usually associated with very slender bodies and very slender delta wings. If the wing has a shallow sweepback angle Λ, wing rock may not occur. Rather, at high enough angles of attack, only a turbulent wake may occur.

A delta wing can operate at much higher angles of attack than a flat plate or a conventional wing. On a conventional wing, if the angle of attack is increased beyond about 10 to 15 degrees, flow separation occurs, accompanied by a sharp reduction in lift coefficient and a large increase in drag. On the other hand, a delta wing is producing less lift at that same angle of attack, but the flow is already separated and the mechanism described in the previous paragraphs is already established. The delta wing can be pitched up higher in order to attain a higher lift coefficient.

A secondary vortex system, counter-rotating to the main vortices, forms near the leading edge (Figure 1.3) [12]. Under the main vortices' influence, the boundary layer flows from the primary attachment line towards the leading edge, but separates along the secondary separation line due to the high adverse pressure gradient that exists in the region, and rolls up to form these secondary vortical structures [2]. This causes a series of flow separation and attachment lines to be located on the upper surface, as shown in Figure 1.7.

In a rather simplistic comparison to a regular wing, both devices can be viewed as a means to harness a vortex. In a regular wing, said vortex would be a horseshoe type, where the bound vortex can be thought of as being "embedded" into the wing. On the delta wing, the vortex would be in the freestream [7,8,13,14].

1.3- Nomenclature

In order to communicate efficiently, the nomenclature illustrated in Figure 1.8 will be used. The right leading edge vortex is omitted for simplicity, but is assumed to be identical except in the sense of rotation. A cylindrical coordinate system is established at the apex, and the local velocity components *u, v,* and *w* are aligned with the vortex core's axial, radial, and angular (or swirl) directions, respectively. The swirl angle Φ can be defined as the angle made

between the velocity components *w* and *u*, i.e., the inverse tangent of (*w/u*) [13,14]. This is usually obtained by injecting dye in water or smoke in air at different radial distances from the core centerline.

1.4- The Delta Wing Main Vortex

The flow on and around a delta wing can be divided into several sections:

1) A viscous boundary layer flow near the wing's surface. This boundary layer, which begins at the lower surface of the delta wing, moves towards the leading edge and separates. Similarly, the upper surface has a boundary layer that, under the influence of pressure gradients, either separates or attaches at different points (Figure 1.7).
2) An inviscid flow outside the delta wing's boundary layer and shear layer that rolls into the leading edge vortices.
3) The shear layer that separated from the leading edge. This region serves to transport vorticity to the leading edge vortices.
4) The vortex core.

The vortex core is almost axisymmetric and has strongly coupled axial and swirl velocity components. It has a nearly continuously distributed vorticity, and may be highly receptive to external disturbances [15]. The core's size increases with distance along the downstream direction up to the point where burst occurs, yet the ratio of size to chord length is essentially independent of chord Reynolds number, Re_c [15]. The physical location of the leading edge vortex, with respect to the wing, is independent of Re_c.

This core itself can also be broken down into two regions: viscous subcore between r= 0 and r= r_v, and an inviscid outer core between r= r_v, and r= r_o (Figure 1.9) [16]. For air, this viscous subcore has a radial size of approximately $0.1\ r_o < r_V < 0.2\ r_o$. The vortex core's size has been reported by some researchers to be on the order of 10% of the wing span or less [16].

The velocity profiles measured, for the axial component *u* and the swirl component *w* in terms of the freestream velocity U_∞, are shown in Figures 1.10 and 1.11. In the axial direction, the profile is similar to that of a typical jet, with a very high peak axial velocity. Similarly, the swirl component also exhibits a typical profile associated with a potential vortex with a viscous core. The velocity components can be fitted by the equations

$$u(r) = U_1 + U_2 \exp\left(-Cr^2\right) \tag{1.3}$$

$$w(r) = \frac{V_1}{r}\left\{1 - \exp\left(-Cr^2\right)\right\} \tag{1.4}$$

The constants U_1, U_2, V_1, and C can be found for a specific experiment [17].

The suction created by the leading edge vortices on the delta wing's upper surface is related to the circulation Γ, induced by the leading edge vortex system. Some have postulated the magnitude of Γ grows linearly in the axial direction, upstream of the vortex burst location [18]. In another set of experiments [19], while the circulation did grow linearly with chord position, there was a value of α above which this linearity broke down. The authors have suggested it is possible that the measurements at high α may have included the influence of the secondary vortex. Visser and Nelson [18] reported that the Γ of the secondary vortex can be as much as 10-15% of the value of the main vortex under certain conditions. Because it rotates in the opposite direction to the main vortex, its inclusion would result in a drop in total measured circulation. According to Johari and Moreira [19], the growth rate dΓ/dx increases with angle

of attack and half-apex angle ζ. More important, the total circulation measured does *not* decrease as the vortex burst moves past the measurement location. Thus, it appears that the bursting process has *no* direct influence upon the total circulation [19].

1.5- Vortex Burst

The main leading edge vortices are unstable in the sense that they are unable to maintain their tight structure indefinitely, and eventually break down (or burst). There are two general categories of burst.

In the first category falls what is called a "bubble" burst, or B-type burst. The most apparent feature is a sudden axisymmetric expansion in the radial size of the vortex, to a diameter many times its original. Also, the axial velocity u, which has been increasing almost linearly along the streamwise direction to a peak value (as much as $u/U_\infty \geq 3$) [20], decreases in a very short distance (about 1 to 2 core diameters) [17] and may form a free-stagnation point at the vortex burst point [13]. The flow's character degenerates into a non-coherent, turbulent-like wake believed to contain not only turbulent components from the free-stream, but also disturbances and other perturbations originally embedded within the vortex before the breakdown event [20]. In vortex tube experiments, this type of vortex burst may also include a secondary stagnation point further downstream of the burst, forming a closed bubble [21]. Within this bubble, a region of recirculating flow is observed.

The second category is known as the spiral burst, or S-type. In its most common manifestation, the S-type form results from the vortex core's transition into an expanding spiral corkscrew that rotates in the same sense as the original leading edge vortex [13]. Both spiral and bubble bursts are observed in delta wing flows, but the S-type is observed more frequently [21, 22] (Figure 1.12).

The vortex burst results in a loss of lift affecting the wing from the point where the burst is located, and continues in the streamwise direction towards the trailing edge. As the vortex burst location moves towards the apex (e.g., with increasing α), there is a reduction in the vortex lift contribution from the leading edge vortex. This is due to a reduction in the suction peak that occurs as a consequence of the leading edge vortex.

Vortex bursting is not a phenomenon restricted to delta wing vortices; rather, it is a feature present in vortex filaments, ranging from trailing vortices in wings, vortex tubes, cyclone separators, and delta wings [21]. Furthermore, the location in space where the burst occurs is not fixed, but oscillates periodically, both along the axial direction and in the crossflow plane [23] (Figure 1.13), in response to the "crowding" of the post-burst regions [24, 25]. In the axial direction, this fluctuation is mostly out of phase (i.e., the left leading edge vortex burst moves forward, the right moves aft). It occurs in the range of $0.04 < fc/U_\infty < 0.1$ over a Re_c range from 40,000 to 2.6×10^6. The amplitude can be as large as 10% of the root chord length in some cases [25, 26]. In most cases, the time-averaged position where the burst occurs is used when reporting results.

A lot of research has been devoted to investigating the vortex burst phenomena because of its deleterious effect on the lift generated, the coherent structure of the vortex, and the fluctuations it causes on nearby aircraft structures (tail, stabilizers, support struts, etc). To better understand the behavior of vortices undergoing bursting, researchers have attempted to replicate vortices in a more controlled environment, either by using vane generators (Figure 1.14, a) or tangential-entry generators (Figure 1.14, b) [17]. These types of vortices will be referred to as "artificially generated" vortices to distinguish them from leading edge, or "delta generated" vortices.

Four important parameters are introduced at this point. These are the Reynolds number based on the vortex tube diameter, the circulation number, the swirl velocity ratio, and the vortex Reynolds number, respectively,

$$Re_d = uD / \nu \tag{1.5}$$

$$\Omega = \Gamma / uD \tag{1.6}$$

$$R = Q / \pi L \tag{1.7}$$

$$Re_V = \Omega\, Re_d = \Gamma/\nu \tag{1.8}$$

where D is the tube diameter, *u* is the mean axial velocity, Q is the volumetric flow rate, and L is the inlet slot's length in tangential entry type devices [27]. The parameter R is really the ratio of radial to tangential velocity at the inflow section of the vortex tube.

There are important differences when comparing artificially generated vortices to the leading edge vortices:

1) In the case of delta wings, the vorticity accumulates and grows almost linearly in the streamwise direction. The vortex core diameter is independent of Re_c [18, 19].
2) Artificial generators have constant vorticity once the flow is established and a stable vortex is formed [17].
3) In a vane-generated vortex, the size and strength is dependent on the tube-diameter Reynolds number, Re_d, and the flow's circulation number. The core diameter is proportional to $(Re_d^{-½})$ [17].
4) In the tangential-entry devices, the total circulation of the vortex is fixed by the roll-up process in the upper part of the device. The core diameter, unlike the vane-type generators, is almost independent of the Re_d [27].

5) Escudier [27] makes the argument that, on vane-type devices, R remains constant as the circulation number increases. The influences of Ω and R cannot be separated. This is not the case in tangential-entry devices.

Within this framework, results derived from artificially generated vortices have shed some light into the leading edge vortices' behavior. On vane-type vortex tubes, it has been found that:

1) The volumetric flow and the amount of swirl affect the location and type of resulting burst. Referring to Figure 1.15, there appear to be four distinct states of swirling flow. Assuming the tube's Reynolds number, Re_d, is sufficiently large to overcome the stable region (Region IV), a high amount of swirl results in the B-type burst (Region I) [21]. For smaller swirls, the axisymmetric breakdown occurs at higher Re_d values. When the Re_d is small, the burst is most likely to be of the S-type (Region II). For a constant Re_d number in vane-vortex filaments, S-type bursts occur at lower values of circulation than B-type bursts.
2) There is a region where hysteresis occurs, i.e., changing the conditions does not change the type of burst, only the location. In this region, both types of burst are sensitive to external disturbances introduced upstream [28].
3) There is a definite region, when the Re_d number is between 1000 and 2000 (Region III), where a third type of vortex burst appears. This type, the H-type, forms 2 helical surfaces, and appears to be a pure helical instability.
4) The burst location moves forward, upstream towards the tube's inlet as the Re_d or the circulation increases. The burst type is predominately of the B-type as the burst moves upstream (Figure 1.16) [28].
5) The swirl angle Φ measured in vortex tubes at a point just before the breakdown event (Figure 1.17) shows that, for the B-type burst, the maximum angle is about 50^o and is

independent of Re_d and circulation number. For the S-type, the maximum angle depends on the circulation number.

6) The burst location changes in response to pressure gradient. The adverse pressure gradient resulting from a diverging tube moves the vortex burst position upstream towards the tube's inlet [29].

7) On tangential-entry type vortex tubes, Escudier has found that

$$\Omega^3 R Re_B = \text{constant} \tag{1.9}$$

where Re_B is the Reynolds number based on the physical distance from the flow's entry point to the burst location,[27]

$$Re_B = U_\infty X_{burst} / \nu \tag{1.10}$$

This compares to the behavior observed on delta wings:

1) An adverse pressure gradient triggers the burst earlier (i.e., closer to the wing's apex), while favorable pressure gradients tend to delay the burst. A delta wing flying at a small angle of attack will experience the vortex burst closer to the trailing edge, while a large angle of attack will result in the burst position being closer to the apex, as shown in Figure 1.18 [30]. The introduction of chordwise camber, or any other method of altering the pressure gradient will affect the burst location as well.

2) In delta wing flows, the S-type vortex burst is more predominant, while the B-type only occurs at higher α. This is probably because the leading edge vortices are only able to attain certain circulation values [17]. Similar to the hysteresis region in vortex tube experiments, the delta wing vortices exhibit a hysteresis region. The exact angle of attack limits of this region depend on the wing's geometry: this author has observed it in the range between 30 to 40 degrees or so for a 70-degree sweep. In this range, the burst type and

location depends on whether the angle of attack is *increasing* or *decreasing*. Others have reported this hysteresis region in an angle of attack range from 35 to 45 degrees, but have not specified the geometry of the wing used [28].

3) The swirl angle Φ is given by the ratio of *w/u*. It can be assumed that these velocities are related, in turn, to the velocity components parallel (influences convection) and perpendicular (influences circulation) to the leading edge. They are, as shown in Figure 1.19, dependent upon geometric factors. As the delta wing's angle of attack α increases, the velocity component perpendicular to the leading edge decreases.
4) Changing the yaw angle changes the local leading-edge sweep, which in turn causes a change in the velocities, producing unequal amounts of circulation in the vortices on the two sides. This causes one of the vortices to burst upstream, closer to the apex, while the other bursts further downstream.
5) As the angle Λ increases, the velocity component parallel to the leading edge increases, changing the ratio. The more slender the delta wing, the higher the angle of attack α for a given vortex burst location.

1.6- Vortex Breakdown Theories

No one theory can completely explain the bursting process. Through the years several theories as to why the vortices degenerate and burst have been put forth, yet there is no one theory which can completely explain all the observed phenomena regarding the bursting process [31]. In fact, it has been suggested that two or more mechanisms may be present and that each becomes dominant under certain conditions [17, 21].

1.6.1- Spiral Instability Theory

The vortex breakdown is the result of hydrodynamic instability. Ludwieg proposed that the vortex burst is due to spiral instabilities that become amplified until a critical amplitude is reached [13, 14]. At this point the flow transitions to a new pattern, similar to the Tollmien-Schlichting waves that, when amplified, force the laminar boundary layer to transition to turbulence [32].

According to Ludwieg, a helical flow of annular cross-section and small height (i.e., a gap between two cylinders) is sensitive to spiral disturbances. A set of velocity gradients are defined,

$$C_\theta = \frac{r}{w}\frac{dw}{dr} \tag{1.11}$$

$$C_x = \frac{r}{w}\frac{du}{dr} \tag{1.12}$$

The flow becomes unstable (stratified) if the following condition applies [13],

$$(1-C_\theta)(1-C_\theta^2) - (\,^5/_3 - C_\theta)\,C_x^2 < 0 \tag{1.13}$$

Even though the original theory is derived for an annular type flow, it has been applied to many different types of vortical flows. In delta wing leading edge vortices, it has been used to predict the vortex burst phenomenon of slender wings, but diverges as Λ decreases [13].

Experiments by Sarpkaya [28] have shown that at certain combinations of low Reynolds and large circulation numbers a double-helix type of burst occurs. This would appear to prove that there are certain spiral instabilities that, when the conditions are correct, manifest themselves.

Unfortunately, there are two main problems with this theory. First, the spiral instability theory is unable to explain the axisymmetric breakdown. Second, the conditions required for this type of mechanism are not found in many cases; bursts have been predicted in flows where no bursting occurs, or in flows that have been shown to be theoretically stable upstream of the burst point [17].

1.6.2- Core Stagnation Theory

An adverse pressure gradient slows down the core's axial velocity. Conservation of momentum requires the size of the vortex to grow, but the proximity of a solid boundary (the wing surface) precludes this. Physical inability of the vortex to grow in radius as the core slows down produces the breakdown [31]. This particular theory, however, requires the existence of an external pressure gradient for the vortex burst to occur, but busting can and does occur in the absence of pressure gradients.

1.6.3- Conjugate States Theory

A vortex can become a fluid-mechanical waveguide that can support energy-dissipating waves. In this theory, a series of wavelets are superimposed on an inviscid, stable vortex core. The velocity of said wavelets is dependent upon the wave's strength. The amplitude of these waves is magnified by the work of pressure gradients, while viscosity tends to dissipate their energy.

Squire (in 1960) first proposed that a series of infinitesimal standing waves could be superimposed on an inviscid cylindrical vortex flow with constant wave propagation characteristics [33]. Since standing waves of indefinite, but great length, would be the first to form as the swirl velocity increased, he proposed that the limiting condition for the existence of such waves be the trigger for the vortex breakdown [33]. Beginning with the continuity and the

Euler equations for a steady, incompressible, axisymmetric flow, where the cylindrical coordinates are as shown previously in Figure 1.8, the following stream function relationships are substituted,

$$v = -\frac{1}{r}\frac{\partial \psi}{\partial x} \tag{1.14}$$

$$u = \frac{1}{r}\frac{\partial \psi}{\partial r} \tag{1.15}$$

The following equation, known as the Bragg & Hawthorne Equation (BHE), is then derived,

$$D^2\psi = \frac{\partial^2 \psi}{\partial r^2} - \frac{1}{r}\frac{\partial \psi}{\partial r} + \frac{\partial^2 \psi}{\partial x^2} = r^2\frac{\partial H}{\partial \psi} - \Gamma\frac{\partial \Gamma}{\partial \psi} = r\left(\frac{\partial v}{\partial x} - \frac{\partial u}{\partial r}\right) \tag{1.16}$$

where ψ is the stream function in terms of (r,x), $\Gamma = wr = f(\psi)$ is the circulation, $H = P/\rho + {}^1/_2(u^2 + v^2 + w^2)$ is the total pressure [33, 34]. The last right-hand term in parenthesis is the vorticity's azimuthal component. Equation 1.16 is the basic starting point for all theoretical analyses on cylindrical vortex flows.

Given equation (1.16) in principle it is possible to calculate the flow's evolution, provided that H and Γ are known at some point. However, it is difficult to measure these quantities. By assuming (1) that the axial velocity u to be constant ($u = u_o$), and (2) splitting the stream function into two components, $\psi = \psi_o + \delta$ (where ψ_o is a constant determined by the first assumption, and the term δ represents a perturbation), equation (1.16) can be reduced,

$$\frac{\partial^2 \delta}{\partial r^2} - \frac{1}{r}\frac{\partial \delta}{\partial r} + \frac{\partial^2 \delta}{\partial x^2} + \left\{\frac{1}{r^3 u^2}\frac{d\Gamma^2}{dr} - \frac{1}{u}\frac{d^2 u}{dr^2} + \frac{1}{ru}\frac{du}{dr}\right\}\delta = 0 \tag{1.17}$$

To complete the solution, a set of boundary conditions is needed. These depend on the type of flow (e.g., leading edge delta, column vortex, etc). and the velocity distributions involved. At this point Squire assumed three different, but physically plausible, swirl velocity

distributions. A range of maximum swirl angles Φ was predicted, between 43 and 50 degrees [21]. These predicted swirl angles have compared favorably with experiments [13, 21].

The problem with the Squire solution is that the wave's group velocities are directed downstream, and cannot propagate upstream (i.e., the flow is supercritical). To allow the waves to travel upstream, it is necessary that the flow be subcritical [33]. This requirement can be used to define a criticality criterion. The absolute velocity of a very long wave propagating in the direction of the flow can be denoted as c^+, while a wave propagating against the flow is denoted as c^-. The positive direction is the flow's direction. A general definition for criticality can then be stated,

$$N = \frac{c^+ + c^-}{c^+ - c^-} \tag{1.18}$$

Waves approaching from upstream towards the downstream direction have necessarily positive values of c^+. The velocity c^-, on the other hand, can have either positive or negative values. Thus, supercritical and subcritical flows will have values of $N > 1$ and $N < 1$, respectively.

In Benjamin's model, the starting point is again equation (1.16). While the exact derivation will not be repeated here, Benjamin established two important features for cylindrical vortex flows with no radial velocity v. First, for any physically possible flow, the curve ψ must represent the extreme of the momentum flux, or "flow force" (as Benjamin calls it) for a cylindrical flow bound at a radial distance a,

$$S = 2\pi \int_0^a (\rho u^2 + \mathrm{P}) \mathrm{r} d\mathrm{r} \tag{1.19}$$

Second, the stream function ψ can have two distinct values, say ψ_A and ψ_B. The two satisfy the original flow, coincide at an end-point, and have very similar values of *S*. As such, momentum is conserved except for what is dissipated by the wave action [33].

Two conjugate, sequential flow regimes must exist: the flow upstream of the burst location has to be supercritical, while the flow in the post-burst region is subcritical [33]. Disturbances in the flow downstream of the burst location produce waves that propagate upstream until the wave velocity matches the oncoming stream velocity. At this point, the waves coalesce and force the vortex to burst.

Vortex bursting occurs when the transition from supercritical to subcritical flow is achieved. It is sudden, spatially concentrated, irreversible, and sensitive to downstream conditions. These features are similar to those observed in the hydraulic jump in an open channel flow, or a supersonic flow undergoing a shock wave deceleration to a subsonic regime.

The problem with Benjamin's theory of conjugate states is that the momentum loss is necessarily small for *S* to match between the supercritical and subcritical regimes. The second problem is that it cannot relate to experiments where the wake is unsteady and non-axisymmetric [34].

Work by Leibovich considered perturbations to a primary flow $\psi(r)$ that incorporated both axisymmetric and non-axisymmetric traveling/rotating waves. Beginning with axisymmetric waves of small but finite amplitude propagating in a columnar vortex of the form,

$$\psi = \psi(r) - \varepsilon \phi_0(r) A(x,t) \tag{1.20}$$

where $\psi(r)$ is the unperturbed flow's stream function, ε is a small amplitude parameter, and $\phi_o(r)$ is an eigenfunction, it was found that the amplitude function A satisfies the Korteweg-deVries Equation [34],

$$\frac{\partial A}{\partial t} + c_o \frac{\partial A}{\partial x} = \varepsilon \left\{ \alpha A \frac{\partial A}{\partial x} + \beta \frac{\partial^3 A}{\partial x^3} \right\} \tag{1.21}$$

where α and β are constants determined by the unperturbed flowfield. The important findings are the following [34]:

1) If ε is assumed small and positive, then a solitary wave of permanent form, a soliton, is a solution to equation (1.21).
2) The wave propagation velocity is dependent on the wave amplitude. As a consequence, the solitons are stationary if the flow is supercritical.
3) If the flow is only slightly supercritical, non-linear solitons are possible.
4) If any value of ε is allowed, then the solution will describe stagnation points and axial flow reversal.

Further work by Leibovich in non-linear waves of finite amplitude and wavelength indicates that the breakdown is associated with the loss of stability of axisymmetric waves to non-axisymmetric perturbations [34].

Work by Maxworthy [35] on vortex tubes, suggests that, while there are several possible types of dissipative waves (solitons, kink waves, standing waves, and axisymmetric waves), only axisymmetric waves have been shown to disrupt the vortex in experiments. In experiments on columnar vortices, increasing the amplitude of core-formed axisymmetric waves results in an increase in sensitivity to spiral (non-axisymmetric) disturbances.

Applying the BHE equation (1.16) to a Burgers vortex (one where the axial velocity distribution is constant) and linearizing results in 4 general solutions or branches: columnar solutions, solitons, periodic wavetrains, and soliton/conjugate flow superpositions. One important result is that achieving criticality in the flow does *not* imply stagnation.

1.7- Prediction of Vortex Burst Location in Static Flow Conditions

It is important to quantify the most probable location where the vortex burst will be located as a function of angle of attack and sweep angle. The loss of lift and change in pitching moment results from the burst point's progression. Being able to predict the burst behavior can be used to predict the behavior of the aerodynamic forces and moments. It is also important because the change in the character of the post-burst flow may impact both the flow quality and fatigue life of structures nearby (e.g., tail surfaces). Finally, there is still some difficulty in completely understanding the mechanisms involved in the burst process, in evidence by the lack of a cohesive and all-inclusive burst theory.

1.7.1- Helical Instability Criterion

Ludweig (in 1960) assumed that the disturbances were the result of helical instabilities present in the flow, and a function [13] of the vortex core edge velocities, denoted by the subscript "o",

$$\frac{w_{\mathrm{o}}}{u_{\mathrm{o}}} = \frac{\sqrt{\mathrm{K} + 0.5}}{\mathrm{K}} \tag{1.22}$$

It can be shown that the profile parameter K is related to the swirl angle Φ at the core's edge.

Ludweig's stability criterion states that the non-dimensional velocity gradients (from equations (1.11) and (1.12)) in the cylindrical and axial directions (C_θ and C_x, respectively) is such that, as shown in Figure 1.20, for any $\mathrm{K} < 1.16$ the vortex will destabilize into the first

helical mode instability. The action of an adverse pressure gradient, a change in vorticity, or some other mechanism can cause the axial velocity u to decrease. This would cause K to decrease. At some point, u has dropped such that K crosses over the critical boundary, and spiral burst becomes likely [13, 14].

Experimental results (Figure 1.21) show that there is a stability boundary for spiral vortex breakdown at K=1.16, but that observed breakdown can occur at profile parameters lower than the critical value.

1.7.2- Q-Vortex Model

First proposed by Lessen, and refined by Leibovich [34, 36], a general model of a leading edge vortex velocity profile can be constructed using the following model

$$u(\mathrm{r}) = u_1 + u_2 \exp(-\alpha \mathrm{r}^2) = u_1\left[1 + \delta \exp(-\alpha \mathrm{r}^2)\right] \tag{1.23}$$

$$w(\mathrm{r}) = \frac{Q}{\mathrm{r}}\left[1 - \exp(-\alpha\, \mathrm{r}^2)\right] \tag{1.24}$$

$$q = \frac{Q\sqrt{\alpha}}{u_2} \tag{1.25}$$

where the factors Q and α are related to the particular velocity profile as shown in Figure 1.22. The factor δ determines if the flow in question has a jet-like profile (δ>1) or a wake profile (δ <1). Of particular importance, the parameter q is related to the ratio of axial to azimuthal vorticity. The parameter q can be used to classify the flow into three categories:

$q > 1.4$	Unconditionally stable
$1.4 > q > 0.4$	Prone to 3-dimensional instabilities
$q > 0.4$	Stable to axisymmetric instabilities

This parameter space compiled by Leibovich is shown in Figure 1.23. This model is now called the *Q-vortex*.

1.7.3- Circulation Criterion

This model is based on empirical evidence from experiments where the leading edge vortices' circulation was measured for a variety of configurations [30]. In its most usual form, the vortex breakdown is related to the circulation in terms of geometric properties (angle of attack α and sweep angle Λ or half-apex angle ζ). For example, Lambourne and Bryer (in 1962) proposed a simple relationship based on the angle γ between the leading-edge and the freestream velocity vector U_∞ [30]. Vortex burst would occur if γ increases above a critical value, $\gamma_{critical}$,

$$\gamma = \cos^{-1} (\cos \alpha \sin \Lambda) < \gamma_{critical} \tag{1.26}$$

This relationship suffers from large scatter at high angles of attack, when the burst is near the apex.

Another relationship, attributed by Gursul to Jumper et al. [30], is based on the circulation increasing linearly with streamwise direction up to a point, such that the burst would occur when the circulation reaches a critical value,

$$\Gamma_{vb} / U_\infty c = 0.132 \tag{1.27}$$

This particular relationship is very good at higher angles of attack, but suffers from increasing scatter at lower angles.

A more complex predictor proposed by Huang et al. [37] suggests the use of a parabolic circulation distribution along the chord, such that a non-dimensional circulation parameter is defined as

$$\overline{\Gamma}(\alpha, \Lambda, x) = \frac{\Gamma}{U_\infty c} = C_o + Bx - Ax^2 \tag{1.28}$$

where the variables are,

$$A = 0.7\text{-}1.17 \sin(90\text{-}\Lambda) + 3.66 \sin^2(90\text{-}\Lambda) \tag{1.29}$$

$$B = 2A \tag{1.30}$$

$$C_o = \overline{\Gamma}\Big|_{\frac{X}{C}=1} - B + A \tag{1.31}$$

$$\overline{\Gamma}_{critical} = -0.3 + 6.82\sin(90-\Lambda) - 10.26\sin^2(90-\Lambda) \tag{1.32}$$

The term C_o contains the non-dimensional parameter $\overline{\Gamma}$, which is evaluated at the trailing edge**.** Vortex burst would then occur when the non-dimensional circulation in equation (1.28) equals the critical value in equation (1.32). This relationship has a better fit, and thus is actually useful as a vortex burst predictor (Figure 1.24).

1.7.4- Negative Vorticity Onset Criterion

Theoretical work done by Brown and Lopez on a columnar vortex structure [38], and further substantiated by experiments on actual delta wing vortices [39], suggests that

1) Only the azimuthal vorticity component, $\eta = \partial v/\partial x - \partial u/\partial r$, is involved in the induction of the axial velocity *u*. The relationship between the vorticity field and the induced velocities is given in Figure 1.25.
2) The increase in *u* is induced most by the local component of η, because any contribution from vorticity in the far field decays rapidly [38] (recall from the Biot-Savart law that the effect diminished to the r^{-3}).

3) The velocity u can only become zero or negative at some location x if the azimuthal vorticity η becomes negative [38]. In delta wing experiments, regions of negative η have been found upstream of the vortex burst stagnation points [39].

4) An angle is defined in terms of vorticity as $\tau = \tan^{-1}(\eta/\omega_{axial})$. This angle τ is analogous to the swirl angle Φ. It appears that an increase in Φ, such that $\Phi > \tau$, is necessary in order to change the sense of the azimuthal vorticity component. As $\Phi/\tau > 1$, η decreases and becomes negative at some radial distance. The higher the ratio of Φ/τ, the shorter the radial distance needed for η to become negative [38]. The appearances of negative azimuthal vorticity regions in the vortex flow field are good indicators that vortex bursting will occur in some close proximity to these regions.

CHAPTER 2

DYNAMIC DELTA WING

While the mechanism that causes vortex bursting is not entirely understood, the *behavior* of the burst under *static* conditions, i.e., when the angle of attack is fixed and the freestream velocity is constant, is well understood. Delta wings are being used more and more, either alone or in combination with conventional wings, on highly maneuverable combat aircraft. This has created an interest in the study of the vortex burst's behavior under *dynamic* conditions where the angle of attack is a function of time.

2.1- Dynamic Vortex Burst Behavior

Results from different authors indicate that the pitching of the delta wing produces a vortex burst behavior different than what has been observed during static testing. A delta wing pitching up will produce a vortex burst that lags *behind* when compared to the burst position at the same angle of attack α under static conditions. This lag has the effect of prolonging the amount of time needed for the vortex burst to move from the trailing edge to the wing's apex. The amount of lag *increases* as the rate of change of the pitch-up ($\omega = d\alpha/dt$) increases, resulting in an enhanced lift-producing ability as the wing is pitched up faster, and an increase in the angle of attack range available for the pitch-up maneuver. As a consequence, comparison of the lift generated, on an angle of attack basis, shows that the pitch-up maneuver results in an increase in lift compared to the static condition [41].

The opposite is true when the wing is being pitched down, and the dynamic vortex burst position now leads *ahead* of the static burst position. This results in a decrease in lift. As the pitch-down rate increases, the burst position lead increases, resulting in decreasing lift-production (Figure 2.1).

The result of the burst position lead-lag as angle of attack changes is a hysteresis loop whose area increases as the rates and/or range of the pitch excursions increase, or if the frequency of the excursions increases. The contribution to this hysteresis area becomes smaller on the pitch-up branch as the pitch rate increases, i.e., the curves eventually begin to collapse on each other. The contribution from the lower branch, the pitch-down, does not exhibit this behavior. It becomes apparent that to maximize the benefit resulting from the hysteresis, rapid pitch-up motions, followed by very slow pitch-down rates, are needed [41, 42].

Leading edge sweep angle Λ affects the velocities that, in turn, generate the vorticity and circulation responsible for the leading edge vortex. As the angle decreases (or the half-apex angle increases), the effect from the dynamic pitch-up/down motion becomes less on the vortex burst location. In fact, if the sweep is sufficiently small, the wing flow will completely detach and shed the leading edge vortices in response to the pitching behavior [43].

2.2- Phase Lag Causes

In the delta wing flow field, the vortex burst's position is affected primarily by two factors: the swirl angle Φ and the pressure gradient. The angle Φ comes from the ratio of axial velocity u induced by the azimuthal vorticity and the swirl velocity w that results from the circulation. The pressure gradient results mostly from geometry, such as camber and angle of attack α. The physics behind the phase lag have remained unclear, although these two factors have been used as a starting point for several possible explanations.

An explanation put forth by Ericcson [44] indicates that the angle of attack changes by the wing's pitching motion, such that an *effective* angle of attack is introduced into the picture. If the delta wing is pitched about the trailing edge, then the effective angle of attack α_{eff} seen at any position x along the streamwise direction is given by

$$\alpha_{eff} = \alpha(t) - \omega(x_{TE} - x) / U_\infty \quad (2.1)$$

where $\alpha(t)$ is the angle of attack as a function of time. This change in effective angle of attack is therefore similar to an increase / decrease in the delta wing's camber, depending on the direction of the pitch motion (Figure 2.2). This pitch-rate-induced camber effect appears to be self-limiting, i.e., it saturates as higher pitch-up rates are imposed, and explains the behavior of the hysteresis curves on the upward branch [45].

Another possible explanation for the phase lag observed in dynamic delta wing aerodynamics is proposed by Gursul [46]. Recall from Chapter 1 that the vortex burst may be the result of an equilibrium being reached between waves propagating upstream in the subcritical flow of the post-burst with a group velocity C_g, and the axial velocity in the vortex core u. The velocity C_g is dependent on the wavenumber k. For example, a column vortex with no axial velocity has a dispersion velocity in the long wave limit of approximately

$$\omega = C_g k \left[1 + 0.1729 \, (k r_o)^2 \ln (k r_o/2)\right] \quad (2.2)$$

For a constant frequency ω, as the wave number k increases, the group velocity $C_g = \partial\omega/\partial k$ decreases. Thus, there is a difference in the group velocities on a dynamic pitching delta wing compared to the static delta wing, say ΔC_g. Referring to Figure 2.3, as the wing pitches up, the group velocity C_g is smaller than the static group velocity C_{go} by an amount ΔC_g. For a given angle of attack, the equilibrium position is farther downstream. Thus the vortex burst lags behind the static case equivalent. Similarly, on pitch down, the equilibrium position is forward than the static case [46].

The problem is that ΔC_g is not known *a priori* for the experiment; it can be obtained from the results by backtracking the derivatives dC_g/dx_B and $dx_B/d\alpha$, such that

$$\Delta C_g = \frac{dC_g}{dx_B}\frac{dx_B}{d\alpha}\omega t \tag{2.3}$$

2.3- Time Scales Involved in the Dynamic Delta Wing

The amount of time required for a disturbance on the leading edge to become entrained and convected to the core changes with chord location. This is due to the vortex core being closer to the leading edge at the apex than at the trailing edge. Because of this, the time involved is almost immediate at the apex, and increases in the chord-wise direction [5]. The vortex core is thus most sensitive to disturbances at the apex.

A second time scale involves the transport of disturbances along the vortex core in the streamwise direction by the axial velocity. This time scale is approximately given by $\tau = c/U_\infty$ [5, 45]. This time scale is the limiting factor in the system's ability to convect new vorticity from the leading edge along the core [5].

A third time scale to consider is the amount of time it takes a vortex to reach equilibrium in the presence of breakdown. In static conditions, the vortex may take a long time (compared to the other time scales presented in dynamic pitching) [44]. The implication is that the vortex burst's location at the beginning of the dynamic pitching phase can affect significantly the evolution of the hysteresis loop [44]. Thus, the starting angle of attack and the range of the dynamic excursion (either pitch-up or pitch-down) may have an effect on the burst location as a function of time.

A fourth time scale involves the length of time for the post-burst flow field to affect the delta wing's surface. This becomes important when dealing with the *loads* and the consequential effect on pitching moment and the non-linearities thereof under dynamic conditions [45].

The interaction of these time scales produces some non-linearities. The following has been observed:

1) Pitch-rate-induced camber is proportional with frequency [45].
2) Rate-induced effects on the magnitude of force and moments are highly non-linear, becoming saturated at moderate pitching rates [47].

As the delta wing is pitched, there is a change in the vorticity generated at the leading edge. If the rate is sufficiently high, a developing vortex may form along the leading edge (Figure 2.4) [44]. This vortex will convect along the shear layer and become part of the leading edge vortex.

2.4- Other Dynamic Delta Wing Experiments

On static tests of delta wings and canards, there are two mechanisms that work to delay the main wing's vortex burst behavior:

1) The canard's flow field produces a downwash on the main delta; this reduces the main delta wing's effective angle of attack, delaying the vortex burst episode.
2) Due to the main wing's influence on the flow field, the canard's vortices are drawn towards the centerline, following a path slightly inboard of the delta wing's main leading edge vortices. The direction of the canards circulation is the same as the main delta, but because they are located inboard, the velocity induced by the main vortex is reduced by the velocity

induced by the canard's vortex. The result is a reduction in the main vortex swirl velocity component, thus delaying the burst [48].

Myose et al. [49] have tested delta wings undergoing dynamic pitching in the presence of a canard. With the canard on the same plane as the main wing, they have shown that there is an increase in the phase lag of the burst position during pitch-up. This lag increases as the canard is brought closer to the apex. The same effect was also noticed during the pitch-down phase. The results also show the phase lag decreases as the pitch-up rate increases, which is consistent with the pitch-rate-induced camber effect saturating at higher frequencies. The canard's sweep angle was not shown to have a large effect on the vortex burst delay during dynamic pitching; no attempt was made to separate the effects due to changing the area or the aspect ratio as the sweep angle was varied.

Extrapolating from the general effect of pitching on a simple delta flow field, it is reasonable to expect that the pitch-rate-induced camber effect applies to both the canard and the delta wing. This reduces the effective angle of attack and delays the burst on the canard, which in turn exposes a larger portion of the main vortex to the unburst canard's vortex.

2.5- Dynamic Freestream Effects

There are several factors that come into play when the freestream velocity U_∞ is not constant:

1) There is a forward movement of the burst position towards the apex as the wing accelerates. Lee & Ho have stated that the time lag in the stabilization of the vortex burst position while a delta wing accelerates is due to a favorable pressure gradient forming. This increases the vorticity flux and circulation of the leading edge vortices. This results in the burst moving upstream [5].

2) Reducing the U_∞ results in a lower Re_c number. It has been reported that this change produces either no change in the behavior of the vortex burst position, or at the very least has produced a very minimal change. This is probably due to the sharp leading edge producing a well marked primary separation point, irrespective of the Re_c. Furthermore, it has been observed that the vortex burst position is approximately the same for a *static* angle of attack over a wide range of Re_c values (from 10^4 to 10^6). This occurs whether the test fluid is air or water, *provided* the burst position is over the delta wing's surface [15].
3) The secondary vortex is subject to the effects of changing the Re_c, as its separation point is not defined by a geometric discontinuity. In particular, it has been reported that *non-slender* delta wings exhibit strong secondary vortices at Re_c = 8000 and an Re = 14000 [50]. It would be expected that interactions between a strong secondary vortex and the LE vortex would be stronger, and thus may affect the vortex burst location. This information would be important to MAV and UCAV designers, and may shed some light into some non-linear interactions observed at higher Re_c numbers as well [50].
4) Gursul and Ho found that, when the burst is located near the delta wing's trailing edge, the position becomes sensitive to freestream velocity disturbances [51].
5) A specific type of perturbation in the shear layer, the Kelvin-Helmholtz (K-H) instability, does not arise at Re_c values lower than about 20,000 to 40,000 [24, 52]. This instability is due to the velocity differential across the shear layer, such that any small change in the layer produces pressure gradients that tend to amplify this original perturbation [53]. The result is a series of small co-rotating vortices being shed at a regular interval. These co-rotating vortices become embedded within the shear layer, parallel to the leading edge, and

eventually become part of the leading edge vortex [54]. Temporal analysis indicates that the frequency associated with this instability is

$$fc/U_\infty = 1{,}625\ (Re_c^{-1/2}) \qquad (2.4)$$

For the instabilities to form, the Re_c of the delta wing flow must be sufficiently high, as the viscosity has the effect of dampening the formation of the K-H instabilities.

6) Work done by Brown and Lopez on columnar vortices indicates that the initial vorticity distribution is Re dependent. While the vortex system's eventual development appears to be Re number insensitive, the original vorticity distribution upstream of the burst point is dependent on the Re number and the energy dissipation which leads to the vortex tube distortion [38].

7) Assume that a column vortex can be analogous to a leading-edge vortex, and if one considers the case of a delta wing that is not in a constant velocity environment, then the previous point has direct implications. The initial vorticity distribution is dependent on Re number, but the subsequent behavior of the vortex is shaped by the balance between vorticity generation and convection away from the leading edge, as well as the vorticity destruction (i.e., energy dissipation) processes that occur. As the freestream velocity increases so does the Re number, and this in turn changes the vorticity distribution. But, increasing the freestream velocity also changes the rate of vorticity generation, vorticity convection at the leading edge, and energy dissipation (since this is a viscous phenomenon). For this example, if the ratio of vorticity generation and convection remains the same, then the change in the LE vortex will be the result of the new vorticity distribution (and subsequent effect on swirl angle) and the rate of energy dissipation. This will become

evident as a transient change in vortex characteristics as energy dissipation reaches a new equilibrium with respect to the new vorticity distribution.

2.6- The "Cobra" Maneuver

An example of a maneuver where vortical flows are subjected to the effects of a simultaneous unsteady freestream and dynamic pitching is the "Cobra" maneuver. First presented in 1989 [55], the Cobra maneuver involves a trade-off in forward velocity as the pitch increases in the vertical plane. This is shown in Figure 2.5 [55, 56, 57]. At the completion of the maneuver, a pitch down maneuver is executed to gain forward velocity. Assuming for a moment that the aircraft in question is the Su-27, the maneuver involves pitching rates up to 70 deg/s, and the angle of attack is increased up to about 110 to 120 degrees in approximately 2 or 3 seconds. The velocity, on average, is reduced from about 350 to 400 ft/s to a minimum of around 100 ft/s, a factor of 4:1. The Cobra maneuver can be divided into 4 phases [58]:

1) In its initial phase, large nose-up pitching moments are demanded of the aircraft by very rapid full elevator-up deflection and thrust vectoring (if available).
2) The second phase, the pitch-up rate decreases as the nose-down pitching moment increases. The aircraft reaches its maximum positive α value through inertia it has built up. At the peak of the maneuver, the negative pitching moment is at its maximum.
3) The pitch-down rate increases as the aircraft seeks its original angle of attack. Elevators are in full nose-down position.
4) At the end of the maneuver, overshoot of the starting angle of attack may take place through the effect of the aircraft's inertia. At this point the aircraft's low angle of attack flow field begins to reform.

While there has been a lot of debate on the maneuver's usefulness in air combat, it is an effective means of rapidly slowing down an aircraft. The following conditions are helpful for aircraft performing a Cobra maneuver [55, 58, 59]:

1) The aircraft should be statically unstable in the longitudinal axis for the range of angles of attack in question.
2) The aircraft must possess an abundance of engine thrust.
3) There should be symmetry of the vortex flows on either side of the centerline.
4) The aircraft must force symmetrical shedding of the forebody vortices through strakes, chines, trips, or other means. Otherwise, it must have the ability to suppress the asymmetrical shedding of vortices from the nose region. This is important because the relatively long distance from the center of gravity of the aircraft to the nose magnifies the effect of small side forces due to asymmetric shedding, resulting in large yaw moments.

In comparison, the following conditions are very important for the success of this maneuver [55, 58, 59]:

1) The yaw stability at high angles of attack must be sufficiently high for the pilot to maintain directional control, such that the aircraft performs the pitch in the vertical plane.
2) There should be a large nose-down pitching moment for angles of attack α greater than 60 degrees, available either through thrust vectoring or aerodynamic design, as the control surface's authority will be seriously degraded.

As the angle of attack increases above some value (about 50 or 60 degrees), the aircraft begins to exhibit tendencies towards yawing and wing rock oscillations. There is also a strong tendency to bank. In numerical simulations of the maneuver, this wing rock is reported as

chaotic in amplitude with a period of 3.5 seconds. Similarly, yaw excursions exhibit similar oscillations with comparable periods of oscillation [58].

2.7- Simulation of the "Cobra" Maneuver

There are several important issues that can affect the maneuver's outcome in full-scale flight. These issues all need to be considered if complete simulation of the maneuver at other scales is to be attempted. First and foremost, the forebody's behavior and effect is very sensitive to Reynolds number. The separation features from the nose are similar in nature to the features observed in circular cones and other axisymmetrical bodies of revolution at non-zero angles of incidence. When the separation line is not defined (i.e., tripped) the separation point is affected by the nature of the boundary layer: laminar, transitional, or turbulent. Assuming a situation where the local Reynolds number is near critical, any body movement like rotation (e.g., an aircraft experiencing wing rock) or translation (e.g., the aircraft yaws) will result in a change in the relative velocity between the flow and the solid surface. If the forebody rotates, the side force due to the rotation (i.e., Magnus effect) becomes discontinuous as the separation point moves. If the cylinder translates, the movement results in a change of position of the transition point due to the moving wall. This results in changes to the flow field around the forebody and on the forces being applied to the aircraft.

Second, tests of symmetrical bodies of revolution at high α values indicate that these conditions, usually initiated by flow asymmetries, couple in such a way that the transition points become asymmetrical. The wake deforms and thus generates a side force vector (Figure 2.6). As the motion accelerates, the transition on the retreating side moves forward (due to the moving wall effect), the separation point moves aft, and the wake changes. The force being developed now decelerates the initial motion and begins to accelerate the body in the direction

opposite to the first excursion. The above scenario repeats itself, and this "coning" motion becomes self-inducing. Thus:

1) The coning motion is initiated when the Reynolds number is close to critical.
2) The transition region controls the forebody's separation and vortex asymmetry features.
3) On many tests, the separation lines are not tripped artificially.
4) At least one author has concluded that high-α dynamic simulation is not possible unless the full-scale Re number is simulated [59].
5) This, of course, is not possible except when done numerically or in a handful of wind tunnels, and thus can be a significant limitation.
6) The frequencies associated with the coning motion are in the range of 3 to 5 Hz, depending on freestream velocity and angle of incidence [60].

In order to focus the study on the leading edge vortex behavior, many researchers have attempted to simplify the flow field's complexity by eliminating the fuselage. In this way, the Cobra maneuver is tested on planar delta wings. The presence of a fuselage, however, does have an effect on the flow. When testing planar delta wings with and without simulated fuselages, the fuselage tends to induce camber on the planar delta wings [61]. Assuming for a moment that the LEX can be functionally represented by a delta wing,

1) The results from delta-circular cylinder body experiments can be replicated using delta wings (no body) that are negatively cambered to simulate the changes in downwash due to the body's presence.
2) Delta-ogive shaped body experiments can be replicated using positively cambered delta wings.

This is important if the results from experiments of one realm (delta only) are to be extended to the other realm (delta plus fuselage).

Third, the pitch up motion takes the delta wing through a process similar to the one described in Chapter 1, Figure 1.2. The length of time that transpires in phase 1 and phase 2 is very small. This should force some of the features described in Figure 1.2 to occur very quickly, almost compressed in time. At the start of the maneuver, the vortex burst is behind the trailing edge. At the maneuver's peak, there may be some portion of the vortex structure still unburst (due to phase lag effect), and some portion of the wing may be experiencing complete bluff-body stalled flow (most likely the trailing edge). The proportions of unburst vortex to burst vortex flow to stalled flow are pitch rate dependent. When the pitch rate exceeds the saturation pitch rate, the exact sequence of events is not clear. Experiments by Rediniotis et al. indicate that the burst process occurs from the inside of the vortex core. The entire vortex succumbs to the vortex burst suddenly and at once while undergoing dynamic pitching [62]. Water tunnel experiments, on the other hand, show that the vortex burst progresses rapidly from the trailing edge upstream. On the pitch down (phase 3), the vortex burst probably has dominated the flow field. Once the cobra maneuver has been completed, the lift-producing aerodynamics will be re-established.

2.8- Summary of Findings

To summarize the delta wing's flow mechanics, a shear layer separates from the sharp leading edge of the delta wing, forming vorticity which then convects away and rolls up into two leading edge vortices. Because the separation line is fixed, the leading edge vortex becomes independent of Reynolds number effects over a wide range of Re_c, though other

structures (i.e., the secondary vortices, boundary layer development on the surface of the delta wing, etc) are not.

Vortices are susceptible to a phenomenon called vortex bursting. While there are several theories as to why bursting occurs, once the delta wing's geometry is chosen, there are but two means of controlling the flow field's behavior:

1) Adverse pressure gradients affect the burst location. Hence, increasing the wing's angle of attack changes the pressure gradient and moves the burst closer to the wing's apex. This effect is dynamic, with faster pitch-up rates resulting in increasing amounts of phase lag in burst location.
2) Freestream velocity changes have a direct effect on the rate of vorticity creation at the leading edge, as well as the rate of vorticity transport, strength of secondary vortex, and growth and thickness of boundary layers on the surface of the delta wing.
3) These two means of control will be explored in future chapters of this investigation. Specifically, dynamic pitch up and dynamic freestream with rapid acceleration (and deceleration) values will be explored. Thus, it is important to understand the mechanism by which these two methods affect the burst position.

CHAPTER 3

PROBLEM STATEMENT

The delta wing leading edge vortex is a complex flow field where many interactions take place. Some of the interactions become emphasized when dynamic conditions are prevalent, resulting in non-linear effects. Previous chapters have discussed the general delta wing flow field, the causes of the vortex burst, the changes due to dynamic pitching, and some modern day applications where vortex burst control would be desirable. It is now necessary to connect these topics.

3.1- Problem

When delta wings with sharp leading edges are tested under static conditions, the leading edge vortex burst location appears to be only weakly sensitive to Reynolds number in the range of $10^4 < Re_c < 10^6$. This means that static vortex burst position comparisons can be made between full-scale aircraft, wind-tunnel model, and water tunnel models. Most experiments are usually run at uniform velocities in a water tunnel setting. This facilitates the observation of the flow's phenomenological features.

Certain delta wing vortex flow features, however, appear to be sensitive to Reynolds number. First the formation of the secondary vortex and its behavior is dependent on the Re number. More importantly, as observed by Ericsson, the forebody's flow features are Re number sensitive (Figure 3.1).

There is renewed interest in high-α and dynamic-α aerodynamics due to the higher level of performance afforded by "hyper-agile" combat aircraft. This has led to a large number of testing programs focusing on delta wing flows, either as delta-only or delta-plus-forebody

experiments. Most of the testing involves replicating the pitching and/or plunging motion of the delta wing at different rates. Consider the following situation:

1) Testing of body-wing combinations under full-scale Re numbers involves large models, which in turn requires large wind tunnels. Dynamic testing in large wind tunnels then involves large drivable mounts to simulate the maneuvers at realistic rates of motion and to withstand the higher loads that result. This poses a practical limitation to the design and execution of certain types of delta wing experiments, both in terms of cost and complexity. For example, the DyPPiR mount (*Dy*namic *P*lunge, *Pi*tch, and *R*oll) at Virginia Polytechnic Institute & State University uses three 20.6 MPa hydraulic actuators to plunge, pitch, and roll large models [63].
2) Water tunnel testing, while restricted to lower Re numbers, does allow smaller models. Consequently, smaller loads result and smaller, less complex mounts can be used to simulate some maneuvers.
3) Water tunnel testing, relevant in that flow visualization allows qualitative assessment of the flow features not sensitive to Re number, cannot correctly simulate those features that *are* Re number dependent.

Using the full scale Cobra maneuver as a starting point and as an inspiration, it can be argued that, while a more complete experimental simulation (i.e., one that incorporates control of more than 1 degree of freedom) is desirable, the added trouble and expense of doing it may not be cost-effective unless the additional effects from the added degrees of freedom are distinct and measurable. Furthermore, assuming for a moment the effect is distinct and measurable, it is not known if that behavior will carry from the full scale aircraft to a smaller scale water tunnel simulation. Since neither question has been thoroughly answered in the

literature, the author feels that there is a need for this kind of research work. Now, using the full scale Cobra maneuver as an example of a type of multiple degree of freedom hyper agile maneuver to be studied, the next question becomes: what would be a reasonable combination of degrees of freedom to be tested in the water tunnel? Again, using the Cobra as an inspiration, the author feels that:

1) Because the volume of liquid involved, the water tunnel would involve very long periods to accelerate/decelerate the flow. The model should move in the flow in order to shorten the time periods by using a carriage system.
2) In this situation, the dynamic pitching motion could be actuated by a simple mechanical device, as long as it is compact and light enough to carry in the carriage.
3) The coning motion, however, would require yawing the model at high angles of attack. This is best accomplished, from a mechanical perspective, by embedding the mechanism in the movable mount; from an electrical perspective, this would mean submersing the motor in the water, thus requiring water-proofing and sealing.
4) Since the coning motion is a periodic yaw of the delta wing, and harmonic periodicity is observed in the wake of a circular cylinder, it might be possible to simulate this periodic wake by some other means.
5) Placing the delta wing in the wake of a cylinder, rather than moving the delta wing periodically, could be one method to simulate a first-order effect due to oscillatory directional motion If the impingement of von Kàrmàn vortex filaments of alternating sense of rotation can modulate the burst location in a manner similar to what would be expected from periodic and harmonic yawing, then the impingement of vortex filaments could lead to a simpler, less expensive mechanism (compared to a submersed yawing mechanism).

3.2- Motivation

1) The maneuverability and performance of contemporary fighter aircraft has far exceeded what was possible only a few years ago. These aircraft designs are pushing at the edge of aerodynamic modeling and, in particular, the prediction of the vortex bursting under dynamic conditions.
2) Part of the problem is the need for experimental data in order to develop models used in prediction of the flight-mechanics of certain maneuvers. This need is particularly acute when non-linear interactions occur in the flow field. In a typical high-α model, a state-space representation of the aircraft's equations of motion is used, incorporating in most cases linearized Taylor-series expansions. The derivatives are assumed either linear or quadratic functions of some state variable, where the coefficients are estimated from experimental data available [58, 64].
3) When experimentally simulating the Cobra Maneuver and other hyper-agile maneuvers, rapid pitch rates may result in large dynamic loads (with the larger models required for Re_c similarity), and complex test facilities.
4) Variable velocity may result in Reynolds number effects to some of the flow field, as well as changes in convection time constants.
5) If a full Cobra experimental simulation is desired, it will require control of several factors (i.e., pitch, velocity, yaw, etc.) simultaneously. Some experiments have replicated the pitch motion (only), while fewer have duplicated the variable speed aspect of the maneuver.

On a secondary level, a water tunnel mount that combines both fast pitching and unsteady freestream can have applications other than for delta wing testing:

1) At the opposite edge of the spectrum, renewed interest in MAV, UAV, and UCAV aircraft has promoted research into time-dependent methods of achieving high wing-loadings, high maneuverability, and small physical size. For example, some of the smallest MAV's available exploit wing "flapping" as a means to achieve the required lift [65].
2) In addition, in flying vehicles of very small sizes, small changes in freestream velocity can result in large changes in their Reynolds number Re_c. While the vortex burst phenomenon appears to be Re insensitive, there are flow features that *are* sensitive and that, at the smaller scales, may influence the flow at least locally.
3) *At the time* when the idea of dynamic testing of delta wings was being considered, there was a possibility that the test facility, the water tunnel at Wichita State University's National Institute for Aviation Research (NIAR), would be unavailable for some time due to possible renovations and upgrades. An important part of the motivation to develop a system to test delta wings was that, if the water tunnel's pump and motor were to be out of service for a lengthy amount of time, at least the tunnel could physically be used as a "towing tank."

3.3- Overall Goals and Intermediate Milestones

The overall goals of this experimental investigation are the following:

1) To quantify experimentally the leading-edge vortex burst location, type, and propagation rate on a 70-degree delta wing. This will be done while the delta wing undergoes:
    a) dynamic pitching and unsteady freestream,

b) fixed angle of attack α while under the influence of a harmonic stimulus generated by a cylinder,

c) dynamic pitching while under the influence of a harmonic stimulus generated by a cylinder.

2) To discuss, inasmuch as the experimental results support it and within the limitations of an optically-based experimental data-gathering system, the physics of the fluid phenomenon observed.

The author believes this is important for 2 reasons:

1) Future aircraft design can benefit from this information, which appears to be lacking. This is particularly important when one considers that certain emerging types of aircraft (UCAV's, MAV's) have high maneuvering capabilities, and can dissipate velocity quickly.
2) The impingement of a cylindrical wake on a delta wing vortex system has not been, to the best of the author's knowledge, published before, and therefore represents a novel implementation.

To accomplish these goals successfully, the following tasks, or milestones, have been established:

1) To design and build a mount that can change pitch dynamically and control the freestream velocity so as to attain appropriate rates of deceleration, comparable to the full-scale maneuver.
2) To develop some experimental methodology and techniques to measure the vortex burst features: burst position, burst movement velocity, and burst type.
3) To take a known delta wing and replicate some previous results; this validates the mount.

4) To execute a test matrix (to be presented at a later chapter), conduct the analysis, and report on the results.

3.4- Circular Cylinder Wakes

It is well known that a cylinder in a uniform flow will shed a series of vortices of alternating rotational direction at regular intervals, called a von Kàrmàn vortex street. The frequency of vortex shedding is dependent on the cylinder's diameter, the flow's velocity U_∞, the location along the cylinder's length, the relationship between the velocity vector U_∞ and the long axis of the cylinder, and the conditions at the end points of the cylinder [66].

Assuming the circular cylinder is perpendicular to the freestream velocity vector, the relationship between the wake's shedding frequency to the flow velocity and cylinder diameter is given by a non-dimensional parameter, the Strouhal number,

$$St = fD/U_\infty \tag{3.1}$$

Roshko [66] determined the shedding to be stable, transitional, or irregular, depending on the Reynolds number based on diameter, Re_d,

Stable Range	$40 < Re_d < 150$
Transition Range	$150 < Re_d < 300$
Irregular Range	$Re_d > 300$

Later, Tritton [53, 66] found that there are at least two distinct values for the Strouhal number, indicating a discontinuity in the range $Re_d = 90 \pm 25$ (there is some disagreement in the published Re_d value of this discontinuity). Below the discontinuity Re_d (Figure 3.2 (a)) the shedding is segmented into "cells" or regions along the cylinder's span. The central region is flanked on both sides by at least one or more regions of smaller frequency. Above the discontinuity, there appears to be one cell. The angle of the shed vortices to the cylinder's

symmetry axis θ also changes, becoming shallow as Re_d increases and eventually becoming asymptotic to a value of about 13 degrees (Figure 3.2, (b)). At the same time, the St number becomes asymptotic to a value of about 0.2 [67].

There has been a lot of debate as to the reason for this discontinuity in the shedding. Tritton suggests that it is the transition between two different triggering mechanisms, while Williamson suggests that it is caused by an interaction to the oblique vortex shedding and the conditions at the ends of the cylinder [67].

The cylinder's ends also affect the shedding frequency in the vicinity, within 6 diameters [68]. The frequency near the free ends is 10-15% less than the regular frequency, called f_2. This produces the existence of a beat frequency in the junction of the two regions of dissimilar shedding. The addition of end plates to the cylinder introduces a third frequency component f_3 higher than f_2 but smaller than the regular shedding frequency. This indicates that, in order for the cylinder's wake to be free of end effects, a distance no less than 6 diameters from the end of the cylinder is needed.

Degani has looked at shedding of an ogive-cylindrical forebody at different angles of attack, and the shedding frequency changes as the angle of incidence to the flow becomes more perpendicular [69]. Progressively, as the angle of incidence of the body increases, the body begins to shed symmetrically at some angle. Increasing the angle of incidence further produces asymmetric shedding between 40 and 60 degrees. A large fundamental frequency corresponding to a $St \approx 0.2$ is observed, along with some high frequency components in the range of $5 < St < 7$. Increasing the angle of incidence increases the power of the higher frequencies relative to the low frequencies. Because the increment in the angle of incidence used by Degani is rather coarse (from 60 to 80 degrees), it is difficult to say where the high

frequencies peak before they begin to be attenuated. When the flow is perpendicular to the forebody's axis (greater than 80 degrees), the shedding frequency produces a St = 0.2, the same as for a cylinder, with none of the higher frequencies observed. The higher frequencies are attributed to traveling-wave instability in the shear layer.

3.5- von Kàrmàn Vortex Street Collisions

Since the shedding frequency of a cylinder in a flow at different angles of incidence can be found, it is a matter of selecting the appropriate cylinder diameter to generate the desired wake frequency at the angle of incidence being tested. This wake is then made to impinge upon the delta wing as it pitches. Four interactions (Figure 3.3) come into play in this scenario:

1) A vortex street to solid boundary interaction occurs as the wake impinges on the delta wing's surface. Experiments on point vortices and vortex streets, where the impinging vortex is parallel to the leading edge of an airfoil, indicate that the relative position, strength, and size of the incoming vortex affect the outcome of the collision. When a single vortex has struck an airfoil head-on, the vortex separates into two smaller ones, to be convected downstream with different velocities [70]. Other work, where the axis of the impinging vortex is perpendicular to the leading edge of an airfoil (and parallel to the chord line) produces substantial changes in the features of the impinging vortex, including a net reduction in circulation (due to negative vorticity being produced at the trailing edge) and an increase in core size [71]. On a third instance, where a vortex filament has impinged a cylinder perpendicular to its axis, two different outcomes have occurred, depending upon the strength and velocity of the incoming vortex filament. The vortex strength and velocity is quantified by an impact parameter number,

$$I = 2\pi \, r_{vortex} \, U_{\infty} \, \Gamma^{-1} \qquad (3.2)$$

When the impact parameter is small (I = 0.03), a tongue of fluid is ejected at the cylinder's front. This fluid, containing a certain amount of vorticity, forms a vortex loop, which then encircles the incoming perpendicular vortex. If the impact parameter is large (I = 0.21), the effect is smaller and of a more two-dimensional nature [72, 73].

No literature has been found on the specific delta wing-point vortex impact situation stated at the beginning. Based on Refs. [70, 71, 72, 73] and extrapolating from their results, it is reasonable to expect that the impinging vortex wake should produce small vortical structures similar to those observed in these cases. How these structures will interact with the established leading edge vortices is unknown (Figure 3.3, upper left).

2) Wake velocity to leading edge vortex interaction occurs as the induced velocity component of the wake's shed vortices harmonically forces a change in the yaw angle at the delta wing's apex (Figure 3.3, upper right). This is the sought-after effect. As discussed earlier, yawing results in an effective reduction of the sweepback angle and, in turn, moves the vortex burst location forward towards the apex.

3) Wake vorticity to leading edge vortex interactions would also be expected to occur. The von Kàrmàn wake can be thought of as a series of line vortices that intersect the leading edge vortices. Since the cylinder will be held perpendicular to the carriage while the delta wing pitches, the relative angle between them will change. In the case where the delta wing's angle of attack is small, the collision will be approximately perpendicular (Figure 3.3, lower left). A similar situation (except for some differences which will be acknowledged later) occurred in an experiment where Görtler vortices (i.e., small counter rotating vortices formed due to the Coriolis acceleration of a curving flow) were observed under the influence of a large perpendicular vortex (Figure 3.4) [74]. In these tests, the

smaller vortex (Görtler vortex, wall eddies, or streaks in Figure 3.4) retained its structure, but eventually "burst" at some distance after encountering the larger perpendicular vortex. This occurred when accelerated flow associated with the larger perpendicular vortex encountered the slower moving fluid associated with the (Görtler vortex) wall eddies. There are two differences: Görtler vortices are of a much smaller scale in comparison to the flow's curvature, whereas the impinging vortex and the leading edge vortices are closer to each other in scale. Second, the Görtler vortices have slow axial velocities compared to the approach velocity of the impinging perpendicular vortex.

4) Additional effects which could be expected include some sort of crossflow interaction from the leading-edge vortices as the yaw component brings them closer together over the delta wing, which might be manifested as a harmonic motion with some sort of phase shift with respect to the impinging forcing of the cylinder's shed vortices (Figure 3.3, lower right).

As it relates to this application, it is reasonable to expect the following events when the cylindrical wake impacts the delta wing under test:

1) Since the velocity vector will be deflected in yaw periodically, oscillation in the vortex burst location is expected, provided the time between successive impacts (i.e., half of the shedding frequency) is comparable to the convection constant needed to transport a disturbance from the apex to the burst. This is the desired effect.
2) As it was observed in the case of dynamic pitching of delta wings, where the effect saturates at high frequencies, it is reasonable to expect that this yaw effect will also saturate at some frequency.

CHAPTER 4

EXPERIMENTAL METHOD

4.1- Facility Description

4.1.1- Water Tunnel

The Wichita State University's National Institute for Aviation Research (NIAR) Water Tunnel (Figure 4.1) is a 3,500 gallon facility with a 2 foot wide by 3 foot high test section. It is driven by a 3-phase AC motor, and is capable of a top speed of 1 ft/s. This corresponds to a maximum Reynolds number between 90,000 and 100,000 per foot, depending on water temperature [75]. The motor itself is driven by a synthesized AC power source with built-in time constants. As it is, this water tunnel has very slow acceleration characteristics, taking in excess of 6 seconds to go from 0 to 0.5 ft/s, and more than 15 seconds to decelerate.

The test section of this tunnel is 6 feet long with Plexiglas® walls on three sides, allowing unrestricted viewing. It is also equipped with a dye delivery system. Using compressed air, it is possible to deliver up to 6 different dye colors through transparent Tygon® hoses. The composition is food-coloring dye diluted 8:1 with water. The rate of dye delivery is controlled by fine-pitch valves on each individual color.

4.1.2- Towing Mount

Due to the test section's length, it was deemed possible to construct a towing device that would allow both dynamic pitching and dynamic freestream velocity. The idea was to design and construct a set of rails upon which a carriage could be driven externally. The initial design constraints were as follows: (a) keep the modifications to the water tunnel to a minimum, (b) keep the unit's complexity to a minimum, (c) build it such that vibrations, shimmy, and other

sources of interference would be minimized, and (d) minimize the unit's cost. A schematic of the towing mount is shown in Figure 4.2. The towing mount is composed of the following:

1) *Frame*: A frame built from riveted aluminum beams was constructed. This material was chosen to keep the weight low and, since the lower part would be submerged, to keep from reacting with the water additives used in the water tunnel. Installing the frame requires the water level in the tunnel to be dropped by 4 inches, resulting in an effective test section of 24 by 32 inches. It is secured to both sides of the water tunnel using rubber-faced C-clamps. The frame is 6 feet long, and deflects less than $^1/_4$ inch at the far end with respect to the other end due to the carriage weight. The total length available for carriage movement is 61 inches (Figure 4.3).
2) *Wave Suppression*: As the strut traverses, it generated a bow wave on the free surface. To minimize this, two thin plastic plates were attached to the frame and submerged a short distance below the water's free surface, forming a "false ceiling." The false ceiling formed a slot along the tunnel's long axis through which the support strut and its parallelogram linkage were able to traverse, while the surface waves formed remained above these plates. It is believed that this arrangement minimized the effect of the bow waves on the test results. Additional benefits came from the plastic's buoyancy which helped support the weight of the frame, and as a means of support for the dye and electrical lines that trailed behind the carriage as it moves. A removable access panel was cut into one of the ceiling halves.
3) *Carriage*: The carriage was derived from an existing plexiglas® sheet. The delta wing was mounted in an inverted position, allowing a camera to view the LE vortices through either

the floor or the side of the test section. The carriage was stiffened with aluminum cross-braces. A schematic of the carriage is shown in Figure 4.4.

4) *Rollers & Guides*: Two 608ZZ ball-bearings on one side were machined with a V-grove. The groove engaged a track on one side of the frame. The track's shape and the V-groove worked together such that it became self-centering, and this guided the carriage's motion. The opposite side rode on a third, non-grooved ball-bearing. This third bearing was a so-called floating bearing (because it could move or float sideways in response to changes in tunnel width), and has an infrared LED/phototransistor pair and a shutter wheel attached. The three bearings provided a three-point support for the carriage which made the travel relatively smooth while allowing for slight variations in the tunnel's width. To maintain zero yaw, however, it was important that the delta model's root chord be aligned to the track that guides the carriage.

5) *Braking*: To brake the carriage, simple foam blocks were placed on either side of the carriage and frame.

6) *Motor Drive*: A DC-motor and appropriate variable-voltage power supply were used to pull the carriage through a 50-lb nylon fishing line. The line was wrapped around an idler pulley, which was driven by the motor via a round belt (Figure 4.5). Tension on the line was initially provided by a stiff spring and turnbuckle. This limited the spring's extension. It was possible, however, under periods of very rapid deceleration (when the line became slack and the spring retracted) for the carriage to exhibit a slight harmonic oscillation of 1 to 2 Hz. It was, however, due to the observed undershoot in velocity during the initial testing of the towing mount using a capacitor discharge system (see Chapter 5 for details) that the spring was eliminated and only the turnbuckle was used to tension the tow line.

7) *Position Data*: Position data was derived from the shutter and LED/phototransistor combination on the free floating bearing (Figure 4.6). This arrangement generated an electric pulse, the frequency of which was related to the carriage's velocity U. This was read via the A/D card on a PC computer, or directly on a digital multi-meter equipped with frequency display.

8) *Dye Injection*: The current system used for flow visualization in the water tunnel was used. The hoses leading from the carriage to the dye reservoirs were coiled to minimize their drag on the system. The hoses were transparent Tygon®, $^{3}/_{32}$" diameter, and the rate of delivery could be estimated by observing the progress of the dye through the tubing.

9) *Model Support*: A vertical rod, $^{1}/_{2}$ inch in diameter, was used for model support. This rod contained an attachment fixture that pivoted about the end of the rod to change the angle of attack. The model was mounted "upside down" with the suction surface facing the floor of the test section. This was done to keep the support rod on the model's pressure side and away from the leading edge vortex system on the opposite face. This also caused the lift vector to point downwards, increasing the normal force on the rollers and making it more difficult for the rollers to skip out of their respective tracks. There had been some discussion as to the static hysteresis of the vortex burst position due to support interference. Taylor et al. found that the use of a support on the delta wing's *suction* side affected the position of the vortex burst in two ways: the vortex burst was moved farther towards the apex, and there was a hysteresis effect to this position [76]. Figure 4.7 shows the complete towing mount installed in the water tunnel test section.

10) *Angle of Attack Control*: A second DC-motor was used to achieve rapid α changes on the model through a reduction gear-drive and a parallelogram linkage (Figure 4.8). This was

necessary because the space between the water tunnel's ceiling and the carriage was limited. A potentiometer on the shaft that controls the extension of the parallelogram was calibrated and used to obtain α position. The range of α was from 0 to 60 degrees, but due to the mechanism's kinematics, a quasi-linear excursion of α was possible in the range of angles between $15 < \alpha < 55$ degrees (Figure 4.9).

4.1.3- Data Collection Equipment

Additional equipment included variable-voltage, regulated DC power supplies to the motors, a switch-box to control the carriage's direction and the model's angle of attack, and a PC computer equipped with an Omega® DAS08 12-bit analog-to-digital converter running on a VisualBasic® program to capture velocity and angle of attack information. The program was configured such that the user could establish the desired number of channels and samples, sampling frequency, and would output the collected information in engineering units to a file after execution. The program read the appropriate voltage-to-unit conversion factors from an external file at start up. Additionally, the user could set to zero any voltage offset (equivalent to a "wind-off zero") at any time.

Images were recorded by a Canon CCD camcorder, used as a camera only, set up as shown in Figure 4.10. The recordings were later analyzed using VisualBasic® code written by the author. Illumination was provided by fluorescent lamps located as shown in Figure 4.10 to evenly illuminate the field of view (FOV). To maximize contrast, the room lighting was turned off while videotaping.

The collected data was also displayed in real-time on the screen, and this information was mixed in with the video from the CCD camera. This provided a video record of the event along with the α and U information from the PC, and recorded via a time-code generator on an S-VHS video recorder.

4.2- Calibration

The following is the description of the steps taken in calibrating the towing mount's velocity and the optical camera set-up.

4.2.1- Velocity

The carriage's average velocity was calibrated using a stopwatch to measure the time to cross two stations along the track. These stations were located near the center and end of the travel. In this location the velocity would have stabilized after the start-up acceleration. This was repeated 5 times and averaged for different carriage motor voltages.

The frequency derived from the idler through the phototransistor was also calibrated using a process similar to the one previously described. The initial intent, however, was to use a digital multi-meter (DMM) with a frequency counter function. It was found that there is a time lag of approximately 1 to 2 seconds involved while the DMM calculates the frequency. This delay was a problem when trying to establish exact velocities. On the other hand, when the frequency was output and captured through the A/D, the velocity information calculated was not as stable.

The velocity was also calibrated using the camera set up and the time code. Because the field of view necessary to observe the entire length of the travel would have resulted in a very small picture of the delta wing, and hence compromised the resolution, the camera was set up perpendicular to the test section at two locations. The support stem's location was then

analyzed with respect to a fixed point on the test section window. The velocity was then calculated using the time code embedded in that video frame and the incremental change in distance.

The result of two runs (one to videotape the left end of the travel and the other for the right end) as well as the average are shown in Figure 4.11. The graph is then a composite of these two runs. Analysis of the videotapes showed that the worst-case speed variation of the carriage (with a fresh rubber belt and no snagging in the dye lines) was on the order of 5%.

4.2.2- Cameras

Once the camera location and zoom setting was established, optical aberrations were quantified by placing a grid with 1 inch squares on the far tunnel wall and analyzing the number of pixels between the squares at 8 locations in the FOV and comparing them to each other. The grid was then placed on the near tunnel wall and the process was repeated. The squares at the corners differed in the number of pixels from the squares at the center of the field of view by a maximum of 3% for the near wall, and 5% for the far wall.

Next, the number of pixels expected at the test section's center was interpolated from the values arrived at from the previous paragraph. A similar grid was then placed at the delta wing model's location and the same process repeated at the left edge of the field of view, the center, and the right edge. The number of pixels from the analysis was compared to each other and to the number of pixels interpolated. The worst-case differences were 5%. Thus, it was decided that the interpolated values could be used as the calibration constant: at the beginning and end of each test or whenever the camera was moved, calibration pictures of the grids at the near and far walls were taken.

4.3- Influence due to Tunnel

The following subsections will describe a series of interference effects that occur when testing delta wings in a water tunnel.

4.3.1- Wall Induced Upwash

Wall interference can produce an upwash on the leading edge, due to the image that the side walls present. This upwash increases as the distance from the leading edge to the side wall decreases. The wing tips see a higher upwash than the delta wing's apex, thus changing the effective angle of attack. A flat delta wing will behave as though it were cambered.

According to Ericsson [77], there were sizeable errors in the observed position of the vortex burst for a wingspan to test section width (b/w) > 0.7. It was assumed that delta wings whose spans were smaller than this criterion exhibited a minimal error. In the present investigation, the wingspan to test section width ratio was 0.364.

4.3.2- Blockage

Blockage was a particularly important source of interference, especially at high angles of attack. Blockage had the effect of accelerating the flow around the model as the cross sectional area was reduced.

The ratio of the wing's projected frontal area at its highest angle of attack to the tunnel cross-sectional area, A_{Delta} / A_{Tunnel}, was an estimator of the severity of the blockage errors. An area ratio $A_{Delta} / A_{Tunnel} < 7\%$ was considered acceptable as per the guidelines published in Ref. [78]. In the present investigation, the maximum cross-sectional area ratio (for an expected maximum angle of attack of 60 degrees) was 4%.

4.4- Vortex Burst and Track Length

4.4.1- Track Length

During initial testing, it was observed that the vortex burst location was not stable until some distance away from the starting point. Recall from Polhamus [4] that the total vortex lift can be broken down into a contribution due to the LE vortex *and* a contribution from the potential flow flat plate. If the water was completely quiescent, the acceleration of the model from a fully stopped position would generate a starting vortex. Therefore, the distance needed to move away from the influence of the starting vortex was subtracted from the track's total length.

An alternative view came from Lee and Ho [5], who stated that the change in the vortex burst position as the velocity increases was the result of the generation of vorticity and the time required to transport it from the leading edge to vortex core, and then the additional time for said vorticity to influence the location. In either case, the location of the vortex as a function of distance from the starting location (Figure 4.12) resulted in half of the track length needed for the vortex burst position to stabilize. The field of view selected for analysis thus avoided the start-up region of the travel.

4.4.2- Time Intervals between Runs

Once the model had been towed to complete one test run, there was some residual turbulence in the water due to the model's wake. It was found that after towing back to the initial starting position, a waiting period of about 20 to 25 minutes allowed the water to settle and become quiescent again. This time interval was arrived at by injecting a small amount of dye as the model was towed back to its starting position, and then observing the motion of said dye. After 15 minutes or so, the dye became static.

This time could be further reduced if the tunnel was briefly turned on, such that the remaining eddies and wake were convected away from the test section and "swallowed" by the pump. In this case, the tunnel was turned on at its slowest velocity, just enough to move the residual dye in the test section. After 2 or 3 minutes, the tunnel was stopped, and then a short time interval (10 minutes) was allowed. Caution was required, as increasing the tunnel's velocity in order to swallow the fluid in the test section often resulted in longitudinal low-frequency sloshing being created. This sloshing often required 20 minutes or more to dissipate.

4.4.3- Flow Quality

An important consideration was the flow quality, and in particular, the possibility of flow angularity in the sideslip and angle of attack planes. Since the model was moved through a static water medium, flow angularities depended upon the track's rigidity, as well as any installation errors when the delta wing was mounted.

The track's vertical motion affected the carriage by changing the angularity in the vertical plane (i.e., angle of attack change). To minimize this, the following steps were implemented:

1) The delta wing was installed outside the tunnel tank, with the pitching mechanism driven completely to its minimum α position, which corresponded to an $\alpha = 0$ condition. Any errors then became a constant offset.
2) The track system moved downward $^1/_4$ inch at its aft end (with respect to the track's fixed front end) when the carriage was at its starting position. When the carriage moved forward, the strain was relieved and the track rose by that same amount. The change in slope due to this slow rise amounted to a $d\alpha/dt = 0.23$ deg/sec ($\kappa = 0.005$). This was an inconsequential amount in additional pitch up.

3) Later, with the oscillating cylinder's additional weight (Chapter 6), the deflection of the track increased with the carriage at its starting position to $^1/_2$ inch. This change in angle of attack was still very small, and represented an additional change in $d\alpha/dt$ of 0.46 deg/sec ($\kappa = 0.01$).

In the horizontal plane, only installation errors contributed to a constant sideslip offset. To minimize this, the distance from the track (assumed to be straight in the horizontal plane) to the center of the carriage was measured to $\pm\ ^1/_{16}$ inch at the carriage's front and rear edges, and marked. In subsequent tests, with the carriage outside the tunnel and measured to be level in roll and pitch with a bubble, plumb lines were dropped from the marked locations. The locations correspond to the delta wing's apex and the semi-span locations when properly installed. Thus, a maximum theoretical deviation of $\beta = \pm 0.6$ degree could be repeated. This was further checked when the marks on the carriage were initially made by running dye on both sides of the apex. The average location of both sides was symmetrical (within ± 0.05 of chord) for an angle of attack α where a mid-chord burst location would be expected.

4.5- VisualBASIC Analysis Software

4.5.1- Analysis Process

The images were recorded, as shown in Figure 4.10, onto an S-VHS tape. This tape was then played back, and individual frames were frozen and captured for analysis of the vortex burst location as well as velocity, angle of attack, and carriage velocity using a VisualBASIC program (Figure 4.13).

4.5.2- Resolution

The experiment's videotape was analyzed for the position of the vortex burst using a VisualBASIC program. A standard NTSC video signal was picked up at the video camera. It was composed of two interlaced video fields recorded at 1/60 sec each with a vertical resolution of 262.5 lines, resulting in one video frame of 525 lines every 1/30 second. The video signal's horizontal resolution, at approximately 640 lines, was larger than the vertical; thus it was not the limiting factor.

The video signal was recorded in S-VHS format, which downgraded the resolution to 400 lines/frame. The image was based on 31 inches of horizontal FOV (half the track length); the vertical image size was then 23 inches. This translated to 11.4 lines/inch vertically.

The field was captured and rendered into a 640 by 480 pixel, 24-bit color bitmap file through the use of a Snappy® video processing accessory controlled through the VisualBASIC program. This corresponded to 20.6 pixels/inch in either direction.

The frame was then displayed by the VisualBASIC code in an Image Box whose dimensions are 9735 by 7335 units (preserving the original 3:4 aspect ratio of the recorded image). Thus 1 inch was equivalent to 11.4 lines = 20.6 pixels = 315 units.

The computer mouse was then used to outline two distances as seen in the Image Box: the root chord (distance from apex to center of trailing edge), and the leading edge vortex length (distance from apex to vortex burst location). The vortex burst location was, then, a function of the user's accuracy and interpretation. The user was able to place the mouse within ±1 unit. The location, however, was limited by the resolving power of the S-VHS videotape. Thus, the resolution was ±1 line = ±0.09 inch in the vertical direction, which translated to ±0.75% of chord.

4.5.3- Refraction and Perspective Errors

Refraction occurs when a light ray passes from one medium to another. In this case, a light ray originating at some point on the delta wing passes through three media: water, Plexiglas®, and air. At each interface the incident angle θ of said light ray changes by an amount specified by Snell's Law,

$$n_1 \sin \theta_1 = n_2 \sin \theta_2 \tag{4.1}$$

where n is the refractive index of the medium (i.e., the ratio of the speed of light of the material to a perfect vacuum).

The real position of features on the delta wing did not coincide with the observed position of these features by the camera. This error, quantified in Figure 4.14, was linear with respect to the distance of the optical centerline (which was always placed at ¾ of the track length) for the FOV used. In other words, the farther the delta wing was from the optical camera lens' center, the more "elongated" the delta wing's features appeared.

Perspective errors arose from the geometric location of the event in relation to the camera's location. Quantification of the perspective error was obtained by analyzing a static run at the left edge and the right edge of the FOV and then comparing it to the center, as shown in Figure 4.15. As can be observed, the uncertainty was relatively small.

4.5.4- User-Induced Errors

As the burst location was ultimately defined by the user's visual and interpretational acuity, it was necessary to minimize this. Initially, an analysis was done by the author to evaluate how repeatable the identification of a known point would be. The analysis was done on one computer, such that any influence the device might have had on the image was consistent from test to test. The author conducted an analysis on the same test, on the same

captured video images, on three different occasions, so as to quantify any user-induced repeatability error. For every occasion 3 data points were extracted for each frame captured. Figure 4.16 shows a scatter plot and the average. Using a Student's *t-distribution*, the 90% confidence interval for each angle of attack plotted is shown in Table 4.1. The user-induced error was the largest contributor to the total error of the analysis set-up. An error of up to ±2% of chord was contributed by variations in repeatability. Note that at lower angles of attack (for $\alpha < 35$ degrees), where S-type bursting occurred, the error was slightly less than at the higher angles where B-type bursting was more prevalent.

TABLE 4.1

ERROR DUE TO ANALYSIS PROCESS

Angle of Attack (deg)	Average x/c	Std. Deviation	90% Confidence Interval Lower Bound	Upper Bound	Deg. of Freedom
25	0.96	0.016	0.953	0.975	7
30	0.68	0.009	0.677	0.688	8
35	0.50	0.008	0.494	0.505	8
40	0.26	0.018	0.249	0.272	8
45	0.20	0.020	0.185	0.210	8
50	0.13	0.011	0.121	0.136	7

On the other hand, the above process assumed that the point being identified repeatedly was in fact the actual burst point. There might be an error in that assumption, for example, due to the way the dye collected, the point being identified might not be the actual burst location. A

different methodology would be to take the results obtained with this system and compare them to the results obtained under similar conditions by another researcher. This was undertaken when the mount was validated, and discussed later in section 4.6.3.

4.5.5- Vortex Burst Location Definition

An interesting problem surfaced during the initial trials. For a B-type burst, the location was readily apparent as the apex of a triangle formed by the "flair-out" of the leading edge vortex (see schematic in Figure 4.17). For the S-type burst, the location was defined as the point where the kink in the leading edge vortex was observed. However, the image displayed by the VisualBASIC program had been reduced to 2-dimensions. Assume that at time t_0 an S-type burst had an azimuth angle of zero. The kink was present, but the location was not clearly defined (see middle drawing of Figure 4.17). A short time later the azimuth angle had increased by $^1/_4$ turn. Now the burst was clearly visible, since the plane formed by the vortex centerline and the kink was at a right angle to the camera. Extending this idea, there were 2 azimuth locations in every revolution of the vortex where the kink's exact location could not be defined. In those cases where temporal regularity (i.e., sampling at a constant rate) was not required (such as static runs), only frames where the kink was in the plane parallel to the tunnel walls were analyzed. In eliminating a few bad frames no reduction in the VB location's spatial resolution was observed, only a slight reduction in temporal resolution. By limiting this technique to configurations where temporal accuracy was not an absolute necessity, no significant compromise in the quality of the data was observed.

In cases where temporal regularity was needed (such as dynamic pitching runs with the cylinder in Chapter 6), some interpretation, color filtering, and/or interpolation between adjacent frames was used. Example 1: the dye used in the von Kàrmàn cylinder was red, while

the dye on the delta wing was blue. In cases where heavy mixing obscured the burst location, it was possible to filter out the video frame's red pixels, leaving only the blue and green pixels. Example 2: In a sequence of three sequencial frames, where frame 1 and 3 showed the burst to be in the same general neighborhood, and frame 2 was too heavily mixed to yield a clear view, it was possible to interpolate the burst's position in frame 2. It was hard to predict what, if any, reduction in spatial resolution would result from the application of these techniques. There were two mitigating factors:

1) Color filtering was reserved only for problematic video frames. These occurred very infrequently on the validation and variable freestream experiments (approximately 10 to 20 video frames out of 8566 analyzed). There was no significant increase in the VB's location error. In the case of Chapter 6, where heavy mixing did occur in the wake of a cylinder, color filtering was used on approximately 1/3 of the video frames analyzed. Any increase in uncertainty or VB location error due to filtering would equal that incurred if the dye color had been changed in mid-experiment.
2) Data interpolation due to elimination of a video frame was used only on Chapter 6 (von Kàrmàn experiments). Between 70 to 150 frames (out of 6300 frames analyzed) were eliminated and the missing data interpolated. This corresponds to less than 2.5% of the frames analyzed.

4.6- Mount Validation

The experimental survey of the delta wing in this new towing mount was divided up into three phases, as shown in Table 4.2. The validation phase (i.e., Phase 0) involved the testing of the mount to produce a known result. Phase 1 and phase 2 involved the expansion of

the known delta wing quantities by using the towing mount's new features. These will be described in detail later.

TABLE 4.2

OVERVIEW OF EXPERIMENTAL INVESTIGATION

Type	Description of Experiment	No. of Runs
Validation	Repeat Myose et al. [49] Results	54
Phase 1	Variable Freestream and Dynamic Pitch	54
Phase 2	von Kàrmàn Interaction	117

4.6.1- Experimental Set-Up for Validation of the Mount

In order to validate the mount, the same delta wing that was used earlier by Myose et al. [49] at this water tunnel (but in a different mount) was used in an attempt to replicate their experiment. The delta wing used was a flat, $^1/_8$ inch thick aluminum with a 70 degree sweepback angle, sharp leading edges beveled at 30 degrees, and a 12 inch chord (Figure 4.18). It was marked along its root centerline at 10% chord intervals, and its trailing edge is blunt. It was equipped with dye ports near the apex, but only the dye port closest to the camera was used for visualization of the LE vortex core. Table 4.3 summarizes the test conditions of the original test and the validation test.

TABLE 4.3

EXPERIMENTAL PARAMETERS OF VALIDATION EXPERIMENT

	Myose et al. Experiment [49]	**Validation Experiment**
Velocity U_∞	0.4 ft/s (4.8 inch/sec)	0.4 ft/s (4.8 inch/sec) ± 5%.
Chord Reynolds No. (Re_c)	33,000	33,000
Non-Dim. Pitch Rate κ	0, 0.1, and 0.2	0, 0.1, 0.2
Angle of Attack α Range	15 to 90 deg	15 to 55 deg (due to physical limitation)

In Myose's tests, a vertical turntable was used to pitch the model, which was being supported by a stem from the trailing edge. The stem was then connected by a cross-brace to the turntable (Figure 4.19). To simulate this stem, the delta wing was fitted with a wooden stem and cross-brace, $^1/_2$ inch in diameter, resembling the mount system they used in dynamic testing at this water tunnel. The simulated stem was only connected to the delta wing's trailing edge. A slight clearance was left between the tunnel walls and the end of the brace.

4.6.2- Static Results

Figure 4.20 shows the validation of static vortex burst locations. These results were the average of 3 runs (Table 4.4). The results, at first, appeared to have a substantial amount of scatter, and the curve's general slope was shallower than that of Myose et al.'s results. Comparison to other results reported for a 70-degree delta wing showed that there was a wide scatter in the vortex burst location, and that the results here obtained were within that scatter.

TABLE 4.4

TEST MATRIX FOR TOWING MOUNT VALIDATION

Model:		12-inch chord 70-degree Delta Wing		
Reynolds Number:		33,000 (At U_∞ = 0.4 ft/s)		
Velocity U_∞ (ft/s)		0.4		
Type of Test	**Angle of Attack α □(deg)**	**Non-Dimensional Pitch Rate κ**	**Stem Points towards**	**No. Runs per Test Case**
Static	25, 30, 35, 40, 45, 50	0	None	3*6 = 18
Dynamic Pitch	15 to 55	0.1		3
		0.2		3
Static	25, 30…45, 50	0	Near Wall	3*6 = 18
Dynamic Pitch	15 to 55	0.1		3
		0.2		3
Static	25, 30…45, 50	0	Far Wall	3*6 = 18
Dynamic Pitch	15 to 55	0.1		3
		0.2		3
			Total number of Runs:	54

4.6.3- Dynamic Results

To qualify the mount dynamically, the wing was pitched at κ=0.1 and 0.2 and compared to previously reported results. There is some discrepancy in the vortex burst's location (Figure 4.21 and 4.22), but it is generally within the error bands of both the original experiment and the towing mount experiment. The only problem here is that the angle of attack range with the

towing mount does not reach as far up as Myose et al.'s results [49] due to physical constraints. In general, the vortex burst locations compared favorably with Myose et al.'s results.

To answer the question posed in section 4.5.4 regarding the uncertainty, one can compare the results between the towing mount and the fixed mount. Indeed, since the wing and the water tunnel are the same, the only difference is the mount used. In Figures 4.20 and 4.21, both Myose et al's curves and the towing mount curves (including the standard deviation bars) fall within a band whose width is between 0.07 and 0.12 x/c. This means that the uncertainty is on the order of ± 0.06 x/c, assuming that the bursting under dynamic conditions has behaved identically on both installations and that the difference between the two curves in the figures is due to the global uncertainty (i.e., including user interpretation and the ±0.02 x/c contributed by the repeatability of the analysis tool).

4.6.4- Stem Results

Removing the stem from the delta wing's back produced a slight change in the location of the vortex burst (Figure 4.23 and 4.24). Placing the stem so it pointed to the side near the camera (i.e., the side of the LE vortex being visualized), and then changing it to the side away from the camera (to the non-visualized LE vortex), produced a slight change in the burst position. Generally speaking, the introduction of the stem into the flow did push the VB location forward towards the apex slightly, although there were some data points where this effect was really in the data scatter (within the standard deviation bars).

CHAPTER 5

VARIABLE VELOCITY EXPERIMENTS

Phase 1 is defined as the experiments beyond the mount validation, but not including the von Kàrmàn vortex impingement which are covered in Chapter 6. Phase 1 includes the unsteady freestream components of the research effort covered in this chapter.

5.1- Experimental Set-Up

5.1.1- Experimental Similarity

The following similarity parameters (Table 5.1) are considered important. The table describes the experimental values compared to those values reported or calculated from information accessible in the open literature (denoted by * in the table). In some cases, the values of the constants have been obtained from measurements of a 1:48 scale model of the Su-27 aircraft. The chord used for the Su-27 is 20 feet. Where velocities are used, a velocity of 0.4 ft/s is assumed for the water tunnel experiments; the Su-27 is assumed to be just entering the Cobra maneuver (U_∞ = 380 ft/s).

Normally, Reynolds number matching is critical for conventional airfoil wind and water tunnel testing. In this case, it is not possible to attain equal Re_c values with the use of a water tunnel. The vortex burst behavior has been said to be comparable over a wide range of Reynolds numbers, specifically when the burst is located above the delta wing's upper surface. With regards to the shedding and coning behavior, however, Reynolds number matching is important; thus the behavior will not be correct, and steps must be taken to force correct behavior.

TABLE 5.1

SIMILARITY AND POSSIBLE TEST PARAMETERS

Parameter Name	Symbol and/or Formula	Experiment	Actual or Estimated	Notes
Root Chord Re Number	$Re_c = U_\infty c / \nu$	33,000	$\approx 10^7$	
Non-Dim. Pitch Rate	$\kappa = \dot{\alpha} c / 2 U_\infty$	0.1, 0.2	0.012* to 0.175	
Angle of Attack Range	α	15 to 55 degrees	"low" to 90-110 deg	Ref. [55, 57]
Pitch-Rate Induced Camber	$\Delta\alpha = \tan\left[\frac{\dot{\alpha}(x - x_{CG})}{U_\infty}\right]$	0.035 deg at apex	0.02 at apex*	
Convective Time Constant	$\tau = c / U_\infty$	0.4	0.1*	
Velocity Ratio	$U_{max\,\alpha} / U_\infty$	0.5, 0.75 (Chapter 5)	0.25	Ref. [55]
Average Deceleration	dU_∞ / dt	0.023, 0.046, and 0.092 ft/s^2 (Chapter 5)	28 ft/s^2 *	
Deceleration Distance	$\dot{U}_\infty / c$	1.3 to 2.6 chord lengths	133 chord lengths*	
Coning Freq.		3 Hz, 5 Hz (Chapter 6)	3.5 to 5 Hz	

* Information available in open literature

In delta wing dynamic testing, the more important parameter to match is the pitch rate κ. The experiment is usually run at pitch rates of 0.1 and 0.2 in order to compare to previously available data. The value of κ for the airplane, however, depends on the chord length used to non-dimensionalize, and has been estimated as low as 0.012 or as high as 0.175. If one assumes that the lower number is correct, the effect on the flow field will be to reduce the phase lag between static and dynamic vortex burst results.

The angle of attack range is limited in the experiment because of space constraints found during the dynamic mount's construction: the total range of motion is from 0 to 55 degrees, but the linear range (where a ramp pitch is attainable) starts at 15 degrees. Through the use of a wedge it is possible to mount the delta wing such that the initial angle of attack is higher by some value $\Delta\alpha$, but since the range is the same, the upper angle of attack will increase by the same $\Delta\alpha$ value.

The pitch rate induced camber refers to the change in angle of attack at the apex caused by the pitching action. In the water tunnel, the pitching occurs at the half chord location. The Su-27's center of gravity was estimated at $^1/_4$ of the main wing's chord length. The expected difference in a mismatch here would be in a slight change in position of the vortex burst related.

The convective time constant is an approximate measure of the time it takes to convect disturbances into the vortex core [63]. The estimated time constant for the full-scale aircraft is $^1/_4$ that of the experiment, indicating the experiment is more likely to react quicker to disturbances and perturbations. The significance of this is not known.

The velocity ratio, average deceleration, distance to decelerate, and coning frequency are included for comparison to the experiment. The velocity ratio can be interpreted as the variation in Reynolds number experienced by the aircraft during the Cobra maneuver, and should also be attained by the experiment. In other cases, such as the average deceleration and distance to decelerate, it is physically impossible to match the experiment within the water tunnel's constraints. These are included for the sake of completeness. Notice that the coning frequency associated with the experiment is the von Kàrmàn impingement frequency, which will be discussed in more detail in Chapter 6.

5.1.2- Variable Velocity Set-Up

The experimental set up is the same as that for the validation runs, including the use of the towing mount, the 12-inch chord length delta wing, and the VisualBASIC analysis tools. Several modifications to the power supply were made to allow for the drive motor voltage to be varied from 0 to 10 volts. At the initial stage, a capacitor bank was used as a "proof of concept" to prove that an effect could be observed when decelerating the flow. Later on, a more sophisticated method called Pulse Width Modulation (PWM) was used. PWM allowed both acceleration and deceleration velocity profiled to be implemented.

5.1.2.1- Capacitor Discharge Method

A bank of capacitors (19,900 μF) was placed in parallel across the DC motor. A step change in voltage to the motor resulted in a gradual reduction in the motor's velocity. The capacitance value was chosen so that the carriage's deceleration was linear in the range of velocities to be tested. The single, constant value of dU_∞/dt (i.e., the slope) derived from the discharge of the capacitance through the motor windings meant that, as the maximum velocity ratio $U_{max\ \alpha} / U_\infty$ increased, smaller time intervals between the beginning and the completion of the deceleration were observed. The disadvantages of this method are that only a speed reduction can be achieved (as the capacitors discharge the voltage reduces), and that very large values of capacitance are needed.

5.1.2.2- Pulse Width Modulated Method

To explore different values of dU_∞/dt (both positive and negative), a small DC gearhead motor was coupled to the potentiometer shaft of the power supply to the carriage drive system. The gearhead motor was then supplied with a pulse-width modulated (PWM) DC current. A square wave of fixed frequency and full voltage is applied to the gearhead, but the wave's duty

cycle (i.e., the percentage the motor is on in a given period) can be manipulated. This allowed the potentiometer's rotational velocity to be increased or decreased in very small increments without stalling or stopping. The schematic of the PWM circuitry is included in Appendix 3. The advantage of this method is that both small and large values of dU_∞/dt can be dialed in. The disadvantage is its complexity, and the gearhead motor can be burned up by the back EMF produced by its own windings (unless protection is designed as part of the circuit).

5.1.3- Experimental Matrix

Table 5.2 shows the proposed and the completed Phase 1 experimental schedule. The angle of attack at which the velocity will begin to increase is important. Based on experience from the preliminary stage, the slow down process should begin at around a value of $\alpha = 30$ degrees, and several decelerations should be tested. Due to the track's length, the decelerations of the full-scale aircraft could not be matched.

TABLE 5.2

EXPERIMENTAL MATRIX FOR VARIABLE FREESTREAM EXPERIMENTS

Model:			12-inch chord 70-degree Delta Wing									
Reynolds Number:			33,000 (At U_∞ = 0.4 ft/s)									
Proposed Matrix						Performed Matrix						
								Accelerating:		Decelerating:		
Angle of Attack α (deg)	Velocity U_∞ (ft/s)	Start / End α (deg)	Type of Test	Pitch Rate κ (at initial U_∞)	No. of Test Runs	Deceleration by	Start / End α (deg)	No. of Test Runs	No. Video Frames Analyzed	No. of Test Runs	No. Video Frames Analyzed
15 to 55	0.4 to 0.3	30/50	Deceleration / Pitch-Up	0.2	3	PWM Motor	30/50	4	214	4	237
15 to 55	0.4 to 0.2	30/50		0.2	3	PWM Motor	30/50	4	142	4	286
15 to 55	0.4 to 0.3	30/45		0.2	3	PWM Motor	45→	3	140	4	235
15 to 55	0.4 to 0.2	30/45		0.2	3	PWM Motor	45→	4	181	3	212
15 to 55	0.4 to 0.3	30/40		0.2	3	PWM Motor	30/40				
15 to 55	0.4 to 0.2	30/40		0.2	3	PWM Motor	30/40	4	167	4	197
15 to 55	0.4 to 0.3			0.2		Capacitor	30→			4	337
15 to 55	0.4 to 0.2			0.2		Capacitor	30→			4	330
15 to 55	0.4 to 0.3	30/50		0.1	3	PWM Motor	30/50	3	247	4	350
15 to 55	0.4 to 0.2	30/50		0.1	3	PWM Motor	30/50	3	283	3	294
15 to 55	0.4 to 0.3	30/45		0.1	3	PWM Motor	45→	3	244	4	316
15 to 55	0.4 to 0.2	30/45		0.1	3	PWM Motor	45→	3	249	4	305
15 to 55	0.4 to 0.3	30/40		0.1	3	PWM Motor	30/40				
15 to 55	0.4 to 0.2	30/40		0.1	3	PWM Motor	30/40	3	237	3	397
Total Number of Runs:					**36**			**31**	**2104**	**42**	**3496**
55 to 15	0.3 to 0.4	50/30	Acceleration / Pitch-Down	0.1	3	PWM Motor	50/30	3	275	3	273
55 to 15	0.2 to 0.4	50/30		0.1	3	PWM Motor	50/30	3	314	3	288
55 to 15	0.3 to 0.4	45/30		0.1	3	PWM Motor	45→	4	394	4	346
55 to 15	0.2 to 0.4	45/30		0.1	3	PWM Motor	45→	3	288	3	311
55 to 15	0.3 to 0.4	40/30		0.1	3	PWM Motor	50/40				
55 to 15	0.2 to 0.4	40/30		0.1	3	PWM Motor	50/40	3	250	3	227
Total Number of Runs:					**18**			**16**	**1521**	**16**	**1445**

5.1.4- Experimental Limitations

1) The vortex burst's location is defined as the point where the core flares out (bubble burst), or the location where the first sharp kink (spiral burst) occurs. As such, the identified location may or may not coincide with the actual core stagnation point. The assumption that the two are close, if not coincident, has been made in the past. This was discussed in earlier chapters.
2) The synchronization of the start of the slow-down process is accomplished manually. A switch is actuated when the angle of attack α corresponding to that particular test case is observed in the A/D conversion display. Through practice, it is possible to attain a repeatability of $\pm$ 1.5 degrees from the target α at the beginning of the slow-down.

5.2- Results & Discussion

5.2.1- Capacitor Discharge Method

Figure 5.1 is an example of the type of runs performed in this Chapter, and shows the results of a single run for the case where the velocity goes from 0.4 to 0.2 ft/s (minimum to maximum velocity ratio of 0.5). The top plot shows the vortex burst location in terms of percentage of root chord. The bottom plot presents the carriage's measured velocity. The plot is aligned so that the beginning of the slow-down represents the origin of the elapsed time axis *t*. Notice the three sample photographs (marked A, B, and C) and their corresponding location with respect to the velocity profile and the resulting burst location.

Figure 5.2 represents the same configuration as Figure 5.1, except that four identical runs (i.e., repetitions of the experiment) are presented in the scatter plot (including the run presented in Figure 5.1). This limited number of runs is due to the amount of time needed to let the water become quiescent between runs. The time axis origin represents a slightly different

initial angle of attack for each run, yet the four runs start within 1.5 degrees from the average. The symbol's height in the scatter plots represent the 0.02c uncertainty of the system.

Looking at the top scatter plot as a whole, the burst location starts with a positive forward movement (i.e., positive indicates movement towards the delta's apex) of the VB of approximately 0.18 chord per second (c/s). At $t = 0.7$ seconds the VB's forward propagation begins to slow down, and eventually becomes negative at 1.85 seconds. Between 1 and 2 seconds elapsed time, it can be argued that the VB location oscillates around an *average* of 0.55c. Marching forward in time, the propagation rate becomes –0.09 c/s at $t = 2$ seconds. At $t \cong 2.6$ seconds, the VB locations of the different runs begin to precipitate forward unequally.

The carriage's corresponding behavior indicates a linear deceleration of 0.24 ft/s^2 for values of $0 < t < 1$ second. The desired velocity after slow-down is 0.2 ft/s, but an undershoot occurs between 1 and 2.5 seconds, with a minimum value of about 0.17 ft/s. Therefore, a gentle acceleration of 0.02 ft/s^2 occurs between $1 < t < 2.5$ seconds.

Similarly, Figure 5.3 shows a scatter plot of 4 runs. The average propagation velocity between 0 and 0.75 second is 0.12 c/s, slowing down to almost zero between $0.75 < t < 2$ seconds. As time marches forward, the VB propagation rate becomes 0.12 c/s from $2 < t < 3$ seconds. This propagation rate increases slightly to a value of 0.16 c/s at $t > 3$ seconds.

The carriage's corresponding behavior indicates a linear deceleration of 0.24 ft/s^2 for values of $0 < t < 0.5$ second. The desired velocity after slow-down is 0.3 ft/s, but an undershoot occurs between 0.6 and 1.5 seconds, with a minimum value of 0.245 ft/s. An acceleration between 0.06 ft/s^2 and 0.12 ft/s^2 occurs between $0.6 < t < 1.5$ seconds, depending on the particular run involved.

There are some important things to note at this point. First, the undershoot is obviously due to the tension spring in the tow-line. This undershoot of the velocity is a complicating and unavoidable factor, given the construction of this experimental set-up. Second, there is an apparent increased sensitivity to disturbances in the flow at the higher angles of attack when $\kappa = 0.4$. This might explain the VB's sudden, and unequal, forward movement in Figure 5.2.

Third, there appears to be an almost perfect cause and effect relationship between the position of the minimum velocity point (the "valley" in the velocity plot) and a marked reduction in the VB's forward propagation rate. Figures 5.2 and 5.3 both show this as a distinct "leveling-off" in the burst location scatter plot at or slightly after the minimum velocity valley occurs. Furthermore, this reduced VB propagation rate changes again approximately at the point when the final (lower) velocity is reached. This implies the arresting of the VB's forward motion occurs during the accelerating portion, when the carriage is recovering from the undershoot.

There are two possible explanations to this behavior. First, it is indeed the slight acceleration of the delta wing that produces an increasing change in the axial vortex core velocity. Recall that the vortex core can have axial velocities substantially faster than freestream [17]. This increased axial velocity results in a change to the swirl angle that manifests itself as a favorable change in the VB's propagation. When the acceleration stops, the axial/azimuthal velocity ratio quickly reaches some new values, resulting in a resumption of the VB's forward progression.

The second explanation is that the accelerations are too small; rather, the behavior observed is due to the global reduction in the forward velocity. The phase lag between the beginning of the slow down and the leveling-off in the forward propagation rate is due to the

time needed for the change in vorticity at the leading-edge to become convected to the core by the shear layer.

The pitch rate is constant, and elapsed time t and angle of attack α can be related. Figure 5.4 shows the average VB location of the scatter plots in Figures 5.2 and 5.3 along with the results of this wing undergoing dynamic pitching at constant velocity U_∞ [81]. The error bars indicate the data point spread for the constant velocity dynamic pitch cases only. When the current results are compared, it must be taken into account that the average scatter for the current results is on the order of 0.05c above and below the average line.

For angles of attack $\alpha < 35$ degrees, the scatter overlaps between all the curves. The slope of the current results, in this range of α, is almost a match to the slope of the $\kappa = 0.2$ line. This is referred to as the initial propagation in the figure. It is important to note that at these lower angles of attack the *slope* of the curves will almost always collapse to a common value, regardless of the κ value.

At angles of attack higher than 35 degrees, the κ= 0.2 to 0.4 and κ= 0.2 to 0.27 lines (current results) display what can be interpreted as a gradual change between the κ= 0.2 line and the corresponding κ value resulting from the slower velocity. This is referred to as the final propagation in the Figure. The spacing displayed by the progression from κ= 0.1, 0.2, 0.27, and 0.4 appears to be intuitively correct.

5.2.2- PWM Method

The Pulse Width Modulation method to test several configurations allowed the extensive test matrix (Table 5.2) to be completed. In general, twelve combinations of acceleration and deceleration, pitch up and pitch down rates, and range of angle of attack α were tested. A minimum of 3 individual repetitions (experiments or runs) of each particular

configuration (i.e., angle of attack range, pitch direction and rate, and acceleration) were performed and plotted per Figure. Each run, on average, was composed of 30 analyzed frames. Hence, Figures 5.5 through 5.34 represent at least 3100 individually analyzed frames. It was decided to include the totality of the experiments performed in this document so that

1) the reader could better appreciate the amount of work involved, and
2) as a means to preserve for posterity the results from individual runs.

It is important to note that it is sometimes difficult to distinguish the burst position, or the burst may not be present, at the lower angles of attack. In these cases, the burst location in the Figures may not be present at low angles of attack. In some cases, the values may not be available until the burst is nearer to the mid-chord location than the trailing edge.

Figure 5.5 presents the results for *accelerating* from 0.2 to 0.4 ft/sec (minimum to maximum velocity ratio of 0.5) and pitching up at an initial rate of $\kappa = 0.2$ from 15 to 55 degrees. The acceleration occurs between $30 < \alpha < 50$ degrees. The burst location along a chordwise coordinate s/c for the three runs indicates that good repeatability can be obtained, as the amount of scatter is small. There is a slight downward inflection in the burst location curves at approximately 4 seconds, indicating an acceleration in the VB's forward propagation. This phenomenon occurs between 1.75 and 2 seconds after the beginning of the velocity ramp-up (acceleration from 0.2 ft/s).

Figure 5.6 presents the converse situation where a deceleration from (0.4 to 0.2 ft/s) occurs for the same configuration. In this instance, a reduction in the vortex burst propagation velocity is apparent at about 1.5 seconds after the freestream velocity begins to decelerate. This retardation delays the VB's forward propagation (towards the apex). The forward

propagation resumes about 5 seconds elapsed time, and is initially more pronounced (i.e., the slope of the burst curve is more negative) than it is at the beginning of the experiment.

Figure 5.7 presents the results for accelerating from 0.2 to 0.4 ft/sec (minimum to maximum velocity ratio of 0.5) and pitching up at an initial rate of κ= 0.2 from 15 to 55 degrees. The acceleration occurs between α=45 degrees and stops at some point after the delta wing has pitched to its maximum α value of 55 degrees. The burst location along a chordwise coordinate s/c for the three runs presented indicates that good repeatability could be obtained, as the amount of scatter is small to begin with, and gets tighter after the angle of attack α has reached its maximum. There is a pronounced downward inflection in the burst location curves at approximately 4.5 seconds (although it can be argued that a line fitted through the initial part of the scatter cloud would be concave down), indicating an acceleration of the VB's forward propagation. This phenomenon occurs about 0.5 second after the delta wing has stopped pitching, and 2 seconds after the acceleration has started. This indicates that the acceleration has the effect of increasing the VB's forward propagation along the leading edge vortex core. The time, or phase lag, between the initiation of the change of speed and the change in the behavior of the vortex is approximately the same for this Figure and for Figure 5.5.

Figure 5.8, presents the deceleration of the delta wing while pitching up at κ= 0.2, and indicates a forward propagation of the burst location towards the apex with very little change in its propagation velocity. This is probably due to the delta wing having reached its maximum angle of attack α, and its new steady freestream velocity, at about the same time that the burst location has stabilized at its new position near the apex (around s/c= 0.2). This same linear VB propagation along the leading edge vortex is also in evidence in Figures 5.12 and 5.14.

Figure 5.9 also exhibits a highly linear vortex burst propagation while pitching up at κ=0.2 and accelerating from 0.3 ft/s (at α=30 deg) to 0.4 ft/s. There is what appears to be a slight discontinuity at x/c= 0.6 at about 2.5 seconds elapsed time. At first sight it could be interpreted as a missing video frame, but this is not the case, as the velocity and α time histories are complete. Closer examination indicates that on three runs a vortex burst location could not be visualized until 2 to 2.5 seconds, which gives an almost non-propagating burst for the first few frames. One of the runs plotted did exhibit a slight slowing down of the forward propagation (perhaps 1 or 2 frames) before continuing with the original slope. This combination gives the impression of a discontinuity by all four runs.

Figure 5.10 presents the burst behavior during a small deceleration from 0.4 to 0.3 ft/s (minimum to maximum velocity ratio of 0.75) and pitching up starting with a rate of κ= 0.2 between from 15 to 55 degrees. The deceleration occurs between $30 < \alpha < 40$ degrees. In this instance, a reduction in the vortex burst propagation velocity is apparent at 3 seconds elapsed time (approximately 1 second after the freestream velocity begins to change). This retardation delays the VB's forward propagation (towards the apex). The VB's forward propagation resumes about 4.5 seconds elapsed time, and appears to be at the same propagation rate (i.e., the slope of the burst) as it is at the beginning of the experiment. While the length of time that the vortex burst location remains fixed (during the arresting of the forward motion), and the time (or phase lag) between the initiation of the change of speed and the change in the vortex behavior is different between Figure 5.10 and previous decelerations, a pattern is beginning to emerge at this point. At κ= 0.2, for large ranges of angle of attack α, deceleration of the freestream velocity appears to arrest the VB's motion anywhere between 1.5 and 2.5 seconds

after the deceleration began to take place. For smaller ranges of α, it appears the stop in burst location occurs slightly quicker.

Figure 5.11 presents the burst behavior during a small acceleration from 0.3 to 0.4 ft/s and pitching up starting with a rate of $\kappa = 0.2$ between from 15 to 55 degrees. The acceleration occurs between $30 < \alpha < 50$ degrees. In this instance, the location of the vortex burst remained unaffected by the change in velocity, exhibiting only a change in propagation rate at 4 seconds elapsed time. This coincided with the delta wing reaching its maximum angle of attack, and is marked by an increase in forward propagation rate. It would appear that in order to effect a change in the burst movement rate either a minimum acceleration is needed, or a longer time period is necessary.

Figure 5.13 presents the case for acceleration from 0.3 to 0.4 ft/s while Figure 5.14 presents the case for deceleration over a similar velocity range, both starting from a large angle of attack ($\alpha = 45$ degrees). The data indicates that the acceleration precipitates a forward jump in the burst location (starting at about 4.5 seconds elapsed time, about 1 second after acceleration has begun). The deceleration for the same case does not appear to exhibit the arresting that had been observed in other experiments.

Figures 5.15 through 5.24 shows the results obtained during pitch up starting from a slower initial rate of $\kappa = 0.1$. Different combinations of acceleration and deceleration were tested, as laid out in Table 5.2. The general features are the same as those observed during the faster pitch-ups discussed in previous paragraphs: deceleration in the freestream velocity appears to have a beneficial effect, i.e., it arrests the forward motion of the burst location (thereby delaying the VB's propagation towards the apex), so long as it occurs before the angle of attack becomes too large (such as in Figures 5.8, 5.12, 5.14, 5.20, and 5.24). Acceleration in

the freestream velocity appears to have the opposite effect, that of pushing the burst location forward.

A second trait observed during the slower pitch-up tests is that the degree of scatter in the data increases. In some cases, such as Figure 5.15, there is a large fluctuation in the exact moment along the time axis where the forward propagation accelerates (i.e., the slope increases). This can also be observed, for example in Figure 5.16, as a difference in the exact elapsed time when the arresting of the burst location movement "lets go" and the burst location proceeds to move towards the apex. In other cases, such as Figure 5.20, three distinct but similar curves (one for each experiment performed) are traced, each having similar slope but separated from its neighbor by a few fractions of a second. This indicates that, at the slower pitching rate, the experiment is more sensitive to either external noise (such as unavoidable vibrations in the carriage being transmitted to the delta wing), or to something instrinsic within the flow phenomenon. The experiment as it was performed could not isolate the cause of this variability.

Figures 5.25 through 5.34 deal with the results presented during the pitch down at the slow pitch down rate tested ($\kappa = 0.1$). This is done because previous experiments [41, 49] indicate that slower pitch down rates yield vortex burst positions farther aft (towards the trailing edge). In general, the scatter in the data increases compared to the $\kappa = 0.2$ pitch up, but is comparable to that observed at the $\kappa = 0.1$ pitch-up.

Figures 5.25 and 5.26 presents the pitch down while accelerating the carriage (Figure 5.25) from 0.2 to 0.4 ft/s, or decelerating (Figure 5.26) by the same ratio. It appears that, while the burst location migrates aft towards the trailing edge in response to the diminishing angle of attack α, the deceleration promotes this expected behavior to occur faster. This can be

observed from the change in positive slope of the burst position plot (Figure 5.26) at around 4 seconds elapsed time, indicating an increase in propagation rate.

Other plots under similar conditions are not as clear. For example, Figures 5.27 and 5.28 do not show a sufficiently different behavior in the burst propagation except at the end of the test (at about 5.5 seconds elapsed time). Figure 5.29 appears to exhibit a behavior opposite to that seen in Figure 5.26. Comparing reciprocal pairs (i.e., experiments where there is no difference in configuration, only in whether the carriage is accelerating or decelerating), it can be observed that Figures 5.31 and 5.32, as well as 5.33 and 5.34, do not exhibit a large change in behavior. In fact, Figures 5.31 and 5.32 are similar enough to be almost identical.

Having glossed over the general features in each configuration, it is now time to do a comparative analysis. For convenience, a positive outcome is one where the vortex burst's propagation is delayed or arrested, while a negative outcome is one where the burst moves forward faster (or jumps) than normal for a steady-velocity pitch-up. In Figure 5.35 a comparison between acceleration (κ= 0.2, velocity ratio 0.5, dv/dt= 0.092 ft/s^2, 30 < α < 50 degrees) and deceleration indicates that decelerating has the effect of retarding the VB's forward progression, this being in evidence by the level-off in the scatter plot at about s/c= 0.5 (4 secs. elapsed time). The acceleration, on the other hand, shows a definite forward jump in the scatter plot. Comparing with the constant velocity case (validation run from Chapter 4) and extrapolating linearly shows that at least 1 to 1.5 seconds can be gained before the burst has progressed to a spatial location (for example, s= 0.4c) when subjected to a deceleration.

Figure 5.36 (κ= 0.2, velocity ratio 0.75, dv/dt= 0.046 ft/s^2, 30 < α < 50 degrees) indicates that slower accelerations still have a negative effect on the burst location, as a forward jump in the scatter is visible starting at about 5 seconds. The slow deceleration in this case,

however, does not contribute greatly to the delay in the VB's forward propagation, as the scatter plot lies almost parallel to the linear extrapolation for a constant speed pitch-up.

Figure 5.37 (κ= 0.2, velocity ratio 0.5, dv/dt= 0.092 ft/s^2, 45 < α < beyond 55 degrees) indicates that acceleration has a negative effect, deceleration has a mild positive effect, and the angle of attack where the change in the slope of the scatter plot (i.e., the change in propagation velocity) also has an effect. If the reader equates elapsed time with angle of attack α, and compares Figure 5.35 to the current Figure, the point in time where the burst location experiences a change in slope is the same for acceleration and deceleration in Figure 5.35, but different in 5.37: the acceleration precipitates a forward jump sooner than the deceleration arrests the burst progression.

Figure 5.38 (κ= 0.2, velocity ratio 0.75, dv/dt= 0.046 ft/s^2, 45 < α < beyond 55 degrees) indicates that, at the higher extremes, changes in velocity have little impact on the burst position. There is a slight change in the slope at approximately 5 seconds elapsed time. This discontinuity appears in both accelerating and decelerating experiments.

In Figure 5.39 (κ= 0.2, velocity ratio 0.75, dv/dt= 0.092 ft/s^2, 30 < α < 40 degrees) the deceleration appears to have a mild positive effect. So mild in fact, that it is difficult to say whether the downward inflection is the result of the acceleration, or just the normal change in slope that occurs when κ changes value. (Recall that κ changes value in proportion to the freestream velocity.) The acceleration does not appear to have any changes, as the slope remained quasi-linear throughout the maneuver.

To summarize, pitching up at κ= 0.2, at different ranges and velocity ratios, produces a mild to strong negative effect on the burst location when accelerating. This negative effect is almost independent of the actual acceleration or range of α over which it occurs. The positive

delay in the burst movement, on the other hand, appears to be strongest when the delta wing experiences a strong deceleration (dv/dt= 0.092 ft/s^2) over a large range of α values (30 to 50 degrees). This effect becomes much smaller at slower decelerations and/or limited values in the α range. This implies that, perhaps, instabilities (whether inherent or external to the vortex core) could help precipitate the forward jump (as in Figure 5.37), making it easier to lose lift than to keep lift.

Pitching up at half the pitch rate (κ= 0.1), such as is the case in Figure 5.40 (κ= 0.1, velocity ratio 0.5, dv/dt= 0.046 ft/s^2, 30 < α < 50 degrees), produces results where the deceleration has a clear, positive effect on the burst location. The scatter is also increased. Notice that the deceleration produces a slope (at 7 seconds elapsed time) close to that of a constant speed pitch-up at κ= 0.2, which is intuitively correct when one considers that, since U_∞ occurs in the denominator, reducing it to ½ of the initial magnitude should double the value of κ.

In Figure 5.41, the acceleration does not appear to change the slope of the propagation curves. On the other hand, the deceleration produces a mild retardation in the burst propagation. In one run (Run 153, black symbols), a clearly visible change in slope occurred at 5 seconds. The other two runs produced a barely discernible change in slope at approximately 4.5 seconds. Notice that both Figures 5.40 and 5.41 present the results of experiments at the higher dv/dt value (0.046 ft/s^2), but the range of α values tested for Figure 5.41 starts at a very high value of α; thus, the deceleration appears to have a smaller effect when started at a higher angle of attack.

Figures 5.42 and 5.43 are similar in that the experiments occurred at the lower value of dv/dt tested (0.023 ft/s^2). In both cases, it is hard to observe any clear effect due to the change in velocity, as there is no discernible change in slope, particularly during the deceleration portion. The acceleration of the experiments in Figure 5.42 did change the slope towards the end (at approximately 5 seconds elapsed time), but the change was to flatten (delay) the VB's forward motion. This change in slope was probably due to the fact that the pitch-up was close to the end point.

To summarize, pitching up at $\kappa = 0.1$, at different ranges and velocity ratios, produced mild to non-observable negative and positive effects. Both effects appeared to occur when the delta wing experienced a strong deceleration (dv/dt= 0.046 ft/s^2) over a large range of α values (30 to 50 degrees). At slower decelerations and/or limited values in the α range the effects became almost unobservable in the scatter plots, due in part to the increased scatter. Instabilities (whether inherent or external to the vortex core) or other mechanisms (i.e., laminarity in the viscous regions) could play a more dominant effect at the low Reynolds numbers experienced under these conditions by the delta wing.

Figures 5.44 through 5.46 present the results of a pitch-down at $\kappa = 0.1$ under different values of dv/dt and α ranges. The deceleration does appear to move the burst back towards the trailing edge (a positive effect) faster in the case where dv/dt is high (0.092 ft/s^2). In the other two cases, where dv/dt has intermediate and low values, there is no appreciable difference between accelerating and decelerating. Scatter is well controlled in all three Figures. Thus, the benefits of decelerating the delta wing to delay the VB's forward progression appear to be mostly confined to the pitch-up regime of flight.

The burst type observed is documented in Table 5.3. It can be seen that for the majority of the pitch-up cases the S-type of burst dominates and, in many cases, is the only type seen. When there is a B-type observed in these configurations, it becomes visible at higher angles of attack (say, $\alpha > 40$ degrees). It can also be said that some configurations, particularly those that started at low freestream velocities, were more prone to vortex kinks, and these have been noted in the table. In all cases, however, the kinks were easy to identify and distinguish from an S-type burst because the kink travels downstream from apex to trailing edge along the vortex core like a wave would travel down a rope. The S-type, on the other hand, can be identified rather quickly because it rotates about the core, while the kink does not.

The same table also shows that the B-type VB was very prevalent in all the pitch down cases. When the VB transitioned to the S-type, this transition occurred at a low α value. Freestream velocity did not seem to have any influence on the type of VB in this particular configuration.

TABLE 5.3

TYPE OF VORTEX BURST ENCOUNTERED DURING VARIABLE FREESTREAM EXPERIMENTS

Figure No.	Pitch-Up (UP) or Down (DN)		Freestream Velocity Change			Vortex Burst Type and Evolution
	Rate (k)	Start / End α (deg)	Start / End U_∞ (ft/s)	Start / End α (deg)	Accel. or Decel. (ft/s2)	
5.2	0.2 to 0.4	UP 15 to 55	0.4 to 0.2	30 to 55	-0.2	Spiral $\alpha < 44$ deg. Bubble $\alpha > 44$ deg.
5.3	0.2 to 0.27	UP 15 to 55	0.4 to 0.3	30 to 55	-0.2	Spiral all.
5.5	0.2	UP 15 to 55	0.2 to 0.4	30 to 50	+0.092	Spiral $\alpha < 52$ deg. Bubble while VB stationary during arrest. Spiral at $\alpha = 52$ deg when VB motion resumes.
5.6	0.2	UP 15 to 55	0.4 to 0.2	30 to 50	-0.092	Spiral all. Occasional bubble at $\alpha >$ 49 deg and while VB arrested (i.e., stationary).
5.7	0.2	UP 15 to 55	0.2 to 0.4	45 to beyond 55	+0.092	Bubble all.
5.8	0.2	UP 15 to 55	0.4 to 0.2	45 to beyond 55	-0.092	Spiral $\alpha < 53$ deg. Bubble $\alpha > 53$ deg.
5.9	0.2	UP 15 to 55	0.3 to 0.4	30 to 40	+0.092	Spiral $\alpha < 52$ deg. Bubble $\alpha > 52$ deg.
5.10	0.2	UP 15 to 55	0.4 to 0.3	30 to 40	-0.092	Spiral all.
5.11	0.2	UP 15 to 55	0.3 to 0.4	30 to 50	+0.046	Spiral $\alpha < 52$ deg. Bubble $\alpha > 52$ deg.
5.12	0.2	UP 15 to 55	0.4 to 0.3	30 to 50	-0.046	Spiral $\alpha < 53$ deg. Occasional spiral all.
5.13	0.2	UP 15 to 55	0.3 to 0.4	45 to beyond 55	+0.046	Spiral $\alpha < 52$ deg. Occasional spiral all.
5.14	0.2	UP 15 to 55	0.4 to 0.3	45 to beyond 55	-0.046	Spiral $\alpha < 53$ deg. Bubble $\alpha > 53$ deg.

TABLE 5.3

(CONTINUED)

Figure No.	Pitch-Up (UP) or Down (DN)		Freestream Velocity Change			Vortex Burst Type and Evolution
	Rate (k)	Start / End α (deg)	Start / End U_∞ (ft/s)	Start / End α (deg)	Accel. or Decel. (ft/s2)	
5.15	0.1	UP 30 to 55	0.2 to 0.4	30 to 40	+0.092	Spiral all. Prone to kinks $\alpha < 43$ deg.
5.16	0.1	UP 30 to 55	0.4 to 0.2	30 to 40	-0.092	Spiral $\alpha < 51$ deg. Bubble $\alpha > 51$ deg. Prone to kinks $\alpha < 43$ deg.
5.17	0.1	UP 30 to 55	0.2 to 0.4	30 to 50	+0.046	Spiral $\alpha < 54$ deg. Bubble $\alpha > 54$ deg.
5.18	0.1	UP 30 to 55	0.4 to 0.2	30 to 50	-0.046	Spiral all.
5.19	0.1	UP 30 to 55	0.2 to 0.4	45 to beyond 55	+0.046	Spiral all.
5.20	0.1	UP 30 to 55	0.4 to 0.2	45 to beyond 55	-0.046	Spiral $\alpha < 51$ deg. Bubble $\alpha > 51$ deg.
5.21	0.1	UP 30 to 55	0.3 to 0.4	30 to 50	+0.023	Spiral to $\alpha < 48$ deg. Occasional spiral all.
5.22	0.1	UP 30 to 55	0.4 to 0.3	30 to 50	-0.023	Spiral all.
5.23	0.1	UP 30 to 55	0.3 to 0.4	45 to beyond 55	+0.023	Spiral $\alpha < 51$ deg. Bubble $\alpha > 51$ deg.
5.24	0.1	UP 30 to 55	0.4 to 0.3	45 to beyond 55	-0.023	Spiral all. Occasional bubble at $\alpha >$ 51 deg and when VB stopped at apex.

TABLE 5.3

(CONCLUDED)

Figure No.	Pitch-Up (UP) or Down (DN)		Freestream Velocity Change			Vortex Burst Type and Evolution
	Rate (k)	Start / End α (deg)	Start / End U_∞ (ft/s)	Start / End α (deg)	Accel. or Decel. (ft/s2)	
5.25	0.1	DN 50 to 30	0.2 to 0.4	50 to 40	+0.092	Possible bubble $\alpha > 43$ deg. Spiral $\alpha < 43$ deg.
5.26	0.1	DN 50 to 30	0.4 to 0.2	50 to 40	-0.092	Bubble $\alpha > 35$ deg. Spiral $\alpha < 35$ deg.
5.27	0.1	DN 50 to 30	0.2 to 0.4	50 to 30	+0.046	Bubble all.
5.28	0.1	DN 50 to 30	0.4 to 0.2	50 to 30	-0.046	Bubble all.
5.29	0.1	DN 50 to 30	0.2 to 0.4	45 to below 30	+0.046	Bubble all. Occasional spiral $\alpha < 32$ deg.
5.30	0.1	DN 50 to 30	0.4 to 0.2	45 to below 30	-0.046	Bubble all.
5.31	0.1	DN 50 to 31	0.3 to 0.4	50 to 30	+0.023	Bubble all.
5.32	0.1	DN 50 to 32	0.4 to 0.3	50 to 30	-0.023	Bubble all.
5.33	0.1	DN 50 to 33	0.3 to 0.4	45 to below 30	+0.023	Bubble all.
5.34	0.1	DN 50 to 34	0.4 to 0.3	45 to below 30	-0.023	Bubble all.

5.2.3- Discussion of Observed Behavior

From the results obtained, it is clear that the deceleration has some retardation effect on the VB's progression towards the apex, hence delaying the loss of lift that accompanies the forward motion of the burst. A possible scenario is laid out as follows.

From Figure 1.19, the velocity component that is directly responsible for vorticity production at the leading edge is given by

$$V_{\perp S} = U_\infty \sin\alpha \cos\beta \tag{5.1}$$

From here, it can be seen that cos β is constant for a given installation (i.e., no sideslip component, $\beta = 0$ and cos $\beta = 1$). Taking the time differential,

$$dV_{\perp S}/dt = \{dU_\infty/dt \sin\alpha + U_\infty \, d\alpha/dt \cos\alpha\} \cos\beta \tag{5.2}$$

From here, both dU_∞/dt and $d\alpha/dt$ are for the purpose of these experiments quasi-constant numbers. The relative magnitudes of both numbers sets a balance. The change in the leading edge perpendicular velocity is therefore given by the two terms in the parenthesis. For the given example, we can study the behavior of these terms (Figures 5.47 and 5.48).

In Figure 5.47, a constant pitch up at $\kappa = 0.2$ is modeled numerically in time using equations. (5.1) and (5.2). It produces an apparent increase in the leading edge velocity component perpendicular to the plane of the delta wing. This is due to the change in angle of attack and the pitch rate (the second term, $U_\infty * d\alpha/dt * \cos(\alpha)$, being directly responsible). Thus, even though the freestream is constant, the leading edge experiences an increasing velocity across its sharp radius.

This same case is now modified (Figure 5.48) to include a change in freestream, such that the conditions in Figure 5.35 are represented ($dU_\infty/dt = -0.092$ ft/s^2 and $d\alpha/dt = 9.16$ deg/s = 0.16 rad/s at $\kappa = 0.2$). In this case, when the deceleration begins a large change in the character

of the curves occurs. The increase in velocity perpendicular to the leading edge is initially driven by the cos(α) term. When a dU_∞/dt term is introduced, the combined effect of both terms in equation (5.2) is to reduce the leading edge's velocity, thus reducing the formation of vorticity at its source.

The figures do not include the effect of time delay it takes to convect the vorticity from the leading edge into the vortex core. This time delay will be non-existent at the apex, and increases linearly with chord location towards the trailing edge. Thus, the velocity calculated in Figures 5.47 and 5.48 are first experienced at the apex, then further down the vortex core's length, and at the trailing edge last. This should set up a distribution along the chord direction. In the case of a constant U_∞ the distribution is linear along the chord direction. In the case of a deceleration, the distribution will start linear, then as the slower velocities are convected into the core, this distribution will be altered (Figure 5.49).

CHAPTER 6

VON KÀRMÀN IMPINGEMENT EXPERIMENTS

The von Kàrmàn impingement experiments were inspired by a simple idea: leading edge vortices are susceptible to external influences. An example of this might be a situation where a canard is placed in front of the delta wing. In another example, sometimes the wake of an aircraft's forebody can have vortices at very high angles of attack. In other cases, close proximity of the delta wing to the wake of another aircraft would subject the delta to an external vortical flow. This lead to considering the effect of an impingement from another set of vortices upon the delta wing's leading-edge vortices.

6.1- The Oscillating Cylinder and Fin

In order to affect a change to the LE vortices of the delta wing several ideas for an external forcing function were considered very early in the investigation, but quickly discarded. Very quickly the investigation centered on the use of an external cylinder to generate a von Kàrmàn vortex street. A von Kàrmàn vortex street has a well-known behavior, and it was determined to be an ideal candidate for interaction with the delta wing's leading-edge vortex system. By introducing a circular cylinder of appropriate diameter, it is possible to impinge a regular and repeatable set of vortex filaments at known frequencies.

There was a perceived need to control the timing of a specific vortex filament and its impingement upon the apex of the delta wing, in order to synchronize other events, such as the start of dynamic pitching. Phase control (or time delay between the shedding of a filament from the cylinder and the start of pitching of the delta wing) was desired as a possible means of controlling the affect to the VB ofthe LE vortices. To get an idea of how to control the shedding of the von Kàrmàn filaments, more literature survey was needed.

Cimbala and Leon [79] and Cimbala and Garg [80] indicated that a splitter plate placed on the lee side of a cylinder that was free to rotate about its length, would result in the cylinder rotating such that the attached fin would settle at a stable angle with respect to the freestream velocity vector. The splitter plate's angle became greater as the length of the plate decreased. At a splitter plate length to cylinder diameter (l/d) ratio of 1, the angle was stable at 25 degrees to the freestream direction. Increasing the l/d ratio to 3 reduced the angle to about 5 degrees. An interesting observation was that there appeared to be no preference (i.e., there is an equal probability) for the cylinder/splitter to rotate to and remain in the up or down angle position. The presence of the splitter plate did not appear to visually change the cylinder's wake. For cases where $l/d > 2$, the C_d using the rotatable cylinder/splitter plate was similar to that of the cylinder with a fixed splitter plate in the downstream direction. In the case where the ratio $l/d = 1$, Cimbala and Leon[79] noted some discrepancy between the two cases (free to rotate and fixed in the downstream direction), but attributed this to problems with the installation.

In the Cimbala experiments, the cylinder was free to rotate, and the splitter moved to a steady fixed angle as a consequence of the presence of the vortex wake system. By reversing the cause-effect relationship, the wake would responded to the movement of the splitter plate in a predictable and repeatable manner. In this case, it would be a matter of locating the delta wing's apex at some appropriate distance, and oscillating the cylinder/splitter combination at its shedding frequency.

Preliminary experiments done in a (two-dimensional) water table using a cylinder/splitter combination with an $l/d = 1$, indicated that it was possible to lock the phase in step with the splitter plate's oscillation at frequencies close to the shedding frequency. Forcing the splitter to oscillate at frequencies slightly higher or lower than the natural shedding

frequency appeared to have no visible effect on the wake. Further experiments in the water tunnel, where the full three-dimensional flow could be evaluated, resulted in a similar response. Figure 6.1 shows how the von Kàrmàn filament of a particular sense was generated and convected with the phase of the oscillating cylinder.

Thus, a small fin attached to the cylinder as described in the preceding paragraph would serve two purposes:

1) It would allow the von Kàrmàn filaments to be controlled, such that it would allow the delta wing's pitch up to be synchronized to a specific filament being shed from the cylinder.
2) It would keep dye on one side of the fin from mixing with a different color on the opposite side of the fin, allowing distinct separation between the two von Kàrmàn filaments that are shed in one cylinder's oscillation cycle.

6.2- Experimental Set-Up

The same installation as has been described previously (the Water Tunnel at Wichita State University's NIAR) was used. Attached to the carriage is a mechanism which allows a circular, commercially available brass tube to be used as a cylinder. The mechanism uses a DC-motor to oscillate this cylinder at a frequency given by the supply voltage. This allows the natural shedding frequency to be matched by the forced oscillation.

6.2.1- Large Cylinder

Two sizes of cylinder were used (Table 6.1). A commercially available brass tube $^{3}/_{8}$ inch diameter, with a small fin attached to it on the downstream side, was used as the large cylinder. The fin is ½ inch wide and has a thickness of 0.02 inch. The cylinder trailing edge (not the fin trailing edge) is then located at a distance of 0.25 chord length ahead of the delta wing's apex when the angle of attack is zero. The cylinder diameter which was chosen is the

closest commercially available so that at the 0.4 ft/s towing velocity the wake shedding frequency is closest to 3 Hz. The fin's width is the smallest commercially available extrusion that was stiff enough to be worked with. The cylinder is held centered along the delta wing's root chord, and with the fin on the downstream side. Dye is injected at several locations at the base on the side of the fin closest to the camera. Thus, only the von Kàrmàn vortex that sheds on the side where the dye injection ports are located entrains dye and becomes visible; the vortex on the opposite side (opposite sense of rotation) is not (normally) visible. The set up is schematically presented in Figure 6.2.

TABLE 6.1

CYLINDER SPECIFICATIONS

Test Velocity (ft/s)	0.4	0.4
Cylinder Diameter (inch)	$^3/_8$	$^1/_4$
Shedding Frequency (St = 0.21)[66]	3 Hz	5 Hz
Diameter Reynolds Number	1100	625

6.2.2- Small Cylinder

In the smaller cylinder test cases, a brass tube $^1/_4$ inch diameter, with a small fin attached to it on the downstream side, was used. The fin is ½ inch wide and has a thickness of 0.02 inch. In this case, the diameter is sized so that the von Kàrmàn wake filaments' wavelength would not be smaller than the optical system's uncertainty at the 0.4 ft/s towing

velocity. In other words, the objective here was producing sufficient separation between the von Kàrmàn vortex filaments for the video analysis tool to reliably distinguish them. The resulting wake shedding frequency was approximately 5 Hz.

6.3- Experimental Issues

Several issues were encountered during the development of the cylinder mechanism.

1) Since the angle of attack will change, so does the angle at which the von Kàrmàn vortex street impinges upon the delta wing. This creates two problems. First, the rotational axis of the two vortices (i.e., the LE vortex and the von Kàrmàn vortex) change orientation with respect to each other during the pitch-up maneuver. This results in a geometric mismatch, with the angle between the two vortices going from nearly orthogonal at low α values to very acute (almost parallel) at very high α values. Second, as a consequence of this change in angular relationship between the two vortices, the von Kàrmàn filament's vorticity contribution also changes as α increases, and is more orthogonal to the LE vortex's azimuthal vorticity component at a low angle of attack.
2) Dye migration from one vortex to another can occur, especially if one vortex is substantially more powerful that the other. Since there is no physical mechanism in place to minimize or prevent this from occurring, the solution is to use contrasting dye colors. In particular, dye markers from opposite ends of the color spectrum (red and blue) were used for the leading edge vortex and the von Kàrmàn filaments. Whenever dye migration was suspected, or to enhance the VB's visual identification, color filtering of the Bitmap images captured was used. For example, red dye injected at the cylinder will become less visible when the image is filtered through Microsoft Photo Editor software with a blue filter.

3) Occasionally the wrong von Kàrmàn filament was visualized. Ideally, only the von Kàrmàn vortex that sheds on the side of the dye injection ports entrains dye and becomes visible; the vortex on the opposite side (opposite sense of rotation) is not visible. Experimentally, it was found that the visualization was sensitive to the rate of dye injection: too much dye would make both vortices visible, while too little dye would make both filaments invisible.
4) As a result of the cylinder having such a long aspect ratio (i.e., length to diameter ratio), and because the cylinder was initially only supported at the top, it turned out that it had very little rigidity. This allowed the cylinder to move sideways (from the point of view of the delta wing, from port to starboard) in phase with its wake shedding. This was particularly true of the small cylinder, which would move ±1 ½ inches from the centerline.

To control the side movement described in point 4, a centerline guide was added to the bottom of the test section. This centerline guide was built on an aluminum frame and dropped into the test section before installing the towing mount. The oscillating cylinder's bottom tip was then modified with a pin that would engage the guide and, it was hoped, would prevent the cylinder's sideways (i.e., port to starboard) movement at the bottom of the test section.

The centerline guide prevented sideways motion, but the reaction imposed on the guide's walls now provided enough force that a non-slip condition developed at the guide-cylinder interface. As a result, the cylinder's rotational motion now translated to a fore-and-aft movement in phase with the oscillation. In order to remove this fore-aft motion, the bottom guide was further modified to accept a small skate. The cylinder's bottom pin would then engage the skate, which itself would ride inside the guide at the bottom of the test section. This solution was reasonably successful in that, with the large cylinder, the added rigidity was able

to control the deflection sufficiently to move the skate along the bottom guide without interfering with cylinder's oscillation. A smooth movement of the carriage-cylinder-skate was possible.

With the small cylinder, however, the fore-aft deflection was only reduced by about $^1/_3$. The small cylinder's lack of rigidity was enough that the cylinder would try to tilt the skate, increasing and decreasing the friction in the system enough to affect the oscillation frequency. Several different attempts were made to reduce this, including different clearance sizes between the cylinder's bottom pin and the skate, and different lengths of skate, and different water-resistant lubricants at the bottom pin (Figure 6.3). The problem was not resolved, and the oscillation frequencies of the small cylinder were erratic. Yet, as will be shown in the results, the vortex burst location tracked the erratic frequencies with a large degree of fidelity.

6.4- Thrust Generated by the Oscillating Cylinder

Based on the behavior observed, it was clear that the cylinder's oscillation at high frequencies (i.e., small cylinder) was resulting in a thrust being generated, which in turn deflected the cylinder. The thrust caused enough deflection to foul the small cylinder's motion. This was a side effect the author had not anticipated would be of such strength.

A quick literature survey on papers by Koochesfahani [82, 83] and Triantafyllou [84] indicated that airfoil sections undergoing oscillatory pitching at reduced frequencies $k' > 2$, the wake rolls up into coherent vortex structures, where the reduced frequency k' used by the author is defined as

$$k' = 2\pi fc / 2\, U_\infty \qquad (6.1)$$

In particular, for an NACA 0012 airfoil pitched at 5 Hz ($k' = 8.35$), a slight amount of thrust could be generated, such that a velocity $U/U_\infty = 1.3$ was attained at a distance of $x/c = 1$.

At this point, assuming the characteristic length c' of the experimental set-up used is the cylinder diameter d plus the fin's width attached to the cylinder, the following reduced frequencies were calculated. For the small cylinder (where c' = $^3/_4$ inch), k'= 4.78, while for the large cylinder (c' = $^7/_8$ inch), k' = 3.35. Hence, in order to maintain the lock on the von Kàrmàn vortex street, a small amount of thrust would have to be generated with the smallest cylinder. On the other hand, the distance from the apex to the cylinder's rear edge would be d = 2.5 inches for the large cylinder, which translates to a distance ratio d/c' = 2.85. For the smaller cylinder, this ratio d/c' becomes 3.5. The assumption would be that, just like a jet, dissipation would reduce the velocity component responsible for the thrust. No attempt to measure this dissipation was done, however.

6.5- Cylinder Results

6.5.1- Experiment Matrix

The following test matrix (Table 6.2) was conducted. When the test matrix was first written, the experiments were extrapolated from the preliminary results observed by using a small, transparent plastic delta wing. In that initial, very early set-up, a small digital camera was installed on the carriage, and it observed the behavior of the leading edge vortices from the top. Those initial results, using the transparent delta at constant angle of attack and constant freestream conditions, suggested that the vortex burst location had moved forward towards the apex, and that there had been a high degree of core distortion. It also suggested that the appearance of dye "clouds" may have been time related. In the process of actual execution, several of the initial ideas were discarded, or replaced with more meaningful experiments. These deviations are noted in the table.

TABLE 6.2

EXPERIMENTAL MATRIX FOR VON KARMAN IMPINGEMENT EXPERIMENTS

Model:	12-inch chord 70-degree Delta Wing								
Reynolds Number:	33,000								
Proposed Matrix						**Actual Matrix**			
Type of Test	**Angle of Attack α (deg)**	**Pitch Rate κ**	**Cylinder Size**	**von Kàrmàn Vortex Phase at Start of Pitch**	**No. Runs per Test Case**	**Angle of Attack α Tested (deg)**	**von Kàrmàn Vortex Phase at Start of Pitch**	**No. Runs**	**No. Video Frames Analyzed**
Static α	35, 40,… 55	0	Large	Fixed Cylinder (i.e., Natural Shedding)	3 trials* 5 = 15	35, 40, 45, 50	Fixed Cylinder	12	1345
	35, 40,… 55 35, 40,… 55 35, 40,… 55	0	Large	Left of Apex Center Right	15 15 15				
	35, 40,… 55 35, 40,… 55 35, 40,… 55	0	Small	Left of Apex Center Right	15 15 15				
Dynamic α	15 to 55 15 to 55 15 to 55	$\kappa = 0.2$	Large	Left of Apex Center Right	3 3 3	15 to 55 15 to 55 15 to 55 15 to 55	Port Center → Starbrd Starboard Center → Port	3 2 3 3	188 98 141 136
		$\kappa = 0.2$	Large			35 to 55 35 to 55 35 to 55 35 to 55	Port Center → Starbrd Starboard Center → Port	3 3 3 3	192 182 171 190
	15 to 55 15 to 55 15 to 55	$\kappa = 0.1$	Large	Left of Apex Center Right	3 3 3	35 to 55 35 to 55 35 to 55 35 to 55	Port Center → Starbrd Starboard Center → Port	3 3 2 3	232 188 160 221

TABLE 6.2

(CONCLUDED)

Proposed Matrix						Actual Matrix			
Type of Test	Angle of Attack α (deg)	Pitch Rate κ	Cylinder Size	von Kàrmàn Vortex Phase at Start of Pitch	No. Runs per Test Case	Angle of Attack α Tested (deg)	von Kàrmàn Vortex Phase at Start of Pitch	No. Runs	No. Video Frames Analyzed
Dynamic α	15 to 55	$\kappa = 0.2$	Small	Left of Apex	3	15 to 55	Port	3	280
	15 to 55			Center	3	15 to 55	Center → Starbrd	3	209
	15 to 55			Right	3	15 to 55	Starboard	3	180
						15 to 55	Center → Port	3	238
		$\kappa = 0.2$	Small			35 to 55	Port	3	289
						35 to 55	Center → Starbrd	3	345
						35 to 55	Starboard	1	91
						35 to 55	Center → Port	3	287
	15 to 55	$\kappa = 0.1$	Small	Left of Apex	3	35 to 55	Port	2	259
	15 to 55			Center	3	35 to 55	Center → Starbrd	0	0
	15 to 55			Right	3	35 to 55	Starboard	3	315
						35 to 55	Center → Port	3	364
Total Number of Runs					117	Total Number of Runs or Frames		76	6301

6.5.2- Quantitative Results with Fixed Large Cylinder

Subsequent to the transparent delta, the 12-inch delta wing was installed and an initial baseline was run. The first set of results plots the time histories of the vortex burst position with the wing behind a stationary large cylinder, such that the excitation is entirely a function of the natural shedding. In general, the plots show periodic fluctuations in the vortex burst location. These fluctuations are non-symmetrical. The vortex burst appears to jump to some location forward towards the apex and then move gradually towards the trailing edge. As the angle of attack increases, the range between the forward-most and rear-most VB positions decreases.

The first set of results is illustrated by the time histories of the vortex burst position at static angles of attack of 35, 40, 45, and 50 degrees (Figures 6.4 through 6.7). These plots are obtained from a 3 second time window around the center of the field of view (FOV), i.e., the time history starts 1.5 seconds to the left of the center of the FOV, and ends 1.5 seconds to the right of center. They are then aligned so that the first valley is shown at the plot's left. The apex is the x= 0 location, where the x-coordinate is horizontal and parallel to the freestream velocity. Three runs at every angle of attack are performed. Also shown are captured images corresponding to the time frames indicated that are representative of the periodic flow behavior experienced by the delta wing.

The plots show periodic fluctuations in the vortex burst location. At the lower values of α tested (Figures 6.4 and 6.5), the vortex burst appears to jump to some location forward towards the apex and then move gradually towards the trailing edge. As the angle of attack increases, the range between the forward-most and rear-most positions of the vortex burst

decreases. This range is large (greater than 0.1c) at α=35 degrees (Figure 6.4). Eventually, it diminishes to about 0.05c at the highest angle of attack tested (Figure 6.7).

The von Kàrmàn vortex filaments are tracked and plotted in terms of their horizontal distance x. When the LE burst location time histories are plotted and the wake filaments are extrapolated, the interaction between the two vortices can be observed. Figures 6.4 through 6.7 show the interaction (i.e. the extrapolation of the wake filaments) for 1 run at each angle of attack, and are representative examples of what is observed in all runs. The passing of the wake vortex filament provokes the VB to forward jump (towards the apex), which then moves aft at approximately the same velocity as the passing of the filament. This relationship holds best at α=40 degrees, but is still evident at the highest α tested.

Compared to the basline (no impingement) burst location, Figure 6.8 shows that the vortex burst moves forward towards the apex (denoted as the lower bound in the figure) when the wake impinges. The average burst location coincides with the static burst position for this delta wing, in this mount, under unperturbed freestream conditions. The VB's range of motion under the wake impingement remains relatively constant on either side of the average. There is a slight reduction in the range at the highest α tested, particularly in the lower bound.

6.5.3- Qualitative Observations with Fixed Large Cylinder

During the experiment, two phenomena were observed as the LE vortex is impinged by the von Kàrmàn wake. They are illustrated in Figure 6.9 and 6.10. First, there is the core's distortion in the form of waves that travel along the core. The distortions are not uniform in amplitude, nor do they appear at regular intervals. Second, close observation of the LE vortex core shows that the dye clumps into small, but regularly spaced concentrations. These areas are convected along the core up to the burst. While no attempt was made to correlate the location

of these dye concentration areas with the wake vortex filaments (their dye in the wake filaments has become too faint to reliably accomplish this), it is fair to assume, by virtue of their regularity, that they are related.

After close observation of the wake vortex filaments and the LE vortex core, it appears they become interlaced as the vortex core entrains the wake filaments as shown in Figure 6.11. It appears the wake vortex filaments are wrapped around the LE vortex core by the shear layer, such that there is substantial deformation of the wake filament.

While the results obtained with the optical technique are not sufficient to put forth a complete picture of the flow mechanics responsible for the behavior, a possibility suggested by the regular dye concentrations in Figure 6.10 is that the entrained filaments' vorticity induces changes in the vortex core's axial velocity, resulting in a periodic change in swirl angle.

Even though only one LE vortex was tracked, an asymmetric interaction, where the opposite LE vortex has a mirror-image response, would be expected. This is based on the fact that alternating von Kàrmàn filaments of different sense of rotation are convected downstream. This induces an alternating cross-flow velocity field that could be similar to that found on delta wings subjected to periodic yaw oscillations. Although the initial arrival of a von Kàrmàn vortex precipitates a forward jump, the fact that the burst point moves aft suggests some mechanism to move the burst aft in a periodic manner may be possible.

6.5.4- Quantitative Results with Large Oscillating Cylinder

At this point, the cylinder was oscillated at a rate that would match its natural shedding frequency. It was fairly easy to distinguish when the oscillations were at the right frequency: long dye filaments would form in the cylinder wake when the frequencies were matched. This would require two to four practice runs to get the match right.

The delta wing's pitch up was synchronized via the LED and shutter mechanism (Figure 6.2) so that it would commence when the fin behind the cylinder was at its full port, full starboard, in the center going port, or center going starboard. The intent was to have some control of the cylinder's phase in relation to the start of the pitching mechanism. If the cylinder's oscillation and the delta wing's rate of pitch were repeatable, then a distinct phase shift would be observable when plots for a given pitch rate were to be collapsed on top of each other. In practice, there was enough variability in the cylinder oscillation frequency that plotting the individual runs did not result in a clearly visible phase shift.

Figures 6.13 through 6.46 show the results of each experiment's individual repetition. The bottom horizontal axis is the elapsed time from the beginning of pitch-up, while the upper axis is the angle of attack α (deg), beginning at around the first angle where a burst is distinct and visible. The burst locations have been transformed to an x/c coordinate. Also, note that the cylinder's oscillation is plotted in terms of port and starboard extremes of their travel (Figure 6.12). As noted in Table 6.2, 3 attempts at each configuration were performed and plotted. In just a few cases, however, fewer than 3 repetitions were plotted for a particular configuration. This was usually the result of dye becoming difficult to visualize in the analysis.

The first group deal with a large α range (15 to 55 degrees) at the fast pitch up rate of κ= 0.2 (Figures 6.13 to 6.23). In all three cases there are discontinuities, or jumps, in the vortex burst position, and appear to be related to the cylinder's position. Recall that the dye port on the delta wing visualizes the port leading edge vortex. At the same time, dye visualizes the von Kàrmàn vortex filament on the port side. The passing of the port vortex filament appears to synchronize with the VB's aft movement of the port leading edge vortex very well (in most cases), and is completely in line with observations previously discussed.

In some cases (e.g., Figure 6.16), the total magnitude of the excursions in the burst location (i.e., the difference between the fore and aft movement in a given jump) is small when compared to other experiments within the same group (configuration and trigger point). This variability in the experiments, is intriguing, and could be caused by slight variations of the cylinder's oscillating frequency resulting in an irregular mixing of the vortices. Borrowing from basic vibration theory, if two close frequencies are summed, a third heterodyned frequency of large magnitude, but lower frequency than the other two, is the result. Likewise, if the oscillation frequency and the natural shedding frequency are close (but not identical), a third frequency, lower in magnitude, could produce a large enough disturbance that large jumps in the vortex burst location result as it is convected past the wing. This could be supported by the fact that, due to friction, it was very difficult to maintain a perfect oscillating frequency, but countered by the fact that, throughout the analysis, no evidence of large eddies or other disturbances were observed.

It was also observed that, in general, more scatter and larger variations in the burst location occurred at the lower angles of attack, and that both scatter and burst movement became less as the wing attained the higher values of α. The discontinuity in the burst location was usually started by movements aft towards the trailing edge along with the convection of the von Kàrmàn filaments. A new bubble burst region would form upstream of the first one, and it would be convected downstream. As this second region moved away from the front of the wing, a third region would suddenly form along the leading edge vortex core, to be convected aft. When plotted in two-dimensions, this gives the impression of a forward "jump," but in reality a new burst is what forms at each discontinuity. In this regard, this is very much as

observed in the previous case (fixed cylinder), except that the amount of mixing occurring was much larger.

The second group of Figures (Figures 6.24 to 6.36) deal with a small α range (35 to 55 degrees) at the fast pitch up rate of $\kappa = 0.2$. In these cases, the behavior previously described was also in evidence. However, the VB's average location appeared to progress forward towards the apex at a shallower slope, i.e., a slower propagation velocity. If a line were to be fitted to represent the average of the scatter, then closer scrutiny of that line would suggest that the initial jump forward was very abrupt (occurring below $\alpha = 40$ degrees), followed by a very slow movement forward towards the apex (at about 0.1 x/c per second). This is somewhat different in that the previous group of Figures exhibited a higher forward propagation velocity (at about 0.2 x/c per second) for a longer period of time, resulting in an almost linear average burst location from 35 degrees α to 50 degrees. This behavior is, perhaps, to be expected in that the group of Figures whose α started at 15 degrees had additional time for their burst location movement to accelerate and stabilize. By the time the burst became visible at mid-chord, the propagation towards the wing's apex had achieved a stable rate.

The third group of Figures (Figures 6.37 to 6.46) deal with the same small α range (35 to 55 degrees) at the slow pitch up rate of $\kappa = 0.1$. The reason for this α range was that this was, given the pitch rate, what could be done with the 6 ft of carriage travel available. In these Figures, a very linear average propagation rate is noticed, even when there are cases (such as Figure 6.41) where the large deviations in the burst location occur (larger than 0.2 x/c) in response to the passage of a von Kàrmàn filament. This rate of propagation is also very shallow (equal or less than 0.1 x/c per second). All cases exhibited a good cause and effect

relationship between the passage of the von Kàrmàn filaments and the discontinuities of the vortex burst propagation.

6.5.5- Quantitative Results with Small Oscillating Cylinder

In the next set of Figures (Figure 6.47 to 6.76), the results of the smaller cylinder oscillations are presented. The same cases as were performed with the larger cylinder were repeated. These include two α-ranges at the fast pitch rate, and one slow pitch rate case. In general, the smaller cylinder's results were much harder to obtain given the smaller spacing between von Kàrmàn filaments, the difficulty in obtaining a constant and consistent friction in the system due to the small cylinder's higher compliance, and the more thorough mixing due to the smaller length scales.

The fourth group of Figures (Figures 6.47 to 6.58) deal with a large α range (15 to 55 degrees) at the fast pitch up rate of κ= 0.2. Similarly to what has already been observed in previous results, the discontinuities in the vortex burst position appear to be related to the cylinder's position: the passing of the port vortex filament appears to synchronize with the aft VB movement of the port leading edge vortex very well (in most cases), and is completely in line with observations previously discussed. In particular, it can be noticed that the oscillation frequency is faster than in the large cylinder's case, but at the same time it is irregular. In most cases, the time period between oscillations changed from one peak to the next. At the same time, by tracing the von Kàrmàn vortex filaments' position histories (solid slanted lines), it can be seen that the discontinuities in the leading edge vortex burst position coincide with the filaments' passage, even when the frequency (or the period between successive port excursions of the cylinder) is irregular.

In this set of Figures, the average vortex burst propagation average appeared to jump forward at a very fast rate at first (between $15 < \alpha < 30$ degrees), followed by a slow forward progression in the neighborhood of 0.1 x/c per second, stabilizing at 0.1 x/c. The character in the burst position's jump was such that the magnitude of the change with the passage of the von Kàrmàn filaments varied slightly with angle of attack α. At low values of α, the magnitude was largest (around 0.2 x/c), reducing in magnitude as the angle α increased. This is a consequence of an apparent change on the strength of the vortex burst. At low angles of attack, there is a small enough swirl velocity so that the mixing from the von Kàrmàn filaments promotes a large change in position. As the swirl velocity increases with the pitch-up, it becomes more difficult for the passing filaments to "dislodge," or move the burst axially. This behavior had also been observed, to some extent, with the fixed cylinder and the large oscillating cylinder. However, the large oscillating cylinder's mixing would tend to dominate the flow field, even at large angles of attack, making this trend more difficult to observe.

Continuing with the restricted α-range (35 to 55 degrees) in Figures 6.59 through 6.69, the high pitch rate replicated, generally speaking, the same trend. In fact, the forward movement in the burst location occurs during the first 5 or 10 degrees of α movement, followed by an almost static burst behavior, indicating that the equilibrium position had been reached. This initial movement was in some cases more like a discrete jump, rather than a smooth movement.

The last group of figures (Figures 6.70 to 6.76) shows the slower pitch rate effect (κ= 0.1) with the reduced α-range. This group of pictures is somewhat of reduced size compared to the other groups previously discussed. The combination of pitch rate, small range of angles of

attack, and small cylinder, resulted in very small features. In the interest of maintaining the highest level of accuracy a number of runs were thrown out based on the following criteria:

1) Sometimes, large mixing occurs during the collision between vortices, resulting in a blurred VB image. A clear and defined burst location is necessary in order for the frame to count. If the burst location is not apparent, then that frame is skipped.
2) If more than 2/3 of the frames are skipped throughout the run, or if enough frames are skipped consecutively such that the plotted data becomes disjointed, the run is eliminated from consideration. This reduced the number of runs available for analysis.

In general, these experiments (with slower pitch rate and reduced α-range) exhibited a smaller disturbance in the vortex burst location due to the von Kàrmàn filament passage than in previous experiments. The VB's forward propagation was also at a slower pace, less than 0.1x/c per second.

As a group, a sample of several large and small cylinder runs were plotted together (Figures 6.77 to 6.82). For the large cylinder case at a fast pitch rate (κ= 0.2), it can be seen that almost all the burst propagation movements were aft of the curve obtained when no cylinder was used to excite the flow (in Figure 6.77, represented by the bold solid line). An approximate envelope can be drawn that extends 0.05x/c forward of this line, and 0.15x/c aft of a line at 55 degrees, increasing to 0.3x/c aft at 45 degrees.

For the small cylinder at a fast pitch rate (Figure 6.78), the burst propagation movements occurred both forward and aft of the no-cylinder burst locations (bold line). At low values of α the envelope was observed to encompass a maximum of 0.3x/c fore and aft the bold line (at α= 35 degrees), with complete runs falling either forward (such as the center-starboard and starboard phase cases) or aft (such as the port phase cases). As the angle of attack

increases, the envelope converges somewhat, but not symmetrically. The runs whose burst positions started aft of the bold line (at a lower α) remained a considerable distance aft at the highest values of α, while the runs forward of the bold line migrated aft. This gives the impression, at very high values of α, that the burst propagation movements were constrained to locations aft of the bold line. This behavior also gives the impression of two distinct groups of data, with one group shifted vertically with respect to the other. It should be noted, however, that the starboard side burst should be experiencing a mirror image response. That is, the starboard side leading edge vortex would burst forward of the bold line while the port side burst would be aft. Conversely, the starboard side burst would be aft of the bold line while the port side burst would be foreward.

This initial comparison between the large cylinder, whose envelope was non-symmetrical (i.e., the burst movement forward of the no-cylinder burst line was much smaller compared to the aft movement), and the small cylinder that had an almost symmetrical displacement fore and aft of this solid bold line, is interesting. However, the limited number of runs for the small cylinder case makes these observations rather than absolute conclusions about their behavior. One possible explanation, if indeed these observations are true, is that the small cylinder had more energy (due to the small cylinder's faster angular movement), thus was able to excite perturbations within the leading edge vortex core at levels high enough to trigger bursting farther upstream (or downstream). As we have observed earlier, the small cylinder was also able to produce enough thrust to deflect the cylinder.

A second possible explanation is that the shorter wavelength between von Kàrmàn filaments was able to excite certain instabilities. For example, a spring-mass system will tend to resonate when excited at or near its natural frequency, thus exhibiting a filtering effect. This

higher frequency of excitation as seen by the delta may have triggered components of internal instabilities in the vortex core, leading to a faster growth than otherwise in a normal non-disturbed flow.

Figures 6.79 and 6.80 (large and small cylinder at a reduced angle of attack range from $35 < \alpha < 55$ degrees, respectively) indicate that the burst location is almost symmetrically distributed fore and aft of the no-cylinder bold solid line. This same behavior, perhaps with a slightly smaller range of movement, was also observed in Figures 6.81 and 6.82 (large and small cylinder, slow pitch rate, reduced α-range). This was different to what was observed in Figure 6.77 in the extent of the movement observed when using the large cylinder. Comparing Figures 6.77 to 6.79 and 6.81, and since the experiment was repeated with a small α-range at both high and low pitch rates, at face value one must conclude that starting the pitch up at α= 15 degrees changes the extent of the expected vortex burst location shift to an envelope mostly aft of the bold solid line.

The vortex burst type is documented in Table 6.3. For the static α cases the S-type burst was seen at low angles of attack. For high angles of attack, the B-type burst became the prevalent type at some point between $40 < \alpha < 45$ degrees. When the large cylinder was inserted in the flow, the same general behavior was observed, i.e., the transition from S-type to B-type occurred approximately at 45 ± 5 degrees. This indicates the mechanism causing the burst type transition was not appreciably affected by the large cylinder. On the other hand, introducing the small cylinder did not produce a consistent set of observations. It would appear that either the higher frequency or the heavier mixing due to driving the small cylinder did affect the burst type transition.

TABLE 6.3

TYPE OF VORTEX BURST ENCOUNTERED DURING VON KÀRMÀN WAKE EXPERIMENTS

Figure No.	Pitch-Up (UP) or Down (DN)		Large or Small Cylinder	Vortex Burst Type and Evolution
	Rate (k)	Start / End α (deg)		
6.4	Static	35 deg	Large	Spiral all.
6.5	Static	40 deg	Large	Spiral all.
6.6	Static	45 deg	Large	2/3 of experiments were bubble.
6.7	Static	50 deg	Large	Bubble all.
6.13 to 6.23	0.2	15 to 55	Large	Spiral to α= 45 deg (+/- 5 deg).
6.24 to 6.35	0.2	35 to 55	Large	Mostly spiral to α= 45 deg (+6 /-5 deg). Occasional (less than 1/3 experiments) were bubble all.
6.36 to 6.46	0.1	35 to 55	Large	Spiral to α= 43 deg (+5 /-3 deg).
6.47 to 6.58	0.2	15 to 55	Small	Mostly bubble all. Occasional (3 out of 10 experiments) were spiral to α= 48 deg (+/- 1 deg). 2 runs had some vortex kinks.
6.59 to 6.68	0.2	35 to 55	Small	Half the runs exhibited spiral to α= 47 deg (+3 /-5 deg). Otherwise bubble all.
6.69 to 6.76	0.1	35 to 55	Small	Mostly spiral to α= 42 deg (+4 /-2 deg). Some kinks observed.

CHAPTER 7

CONCLUSIONS

A series of experiments was performed at the Wichita State University's NIAR Water Tunnel on a 12-inch root chord, 70-degree sweep sharp leading-edge delta wing, using a self-constructed towing mount. These experiments were the main thrust of an investigation into the behavior of the leading edge vortex burst under a series of variable freestream velocity and von Kàrmàn impingement conditions.

An optical methodology was used to determine the leading edge vortex's burst location. A video camera was used to record the images to S-VHS tape, which was then analyzed for burst location with respect to root chord using a VisualBASIC computer code. An uncertainty between 0.02 and 0.06 x/c was attained with this system. The ratio of projected frontal area to tunnel cross-sectional area, as well as the ratio of wing span to tunnel span, were considered acceptable for low test section interference (as per the published results on ground facility interference by Ericsson [77]).

Several disadvantages were found when using this towing system. The towing mount's greatest disadvantage, it was discovered, was the long time necessary to attain quiescent water after a run. This limited the number of runs for any one configuration to 3 or 4 per hour.

The second greatest disadvantage was that a limited amount of time was available for any given run, since the track's length was limited by the length of the water tunnel test section. In a related disadvantage, because the towing mount was sized by the test section's dimensions, a limited angle of attack range was possible, and only small motors could be mounted onto the carriage.

7.1- The Towing Mount Validation

The towing mount's validation was carried out by performing both static-α and pitch-up surveys at two different pitch rates. The validation's results can be summarized as follows:

1) During the static runs between α= 20 degrees and α= 55 degrees (in 5 degree increments), it was found that the burst position appeared to have a substantial amount of scatter, and the general slope of the curve is shallower than that of Myose et al.'s previously reported results [49]. This comparison set was performed in that same water tunnel, but using a fixed mounting system. Comparison to other results reported for a 70-degree delta wing showed that there was a wide scatter in the vortex burst location, and that the results here obtained were within that scatter.
2) Another factor thought to contribute to the discrepancy in the results was the mounting arm's position in the initial investigation by Myose et al. [49]. Literature was found that indicated an effect is to be expected when a solid object is placed in the delta wing's flow field downstream of the burst location. With this in mind, the mounting arm used by Myose et al. [49]. was simulated on the present towing mount. It was found that the simulated stem behind the delta wing did produce a slight change in VB location. This change in position, however, was not consistent (for a given angle of attack) with the direction in which the stem was installed (i.e., pointing towards the port or the starboard side of the wing).
3) To qualify the mount dynamically, the wing was pitched at κ= 0.1 and 0.2 and compared to previously reported results. There was some discrepancy in the location of the vortex burst, but it was within the error bands of both the original experiment and the towing mount

experiment. In general, the vortex burst locations compare favorably with Myose's results [49].

7.2- Variable Freestream Velocity Experiments

Two methods were attempted to attain a variable freestream velocity with the towing mount. In the first method, a capacitor bank was made to discharge through the drive motor's windings, resulting in an exponential deceleration that was almost linear in the range of speeds tested.

1) When using the capacitor discharge deceleration, the towing mount had not matured yet to a high level of robustness. This resulted in a heavily damped carriage oscillation whenever its velocity was changed. In the case of decelerating flow, the target velocity was undershot due to the tension spring on the tow line. This undershoot of the velocity is a complicating and unavoidable factor, given the construction of this experimental set-up.
2) There appeared to be an almost one-on-one relationship between the position of the minimum velocity point (the "valley" in the velocity plots) and a marked reduction in the VB's forward propagation rate. A distinct "leveling-off" in the burst location scatter plot at or slightly after the minimum velocity valley was observed.
3) This reduced VB propagation rate changed again approximately at the point when the target (lower) velocity is reached. This implies the arresting of the VB's forward motion occurred during the accelerating portion, when the carriage was recovering from the undershoot.
4) Two possible explanations to this observed behavior were proposed. In the first one, it was the delta wing's slight acceleration that produced an increasing change in the axial vortex core velocity. In the second explanation, the behavior observed was due to the global reduction in the forward velocity. The phase lag between the beginning of the slow down

and the leveling-off in the forward propagation rate was due to the time constant needed for the change in vorticity at the leading-edge to become convected to the core by the shear layer.

5) For angles of attack $\alpha < 35$ degrees, the scatter overlapped between all the curves. The slope of the results, in this range of α, was almost a match to the slope of the $\kappa = 0.2$ line.

6) At angles of attack higher than 35 degrees, the $\kappa = 0.2$ to 0.4 and $\kappa = 0.2$ to 0.27 lines displayed what can be interpreted as a gradual change between the $\kappa = 0.2$ line and the corresponding κ value resulting from the slower velocity. The spacing displayed by the progression from κ= 0.1, 0.2, 0.27, and 0.4 appeared to be intuitively correct (i.e., with changes in the curve's slope that are consistent and proportional to the increase in κ value).

With the second method (Pulse Width Modulation) it became possible to test up to twelve combinations of acceleration and deceleration, pitch up and pitch down rates, and range of angle of attack α were tested. At least 3100 frames were analyzed.

1) One possible means to non-dimensionalize the time axis is to introduce

$$t' = (t * a) / (\omega * c) \tag{7.1}$$

where t= elapsed time, a= acceleration, ω= pitch rate, and c= chord.

2) Accelerating from 0.2 to 0.4 ft/sec (an initial to final velocity ratio of 0.5) and pitching up at κ= 0.2 between 15 to 55 degrees, there was a slight downward inflection in the burst location curves at approximately 1.75 and 2 seconds (t'= 1.01 to 1.15, respectively) after the beginning of the velocity ramp-up (acceleration from 0.2 ft/s).

3) Decelerating from 0.4 to 0.2 ft/s, a reduction in the vortex burst propagation velocity is apparent at about 1.5 seconds (i.e., t'= 0.863) after the freestream velocity begins to decelerate. This retardation delays the VB's forward propagation (towards the apex).

4) During a small deceleration from 0.4 to 0.3 ft/s (a minimum to maximum velocity ratio of 0.75) and pitching up at a rate $\kappa = 0.2$ between 15 to 55 degrees, a reduction in the vortex burst propagation velocity is apparent at approximately 1 second after the freestream velocity began to change ($t' = 0.288$). This retardation delays the VB's forward propagation. The VB's forward propagation resumes at about 4.5 seconds elapsed time ($t' = 1.294$), and this appeared to be at the same propagation rate (i.e., the slope of the burst) compared with the experiment's beginning.

5) It was concluded that at $\kappa = 0.2$, for large ranges of angle of attack α, the freestream velocity's deceleration appeared to arrest the VB's motion anywhere between 1.5 and 2.5 seconds after the deceleration began to take place (i.e., $0.863 < t' < 1.438$). The positive delay in the burst movement appeared to be strongest when the delta wing experienced a strong deceleration ($dv/dt = 0.092$ ft/s^2) over a large range of α values (30 to 50 degrees). This effect became much smaller at slower decelerations and/or limited values in the α range. This implies that, perhaps, instabilities (whether inherent or external to the vortex core) could help precipitate the forward jump making it easier to lose lift than to keep lift.

6) It was concluded that the acceleration had the effect of increasing the VB's forward propagation along the leading edge vortex core. At different α–ranges and velocity ratios, accelerating produced a mild to strong negative effect on the burst location when accelerating. This negative effect was almost independent of the actual acceleration or range of α over which it occurred.

7) The results obtained during pitch up at the slower rate of $\kappa = 0.1$, for different combinations of acceleration and deceleration, exhibited the same general features as those observed during the faster pitch-ups: deceleration in the freestream velocity appeared to have a

beneficial effect, i.e., it arrested the VB's forward motion (thereby delaying the VB's propagation towards the apex). Acceleration in the freestream velocity appeared to have the opposite effect, that of pushing the burst location forward.

8) A second trait observed during the slower pitch-up tests was that the degree of scatter in the data increased. In some cases there were large fluctuations along the time axis where the forward propagation accelerated. In other cases slightly different curves (one for each experiment performed) were traced, each having identical slope but separated from its neighbor by a few fractions of a second. This indicated that, at the slower pitching rate, the experiment was more sensitive to either external noise (such as unavoidable vibrations in the carriage being transmitted to the delta wing), or to something instrinsic within the flow phenomenon. The experiment as it was performed could not isolate the cause of this variability.

7.3- The von Kàrmàn Impingement Experiments

The von Kàrmàn impingement experiments were inspired by two simple ideas. One, leading edge vortices are susceptible to external influences, e.g., the fuselage forebody vortices, or the placement of canards in front of a delta wing. This leads to considering the effect of an impingement from another set of vortices upon the delta wing's leading-edge vortices.

The second idea was that a known forcing function could be used to impinge upon the delta wing. A von Kàrmàn vortex street has a well-known behavior, and it was determined to be an ideal candidate for interaction with the delta wing's leading-edge vortex system. By introducing a circular cylinder of appropriate diameter, perpendicular to the flow and to the span of the delta wing, it is possible to impinge von Kàrmàn filaments at known frequencies.

A set of experiments with both a large and a small cylinder mounted in front of the delta wing were performed. It was initially thought that phase comparisons would be possible, so in order to control this phase, a small fin was placed on the cylinder's wake side. The cylinder would then be driven at its natural shedding frequency, and so the von Kàrmàn filament's phase would be known. There was some variability in the driven cylinder's frequency due to uneven friction in the cylinder guides and oscillating mechanism, particularly the guide at the bottom of the tunnel. Nevertheless, the following conclusions could be drawn from this part of the investigation:

1) Initially, a fixed cylinder was used to prove the concept. It was possible to modulate the vortex burst location in response to the passage of the von Kàrmàn filaments shed from the cylinder.
2) These initial results yielded a general picture: at the lower values of α the vortex burst appeared to jump to some location forward towards the apex and then move gradually in the downstream direction. This process repeated itself as von Kàrman filaments were convected past the delta wing and the LE vortex. As the angle of attack increased, the range between the forward-most and rear-most positions of the vortex burst decreased. This range was large (greater than 0.1c) at α= 35 degrees, but diminished to about 0.05c at the higher angles of attack.
3) The von Kàrmàn vortex filaments were tracked and plotted in terms of their time histories. A good cause and effect relationship between the passing of the wake vortex filament and a forward jump (towards the apex) of the LE burst was found. This forward burst of the LE vortex would then move aft at approximately the same velocity as the passing of the filament. This relationship held best at α= 40 degrees.

4) The average vortex burst position under the wake impingement regime moved forward towards the apex at lower angles of attack, when compared to the static burst location (no impingement). Except for Figure 6.77, the average burst location coincided with the static burst position for this delta wing, in this mount, under unperturbed freestream conditions.
5) In general, the VB's range of motion under the wake impingement due to a fixed cylinder remained constant on either side of the average. There was a slight reduction in the range at the highest α tested, particularly in the lower bound.
6) Similar features were found when using the cylinder as a driven member in the flow field. The main difference was the extent of the mixing: due to the more energetic von Kàrmàn wake, larger burst location movements at low to mid values of α were produced.
7) Starting a fast pitch up at α= 15 degrees (i.e. Figure 6.77) changed the expected VB location to an envelope mostly aft of the no-cylinder burst location line. Other cases had a more symmetric burst distribution both fore and aft of the no-cylinder burst location.

7.4- Observations and Recommendations about the Experimental Investigation

With regards to the experimental investigation as a whole, there are several concluding remarks that must be made:

1) The short time available for experimentation and observation, coupled with the long time to wait between runs, make the towing mount a difficult device to work with as it is currently implemented. The limited productivity must be balanced with the need for fast velocity changes that can be accomplished using the mount.
2) Increased capability resulted from modifying the towing mount to use a PCM variable speed drive. Capacitor discharge works very well with an almost linear velocity decay, but requires a large bank of capacitors given the small time constant (i.e., motor's internal

resistance is small). The PCM drive allowed not only controlled deceleration, but also controlled acceleration.

3) 6481 video frames were analyzed for the von Kàrmàn experiments, and 8566 video frames were analyzed for the variable velocity experiments, which represents 222 runs and more than 500 seconds of data in total. An additional 30 to 50 runs were not used in the final analysis, but were carried out in the water tunnel. This compendium represents a significant experimental effort in two areas where there have been few experiments: dynamic pitching of a delta wing *with* dynamic freestream, and von Kàrmàn wakes impinging a delta wing.
4) While the towing mount was inspired by the fast changes in velocity and attitude observed during the Cobra maneuver, comparisons with the actual aircraft are difficult. From a pure dynamic freestream point of view, the towing mount was a success in that it demonstrated significant changes in leading edge vortex bursting with changes in velocity faster than could be attained with the water tunnel pump only.
5) The von Kàrmàn impingement experiments lead to some interesting results, the most important of which is that burst location can be modulated by an external forcing, even when the axis of the impinging vortex changes in orientation: as the delta wing pitched up, the von Kàrmàn filaments remained oriented vertically, thus changing the angle between them.
6) The addition of a skate to guide the oscillating cylinder's bottom tip required significant experimental effort to reduce friction, but the modification succeeded in reducing the cylinder's longitudinal and lateral movements, and thus producing valuable results.

7) While it appears that the results presented here are not a direct analogy to the Cobra maneuver because the degree of mixing is difficult to control, they do show that it is possible to improve upon the current Cobra maneuver tunnel experiment by simultaneous use of two variables (variable velocity and a second variable, such as oscillatory yaw or external forcing). In this regard, the experiments performed here represent an initial first look towards a more complex Cobra maneuver set-up.

7.5- Future Work

There are some avenues of work that were not covered by the current research effort and, in this author's opinion, would be of interest for future work. Some of these are outlined as follows:

1) Combination of variable freestream with von Kàrmàn vortex collision. This is the final extension of the current work, as it would combine all the elements tested.
2) Ground effect changes to vortex structure, either in delta wing or in conventional wing. One benefit of the towing mount is that, with additional work, it can be modified so that the model can approach the tunnel's bottom. Or, a false floor can be installed at some distance from the model, making ground effect experiments possible.

REFERENCES

LIST OF REFERENCES

[1] Anderson, J. D., *Fundamentals of Aerodynamics*, 2nd ed., McGraw-Hill, 1991.

[2] McCormick, B. W., *Aerodynamics, Aeronautics, and Flight Mechanics*, Wiley, 1979.

[3] Sprague, R. A., "Wind Tunnel and Water Channel High Angle of Attack Delta Wing Study and Comparisons, with Particular Reference to Vortex Core and Burst Locations," M.S. Thesis, Department of Aerospace Engineering, Wichita State University, Wichita, KS, Aug. 1989.

[4] Polhamus, E. C., "Predictions of Vortex-Lift Characteristics by a Leading-Edge Suction Analogy," *AIAA Journal of Aircraft*, Vol. 8, No. 4, Apr. 1971, pp. 193-199.

[5] Lee, M. and Ho, C. M., "Lift Force of Delta Wings," *ASME Applied Mechanics Review*, Vol. 43, No. 9, Sept. 1990, pp. 209-221.

[6] Didden, N., and Ho, C. M., "Unsteady Separation in a Boundary Layer Produced by an Impinging Jet," *Journal of Fluid Mechanics*, Vol. 160, 1985, pp. 235-255.

[7] Wu, J.Z., Vakili, A. D., and Wu, J. M., "Review of the Physics of Enhancing Vortex Lift by Unsteady Excitation," *Progress in Aerospace Science*, Vol. 28, 1991, pp. 73-131.

[8] Wu, J. M., and Wu, J. Z., "Vortex Lift at a Very High Angle of Attack with Massively Separated Unsteady Flow," *Fluid Dynamics of High Angle of Attack*, edited by Kawamura and Aihara, Springer-Verlag, 1992.

[9] Polhamus, E. C., "Predictions of Vortex-Lift Characteristics of Arrow, Delta, and Diamond Wings," NASA TN D-6243, Apr. 1971.

[10] Wentz, W. H., and Kohlman, D. L., "Vortex Breakdown on Slender Sharp-Edged Wings," *AIAA Journal of Aircraft*, Vol. 8, No. 3, Mar. 1971, pp. 156-161.

[11] Ericsson, L. E., "The Fluid Mechanics of Slender Wing Rock," *AIAA Journal of Aircraft*, Vol. 21, No. 5, May 1984, pp. 322-328.

[12] Lugt, H.J., "Vortex Flow in Nature and Technology," J. Wiley & Sons, 1983.

[13] Wedemeyer, E. H., "Vortex Breakdown," AGARD LS-121 *High Angle of Attack Aerodynamics*, 1982, Chapter 9, pp. 1-17.

[14] Wedemeyer, E. H., "Stable and Unstable Vortex Separation," AGARD CP-247 *High Angle of Attack Aerodynamics*, 1979, Chapter 13, pp. 1-10.

LIST OF REFERENCES (continued)

[15] Erickson, G. E., "Water Tunnel Studies of Leading-Edge Vortices," *AIAA Journal of Aircraft*, Vol. 19, No. 6, June 1982, pp. 442-448.

[16] Morton, S. A., Guy, Y., Morrow, J. A., and Blake, D.C., "Numerical Simulation of Periodic Suction and Blowing Control of Vortex Breakdown on a Delta Wing," AIAA Paper 99-3195, Jun. 1999.

[17] Leibovich, S., "Vortex Stability and Breakdown: Survey and Extension," *AIAA Journal*, Vol. 22, No. 9, Sept. 1984, pp. 1192-1206.

[18] Visser, K. D., and Nelson, R. C., "Measurements of Circulation and Vorticity in the Leading Edge Vortex of a Delta Wing," *AIAA Journal*, Vol. 31, No.1, Jan. 1993, pp. 104-111.

[19] Johari, H., and Moreira, J., "Direct Measurement of Delta-Wing Vortex Circulation," *AIAA Journal*, Vol. 36, No. 12, Dec. 1998, pp. 2195-2203.

[20] Mitchell, A. M., and Molton, P., "Vortical Substructures in the Shear Layers Forming Leading-Edge Vortices," *AIAA Journal*, Vol. 40, No. 8, Aug. 2002, pp. 1689-1692.

[21] Sarpkaya, T., "Vortex Breakdown in Swirling Conical Flows," *AIAA Journal*, Vol 9, No. 9, Sept. 1971, pp. 1792-1799.

[22] Campbell, M. E., "Control of Vortex Breakdown," http://www.mae.cornell.edu/campbell/vtbk/vtbk.htm

[23] Menke, M., Yang, H., and Gursul, I., "Further Experiments on Fluctuations of Vortex Breakdown Location," AIAA Paper 96-0205, Jan. 1996.

[24] Gursul, I. And Xie, W., "Origin of Vortex Wandering over Delta Wings," *AIAA Journal of Aircraft*, Vol. 37, No. 2, Jan. 2000, pp. 348-350.

[25] Menke, M., and Gursul, I., "Self Excited Oscillatons of Vortex Breakdown Location over Delta Wings," AIAA Paper 97-0744, Jan. 1997.

[26] Mitchell, A. M., Barberis, D., Pascal, M., and Délery, J., "Oscillation of Vortex Breakdown Location and Blowing Control of Time-Averaged Location," *AIAA Journal*, Vol. 38, No. 5, May 2000, pp. 793-803.

[27] Escudier, M. P., and Zehnder, N., "Vortex Flow Regimes," *Journal of Fluid Mechanics*, Vol. 115, 1982, pp.105-121.

LIST OF REFERENCES (continued)

[28] Sarpkaya, T., "On Stationary and Traveling Vortex Breakdowns," *Journal of Fluid Mechanics*, Vol. 45, 1971, pp. 545-559.

[29] Sarpkaya, T., "Effect of the Adverse Pressure Gradient on Vortex Breakdown," *AIAA Journal*, Vol. 12, No. 5, May 1974, pp. 602-607.

[30] Gursul, I., "Criteria for Location of Vortex Breakdown Over Delta Wings," *Aeronautical Journal*, May 1995, pp. 194-196.

[31] Stifle, K. E., and Panton, R. L., "Experiments Concerning the Theories of Vortex Breakdown," AIAA Paper 91-0736, Jan. 1991.

[32] White, F.M., *Viscous Fluid Flow*, 2nd ed., McGraw-Hill, 1991.

[33] Benjamin, T. B., "Theory of the Vortex Breakdown Phenomenon," *Journal of Fluid Mechanics*, Vol. 14, 1962, pp. 593-629.

[34] Leibovich, S., and Kribus, A., "Large-Amplitude Wavetrains and Solitary Waves in Vortices," *Journal of Fluid Mechanics*, Vol. 216, 1990, pp. 459-504.

[35] Maxworthy, T., and Hopfinger, E.J., "Wave Motion on Vortex Cores," *Journal of Fluid Mechanics*, Vol. 151, 1985, pp. 141-165.

[36] Fledderus, E. K., "Mathematical Modeling in Swirling Flows: A Hamiltonian Approach," Ph.D. Dissertation, University of Twente, The Netherlands, http://www.ub.utwente.nl/webdocs/tw/1/t0000002.pdf

[37] Huang, X. Z., Sun, Y. Z., and Hanff, E. S., "Circulation Criterion to Predict Leading Edge Vortex Breakdown Over Delta Wings," AIAA Paper 97-2265, 1997.

[38] Brown, G. L., and Lopez, J. M., "Axisymmetric Vortex Breakdown, Part 2: Physical Mechanisms," *Journal of Fluid Mechanics*, Vol. 221, 1990, pp. 553-576.

[39] Özgören, M., Sahin, B., and Rockwell, D., "Vortex Structure on a Delta Wing at High Angle of Attack," *AIAA Journal*, Vol. 40, No. 2, Feb. 2002, No. 285-292.

[40] Ruzak, Z., and Lamb, D., "Prediction of Vortex Breakdown in Leading-Edge Vortices Above Slender Delta Wings," *AIAA Journal of Aircraft*, Vol. 36, No. 4, Aug. 1999, pp. 659-667.

[41] LeMay, S. P., Batill, S. M., and Nelson, R. C., "Vortex Dynamics on a Pitching Delta Wing," *AIAA Journal of Aircraft*, Vol. 27, No. 2, Feb. 1990, pp. 131-138.

LIST OF REFERENCES (continued)

[42] Rediniotis, O. K., Klute, S. M., Hoang, N. T., and Telionis, D. P., "Dynamic Pitch-Up of a Delta Wing," *AIAA Journal*, Vol. 32, No. 4, Apr. 1994, pp. 716-725.

[43] Gursul, I., Lin, H., and Ho, C. M., "Effects of Time Scales on Lift of Airfoils in an Unsteady Stream," *AIAA Journal*, Vol. 32, No. 4, Apr. 1994, pp. 797-801.

[44] Ericsson, L. E., "Effect of Pitch Rate on Delta Wing Vortex Characteristics," AIAA Paper 96-3405, July 1996.

[45] Ericsson, L. E., "Nonlinear Usteady Aerodynamics of Pitching Delta Wings," AIAA Paper 98-2518, 1998.

[46] Gursul, I., "A Proposed Mechanism for the Time Lag of Vortex Breakdown Location in Unsteady Flows," AIAA Paper 2000-0787, Jan. 2000.

[47] Ericsson, L. E., "Complex Angular Amplitude and Frequency Effects on Delta Wing Unsteady Aerodynamics," AIAA Paper 99-4009, 1999.

[48] Van Dyken, R., Yu, K., Gutmark, E., Tuncer, I., Platzer, M., MacLachlan, B., Bell, J., "Passive Control of Flow Separation Over Delta Wings at High Angles of Attack," AIAA Paper 96-0661, Jan. 1996.

[49] Myose, R. Y., Hayashibara, S., Yeong, P. C., and Miller, L. S., "Effect of Canards on Delta Wing Vortex Breakdown During Dynamic Pitching," *AIAA Journal of Aircraft*, Vol. 34, No. 2, Mar. 1997, pp. 168-173.

[50] Gursul, I., Taylor, G., and Wooding. C. L., "Vortex Flows over Fixed-Wing Micro Air Vehicles", AIAA Paper 2002-0698, Jan. 2002.

[51] Gursul, I., and Ho, C. M., "Experiments on 2- and 3-Dimensional Lifting Surfaces in an Unsteady Freestream," *Bulletin of the American Physics Society*, Vol. 34, 1989.

[52] Gad-el-Hak, M., and Blackwelder, R.F., "The Discrete Vortices of a Delta Wing," *AIAA Journal*, Vol. 23, No. 6, 1985, pp. 961-962.

[53] Tritton, D. J., *Physical Fluid Dynamics*, 2nd Edition, Oxford Science Publications, 1988.

[54] Mitchell, A., Molton, P., Barberis, D., Délery, J., "Vortical substructures in the Shear Layers Forming Leading-Edge Vortices," AIAA Paper 01-2424, June 2001.

[55] Skow, A. M., "An Analysis of the Su-27 Flight Demonstration at the 1989 Paris Airshow," SAE Paper 901001, 1990.

[56] Murayama, K., and Hull, D. G., "The Cobra Maneuver as a Minimum Energy Problem," AIAA Paper 97-3586, 1997.

LIST OF REFERENCES (continued)

[57] Kolano, E., "Flying the Flanker," *Flight Journal*, http://www.flightjournal.com/articles/su27/su27_5.asp

[58] Sibilski, K., "Problems Of Maneuvering At Post-Critical Angles Of Attack-Continuation and Bifurcation Methods Approach," AIAA Paper 2003-0395, Jan. 2003.

[59] Beyers, M. E., and Ericsson, L. E., "Unsteady Aerodynamics of Combat Aircraft Maneuvers," AIAA Paper 97-3647, 1997.

[60] Ericsson, L. E., "Cobra Maneuver Unsteady Aerodynamic Considerations," *AIAA Journal of Aircraft*, Vol. 32, No. 1, Jan. 1995, pp. 214-216.

[61] Ericsson, L. E., "Effect of Fuselage Geometry on Delta-Wing Vortex Breakdown," *AIAA Journal of Aircraft*, Vol. 35, No. 6, Nov. 1998, pp. 898-904.

[62] Rediniotis, O. K., Hoang, N. T., Klute, S. M., and Telionis, D. P., "Dynamic Pitch-Up of a Delta Wing," *AIAA Journal*, Vol. 32, 1994, pp. 716-725.

[63] Schaeffler, N. W., and Telionis, D. P., "Apex Flap Control of Dynamic Delta Wing Maneuvers," AIAA Paper 96-0662, Jan. 1996.

[64] Tianfeng, J., and Zhenghong, G., "Unsteady Aerodynamic Modeling at High Angles of Attack," AIAA Paper 2000-3908, 2000.

[65] McMichael, J.M., and Col. M.S. Francis, "Micro-Air Vehicles – Toward a New Dimension in Flight," http://web-ext2.darpa.mil/tto/mav/mav_auvsi.html, Aug. 1997.

[66] Roshko, A, "On the Development of Turbulent Wakes from Vortex Streets," NACA Report 1191, 1954.

[67] Williamson. C. H. K., "Oblique and Parallel Modes of Vortex Shedding in the Wake of a Circular Cylinder at Low Reynolds Numbers," *Journal of Fluid Mechanics*, Vol. 206, 1989, pp. 579-627.

[68] Gerich, D., and Eckelmann, H., "Influence of End Plates and Free Ends on the Shedding Frequency of Circular Cylinders," *Journal of Fluid Mechanics*, Vol. 122, 1982, pp. 109-121.

[69] Degani, D., "Effect of Splitter Plate on Unsteady Flows around a Body of Revolution at Incidence," *Physics of Fluids A*, Vol. 3, No. 9, Sept. 1991, pp. 2122-2131.

LIST OF REFERENCES (continued)

[70] Swirydczuk, J., "A Visulaization Study of the Interaction of a Free Vortex with the Wake Behind an Airfoil," *Experiments in Fluids*, Springer-Verlag, Vol. 9, No. 4, June 1990, pp. 181-190.

[71] Wittmer, K. S., and Devenport, W. J., "Interaction of a Streamwise Vortex with a Full-Span Blade," AIAA Paper 95-2214, June 1994.

[72] Marshall, J. S., "Models of Secondary Vorticity Evolution During Normal Vortex-Cylinder Interaction," *AIAA Journal*, Vol. 40, No. 1, Jan. 2002, pp. 170-172.

[73] Krishnamoorthy, S., Gossler, A. A., and Marshall, J. S., "Normal Vortex Interaction with a Circular Cylinder," *AIAA Journal*, Vol. 37, No. 1, Jan. 1999, pp. 50-57.

[74] Myose, R. Y., and Blackwelder, R. F., "On the Role of the Outer Region in the Turbulent-Boundary Layer Bursting Process," *Journal of Fluid Mechanics*, Vol. 259, 1994, pp. 345-373.

[75] Johnson, B. L., "Facility Description of the Walter H. Beech Memorial 7 x 10 foot Low-Speed Wind Tunnel," AR93-1, National Institute for Aviation Research, Wichita State University, June 1993.

[76] Taylor, G., Gursul, I., and Greenwell, D., "Static Hysteresis of Vortex Breakdown due to Support Interference," AIAA Paper 2001-2452, June 2001.

[77] Ericsson. L. E., and Beyers, M. E., "Aspects of Ground Facility Interference on Leading-Edge Vortex Breakdown," *AIAA Journal of Aircraft*, Vol. 38, No. 2, Mar. 2001, pp. 310-314.

[78] Rae, W. H., and Pope, A., *Low-Speed Wind Tunnel Testing*, 2nd Ed., J. Wiley.

[79] Cimbala, J. M., and Leon, J., "Drag of Freely Rotatable Cylinder/Splitter-Plate Body at Subcritical Reynolds Number," *AIAA Journal*, Vol. 34, No. 11, Nov. 1996, pp. 2446-2448.

[80] Cimbala, J. M., and Garg, S., "Flow in the Wake of a Freely Rotatable Cylinder with Splitter Plate," *AIAA Journal*, Vol. 29, No. 6, Jun. 1991, pp. 1001-1003.

[81] Heron, I. And Myose, R. Y., "Development of a Dynamic Pitch And Unsteady Freestream Delta Wing Mount For A Water Tunnel," AIAA Paper 2003-3527, June 2003.

[82] Koochesfahani, M. M., "Vortical Patterns in the Wake of an Oscillating Airfoil," *AIAA Journal*, Vol. 27, No, 9, Sept. 1989, pp. 1200-1205.

LIST OF REFERENCES (continued)

[83] Koochesfahani, M. M., "Vortical Patterns in the Wake of an Oscillating Airfoil," AIAA Paper 87-0111, Jan. 1987.

[84] Triantafyllou, M. S., Techet, A. H., and Hover, F. S., "Review of Experimental Work in Biomimetic Foils," *IEEE Journal of Oceanic Engineering*, Vol. 29, No. 3, July 2004, pp. 585-593.

APPENDICES

APPENDIX A

FIGURES

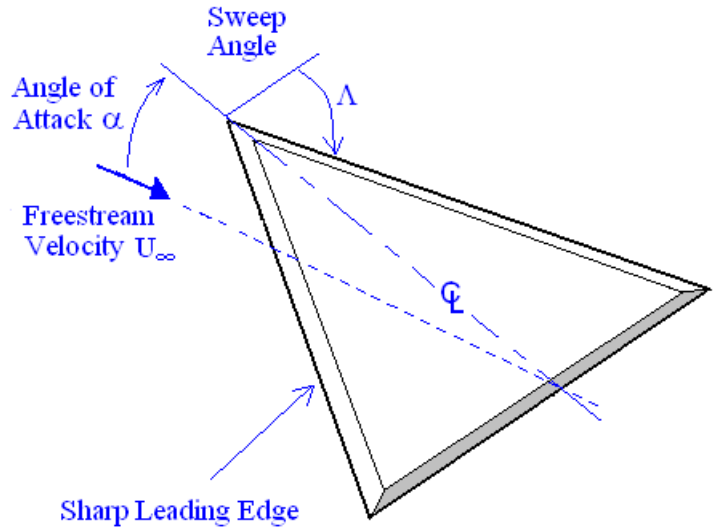

Figure 1.1. The Delta Wing [1, 2].

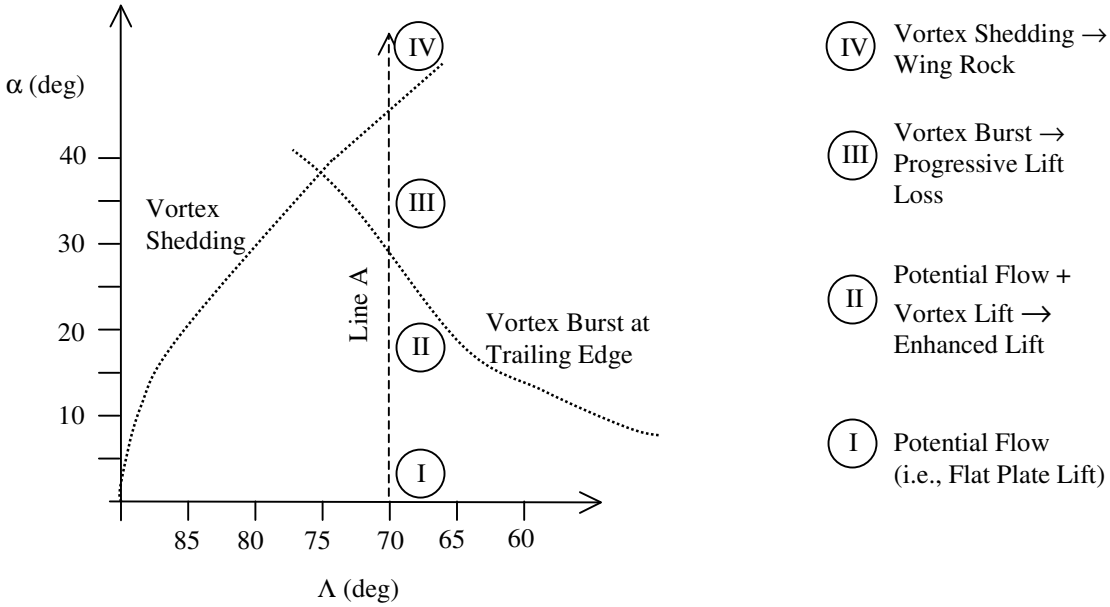

Figure 1.2. Delta Wing Flow Field Features [4, 5, 8].

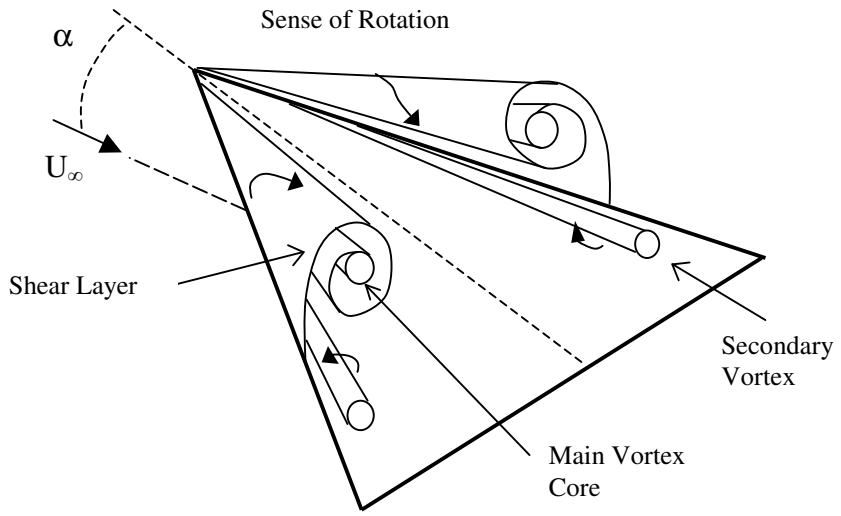

Figure 1.3. Lift Producing Mechanism of Delta Wing [1, 2, 4].

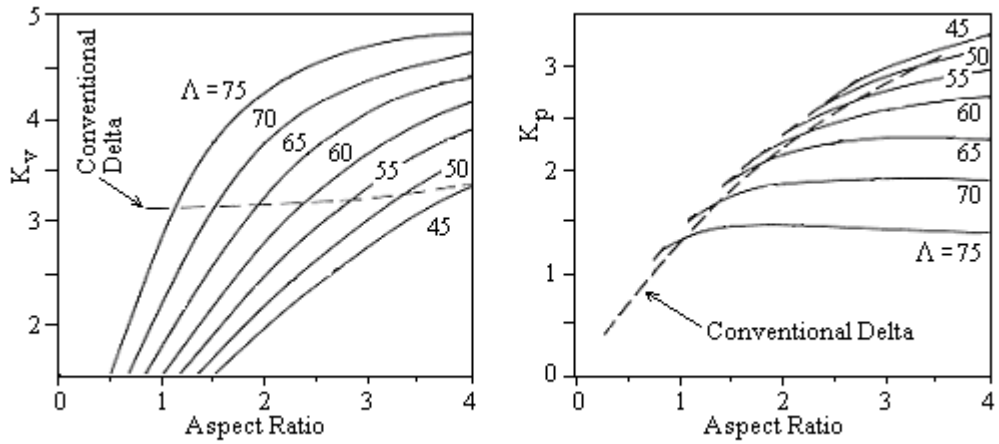

Figure 1.4. K_V and K_P Values [9].

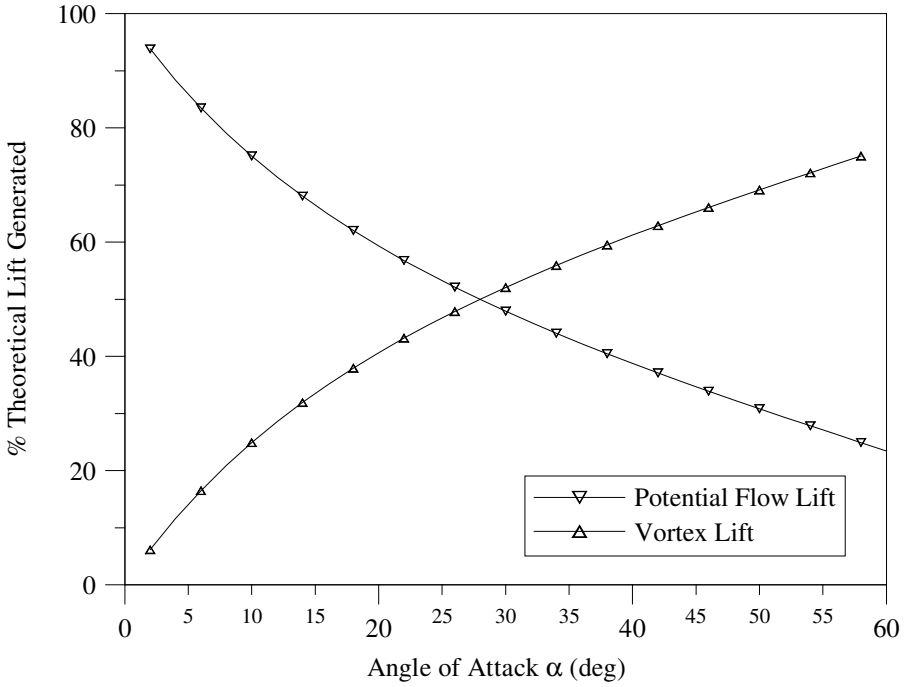

Figure 1.5. Vortex Lift Contribution on a 70-degree Delta (Adapted from Refs. [9, 10]).

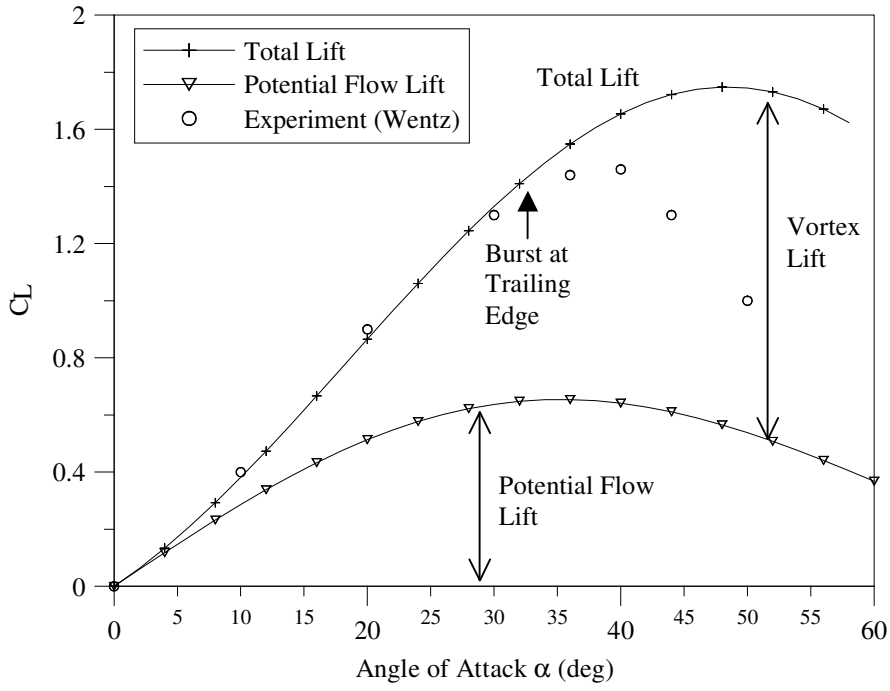

Figure 1.6. Vortex Lift and Potential Lift in for a $\Lambda=70^{o}$ Delta Wing [10].

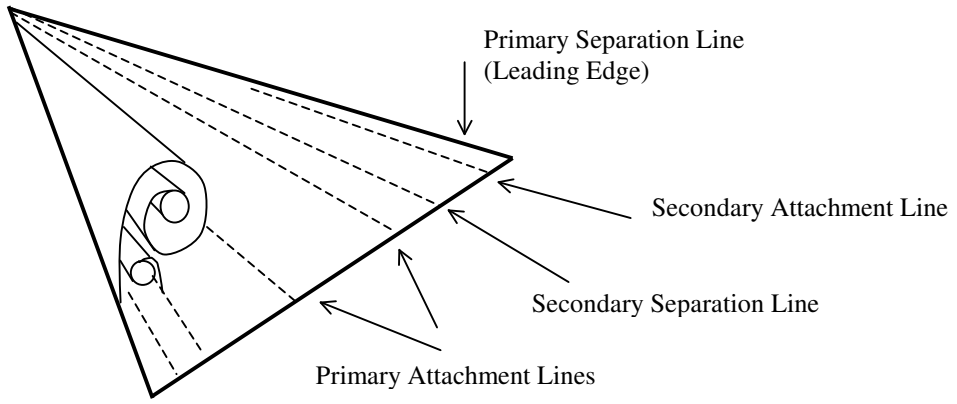

Figure 1.7. Attachment and Separation Lines on the Delta Wing Surface [4, 9, 12].

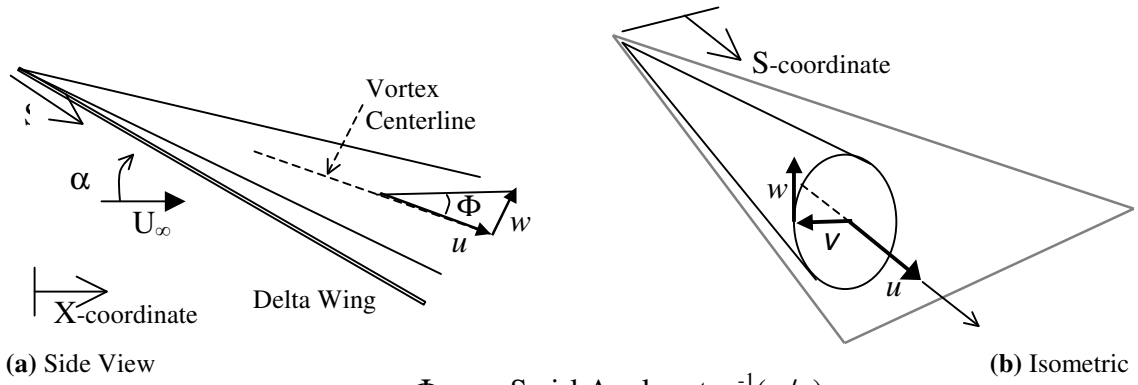

(a) Side View **(b)** Isometric

Φ	Swirl Angle = $\tan^{-1}(w/u)$
u	Axial Velocity
v	Radial Velocity
w	Swirl (or Azimuthal) Velocity

Figure 1.8. Delta Wing Nomenclature [13, 14].

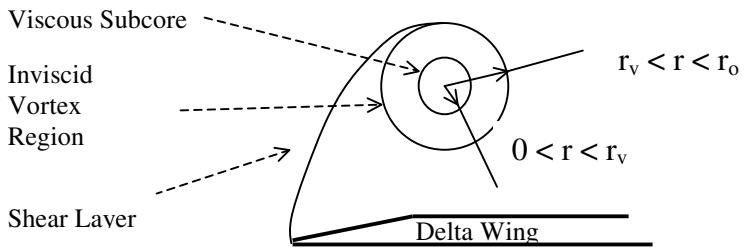

Figure 1.9. Structure of Main Vortex Core [16].

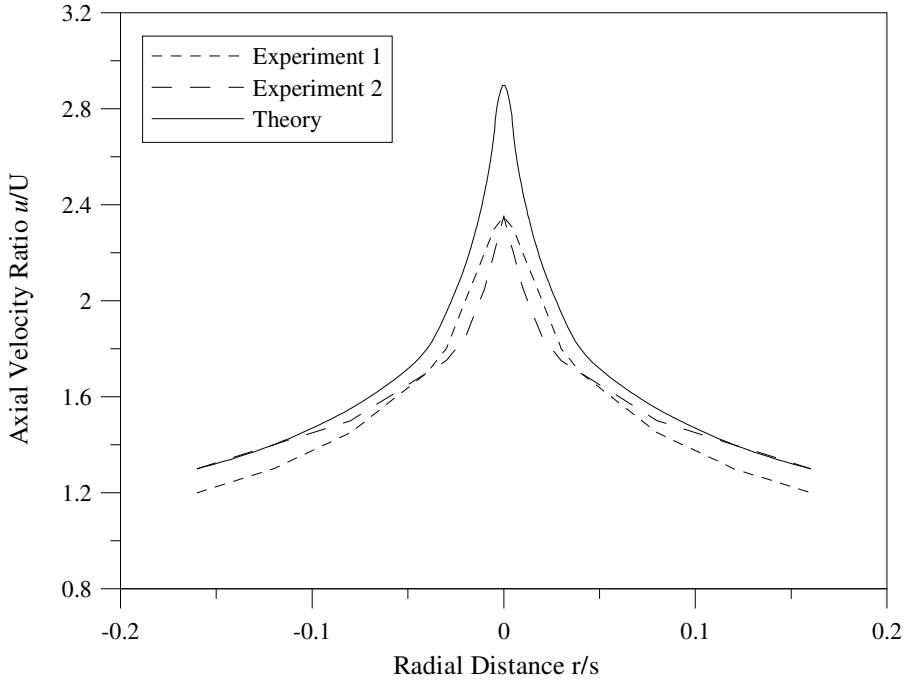

Figure 1.10. Typical Axial Velocity Profile [17].

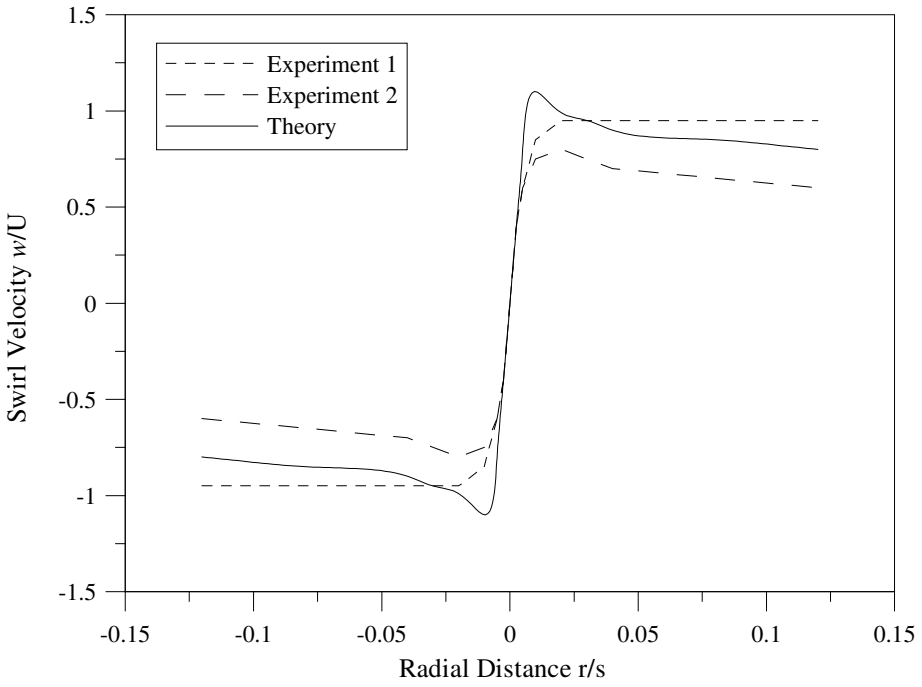

Figure 1.11. Typical Swirl Velocity Profile [17].

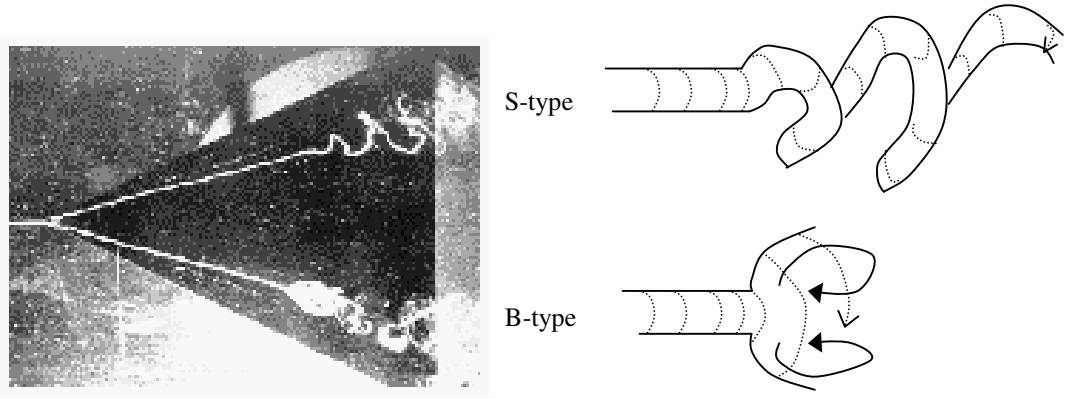

Figure 1.12. Vortex Burst Classification [21, 22].

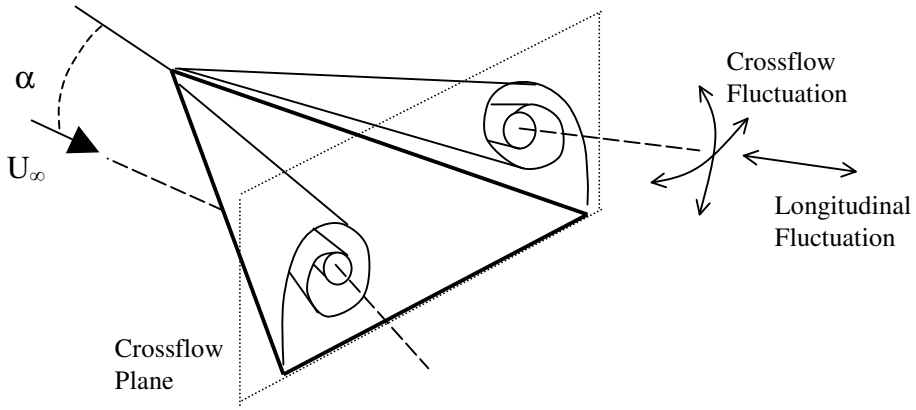

Figure 1.13. Longitudinal and Crossflow Fluctuations in Vortex Burst Position [24, 25, 26].

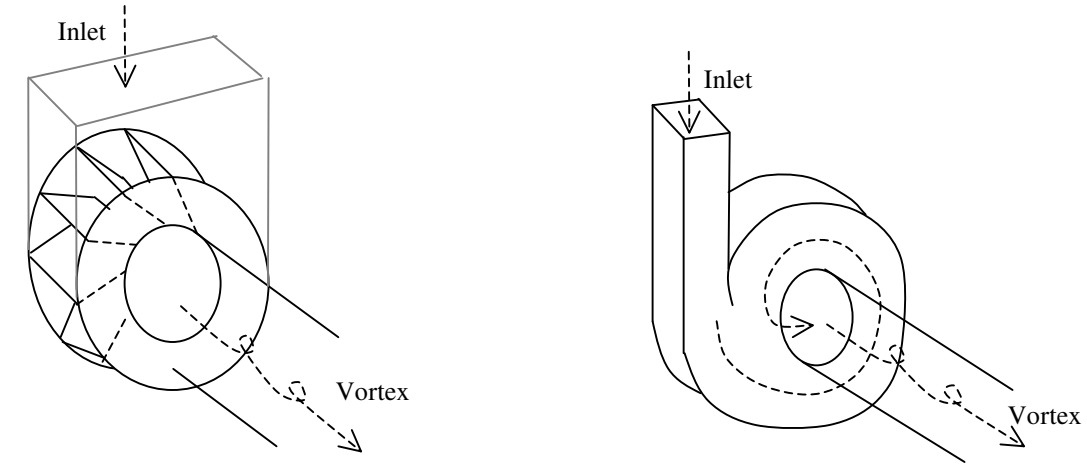

(a) Vane Vortex **(b)** Tangential Entry

Figure 1.14. Two Types of Vortex Tube Generators [17].

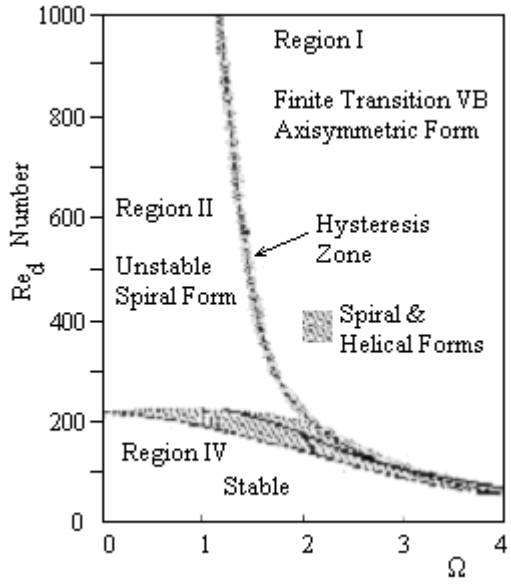

Figure 1.15. The Regions of Swirl and Reynolds Number [21].

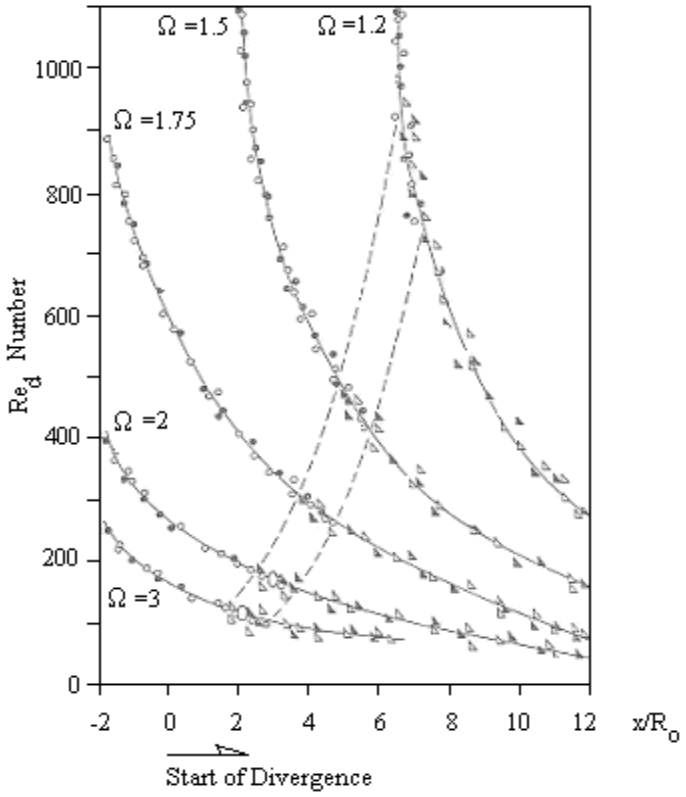

Figure 1.16. Vortex Burst Location in Vane-Type Vortex Tube [28].

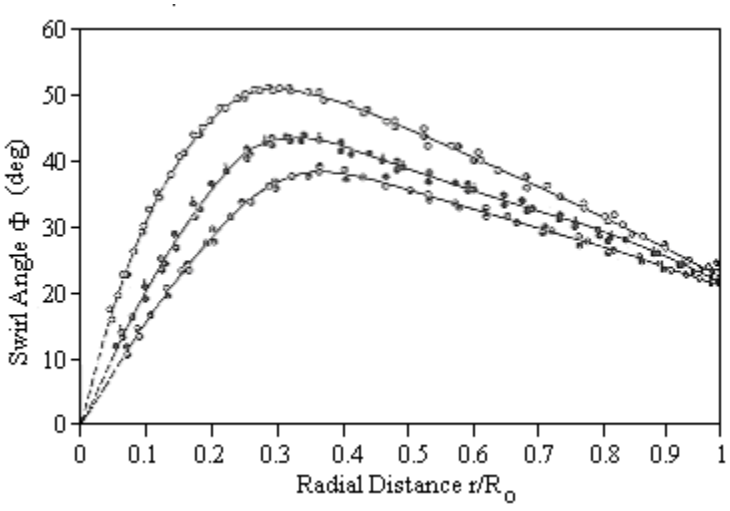

Figure 1.17. Measured Swirl Angle Φ in Vortex-Tubes [28].

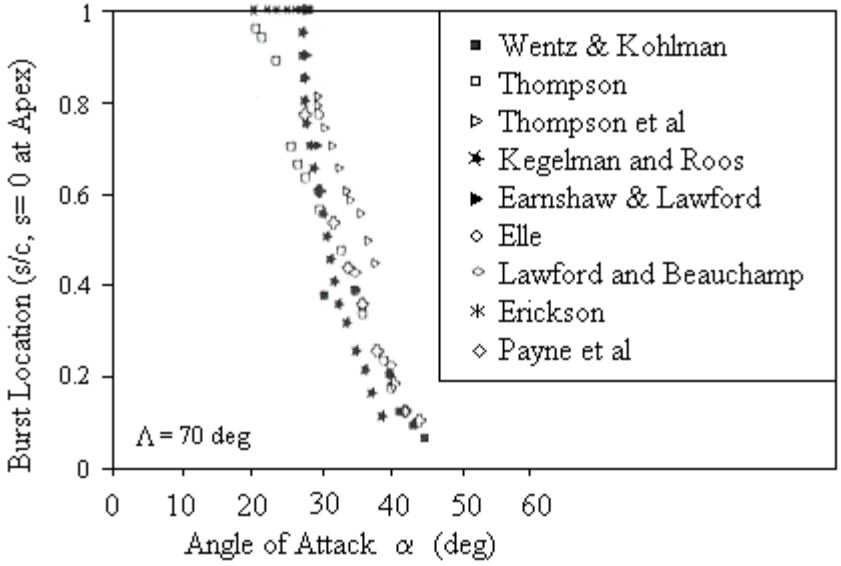

Figure 1.18. VB Position, 70-Degree Delta Wing, Static Pitch, Uniform U_∞ [30].

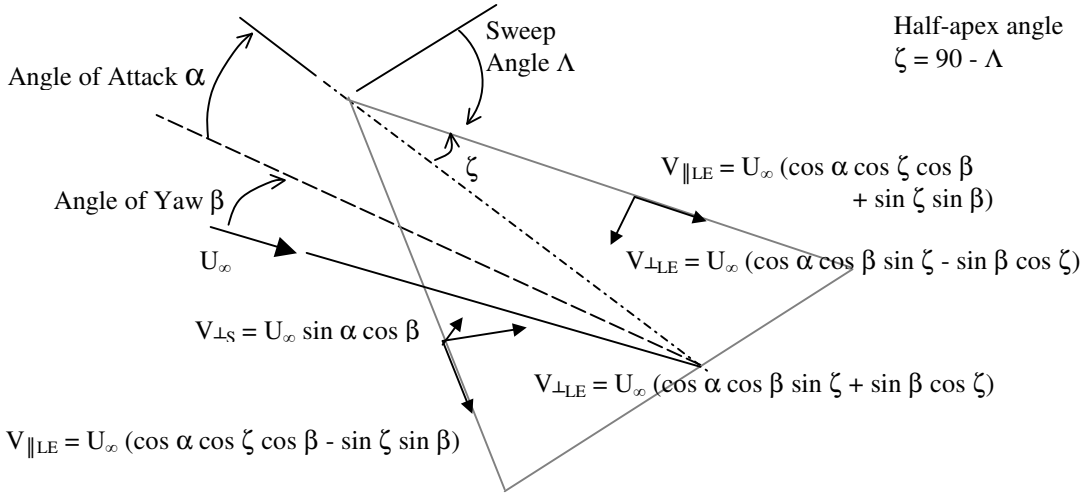

Figure 1.19. Velocity Components on Leading Edge of Delta Wing (Adapted from Ref. [5]).

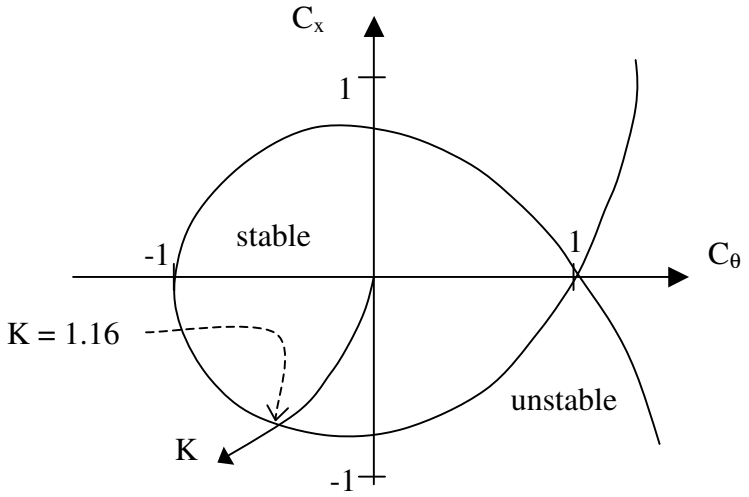

Figure 1.20. Ludweig's Stability Criterion for Spiral Vortex Burst [13].

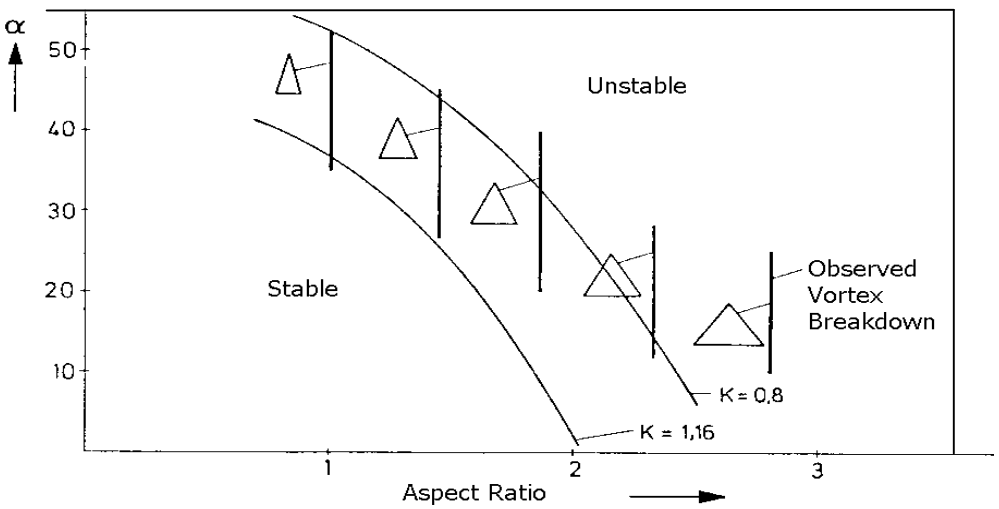

Figure 1.21. Ludweig's Stability Criteria, Experimental Results [13].

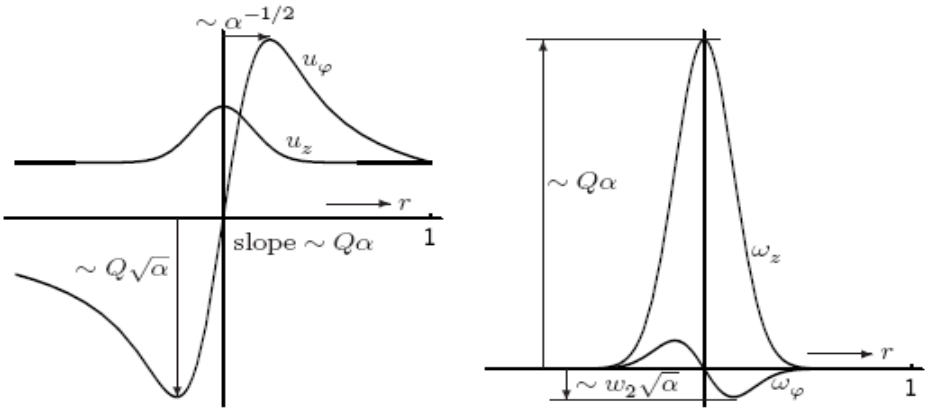

(a) Azimuthal (*w*) and Axial (*u*) Velocity **(b)** Azimuthal and Axial Vorticity

Figure 1.22. Q-Vortex Parameters [36].

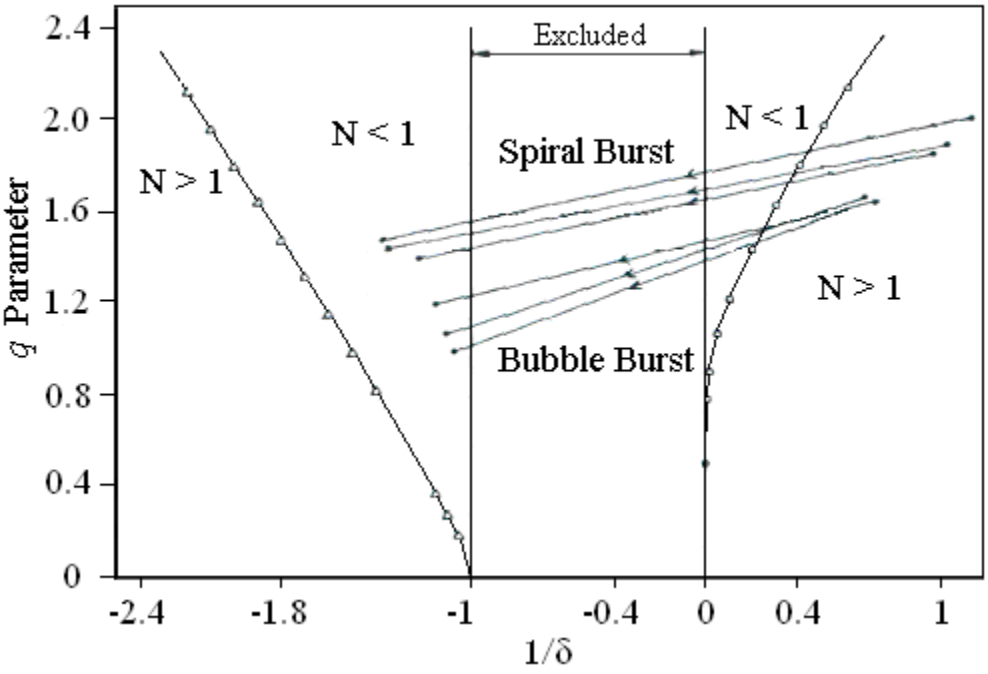

Figure 1.23. Q-Vortex Stability Boundaries [17].

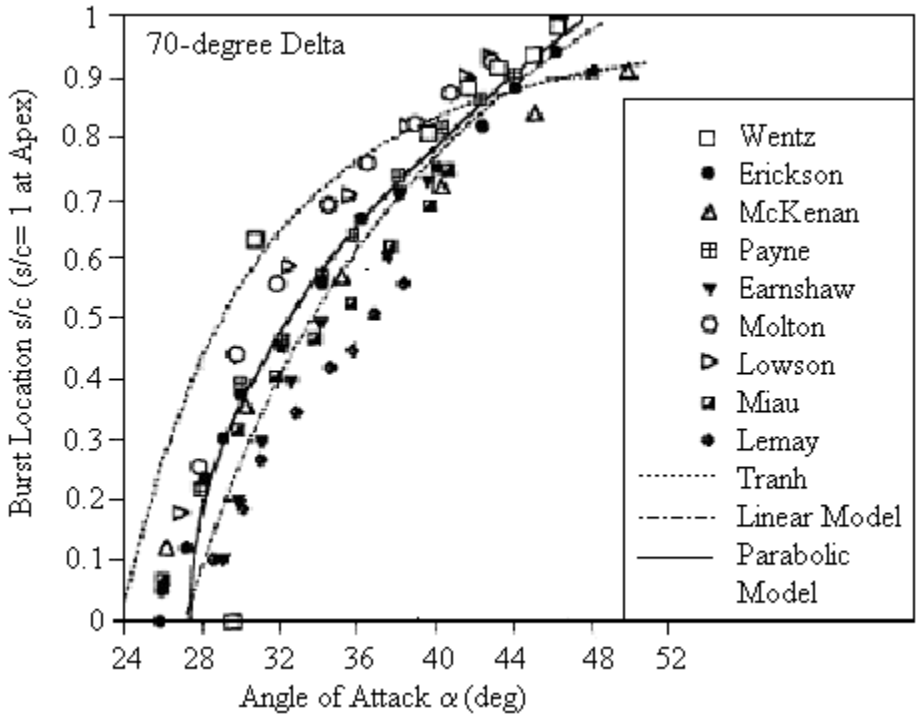

Figure 1.24. VB Location Using Parabolic Axial Circulation Predictor [37].

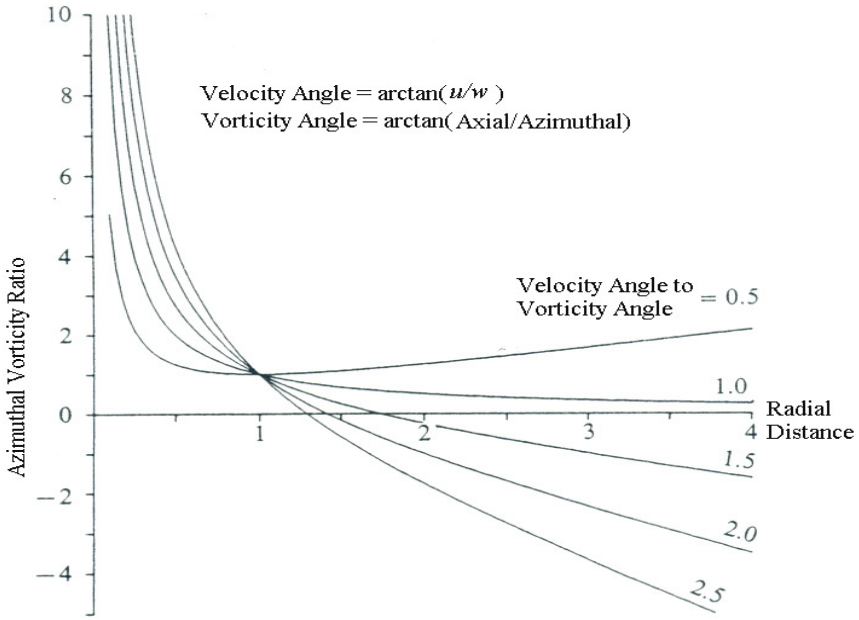

Figure 1.25. Azimuthal Vorticity Behavior [38].

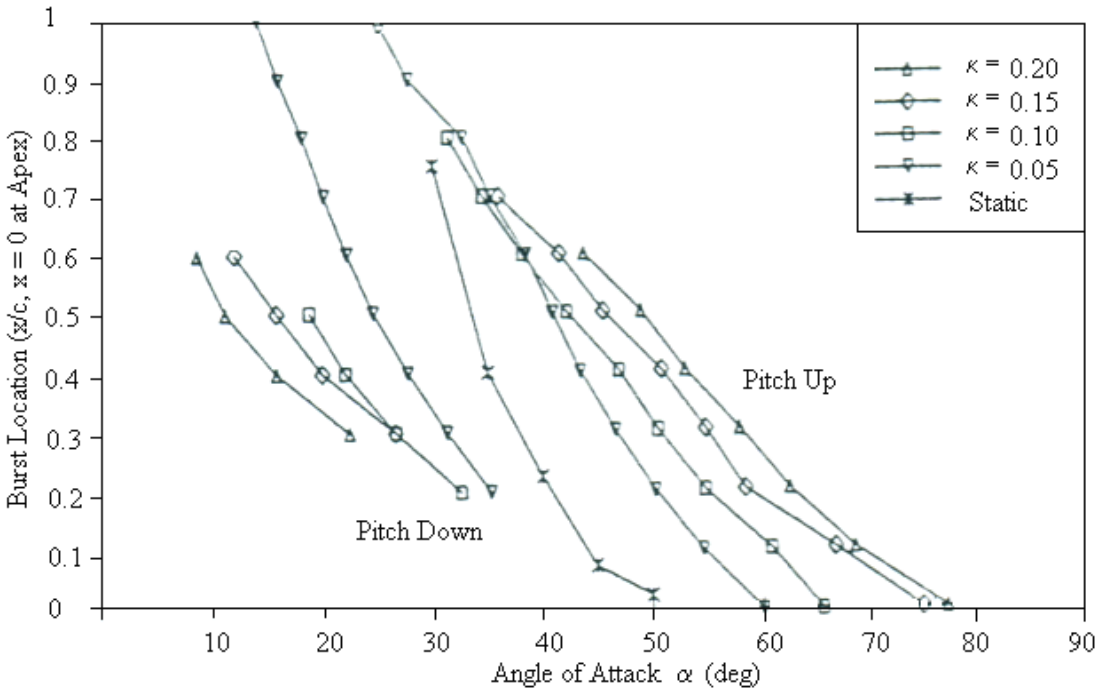

Figure 2.1. Vortex Burst Behavior During Dynamic Pitching, 70° Delta Wing [49].

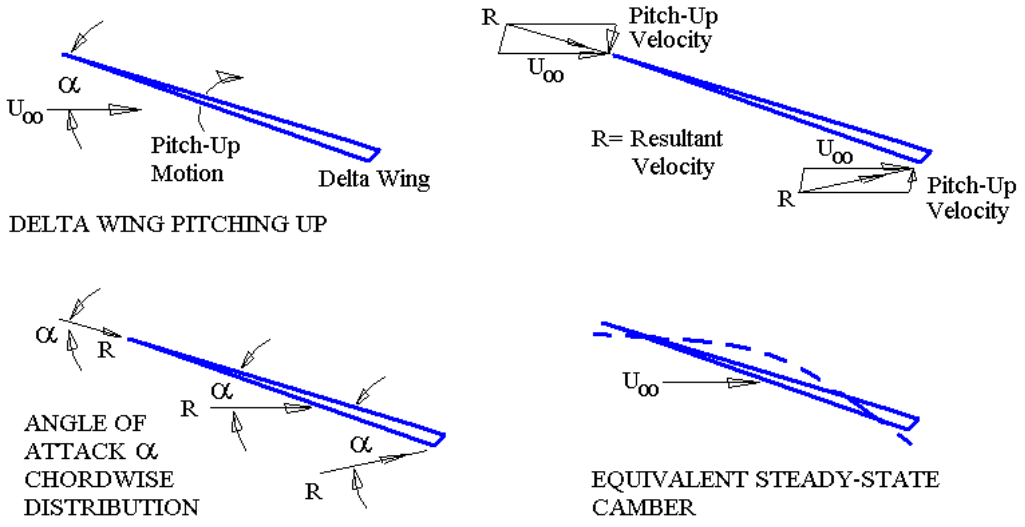

Figure 2.2. Dynamic Equivalent Steady (DES) Effect of Dynamic Pitching [44].

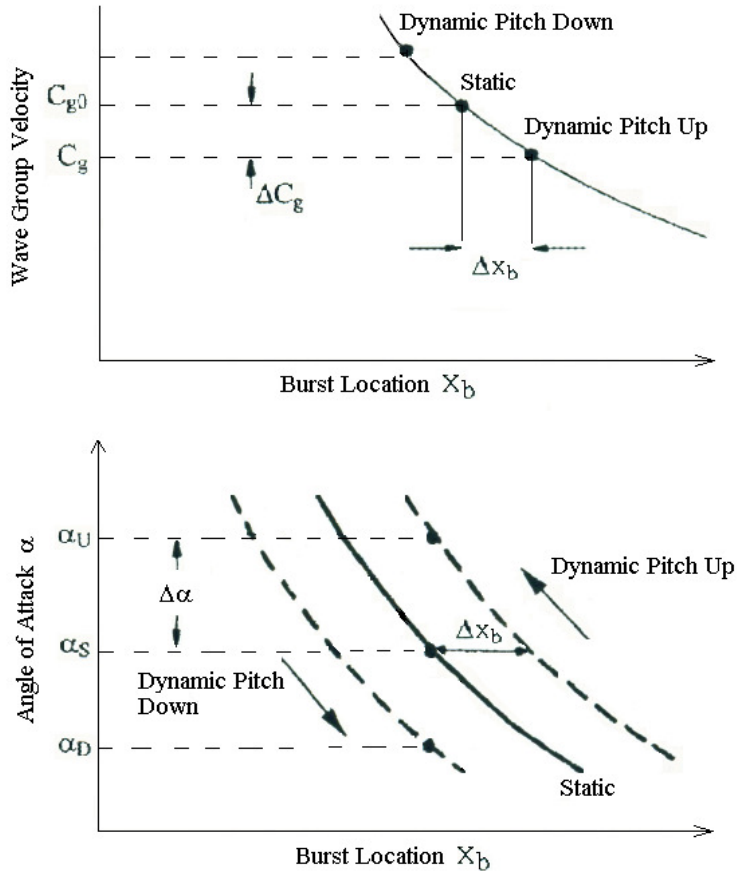

Figure 2.3. Group Velocity Change due to Pitching [46].

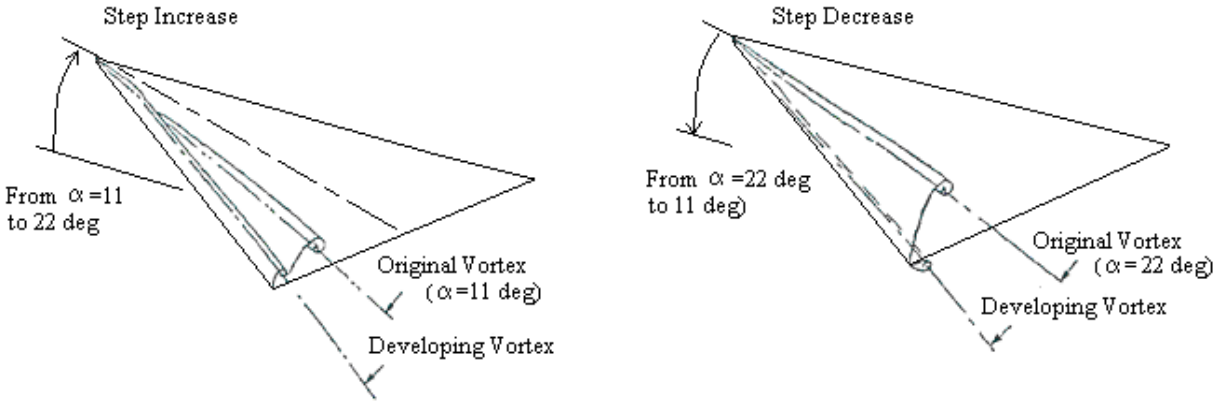

Figure 2.4. Convection of Vorticity from Leading Edge [44].

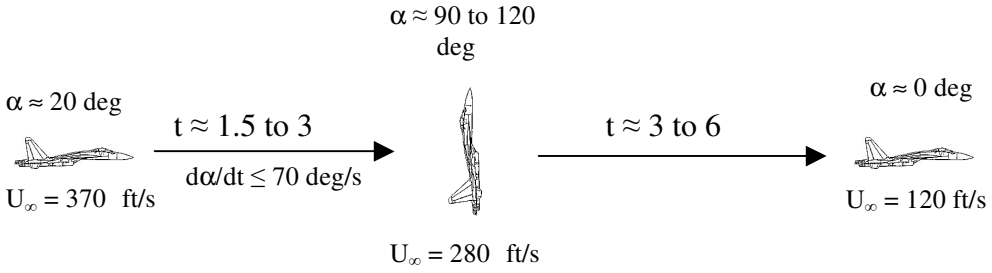

Figure 2.5. The "Cobra" Maneuver [55, 56, 57].

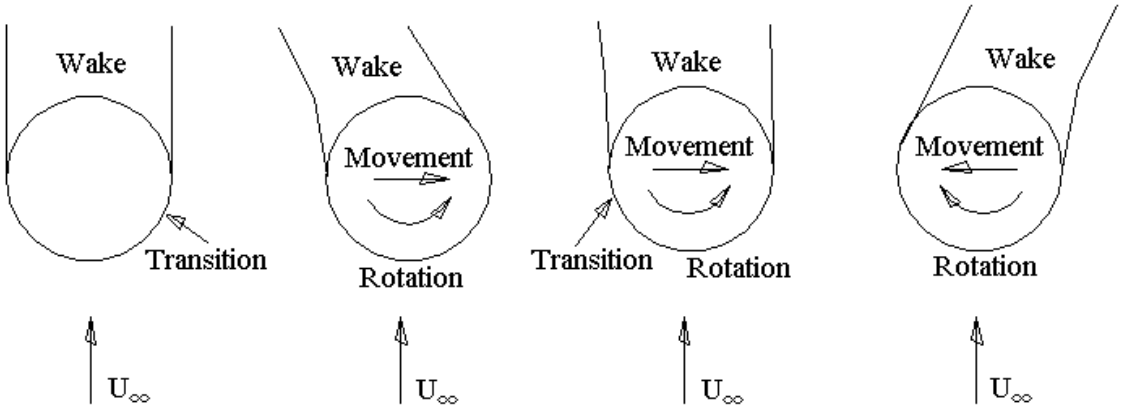

Figure 2.6. The Forebody Coning Motion [60].

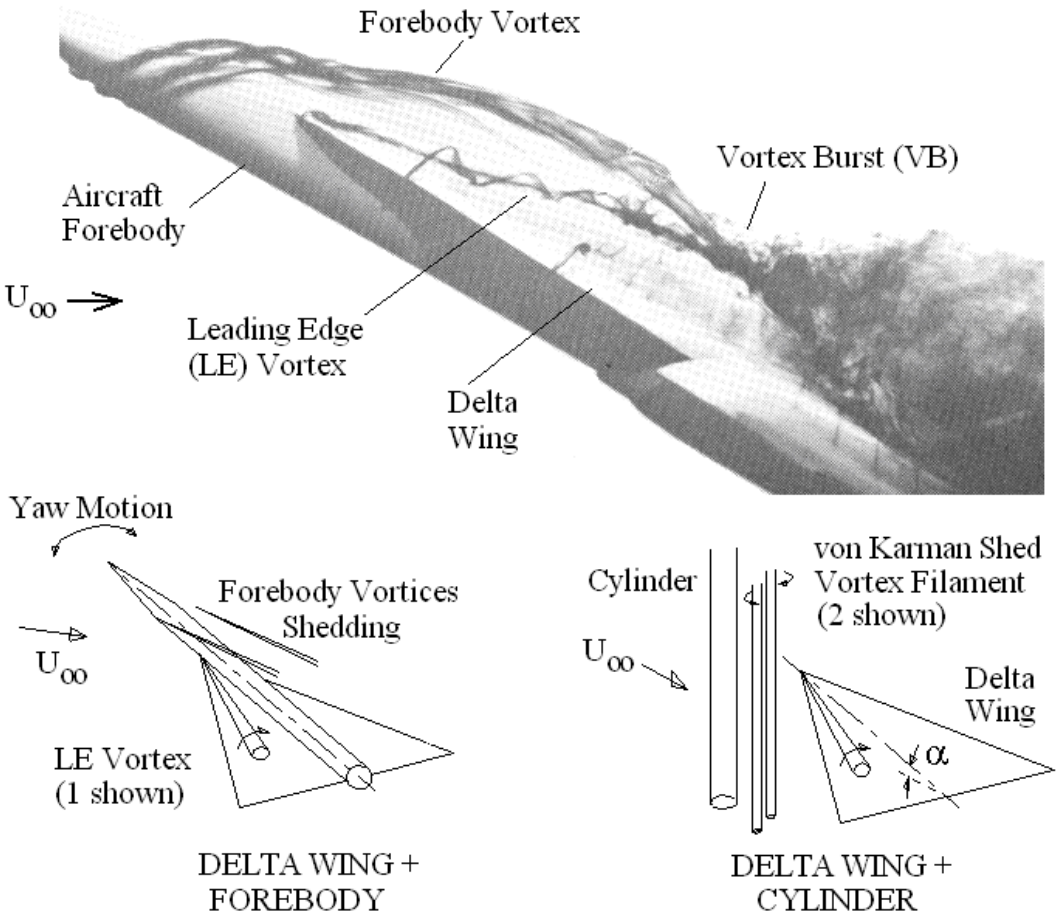

Figure 3.1. The Forebody Vortex and the Leading Edge Vortex [14].

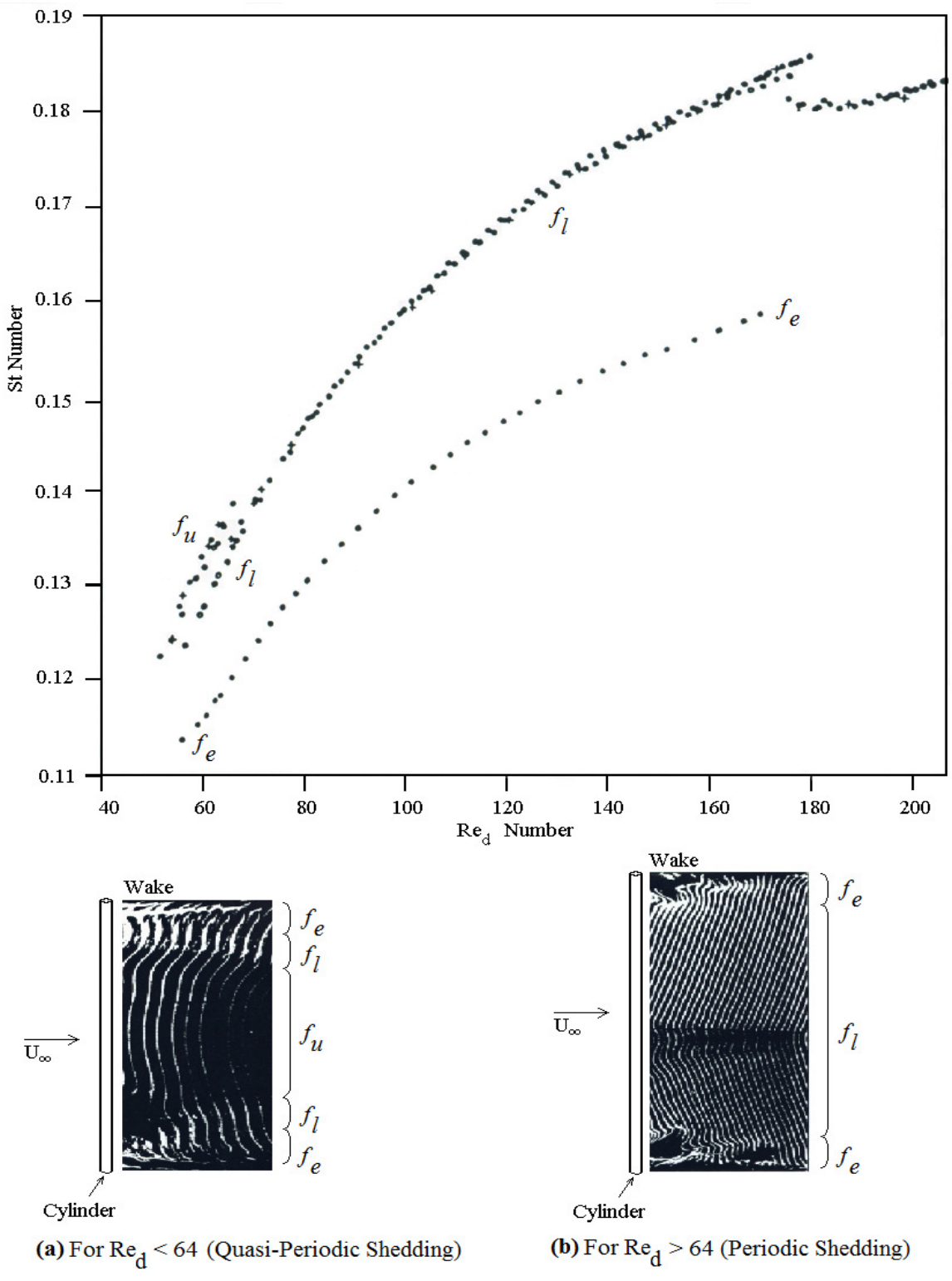

Figure 3.2. Strouhal Number and Vortex Shedding on Long Cylinder [67].

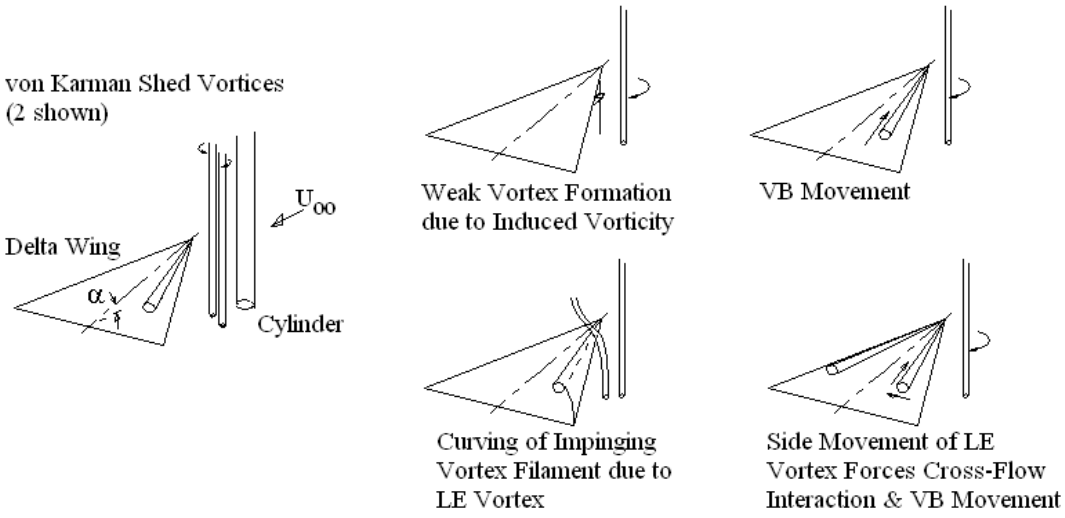

Figure 3.3. Expected LE Vortex Behavior to von Kàrmàn Vortex Impingement.

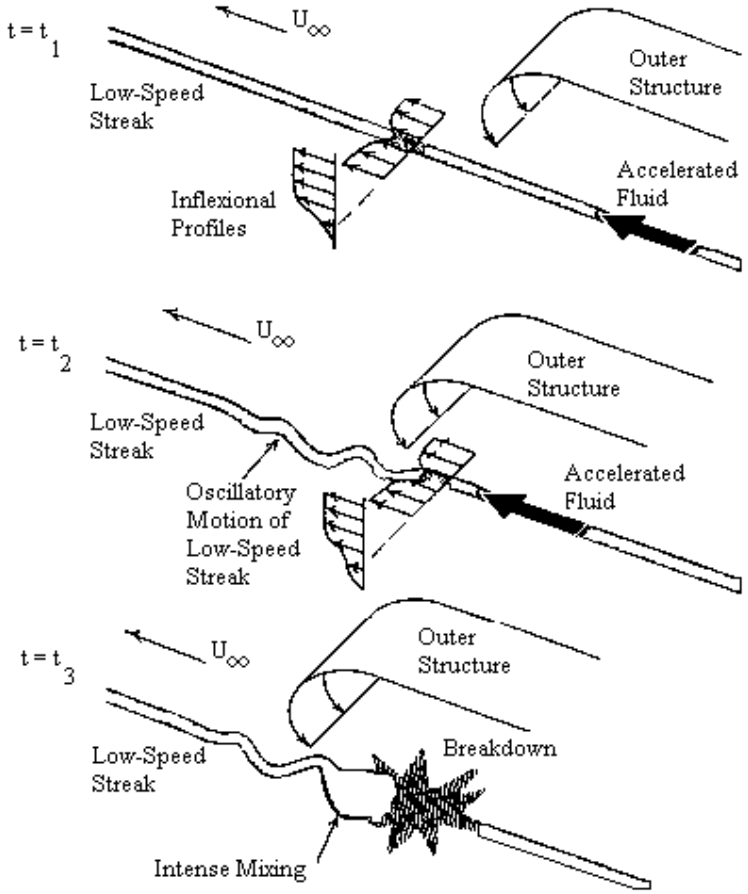

Figure 3.4. Görtler Vortex Interacting with a Perpendicular Vortex [74].

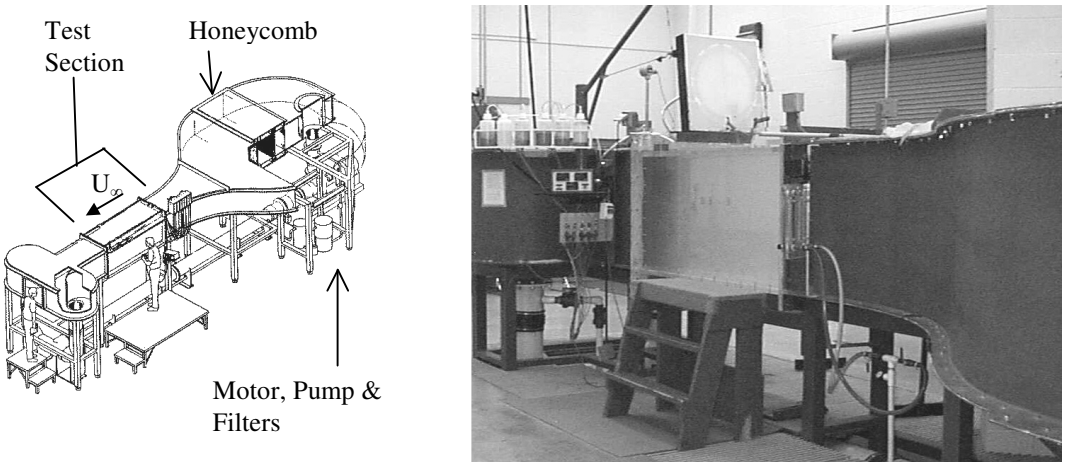

Figure 4.1. 2- x 3-Feet Water Tunnel [75].

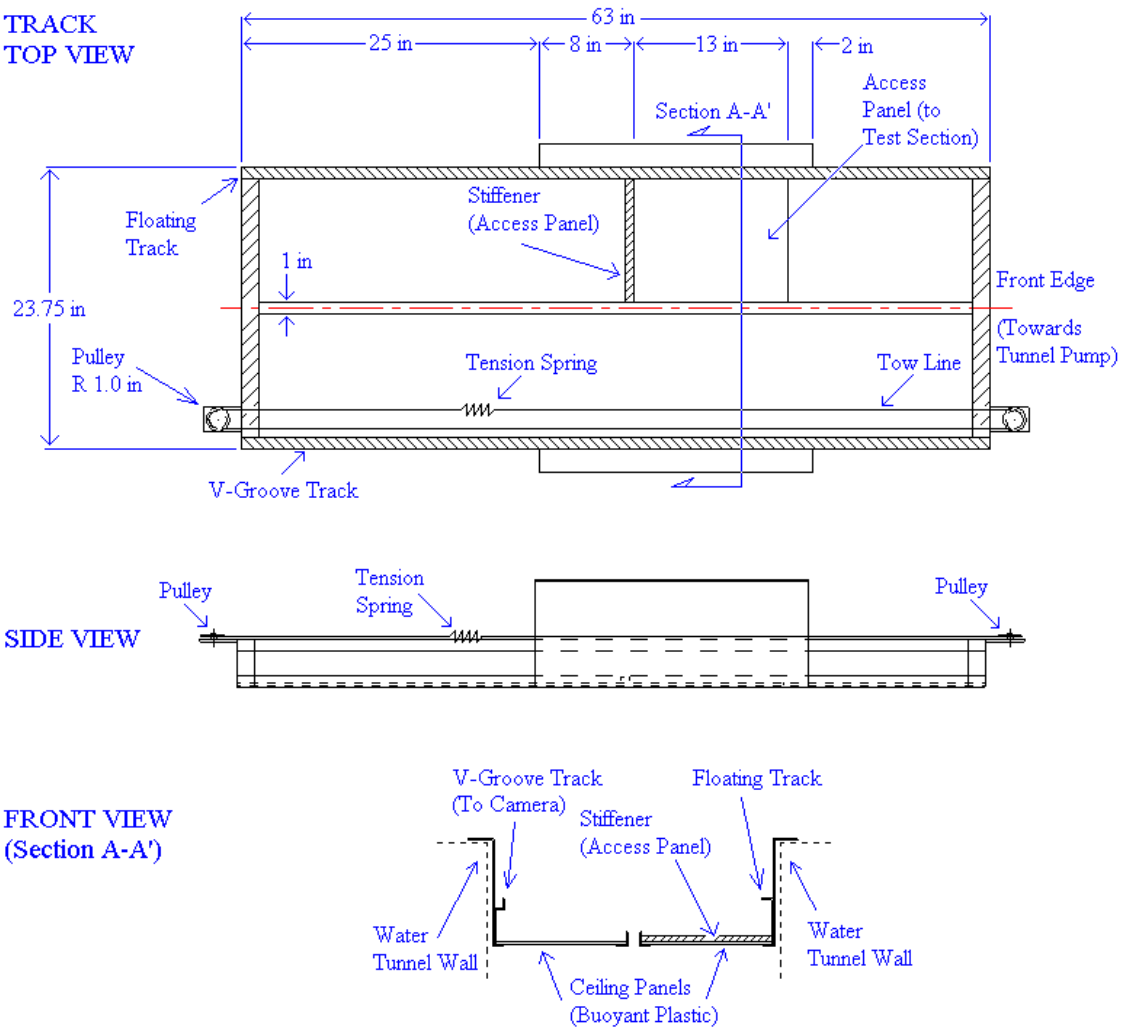

Figure 4.2. Schematic of Towing Mount, Tracks.

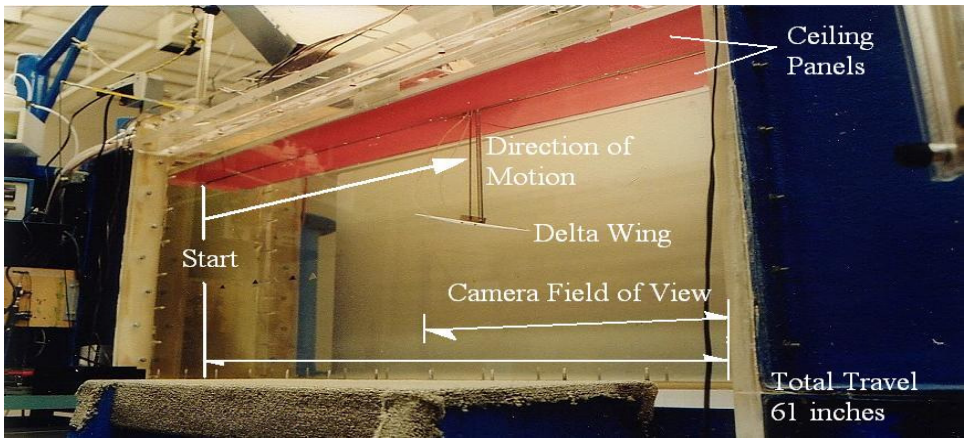

Figure 4.3. Close-Up of Towing Mount in Water Tunnel.

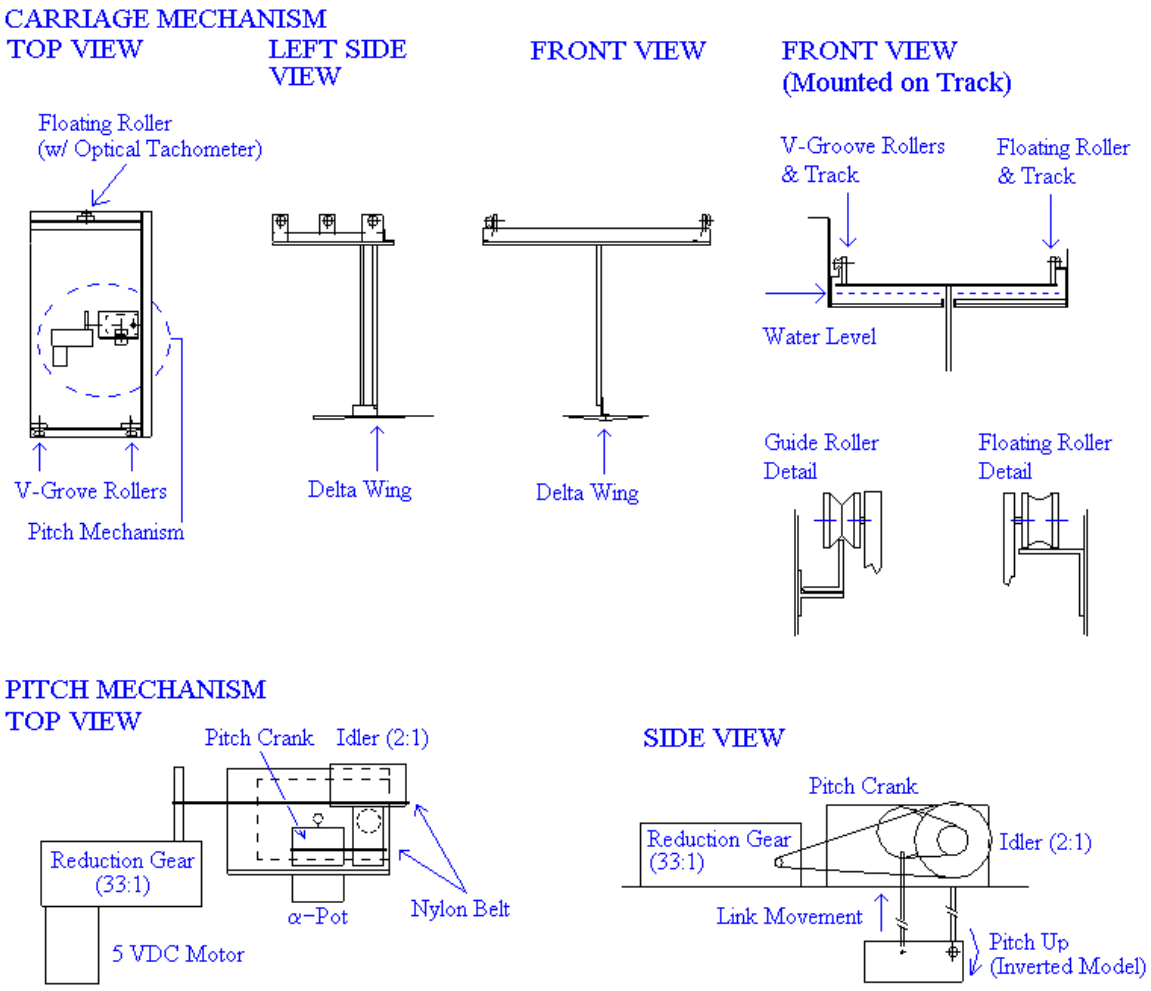

Figure 4.4. Schematic of Towing Mount, Carriage.

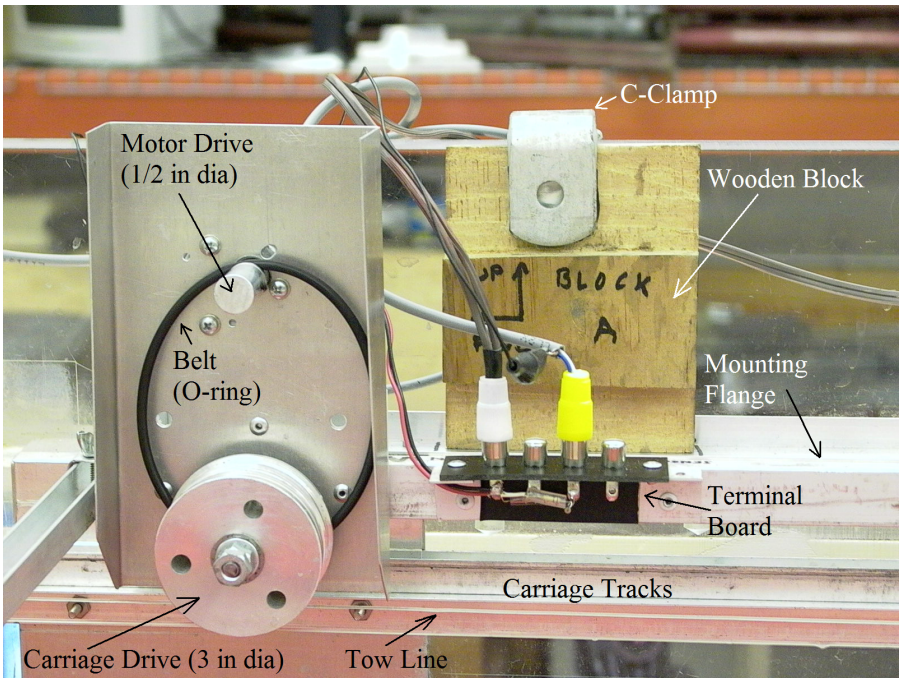

Figure 4.5. Carriage Drive.

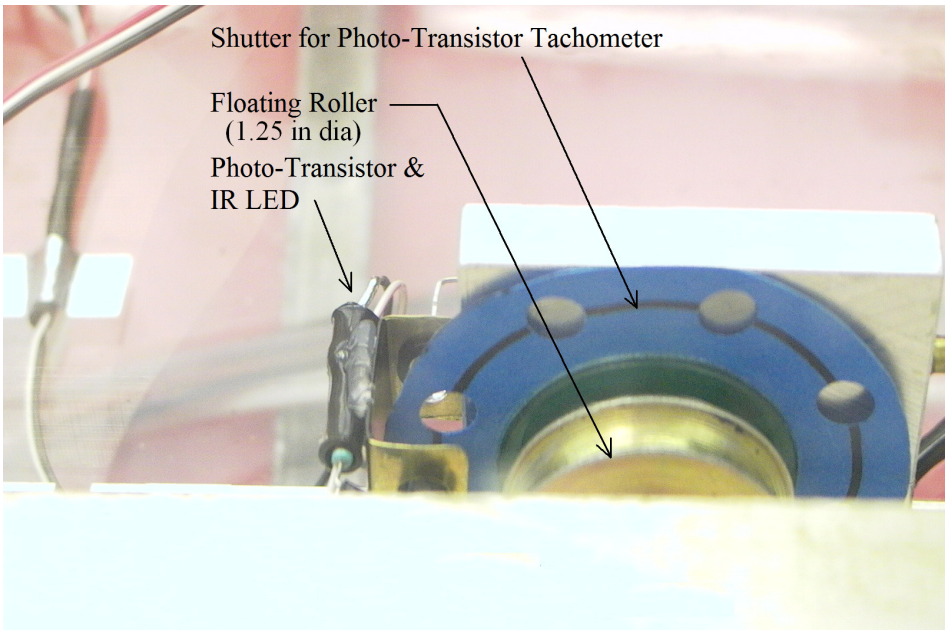

Figure 4.6. Tachometer and Floating Roller Detail.

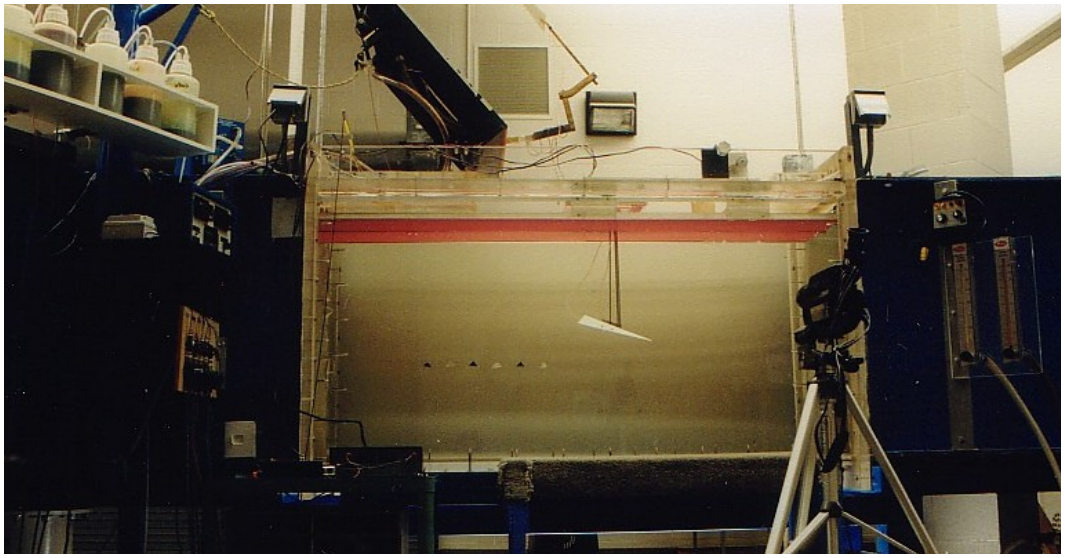

(a) Constant Velocity Validation and Variable Freestream Experiments (Chapters 4 and 5)

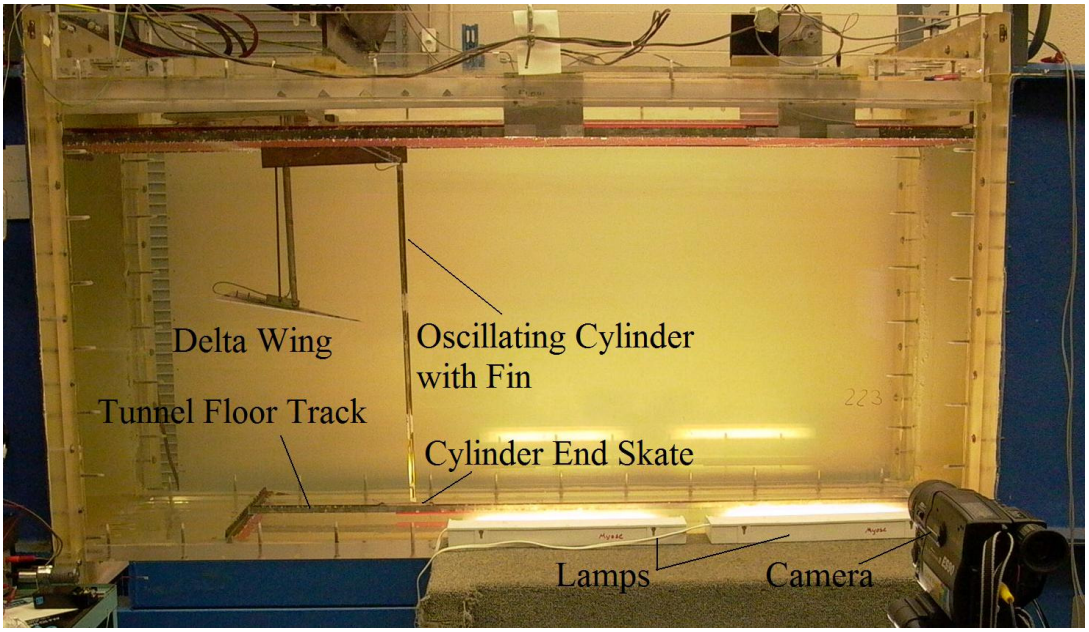

(b) Delta Wing in von Kàrmàn Cylinder Wake Experiments (Chapter 6)

Figure 4.7. Towing Mount Installed in Water Tunnel.

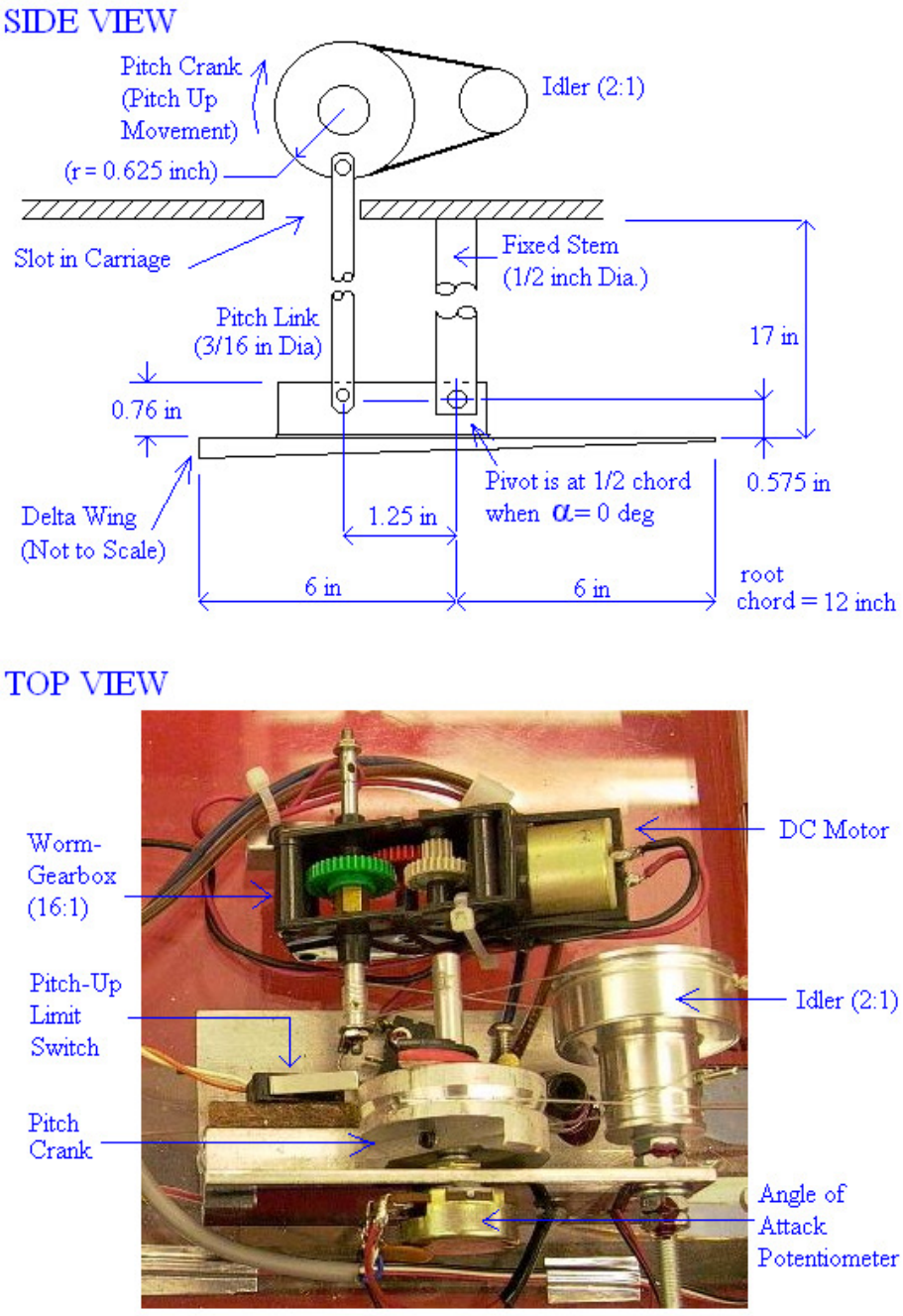

Figure 4.8. Carriage Pitch-Up Mechanism.

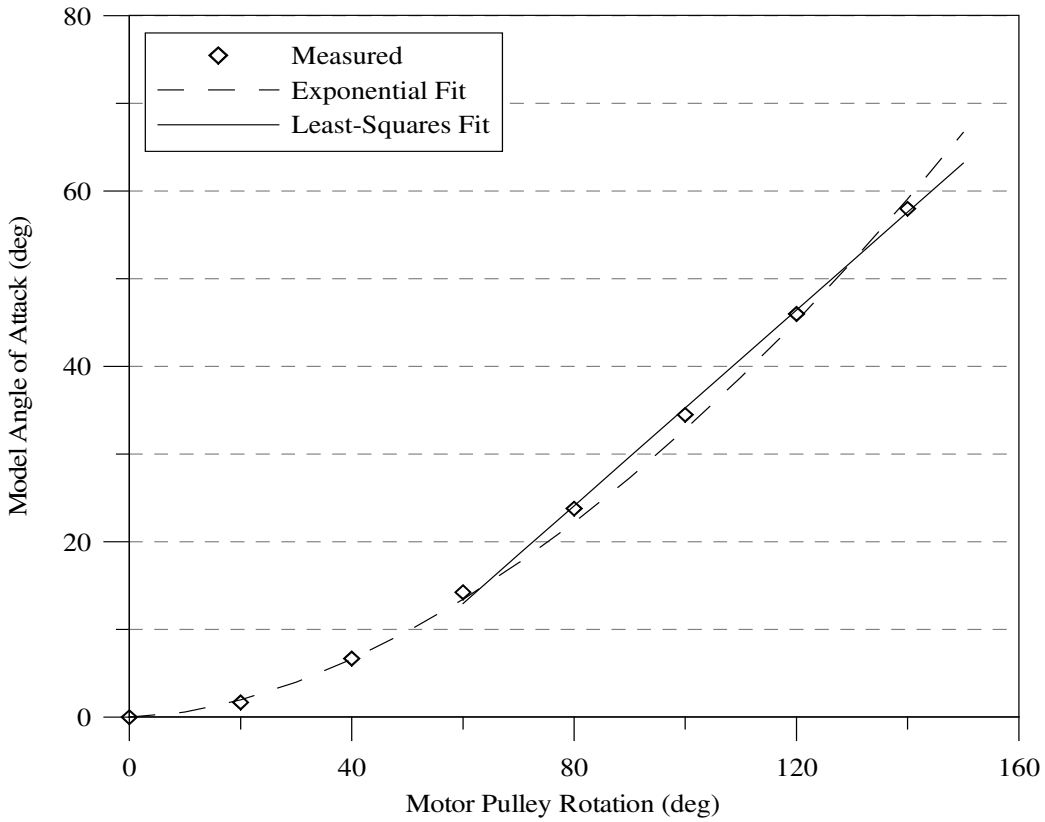

Figure 4.9. Angle of Attack Linearity to Motor Rotation.

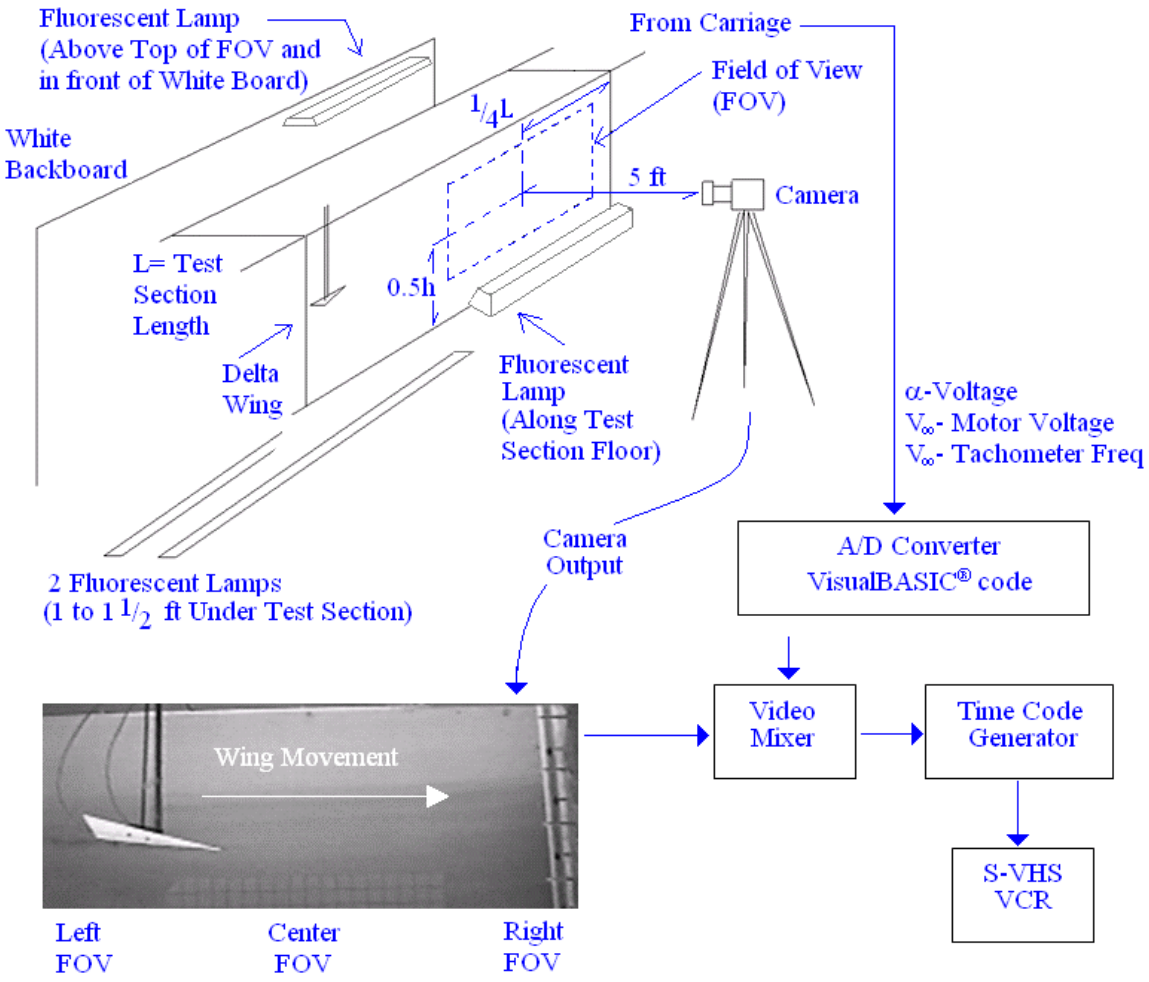

a) Test Installation and Data Capture Set-Up.

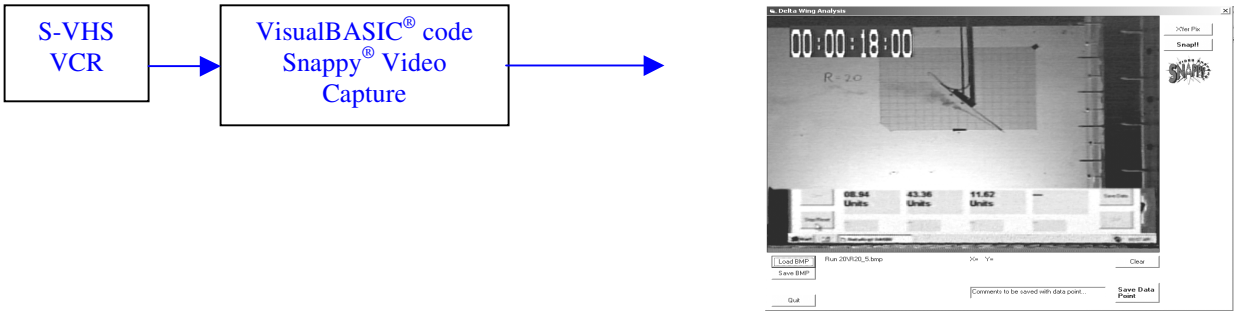

b) Post-Test Data Analysis Process

Figure 4.10. Experimental Set-Up (Mount Validation and Variable Velocity Cases).

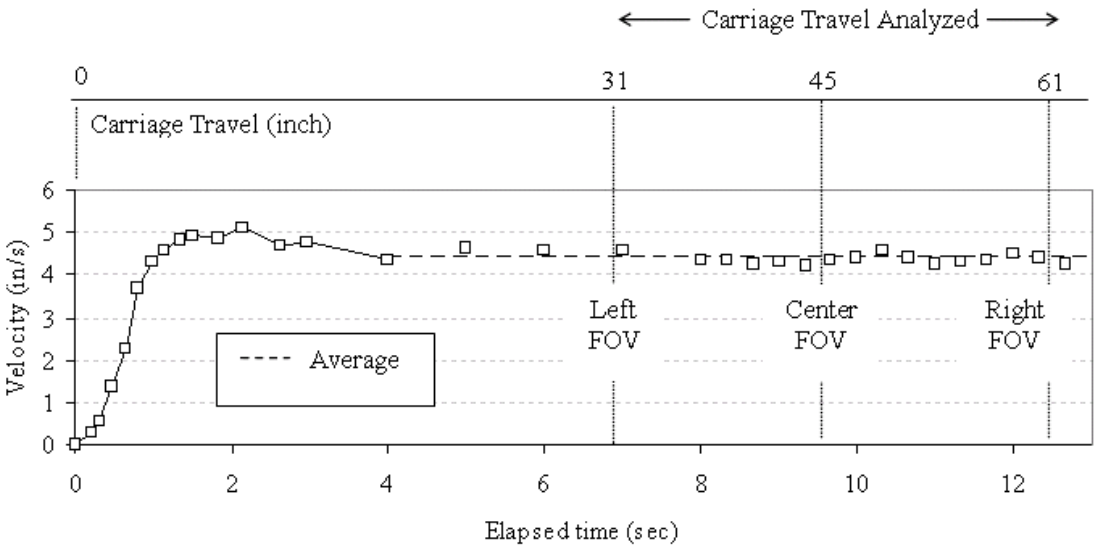

Figure 4.11. Carriage Velocity Behavior.

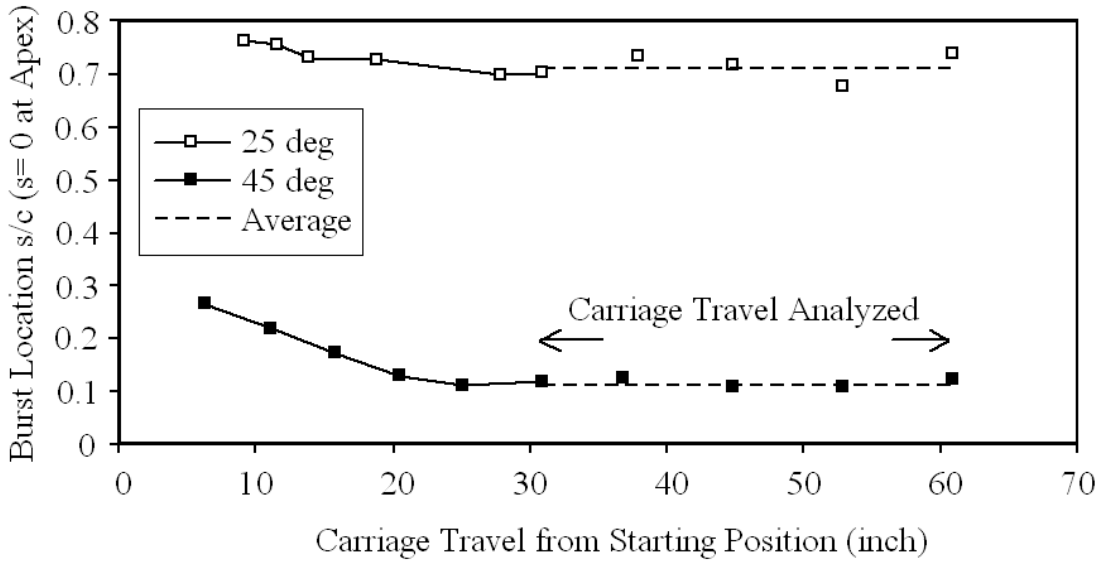

Figure 4.12. Vortex Burst Behavior as Function of Distance from Standstill.

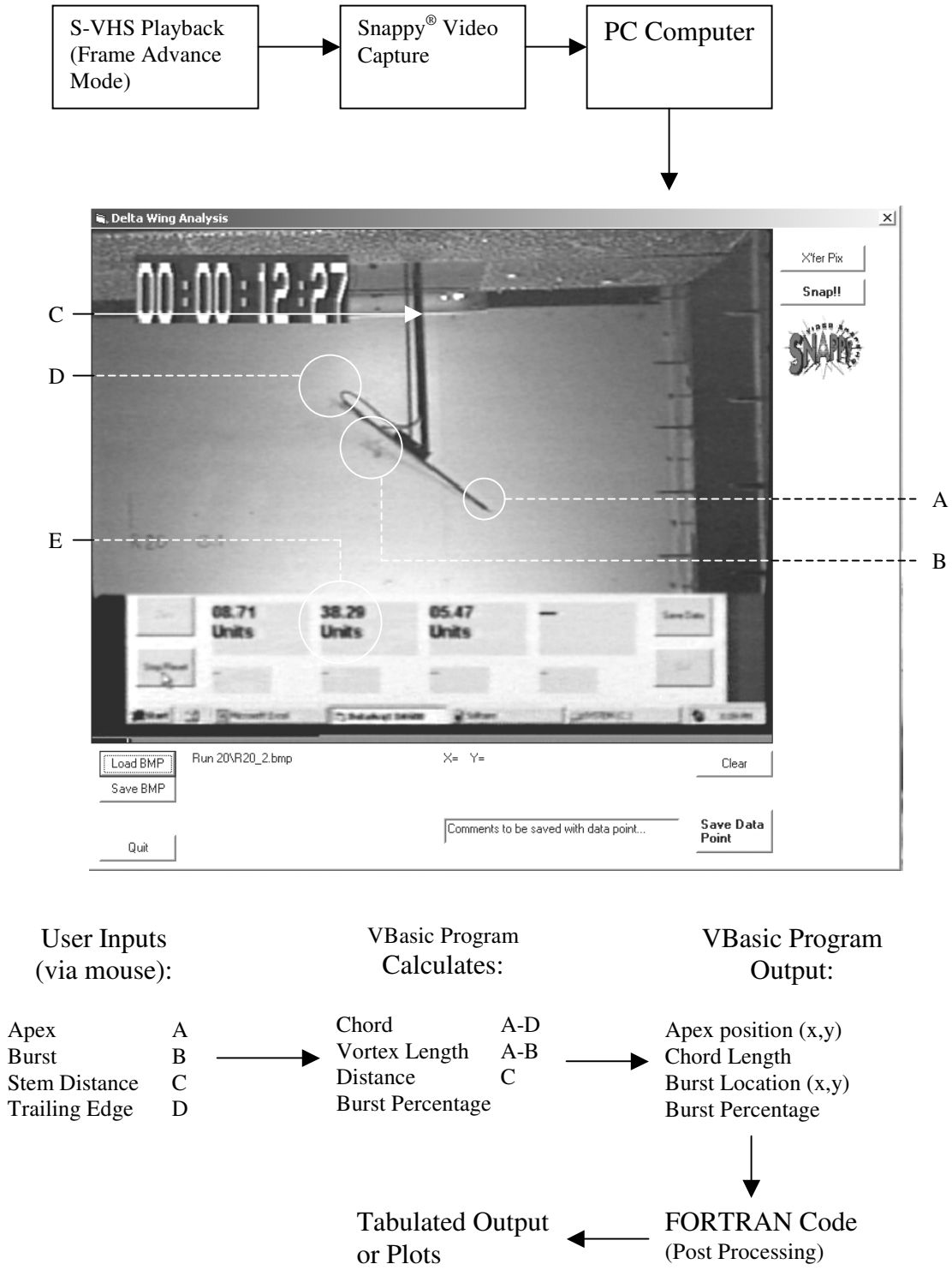

Figure 4.13. Analysis Process.

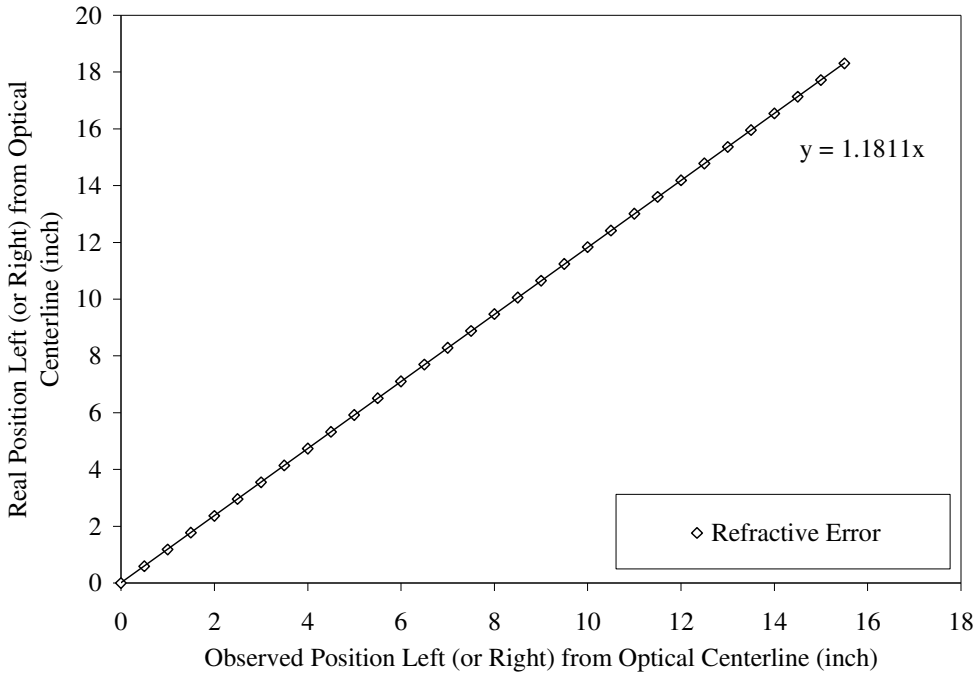

Figure 4.14. Position Error due to Water Refraction.

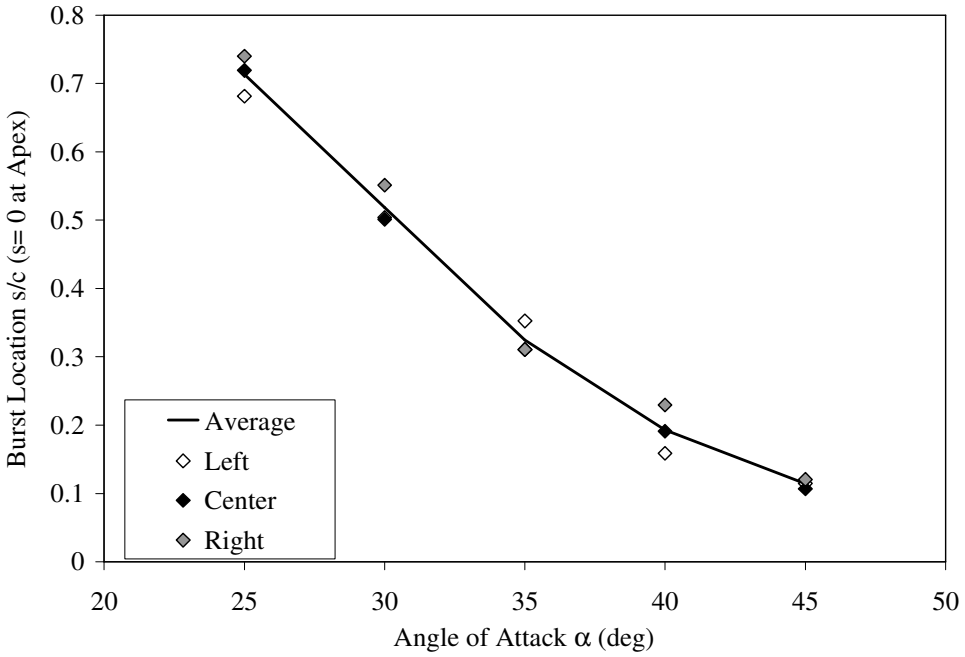

Figure 4.15. Perspective Error due to Camera Position.

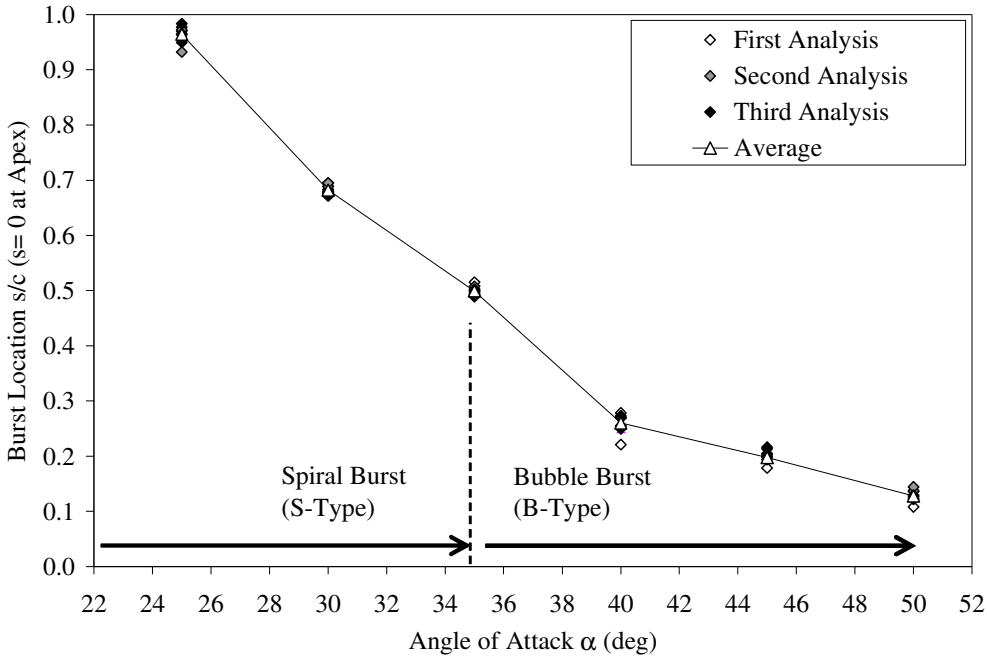

Figure 4.16. Author's Influence on Vortex Burst Analysis Repeatability.

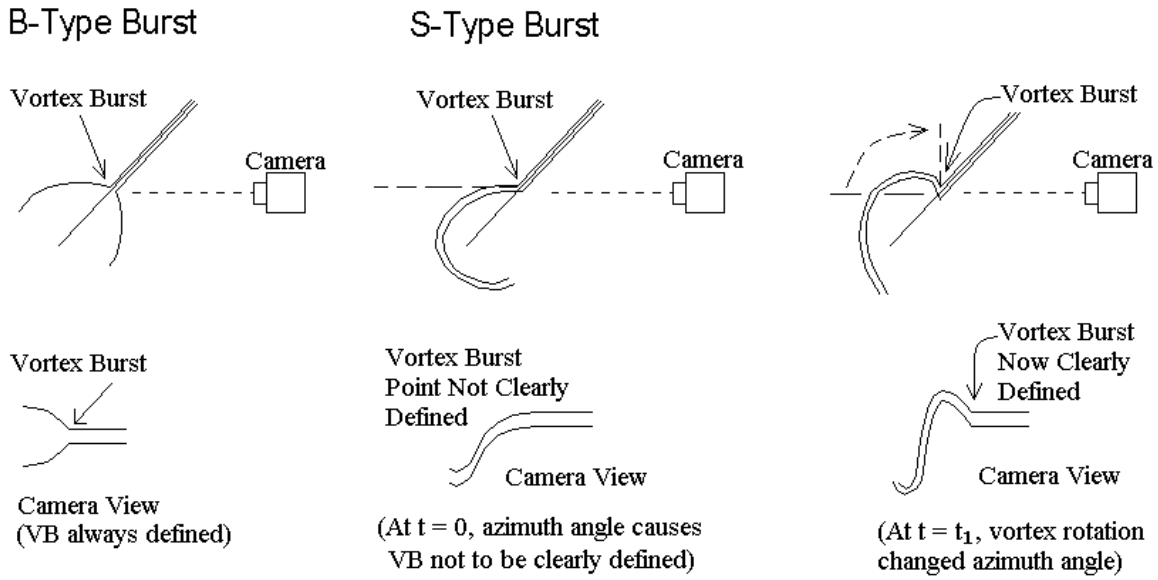

Figure 4.17. Definition of Vortex Burst Point.

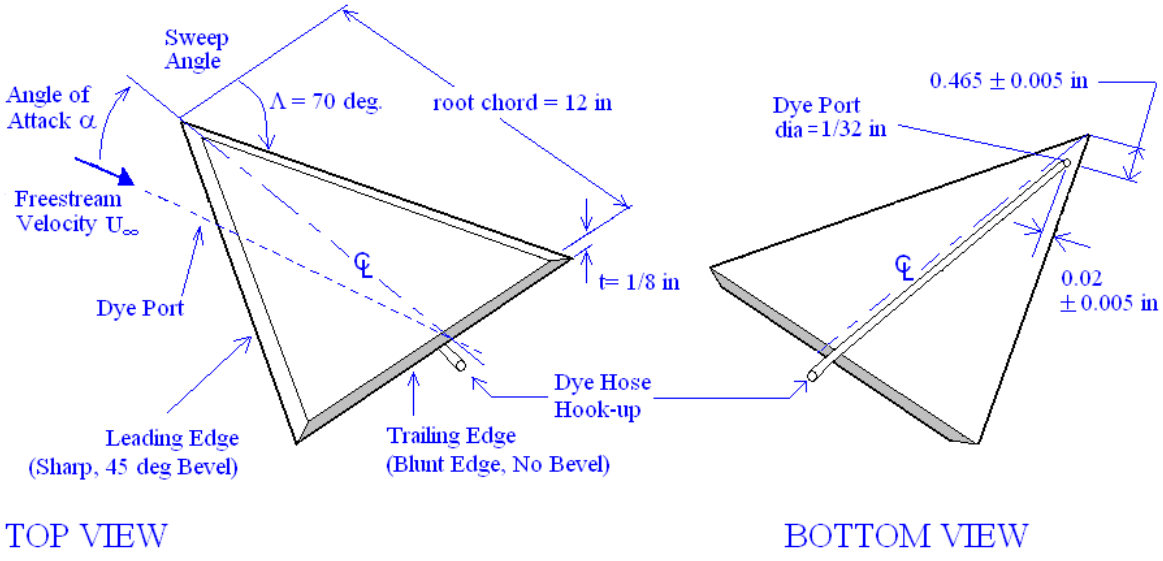

Figure 4.18. Schematic of the Delta Wing Used.

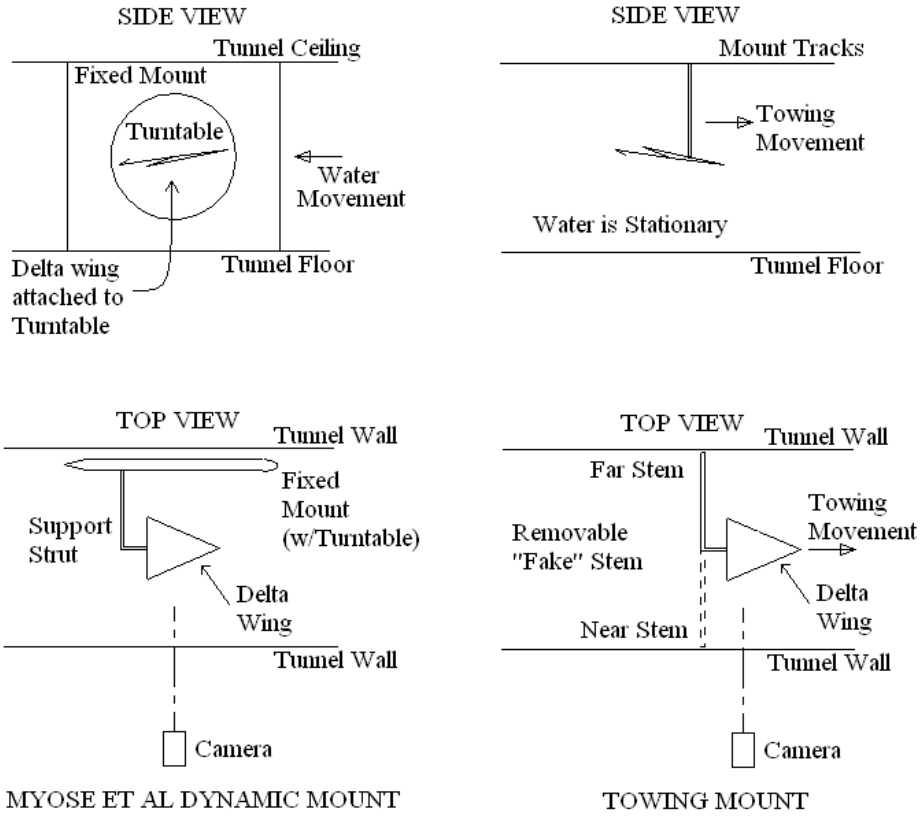

Figure 4.19. Stem Used on Validation Tests.

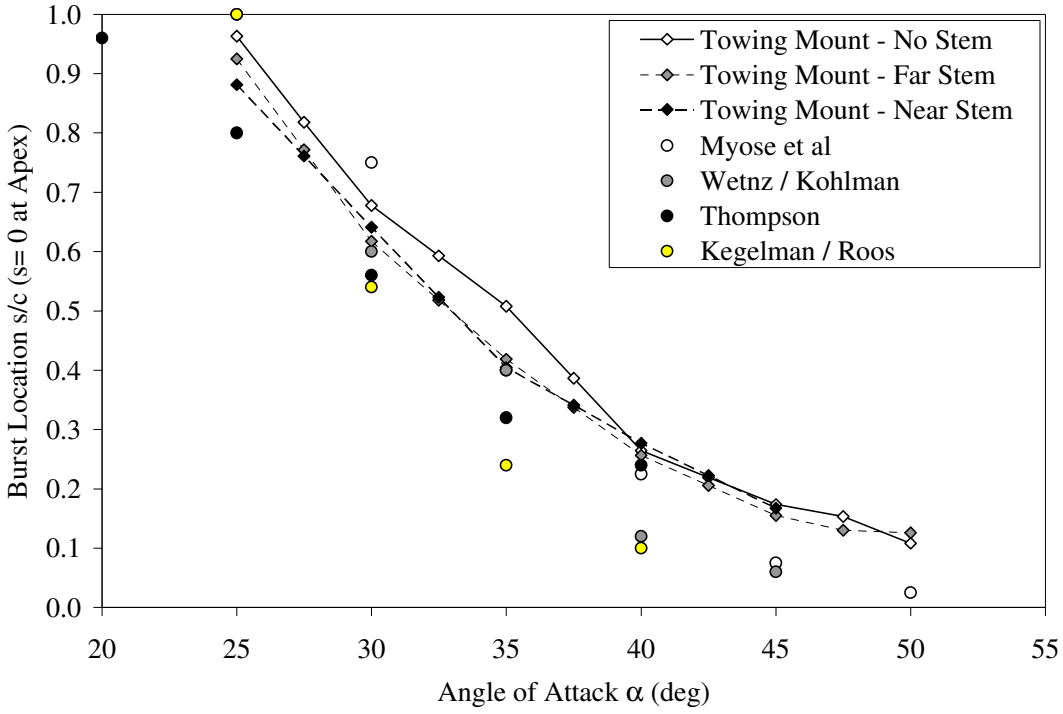

Figure 4.20. Towing Mount Validation - Static Results.

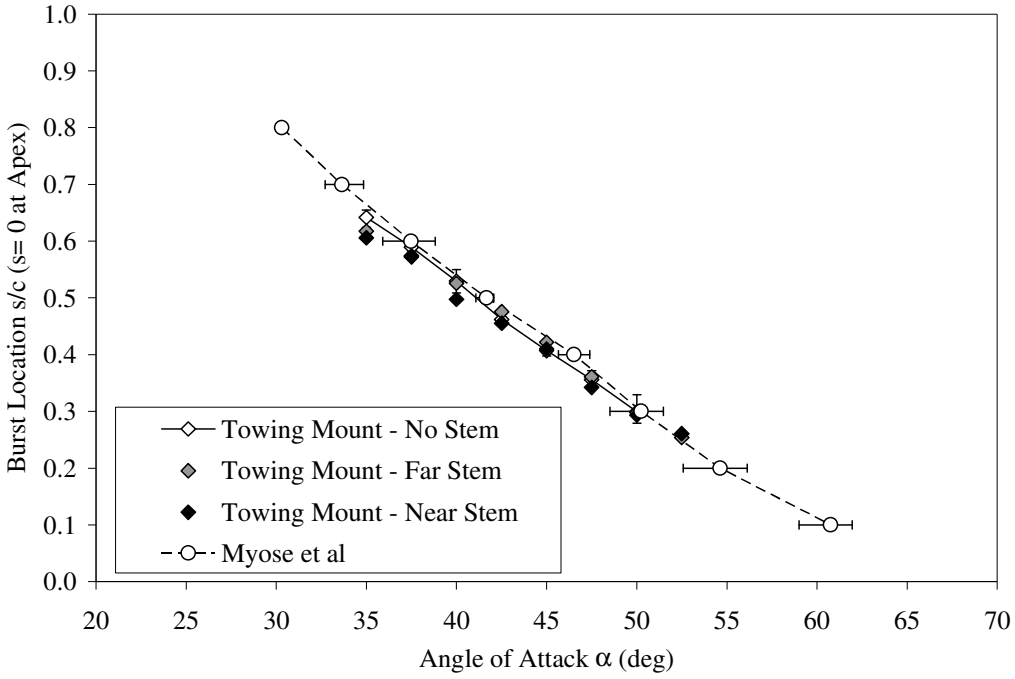

Figure 4.21. Towing Mount Validation - Dynamic Pitch, $\kappa = 0.1$.

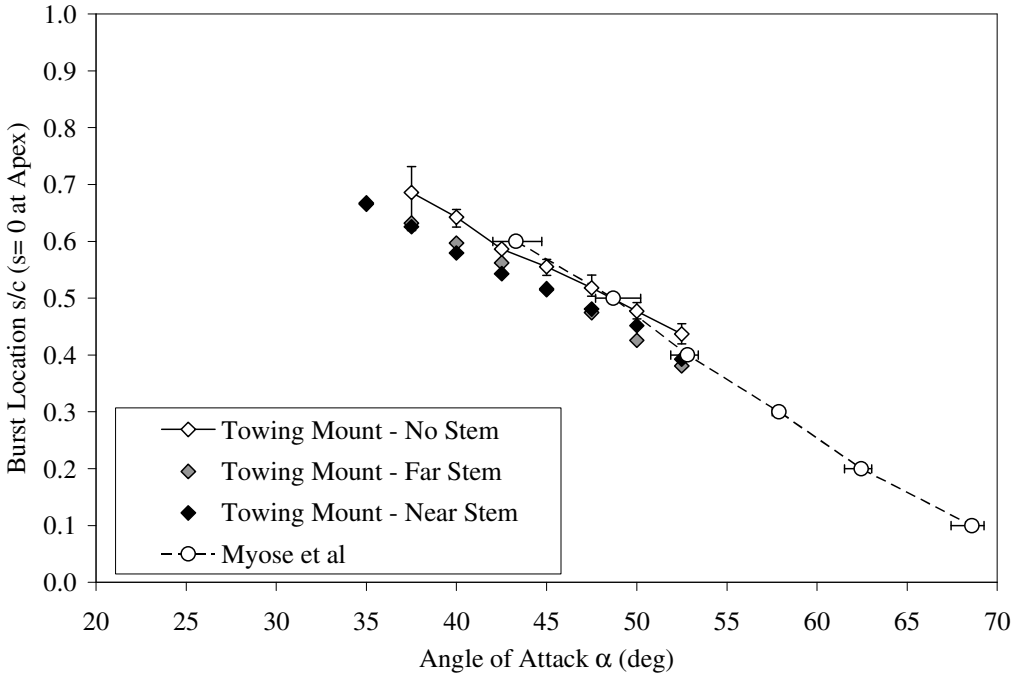

Figure 4.22. Towing Mount Validation - Dynamic Pitch, $\kappa = 0.2$.

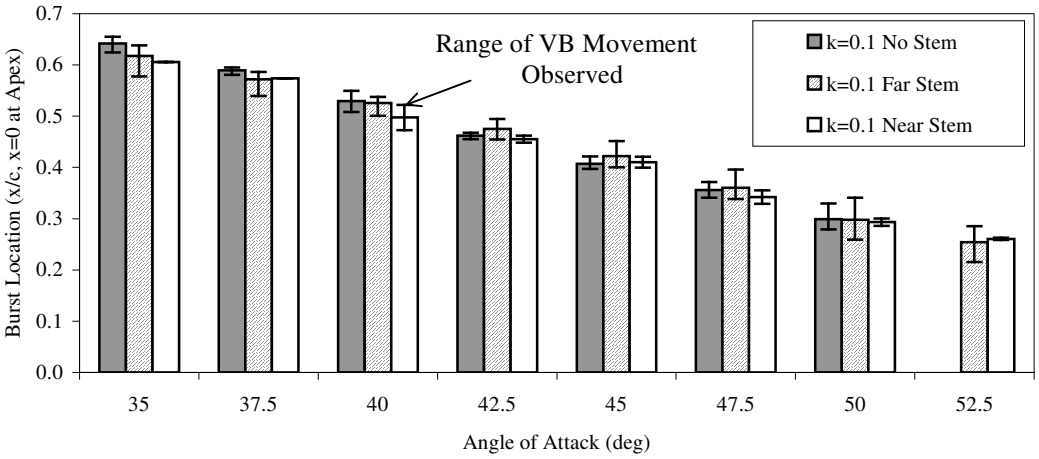

Figure 4.23. Effect due to Stem, $\kappa = 0.1$

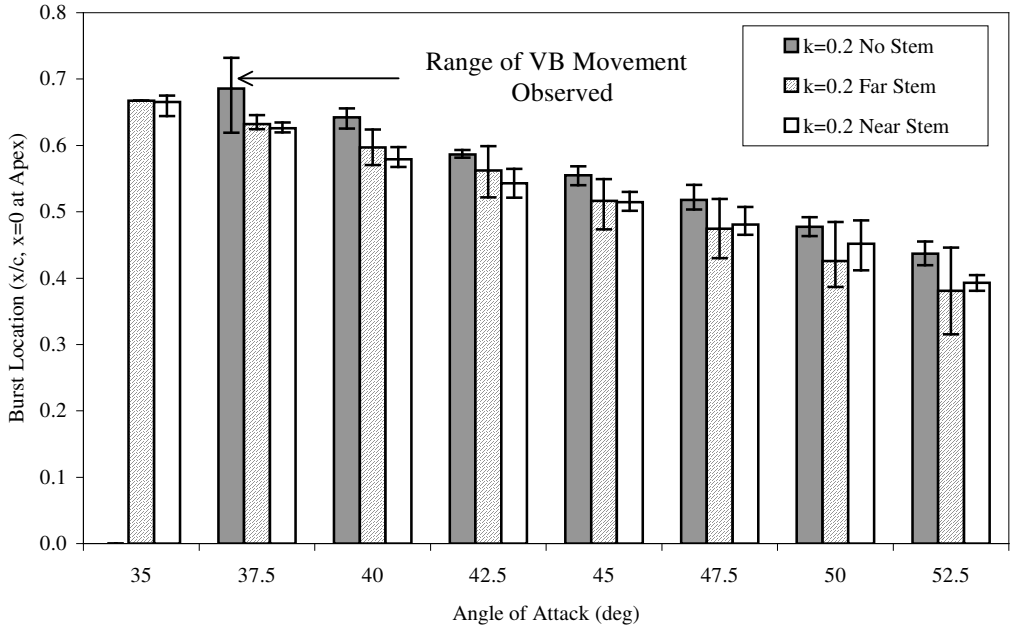

Figure 4.24. Effect due to Stem, $\kappa = 0.2$

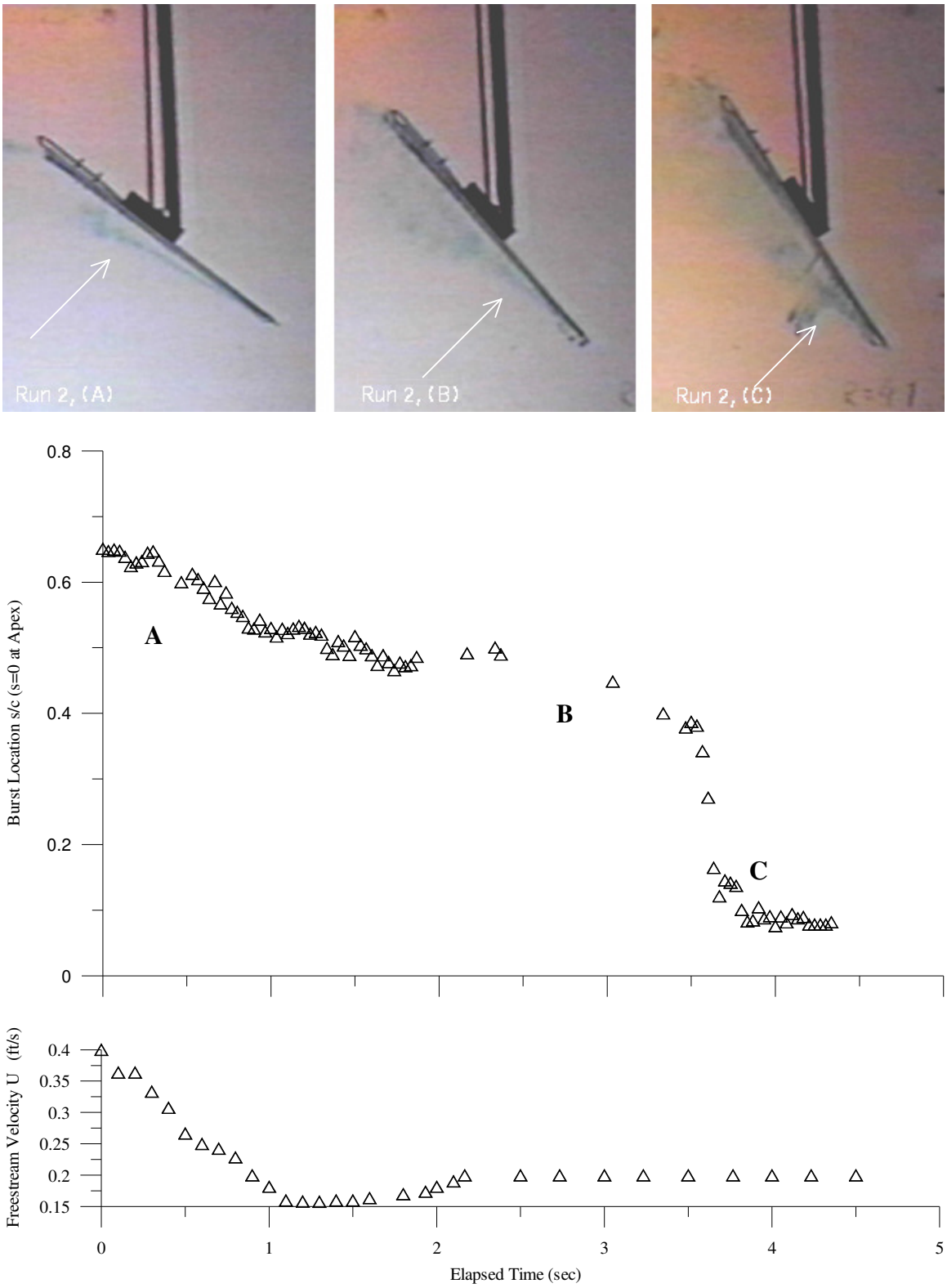

Figure 5.1. Sample Vortex Burst Behavior, Dynamic Pitch and Variable Velocity ($15 < \alpha < 55$ deg, Slow Down from $30 < \alpha < 55$ deg).

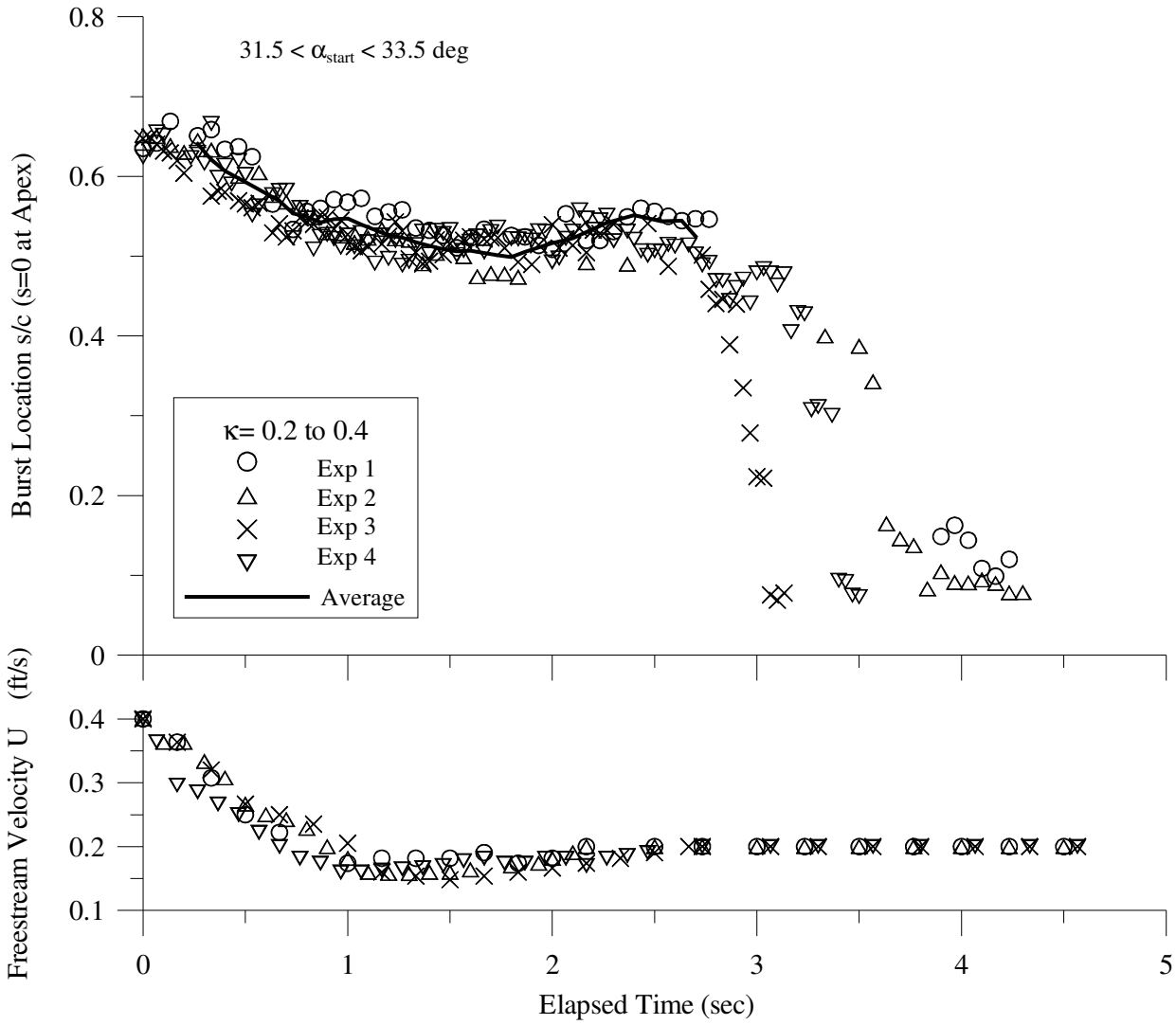

Figure 5.2. Vortex Burst Time Behavior, Dynamic Pitch and Variable Velocity, κ=0.2 to 0.4 ($15 < \alpha < 55$ deg, Slow Down from $30 < \alpha < 55$ deg).

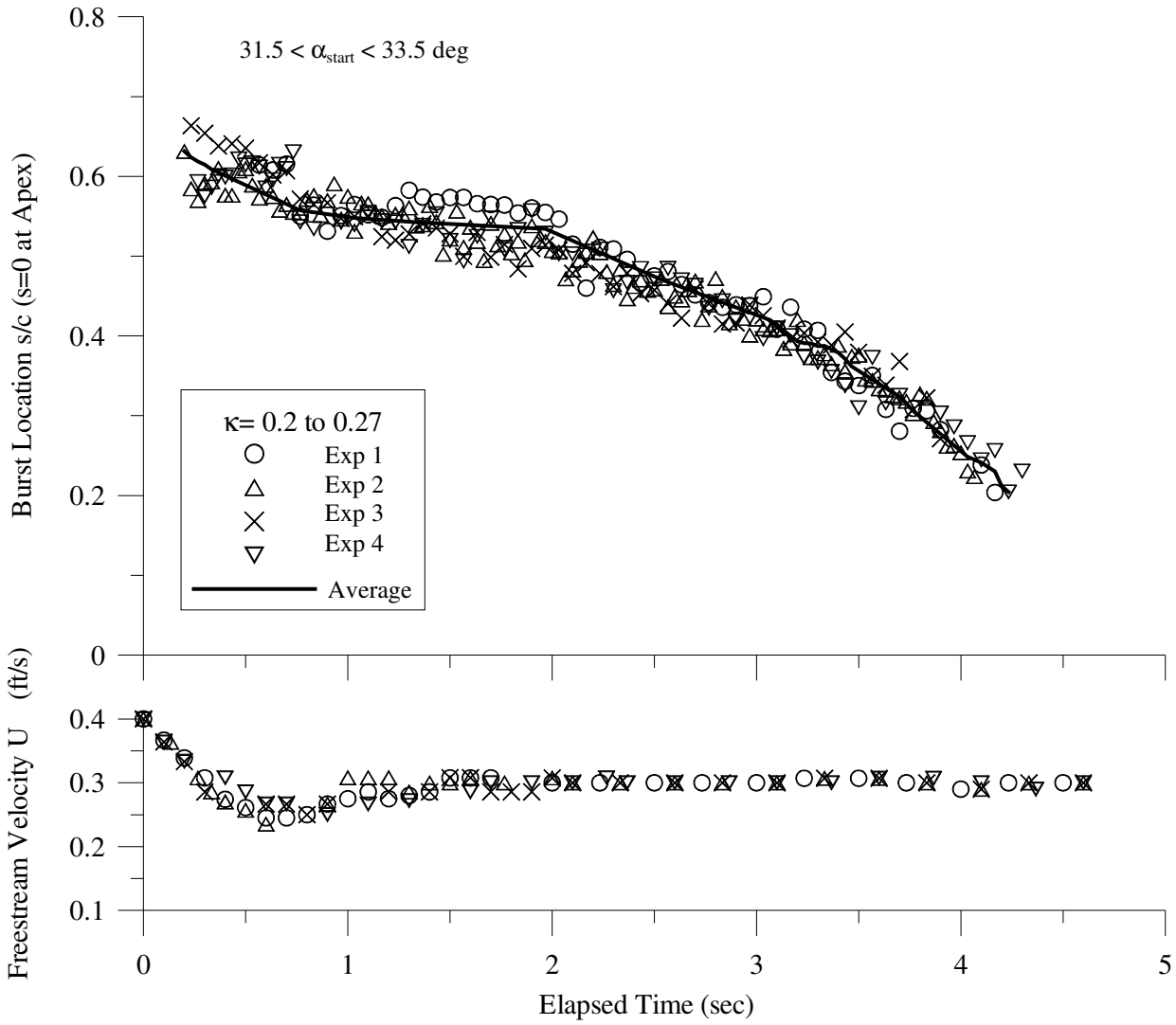

Figure 5.3. Vortex Burst Behavior, Dynamic Pitch and Variable Velocity, κ=0.2 to 0.27 ($15 < \alpha < 55$ deg, Slow Down from $30 < \alpha < 55$ deg).

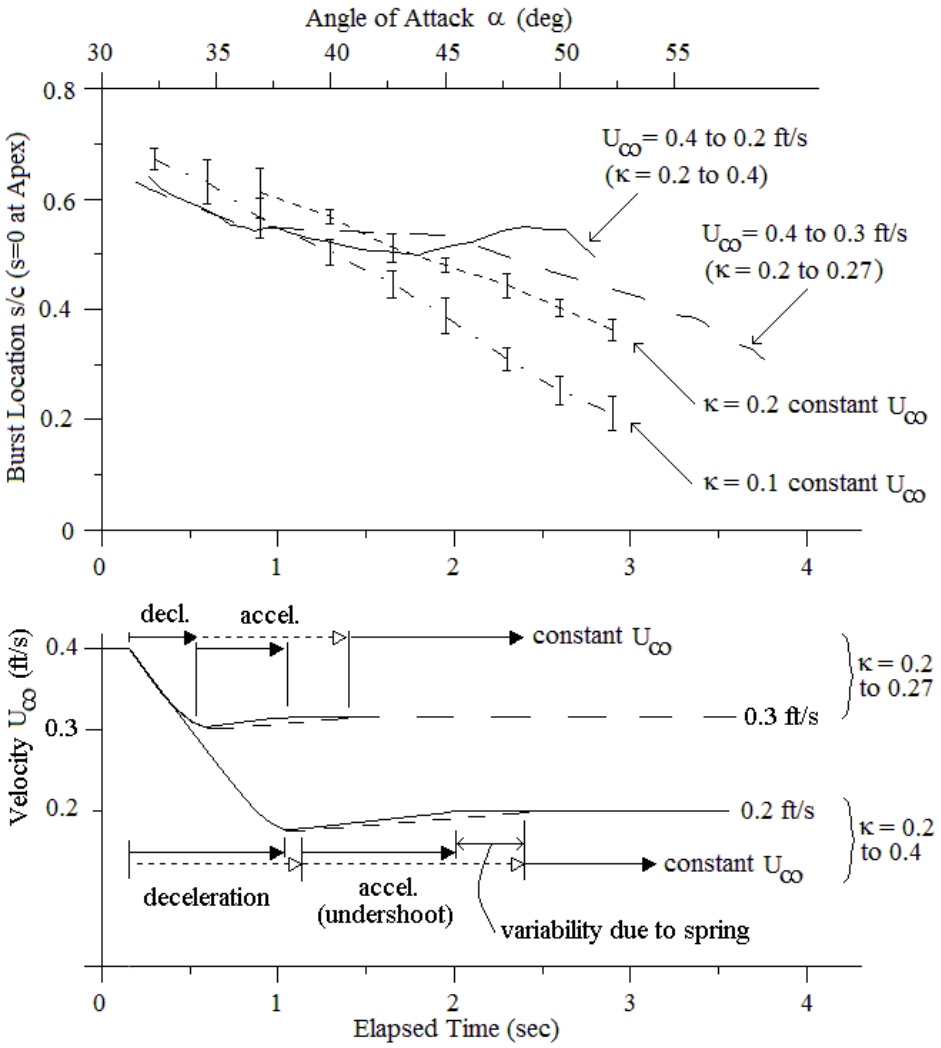

Figure 5.4. Vortex Burst Behavior Comparison, Capacitor Slow-Down.

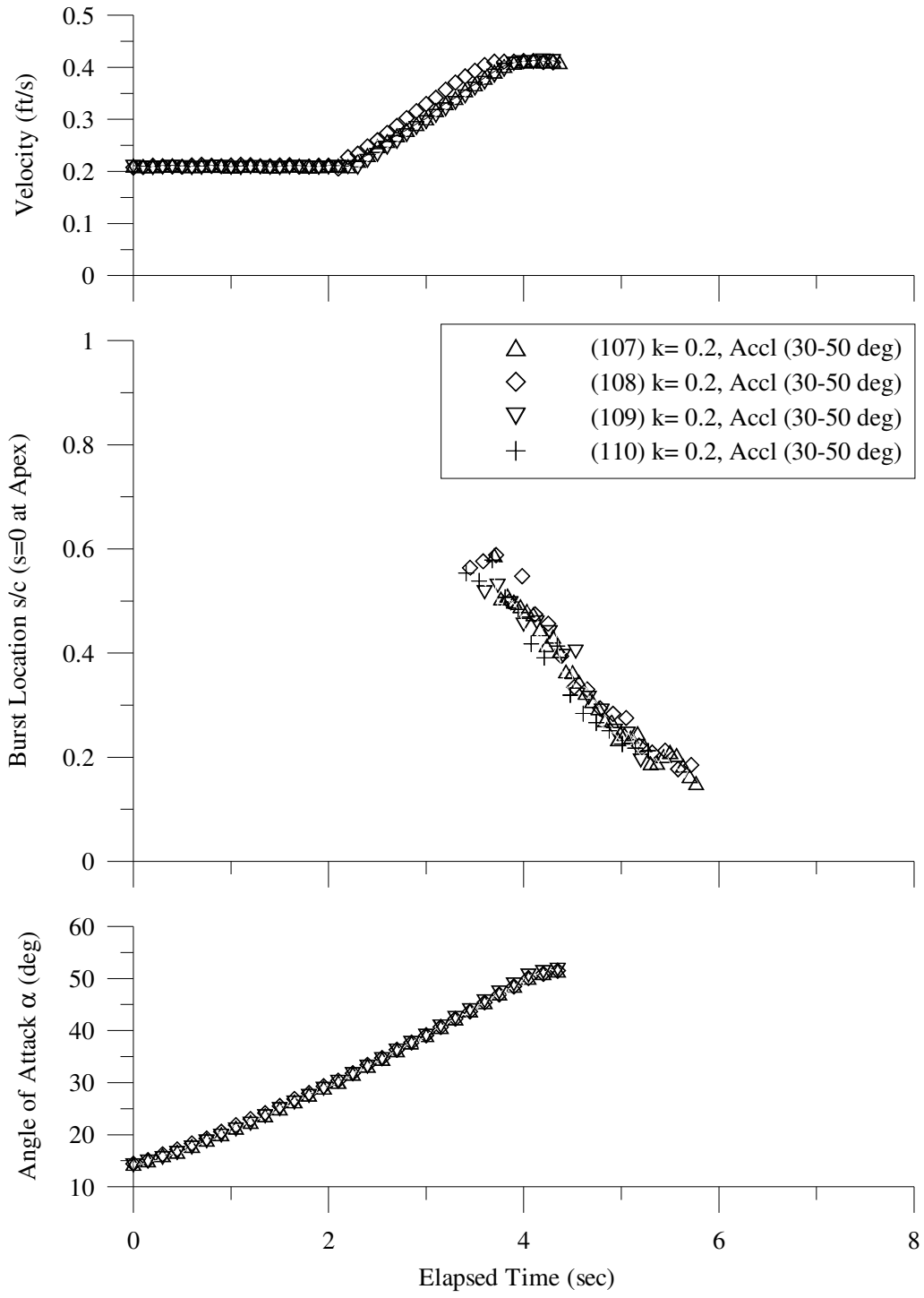

Figure 5.5. Burst Behavior, Pitch Up at κ=0.2,
Acceleration from 0.2 ft/s (30 deg) to 0.4 ft/s (50 deg).

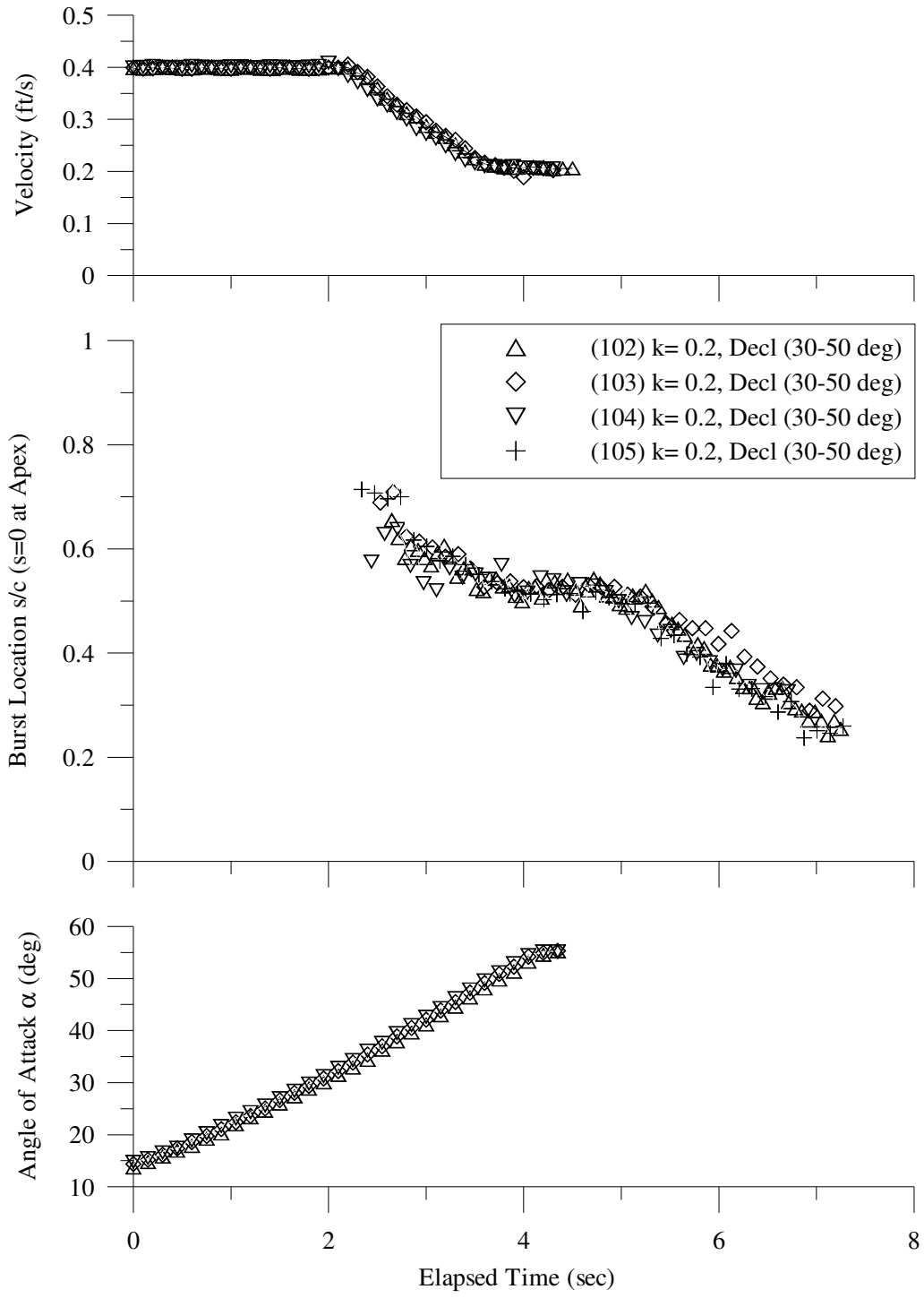

Figure 5.6. Burst Behavior, Pitch Up at κ=0.2,
Deceleration from 0.4 ft/s (30 deg) to 0.2 ft/s (50 deg).

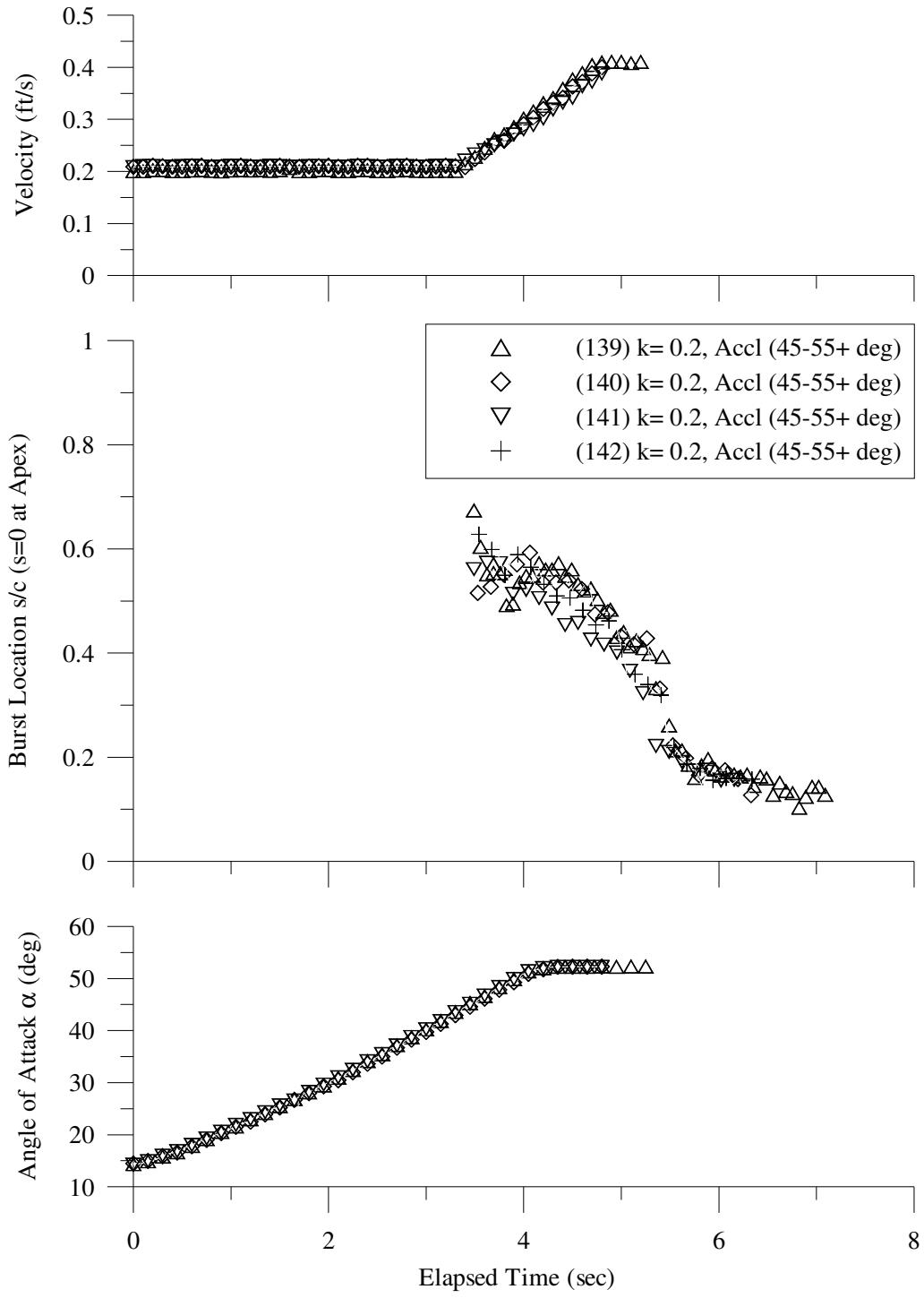

Figure 5.7. Burst Behavior, Pitch Up at κ=0.2,
Acceleration from 0.2 ft/s (45 deg) to 0.4 ft/s (beyond 55 deg).

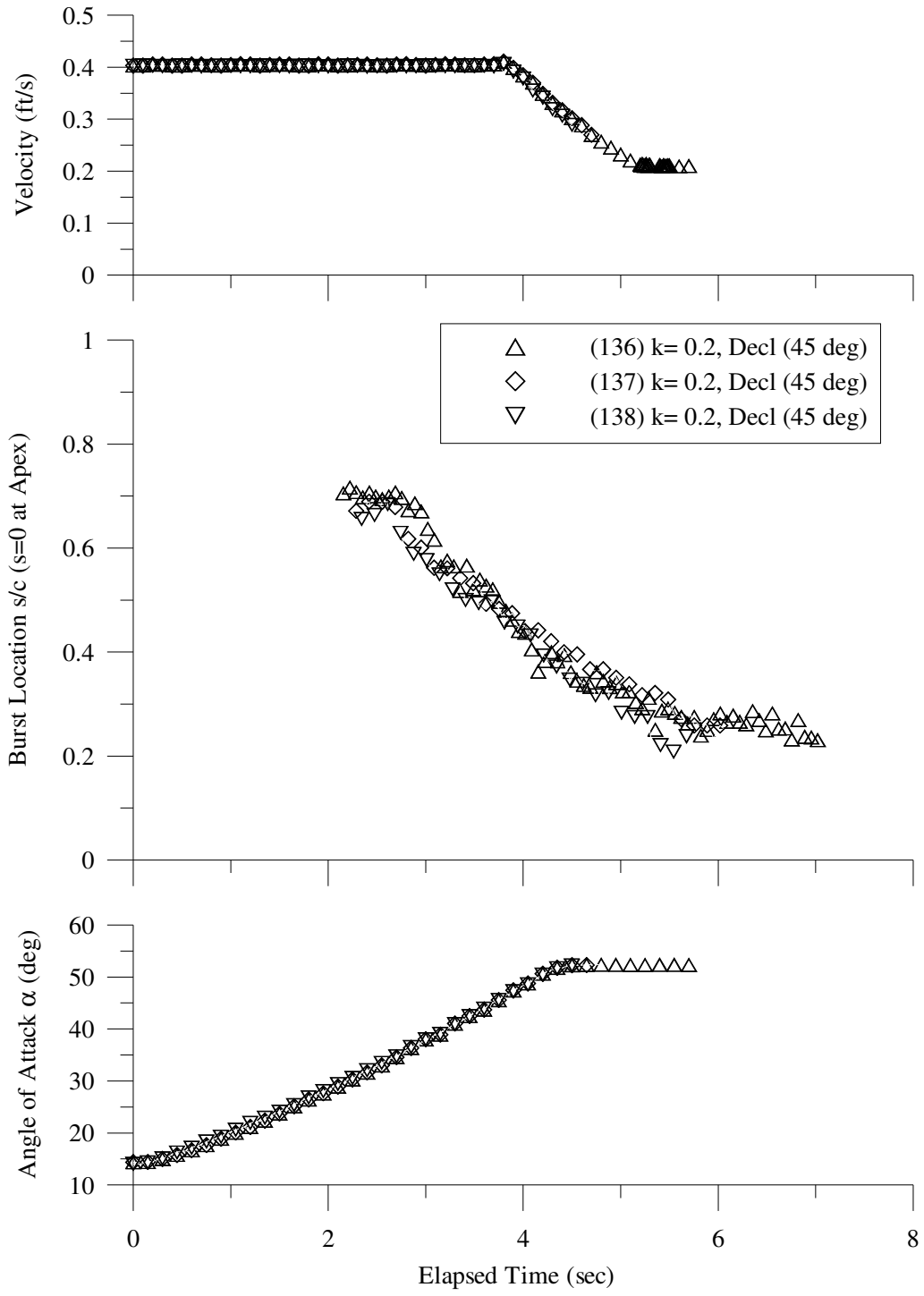

Figure 5.8. Burst Behavior, Pitch Up at κ=0.2,
Deceleration from 0.4 ft/s (45 deg) to 0.2 ft/s (beyond 55 deg).

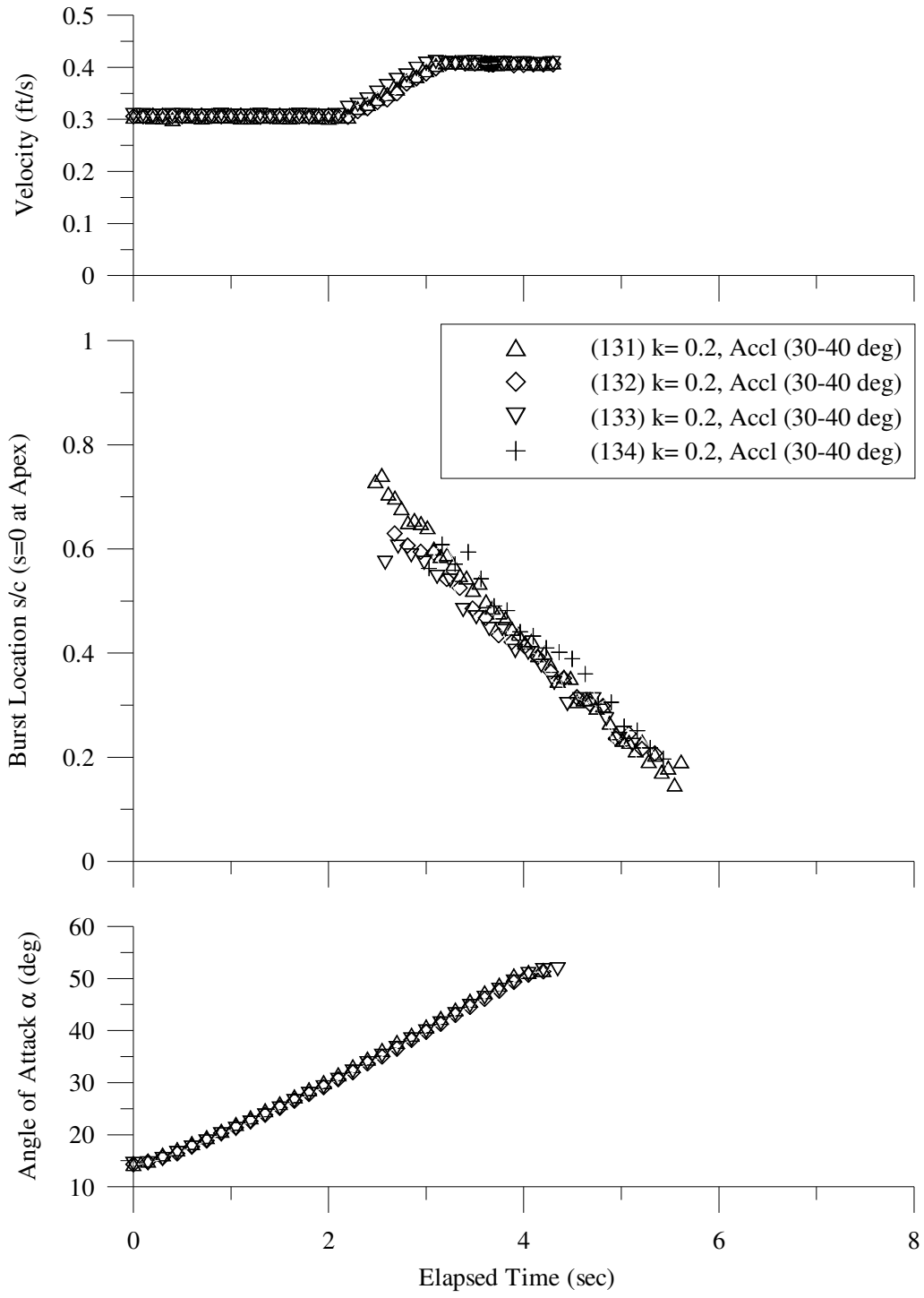

Figure 5.9. Burst Behavior, Pitch Up at κ=0.2,
Acceleration from 0.3 ft/s (30 deg) to 0.4 ft/s (40 deg).

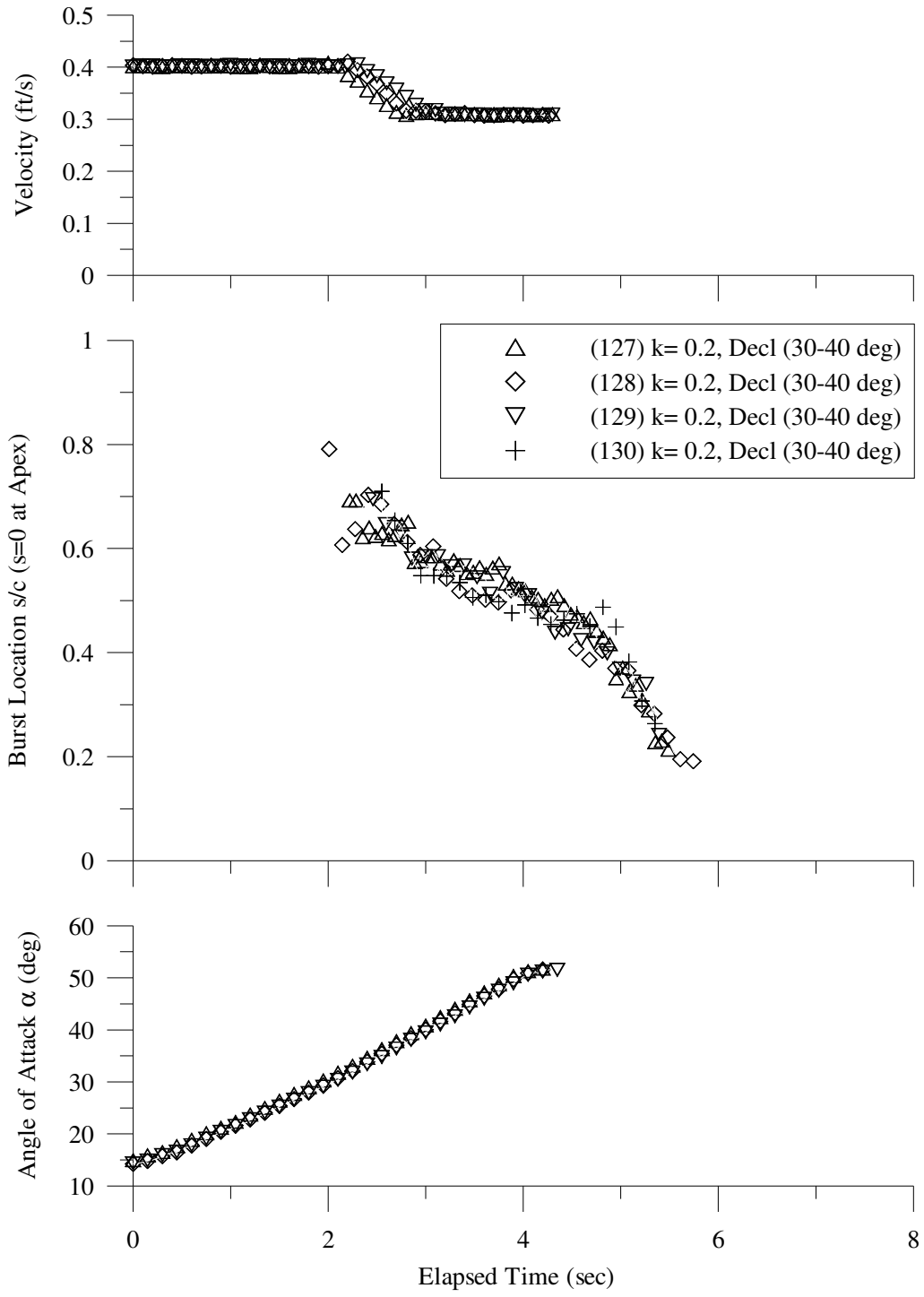

Figure 5.10. Burst Behavior, Pitch Up at κ=0.2,
Deceleration from 0.4 ft/s (30 deg) to 0.3 ft/s (40 deg).

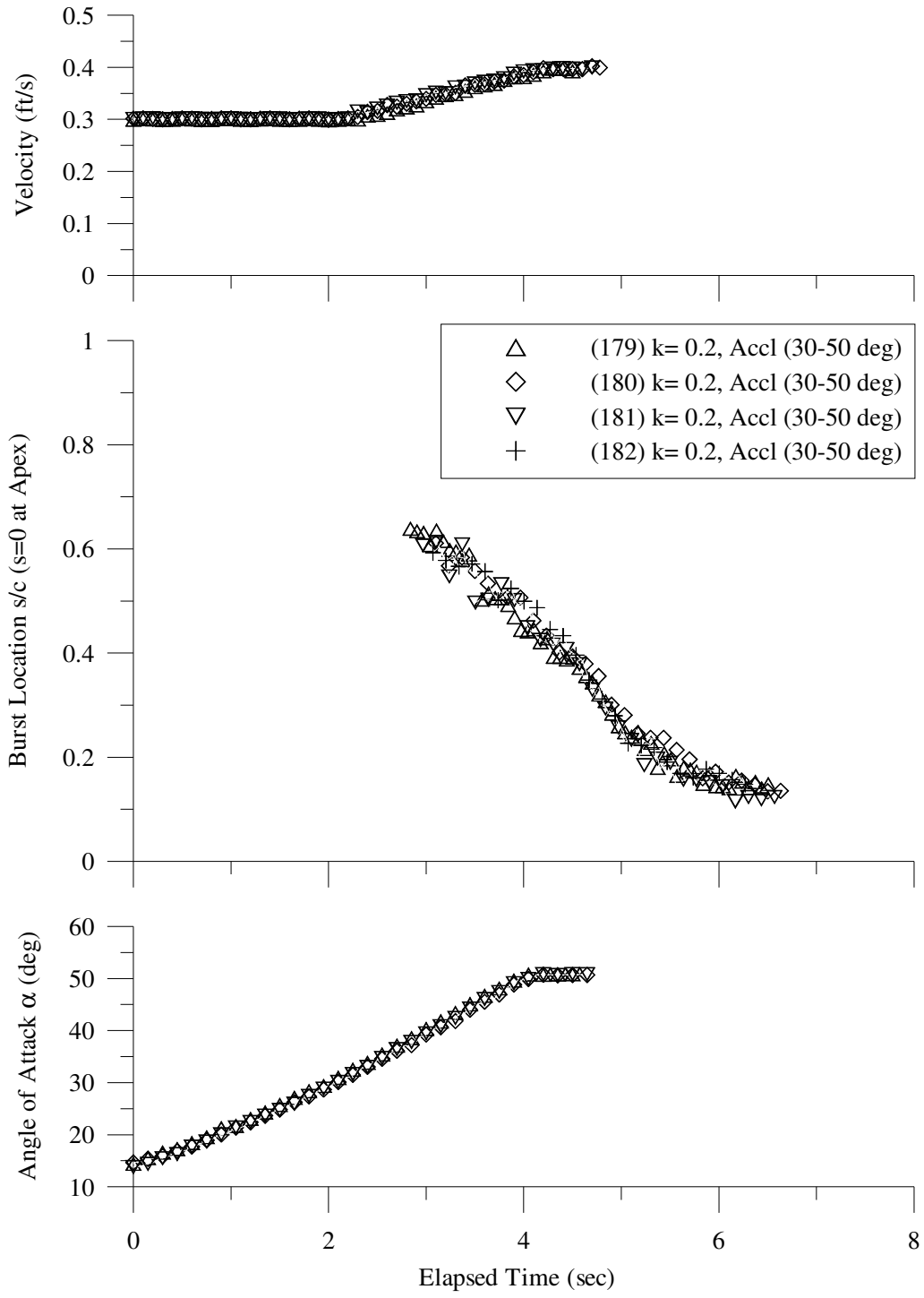

Figure 5.11. Burst Behavior, Pitch Up at κ=0.2,
Acceleration from 0.3 ft/s (30 deg) to 0.4 ft/s (50 deg).

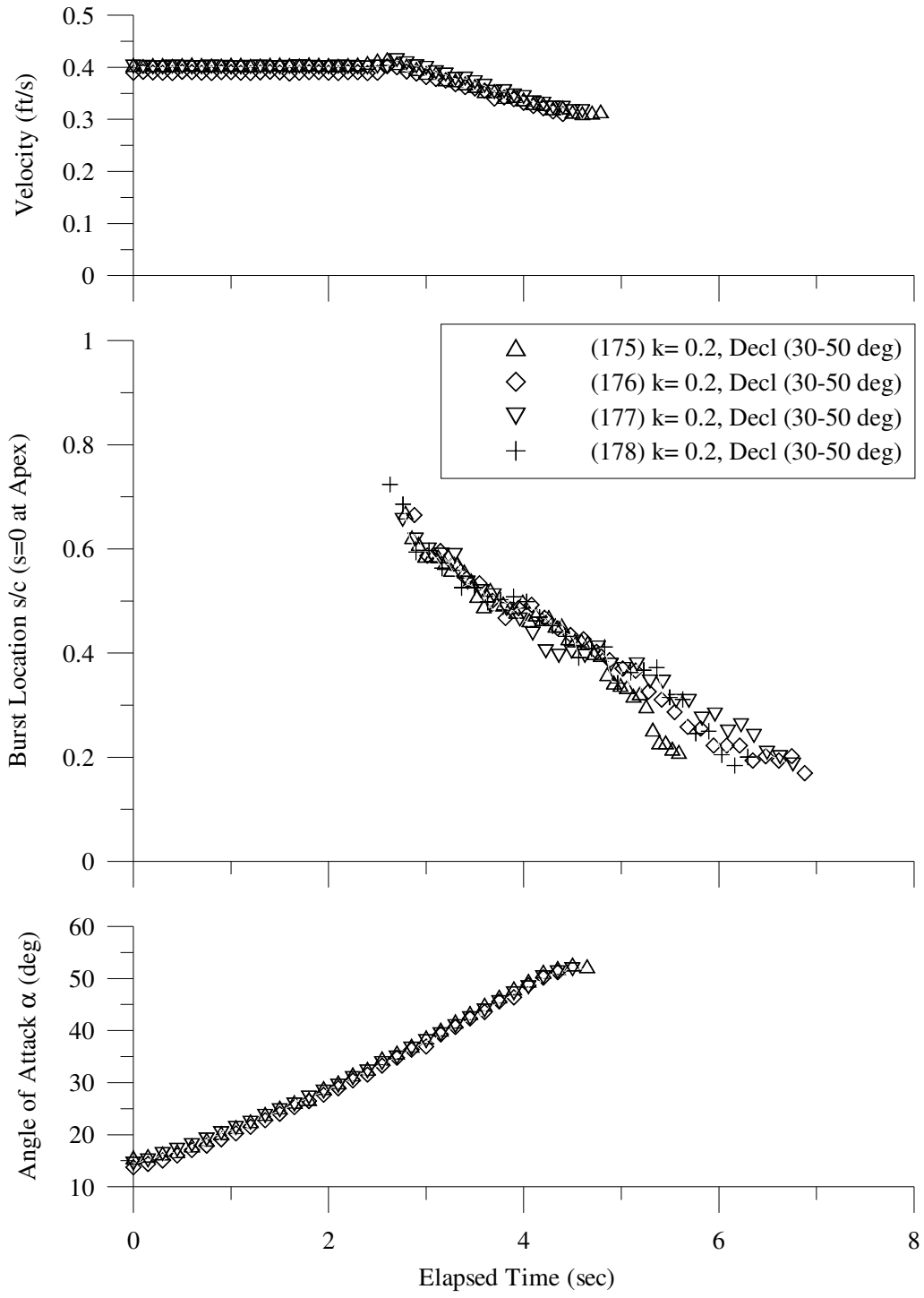

Figure 5.12. Burst Behavior, Pitch Up at κ=0.2,
Deceleration from 0.4 ft/s (30 deg) to 0.3 ft/s (50 deg).

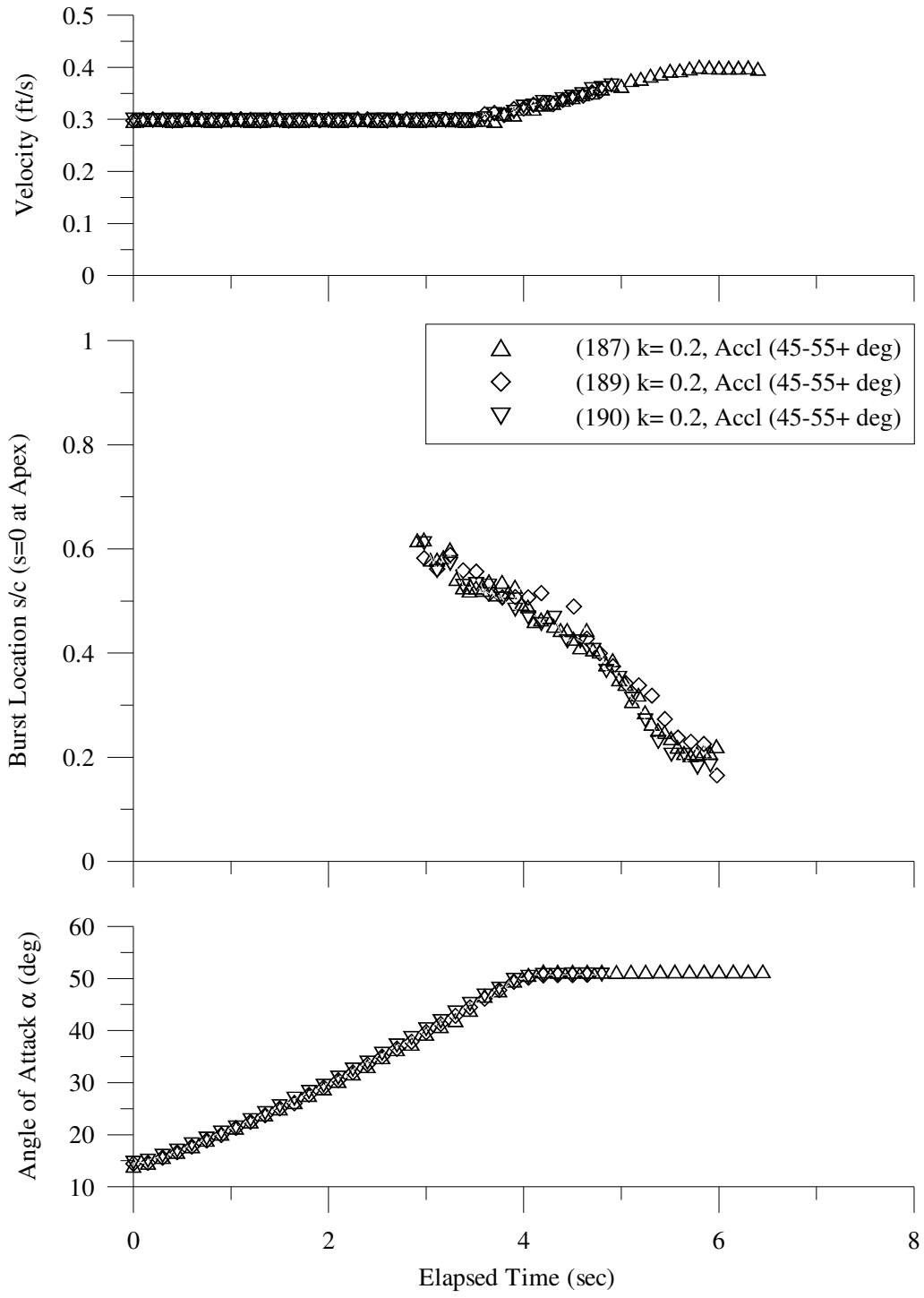

Figure 5.13. Burst Behavior, Pitch Up at κ=0.2,
Acceleration from 0.3 ft/s (45 deg) to 0.4 ft/s (beyond 55 deg).

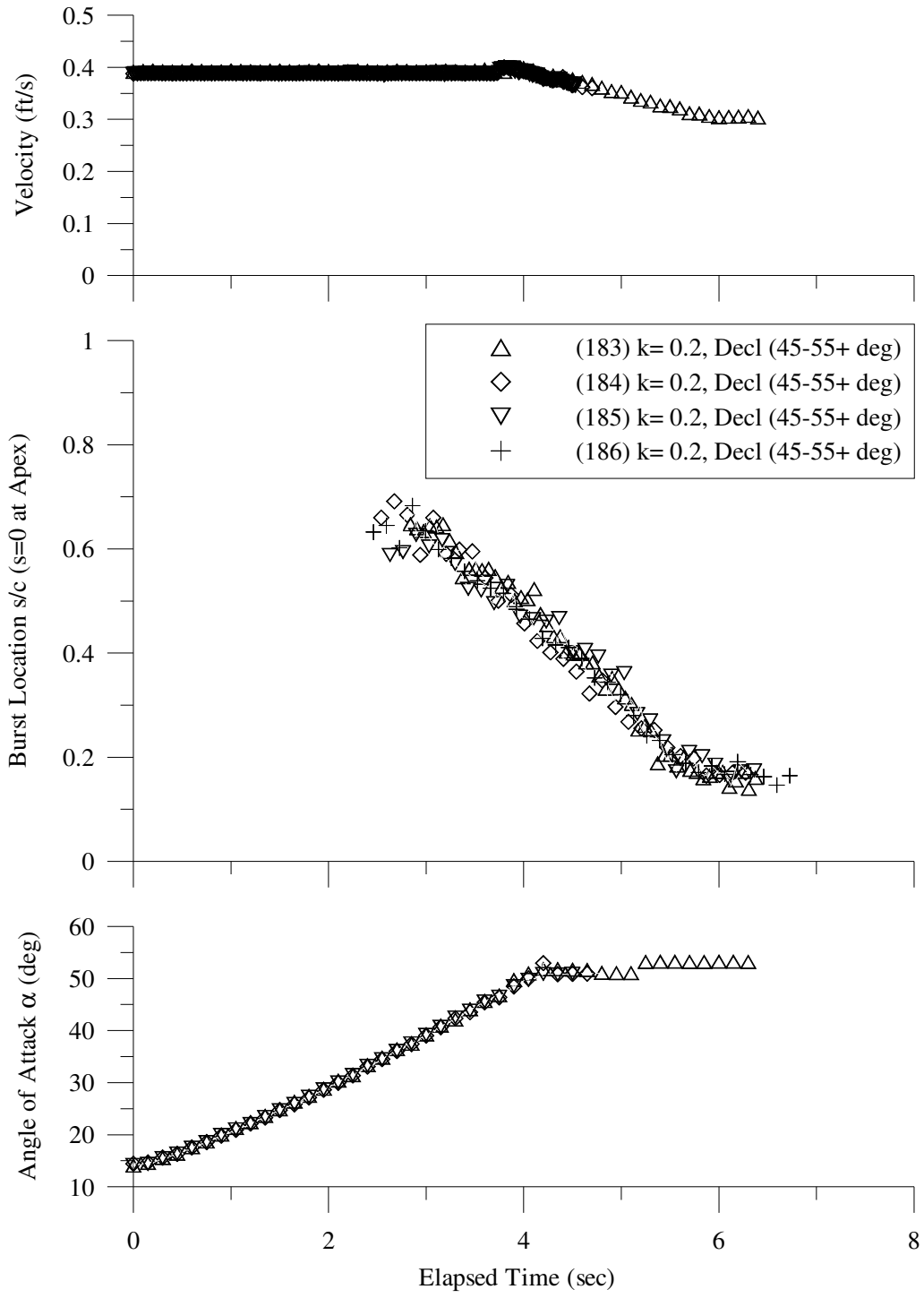

Figure 5.14. Burst Behavior, Pitch Up at κ=0.2,
Deceleration from 0.4 ft/s (45 deg) to 0.3 ft/s (beyond 55 deg).

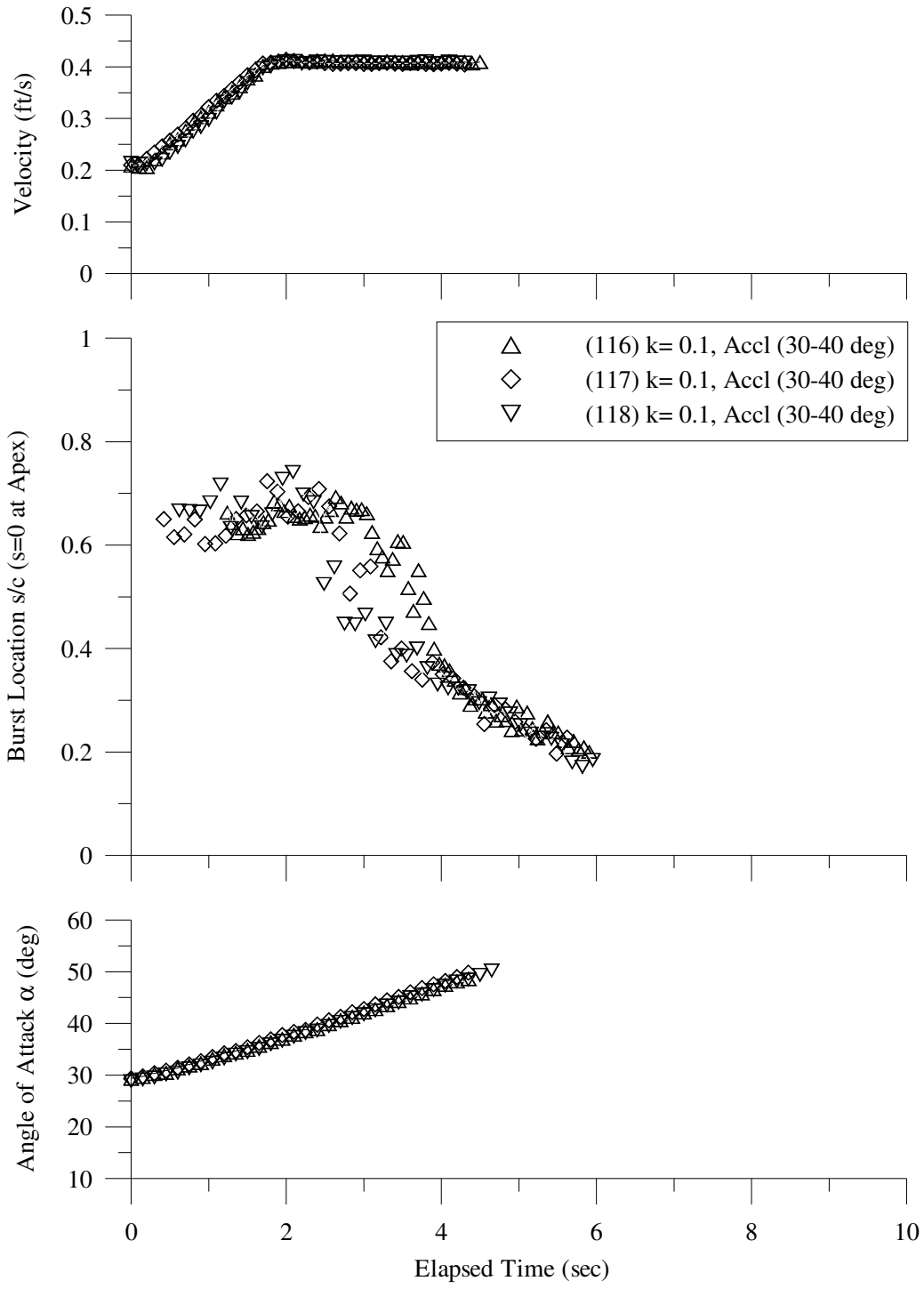

Figure 5.15. Burst Behavior, Pitch Up at κ=0.1,
Acceleration from 0.2 ft/s (30 deg) to 0.4 ft/s (40 deg).

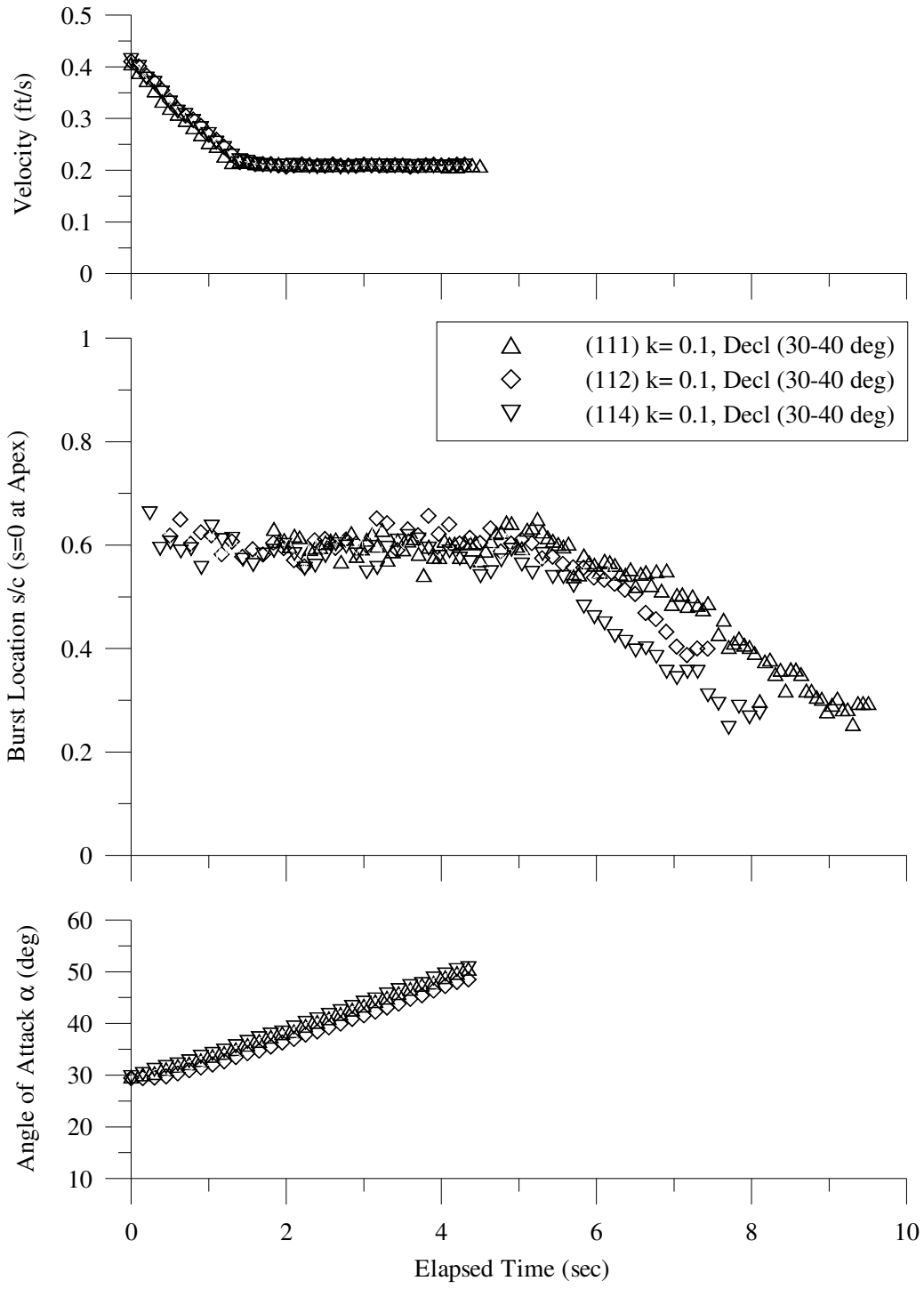

Figure 5.16. Burst Behavior, Pitch Up at κ=0.1,
Deceleration from 0.4 ft/s (30 deg) to 0.2 ft/s (40 deg).

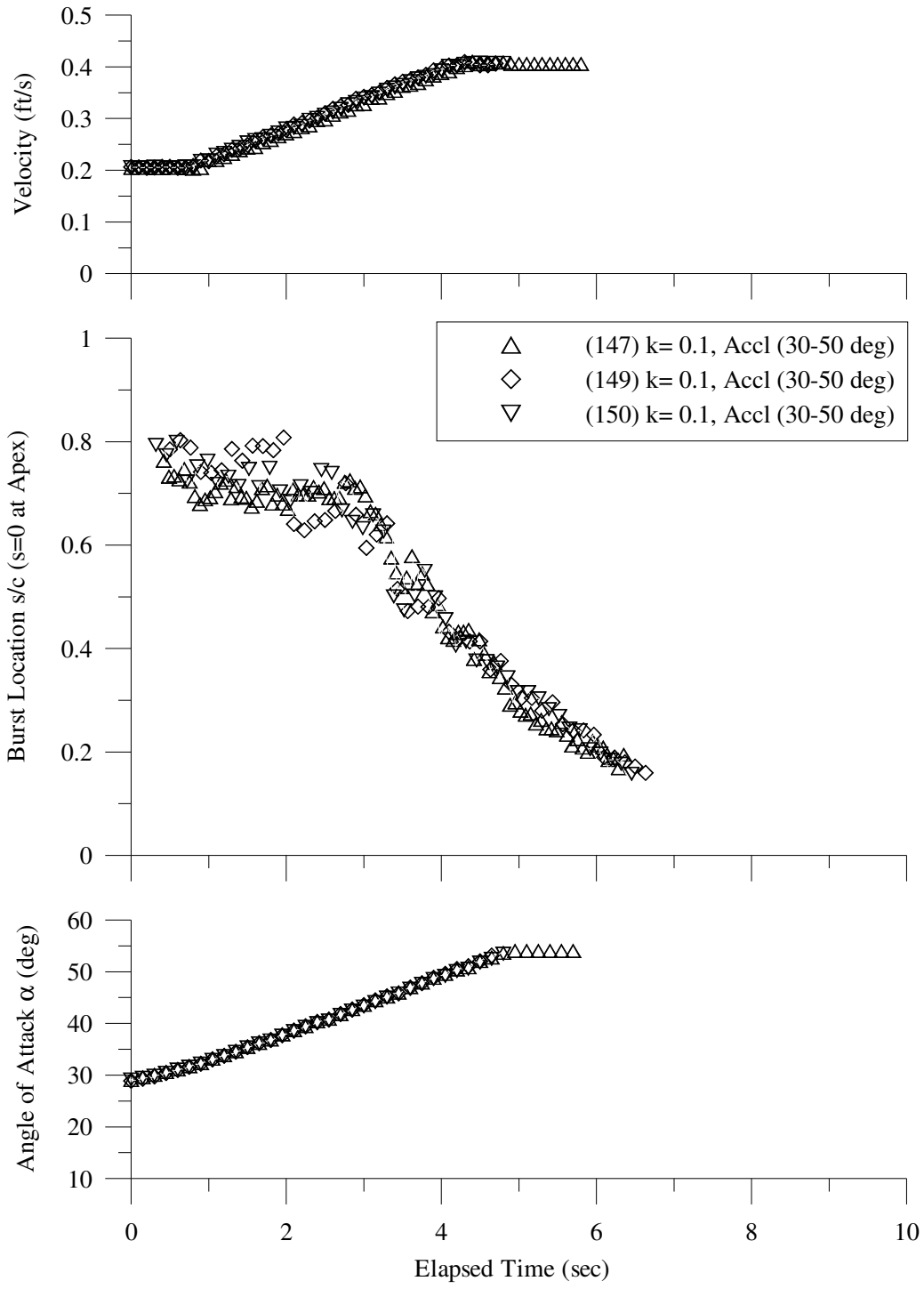

Figure 5.17. Burst Behavior, Pitch Up at κ=0.1,
Acceleration from 0.2 ft/s (30 deg) to 0.4 ft/s (50 deg).

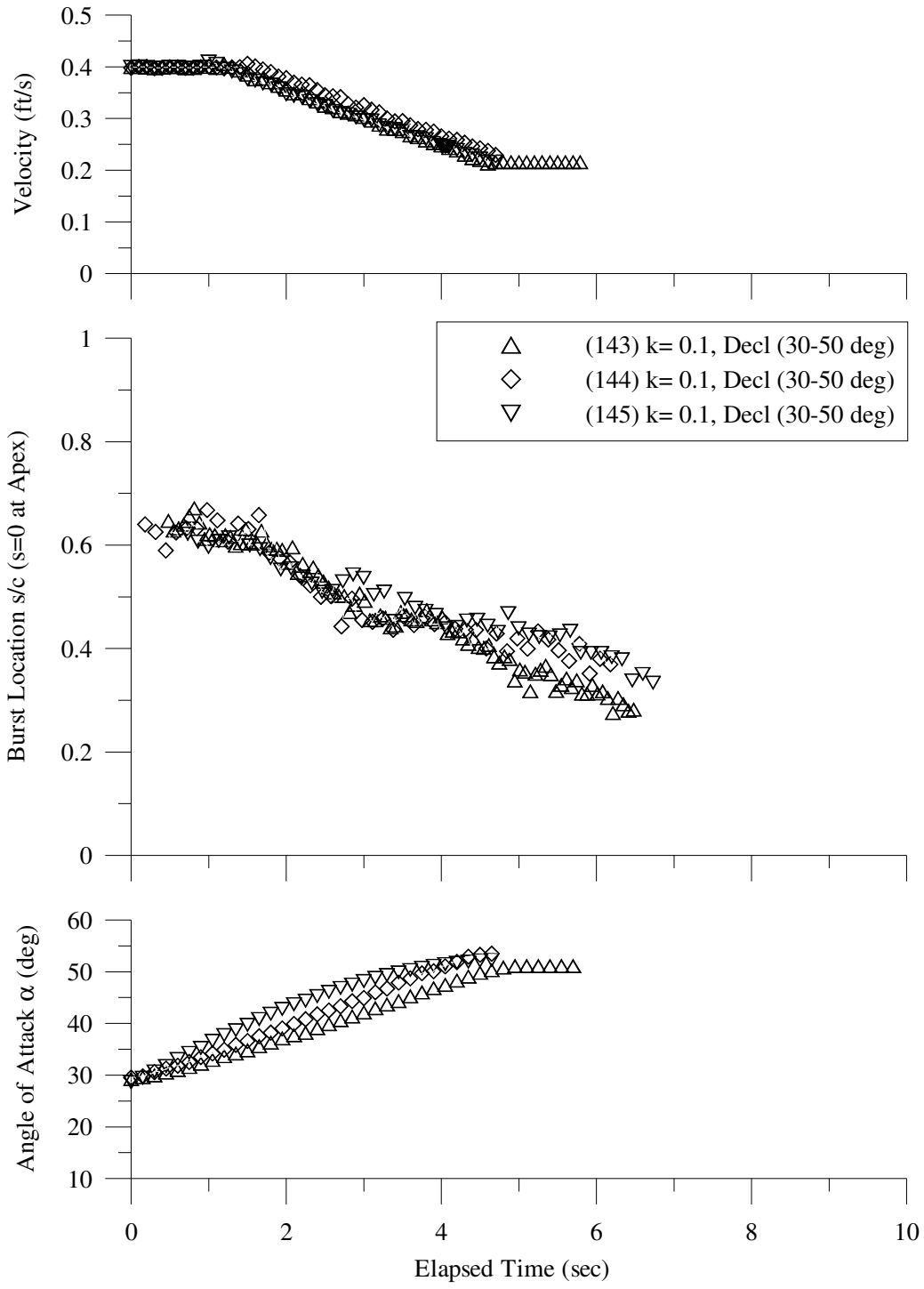

Figure 5.18. Burst Behavior, Pitch Up at κ=0.1,
Deceleration from 0.4 ft/s (30 deg) to 0.2 ft/s (50 deg).

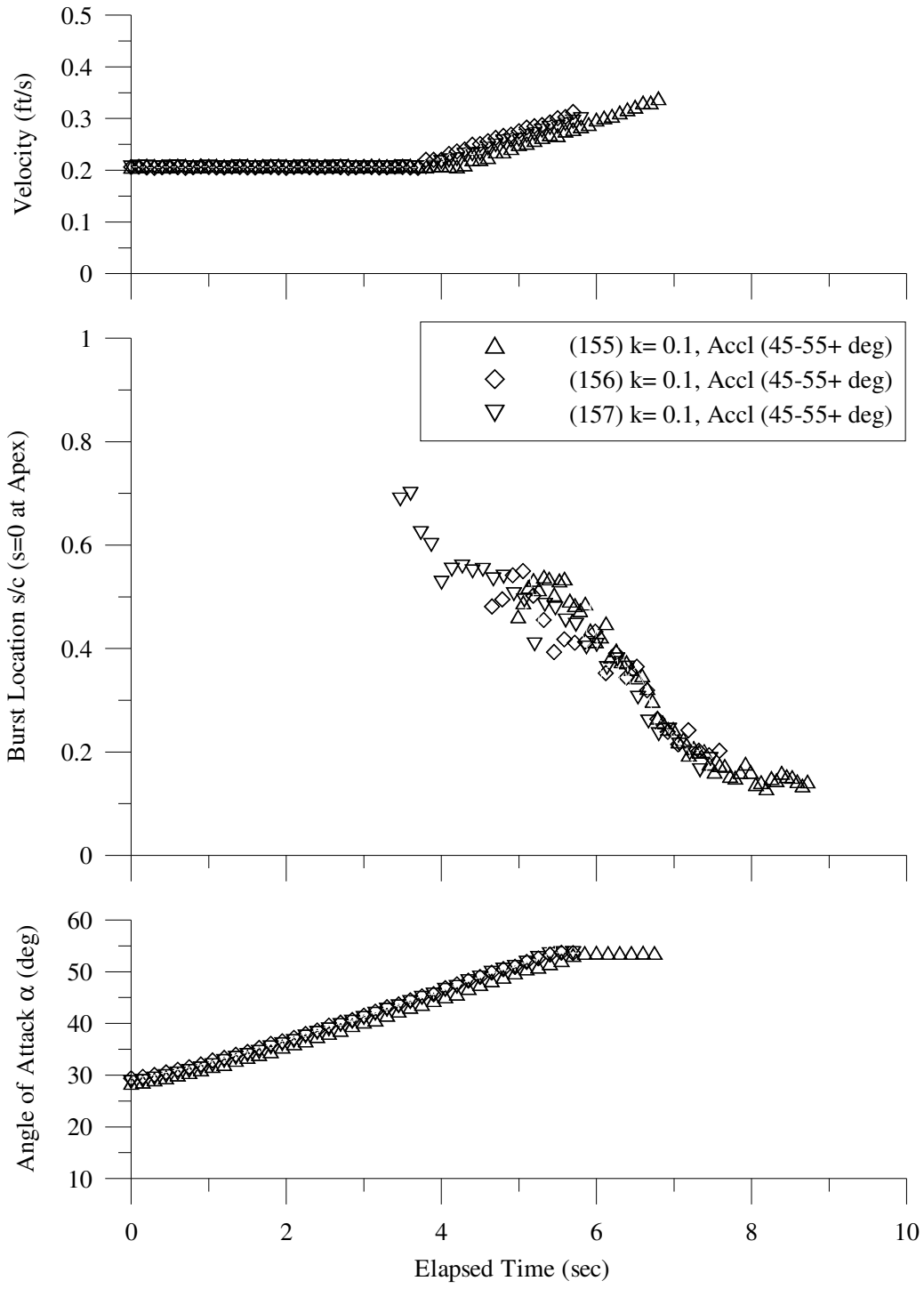

Figure 5.19. Burst Behavior, Pitch Up at κ=0.1,
Acceleration from 0.2 ft/s (45 deg) to 0.4 ft/s (beyond 55 deg).

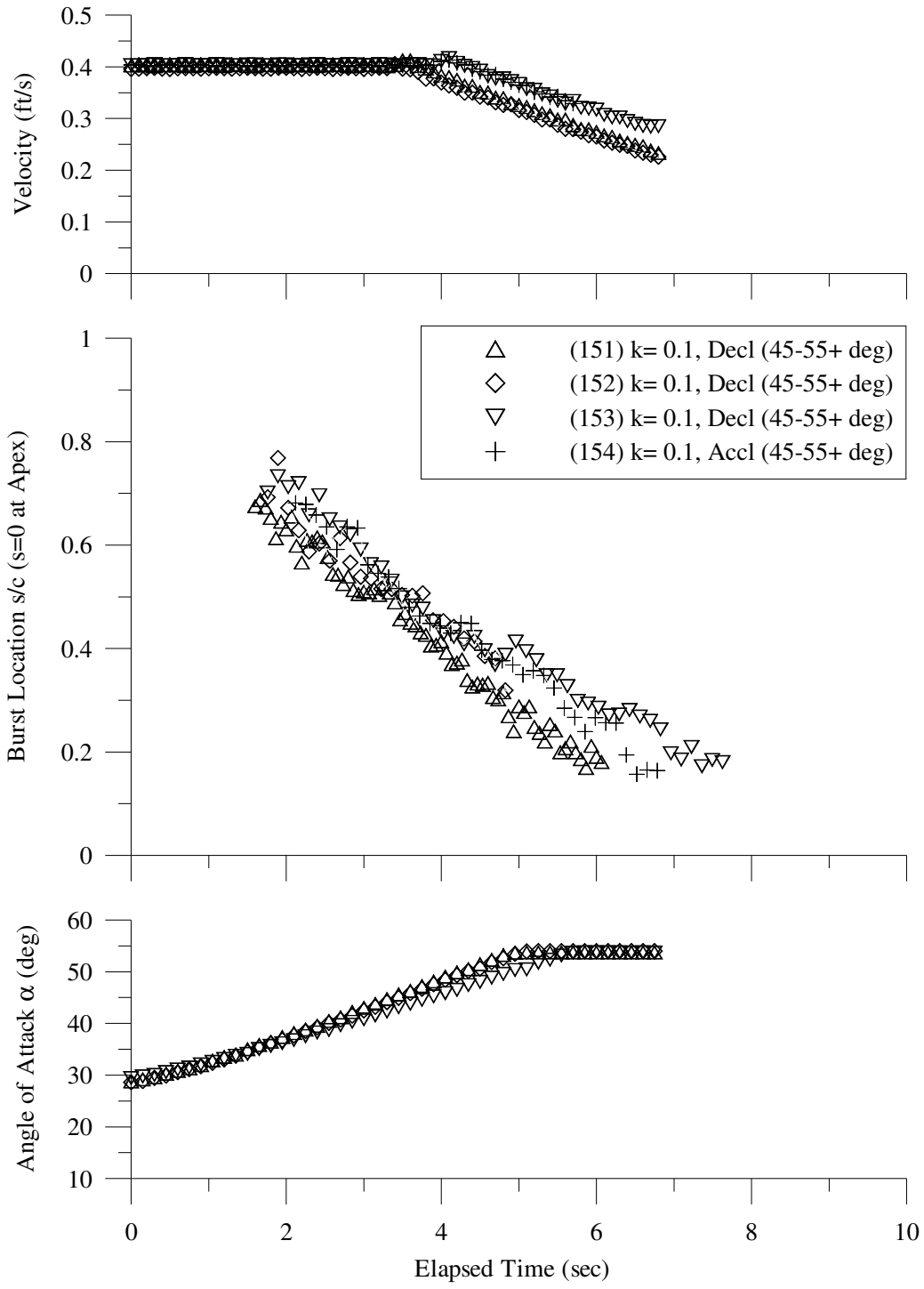

Figure 5.20. Burst Behavior, Pitch Up at κ=0.1,
Deceleration from 0.4 ft/s (45 deg) to 0.2 ft/s (beyond 55 deg).

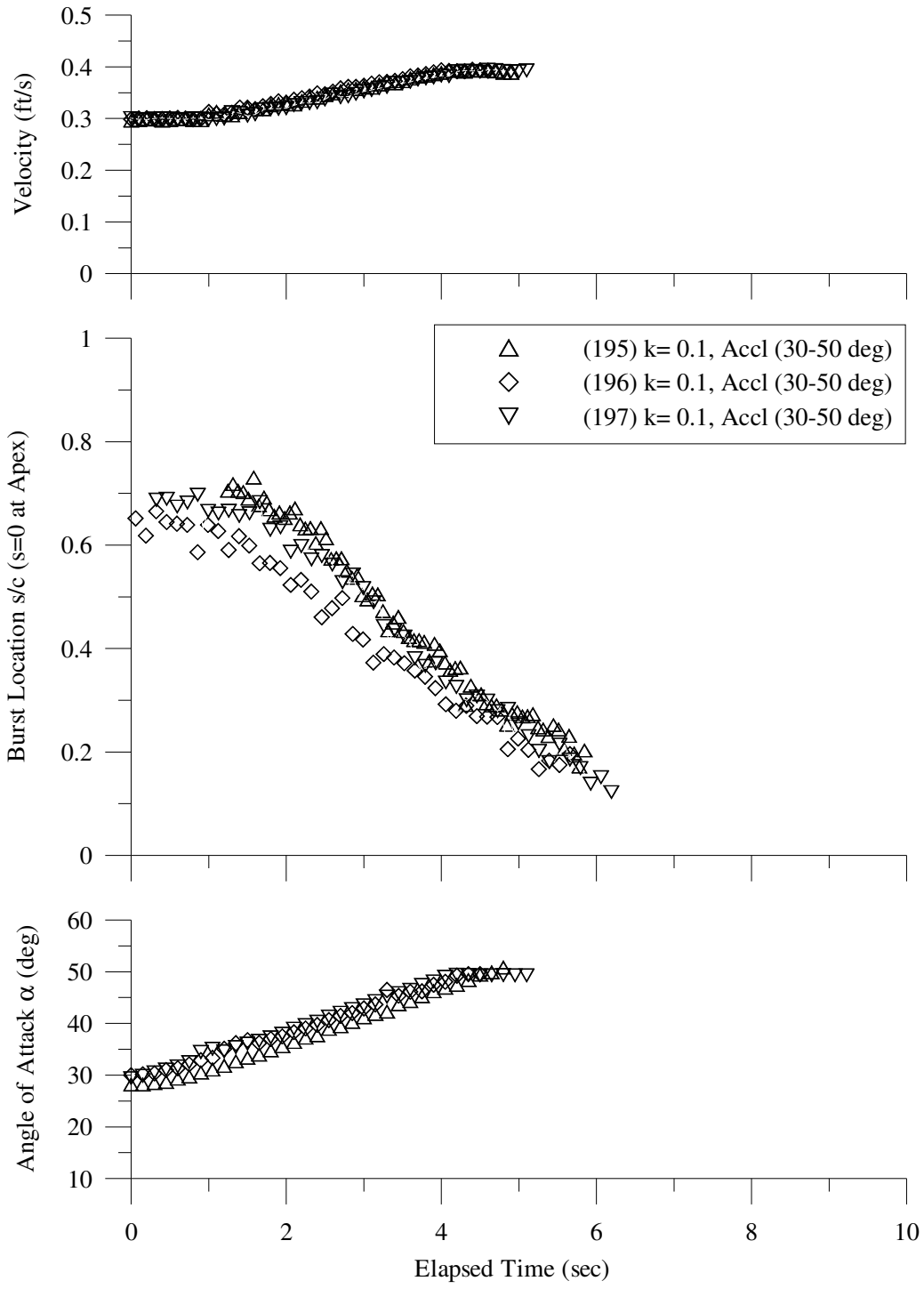

Figure 5.21. Burst Behavior, Pitch Up at κ=0.1,
Acceleration from 0.3 ft/s (30 deg) to 0.4 ft/s (50 deg).

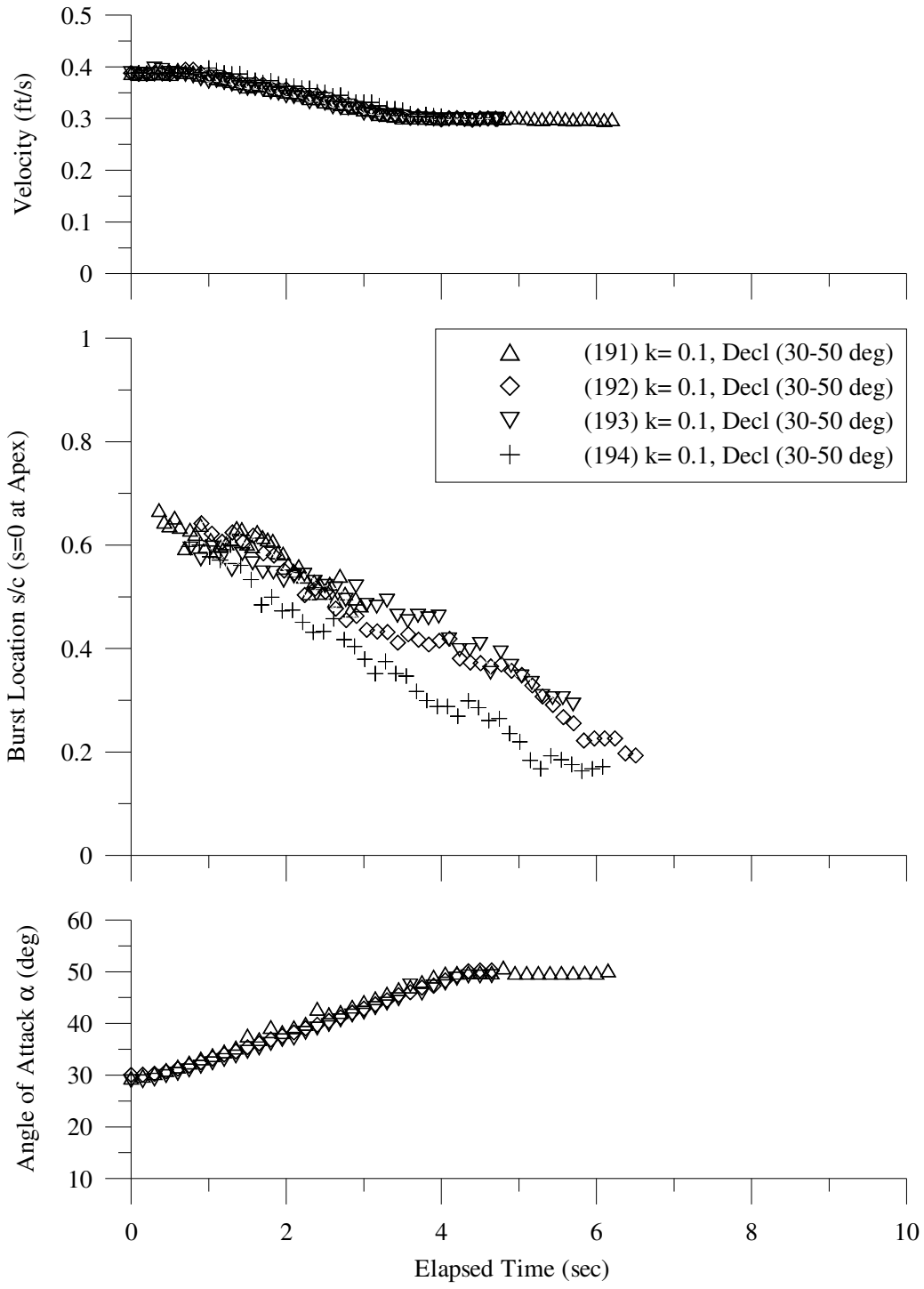

Figure 5.22. Burst Behavior, Pitch Up at κ=0.1,
Deceleration from 0.4 ft/s (30 deg) to 0.3 ft/s (50 deg).

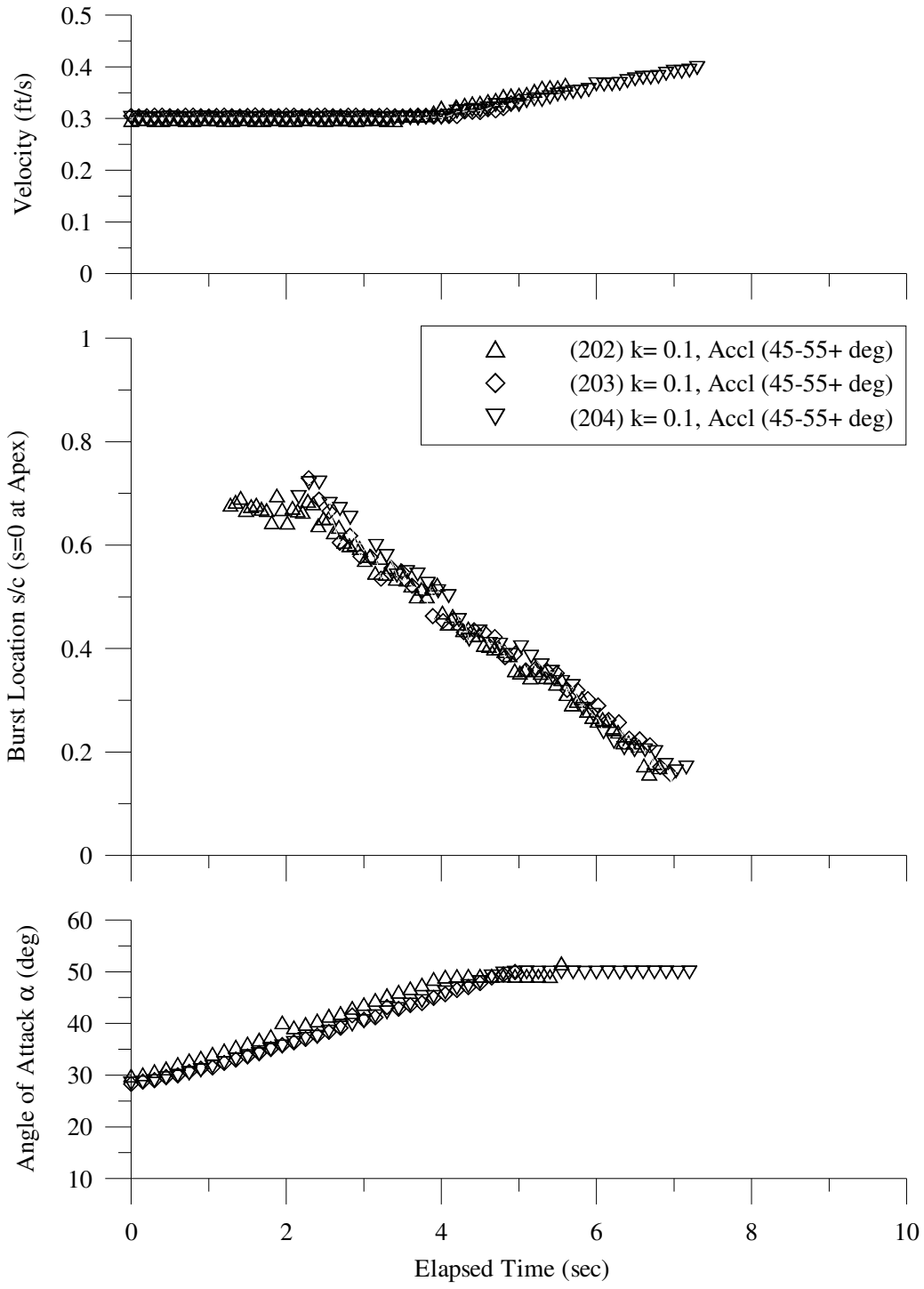

Figure 5.23. Burst Behavior, Pitch Up at κ=0.1,
Acceleration from 0.3 ft/s (45 deg) to 0.4 ft/s (beyond 55 deg).

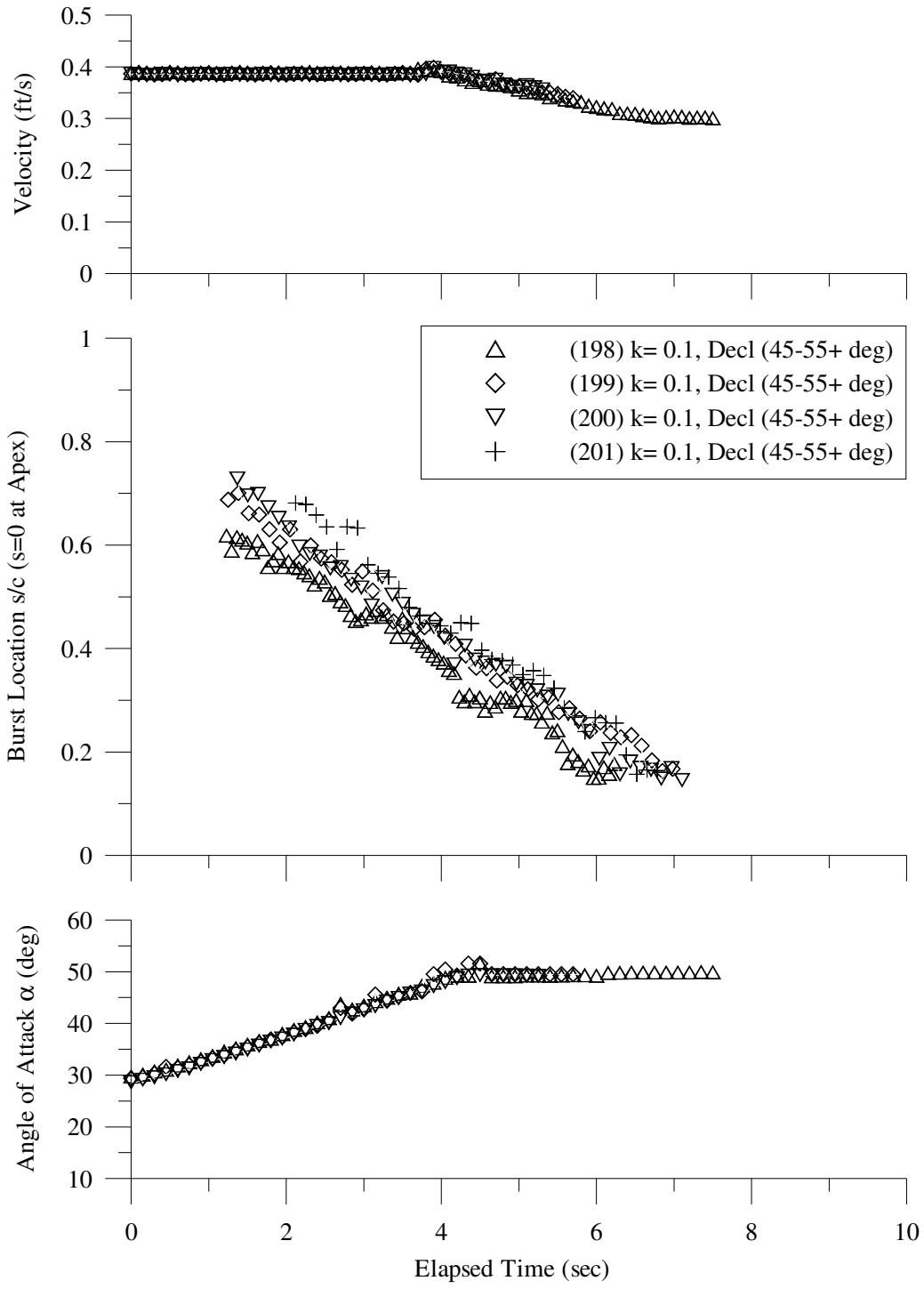

Figure 5.24. Burst Behavior, Pitch Up at κ=0.1,
Deceleration from 0.4 ft/s (45 deg) to 0.3 ft/s (beyond 55 deg).

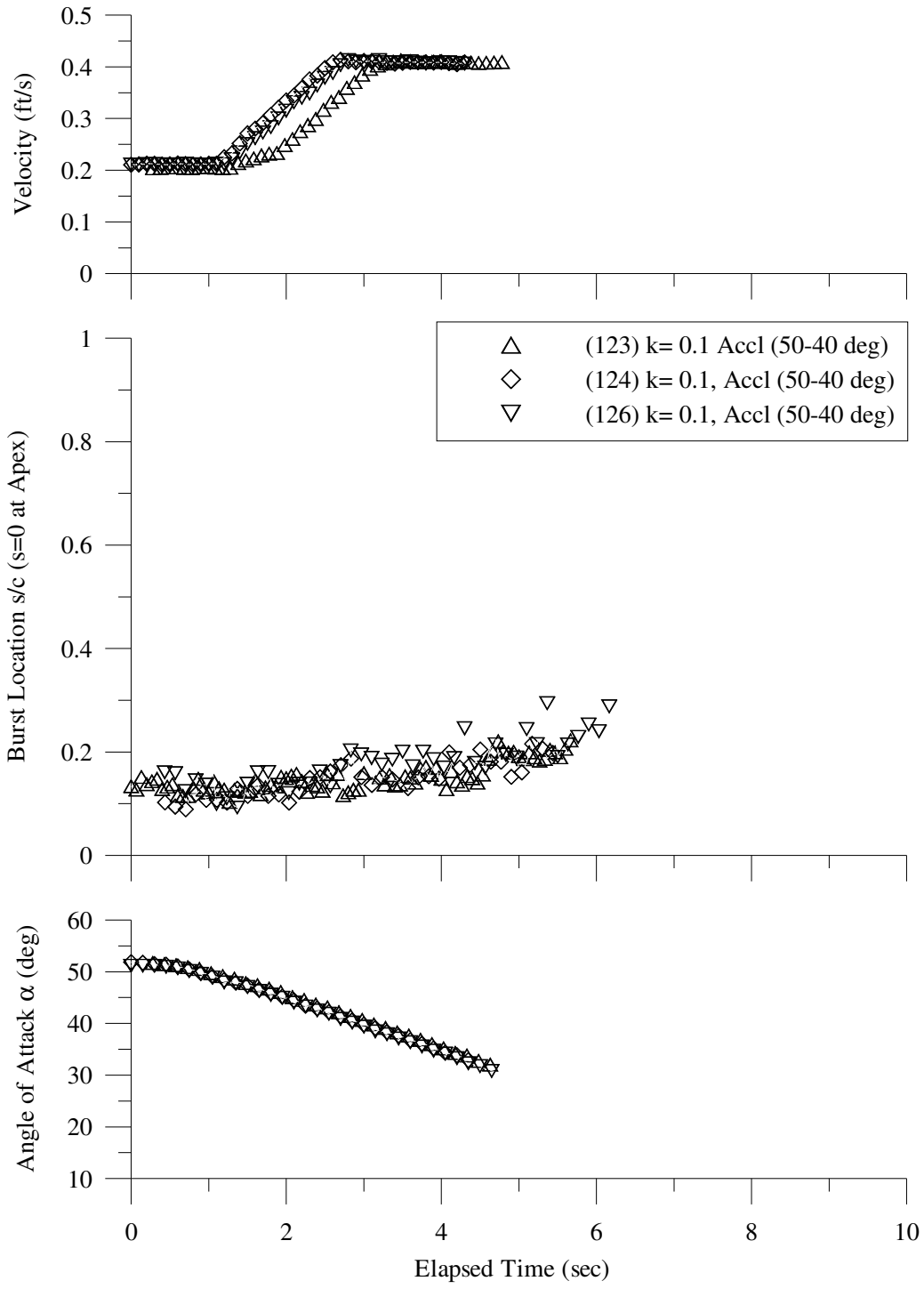

Figure 5.25. Burst Behavior, Pitch Down at κ=0.1, Acceleration from 0.2 ft/s (50 deg) to 0.4 ft/s (40 deg).

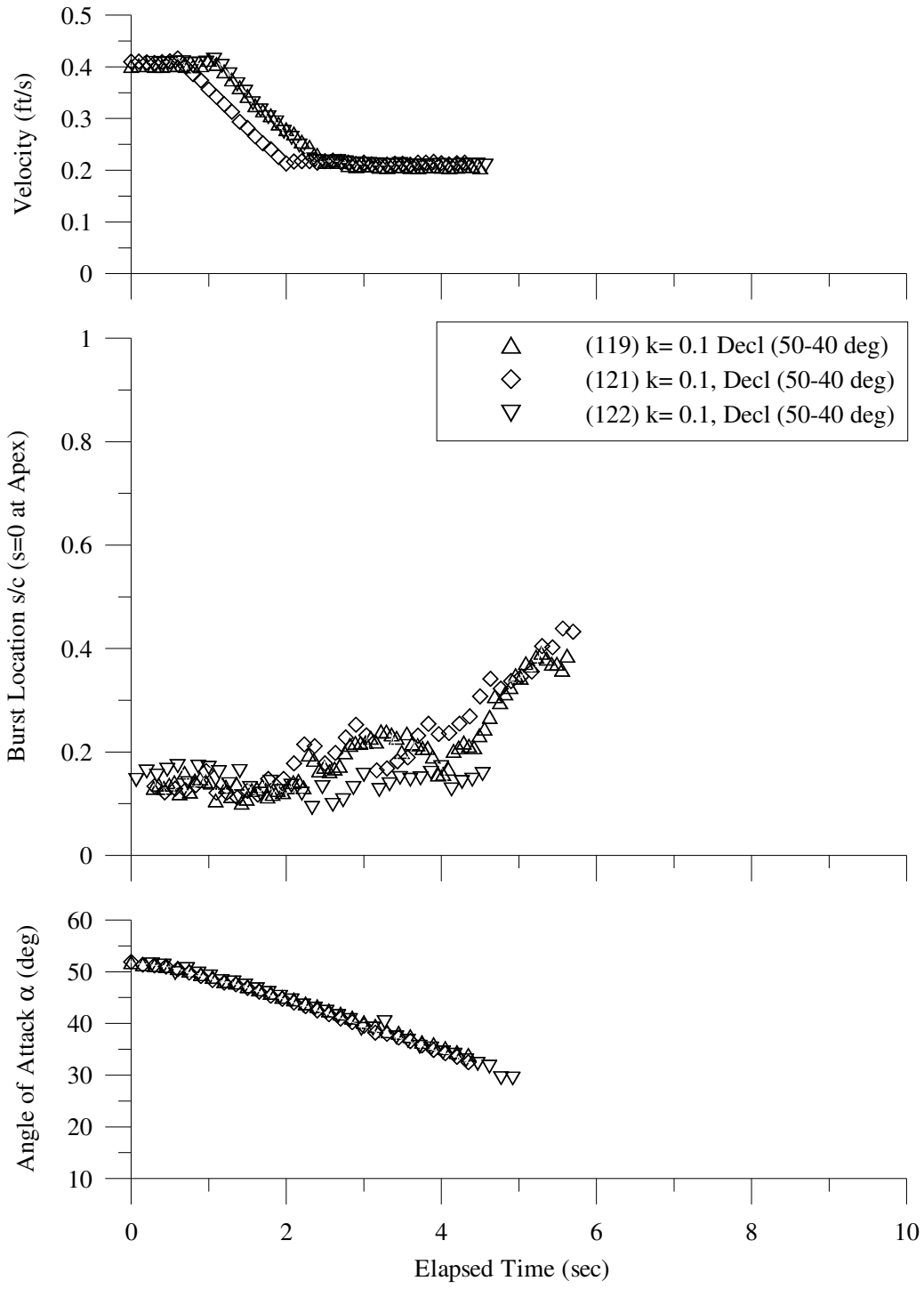

Figure 5.26. Burst Behavior, Pitch Down at κ=0.1, Deceleration from 0.4 ft/s (50 deg) to 0.2 ft/s (40 deg).

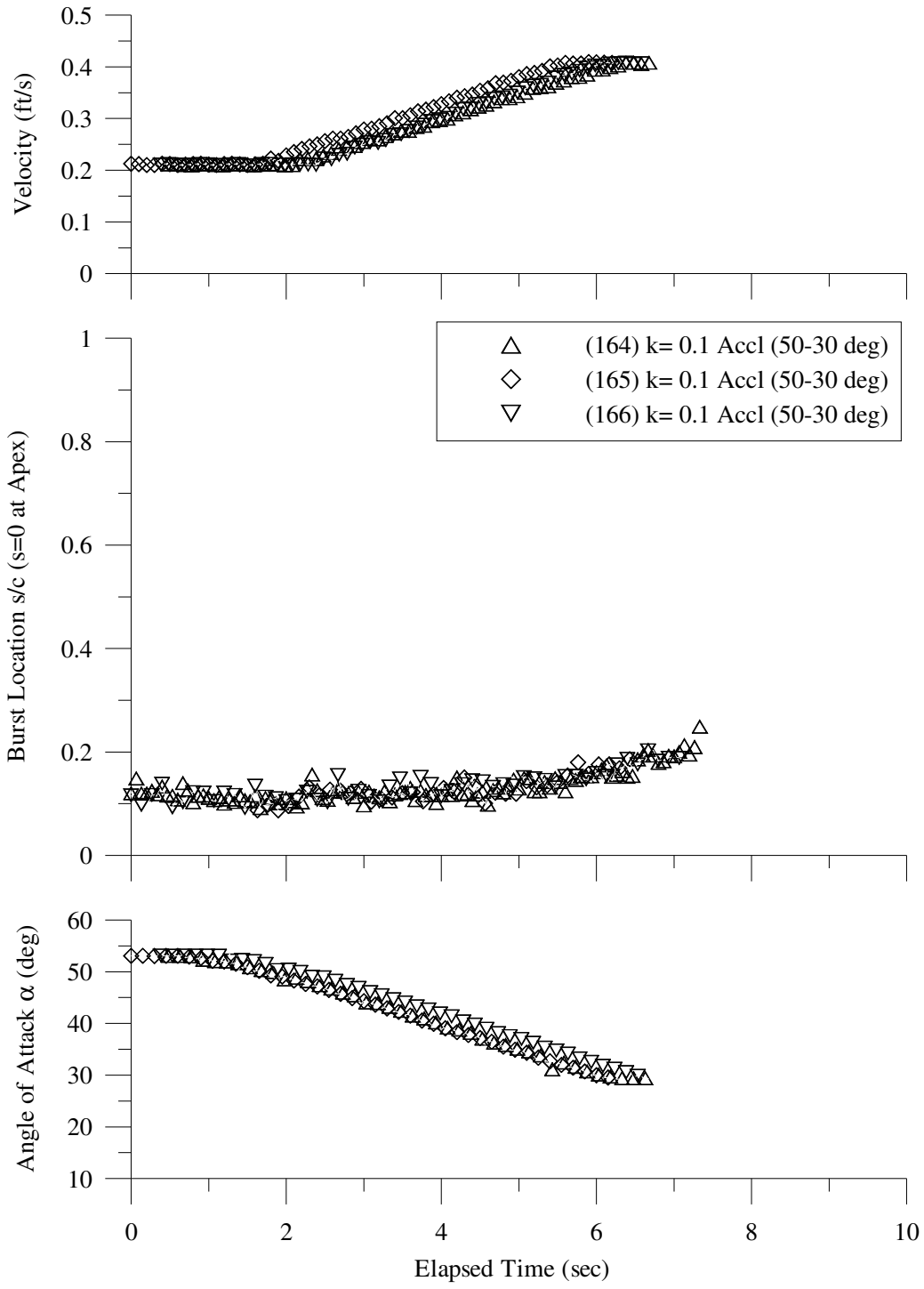

Figure 5.27. Burst Behavior, Pitch Down at κ=0.1, Acceleration from 0.2 ft/s (50 deg) to 0.4 ft/s (30 deg).

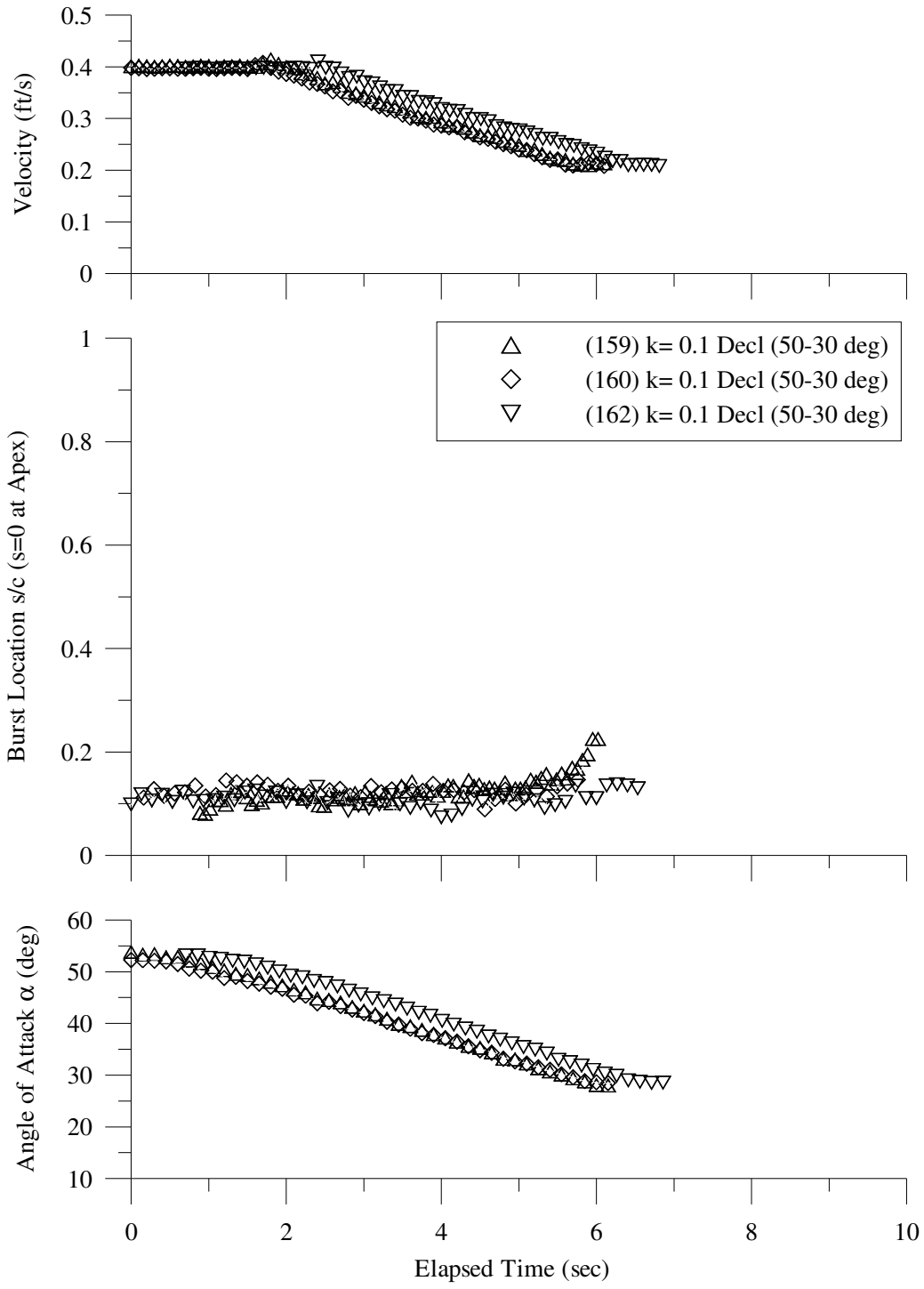

Figure 5.28. Burst Behavior, Pitch Down at κ=0.1, Deceleration from 0.4 ft/s (50 deg) to 0.2 ft/s (30 deg).

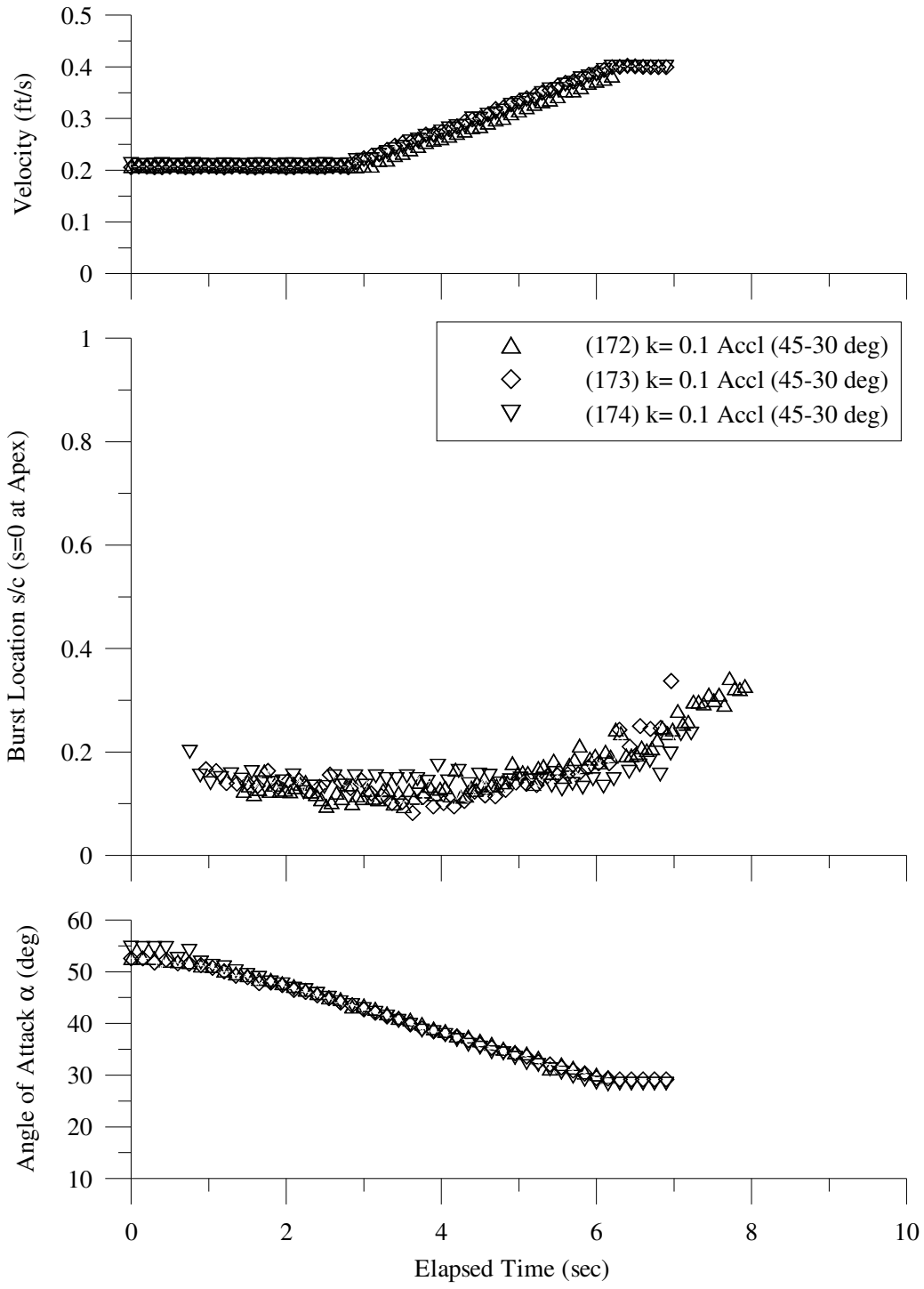

Figure 5.29. Burst Behavior, Pitch Down at κ=0.1,
Acceleration from 0.2 ft/s (45 deg) to 0.4 ft/s (below 30 deg).

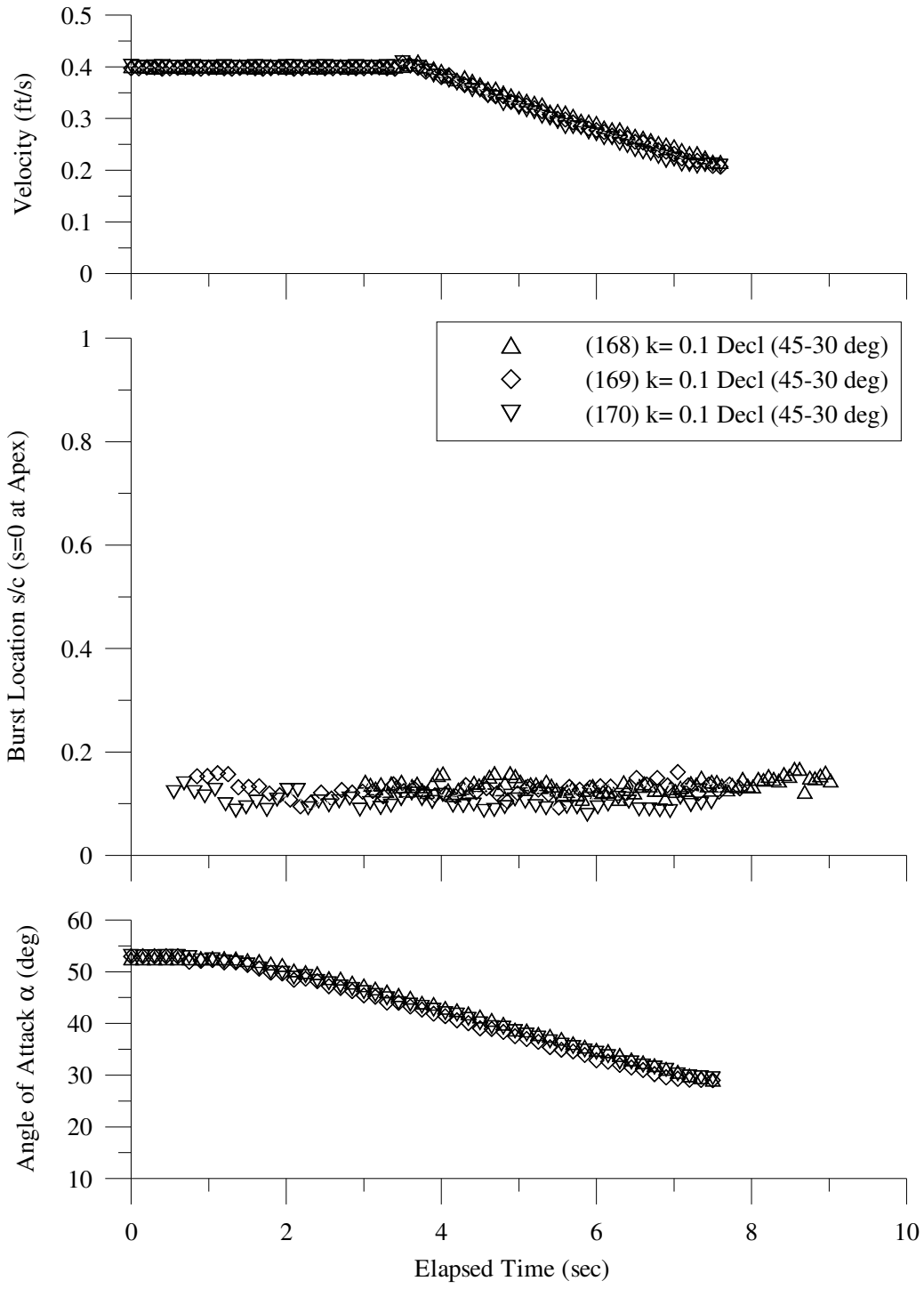

Figure 5.30. Burst Behavior, Pitch Down at κ=0.1,
Deceleration from 0.4 ft/s (45 deg) to 0.2 ft/s (below 30 deg).

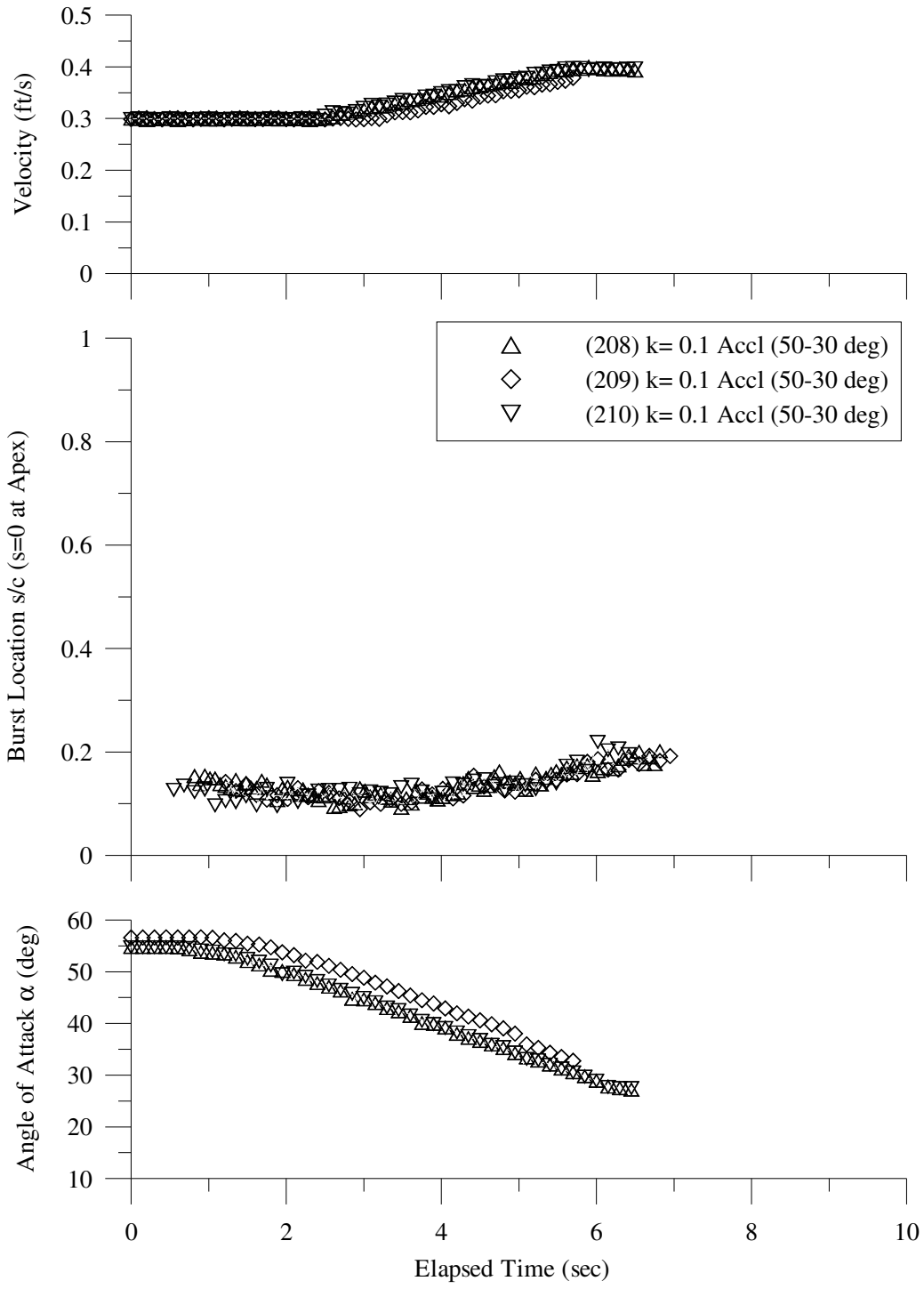

Figure 5.31. Burst Behavior, Pitch Down at κ=0.1,
Acceleration from 0.3 ft/s (50 deg) to 0.4 ft/s (30 deg).

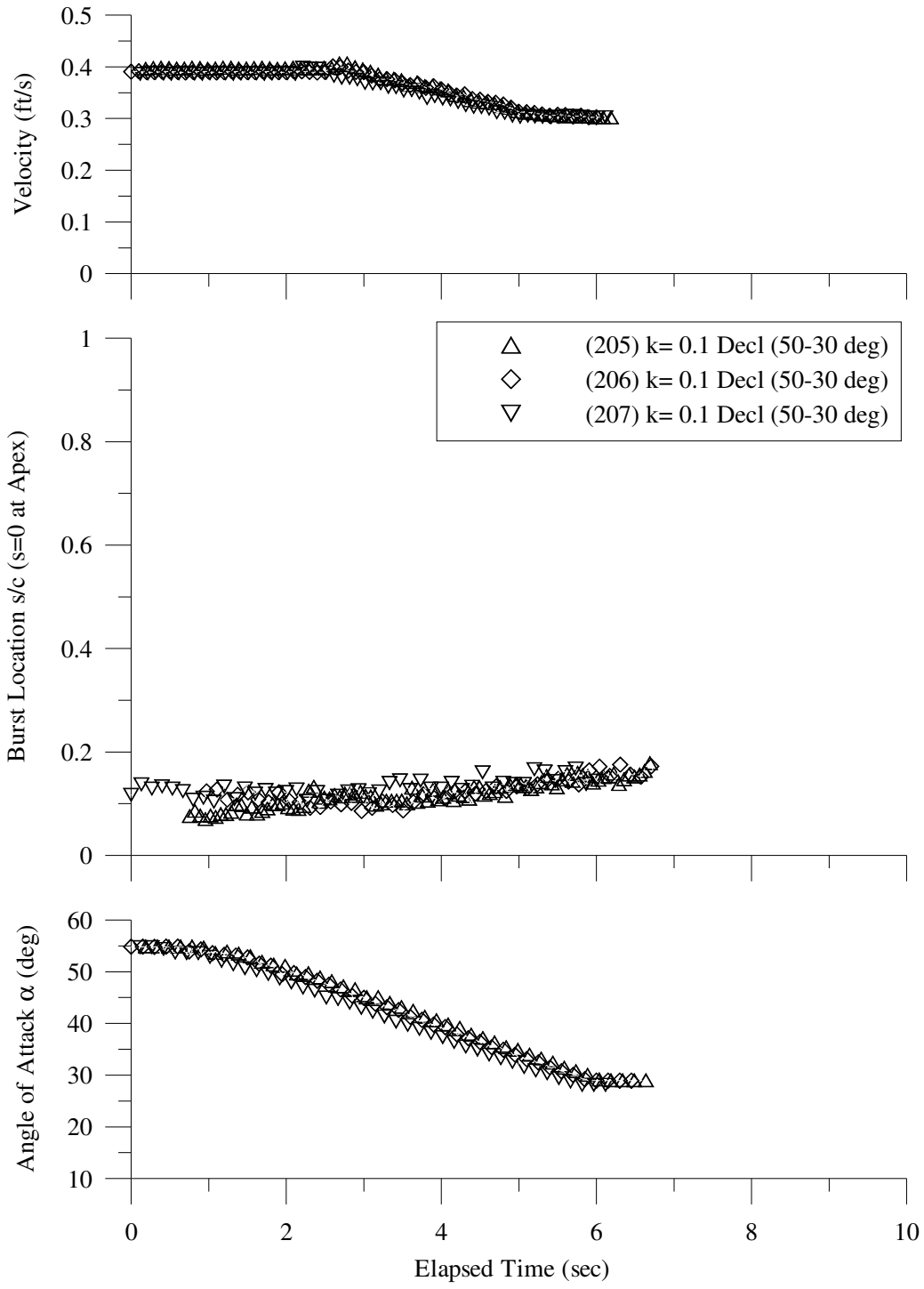

Figure 5.32. Burst Behavior, Pitch Down at κ=0.1, Deceleration from 0.4 ft/s (50 deg) to 0.3 ft/s (30 deg).

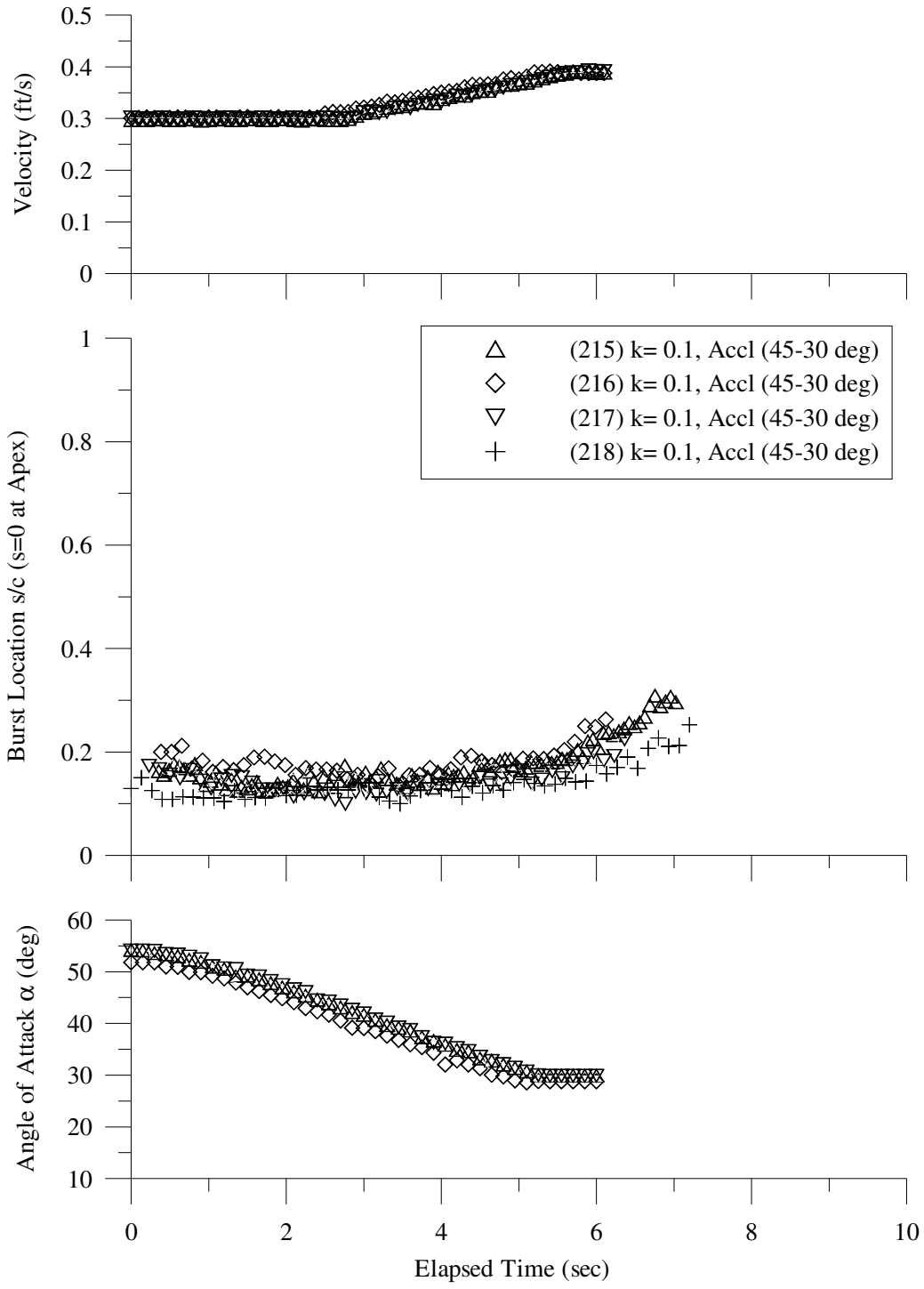

Figure 5.33. Burst Behavior, Pitch Down at κ=0.1,
Acceleration from 0.3 ft/s (45 deg) to 0.4 ft/s (below 30 deg).

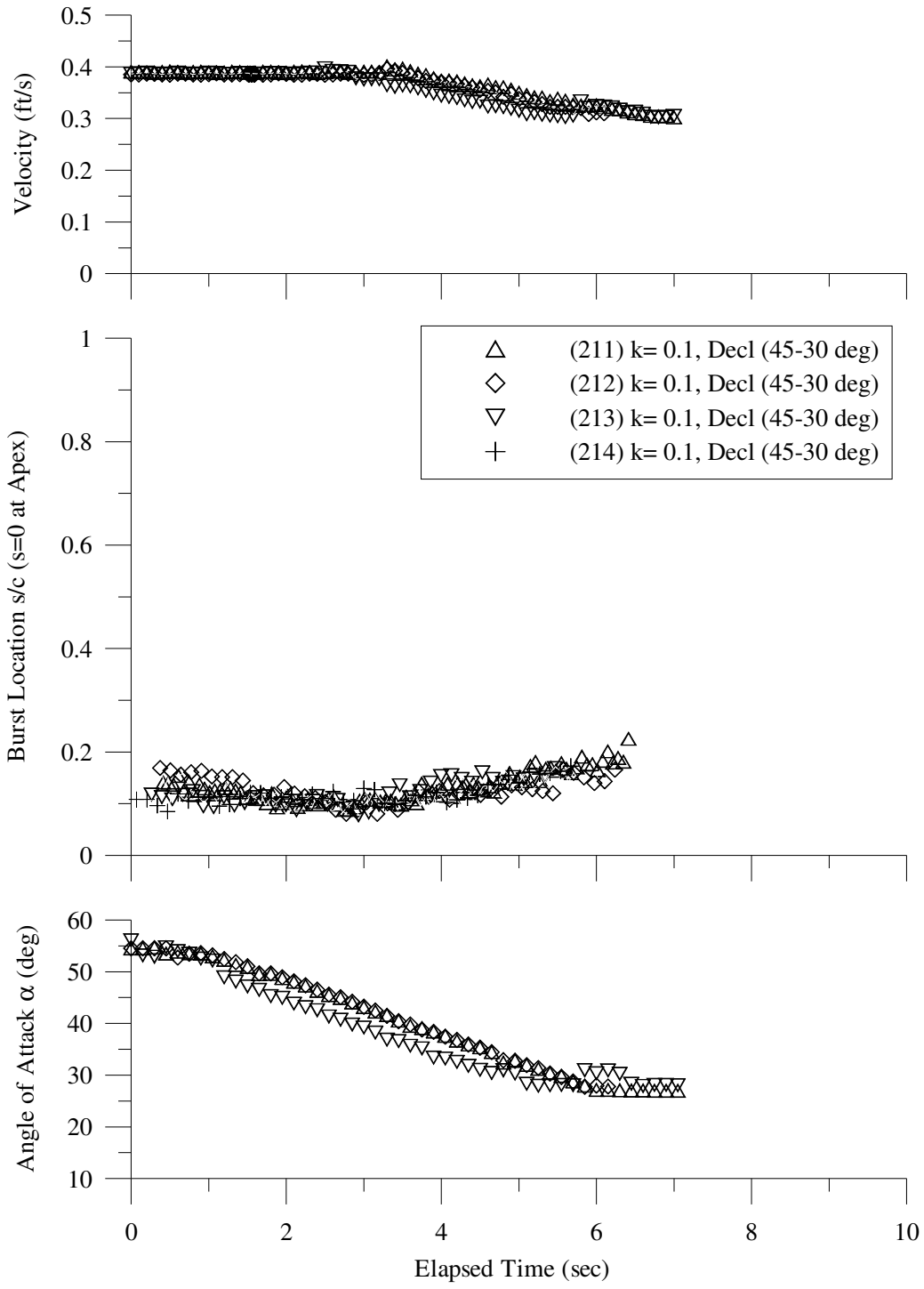

Figure 5.34. Burst Behavior, Pitch Down at κ=0.1,
Deceleration from 0.4 ft/s (45 deg) to 0.3 ft/s (below 30 deg).

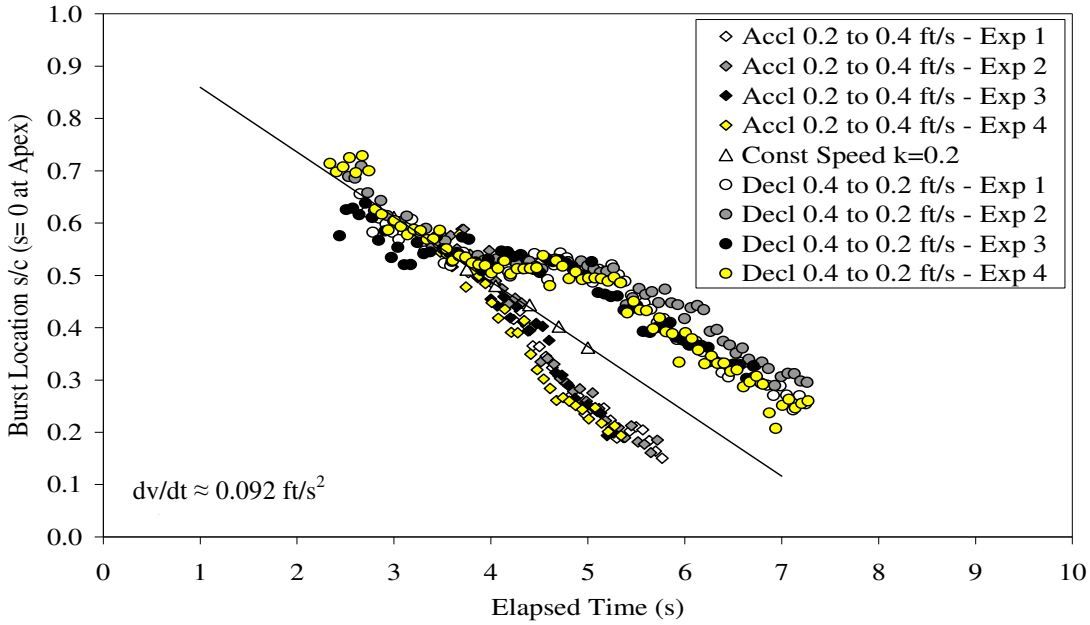

Figure 5.35. Burst Comparison, Pitch Up at κ=0.2,
Acceleration / Deceleration from 0.2 ft/s (30 deg) to 0.4 ft/s (50 deg).

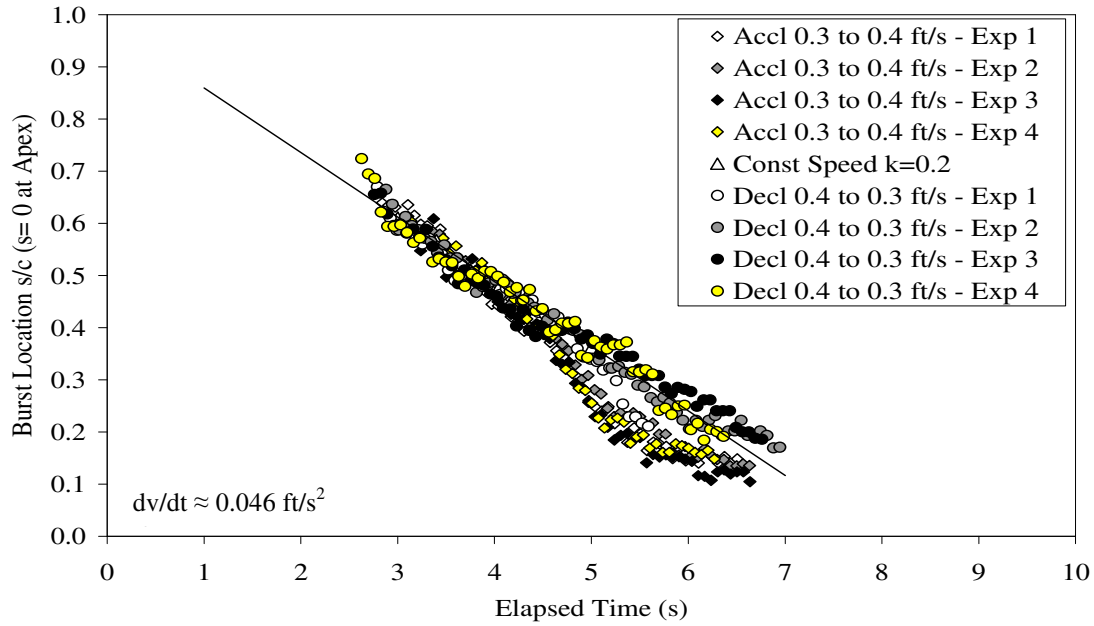

Figure 5.36. Burst Comparison, Pitch Up at κ=0.2,
Acceleration / Deceleration from 0.3 ft/s (30 deg) to 0.4 ft/s (50 deg).

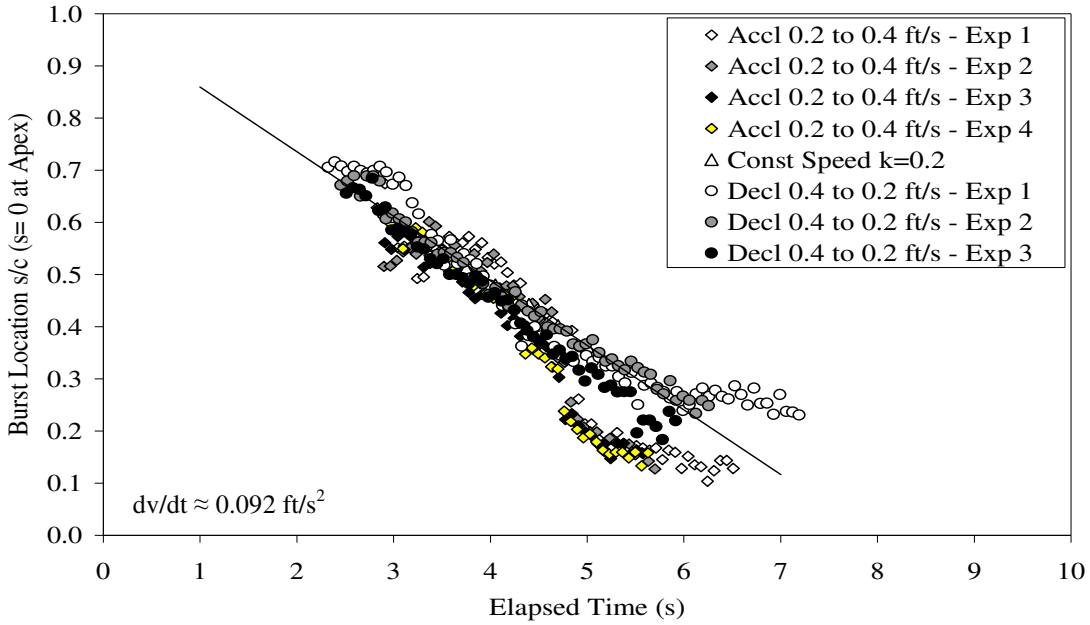

Figure 5.37. Burst Comparison, Pitch Up at κ=0.2,
Acceleration / Deceleration from 0.2 ft/s (45 deg) to 0.4 ft/s (beyond 55 deg).

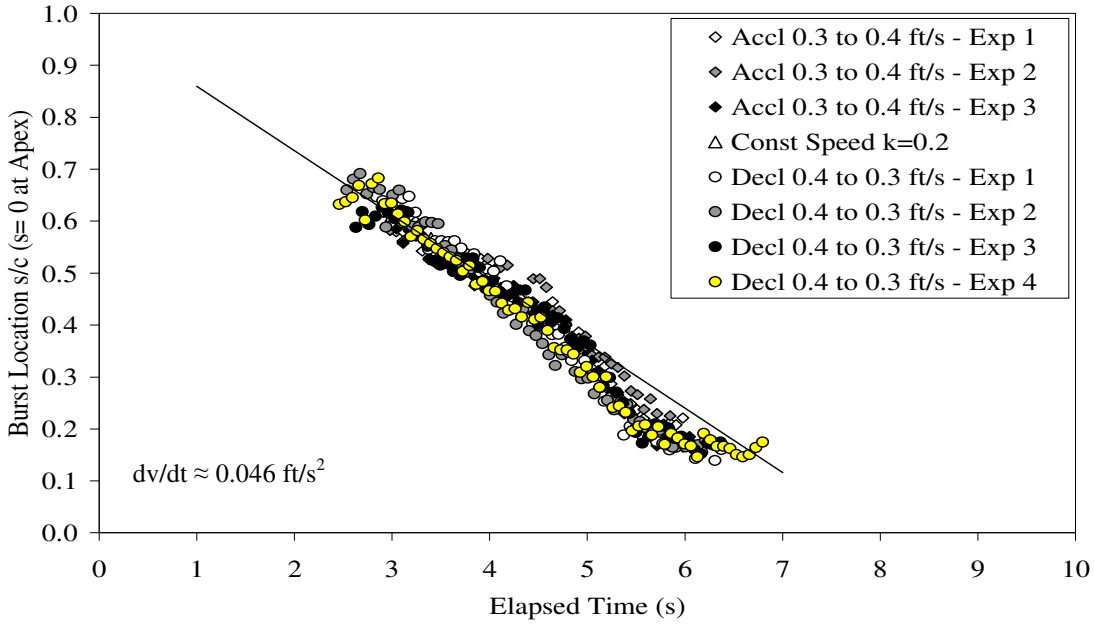

Figure 5.38. Burst Comparison, Pitch Up at κ=0.2,
Acceleration / Deceleration from 0.3 ft/s (45 deg) to 0.4 ft/s (beyond 55 deg).

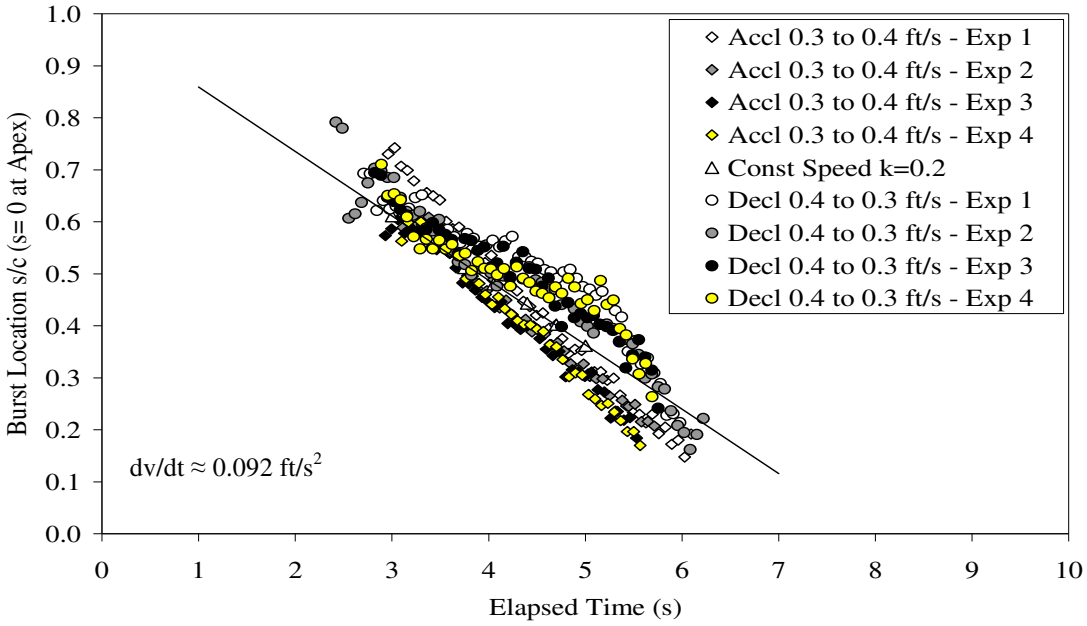

Figure 5.39. Burst Comparison, Pitch Up at κ=0.2,
Acceleration / Deceleration from 0.3 ft/s (30 deg) to 0.4 ft/s (40 deg).

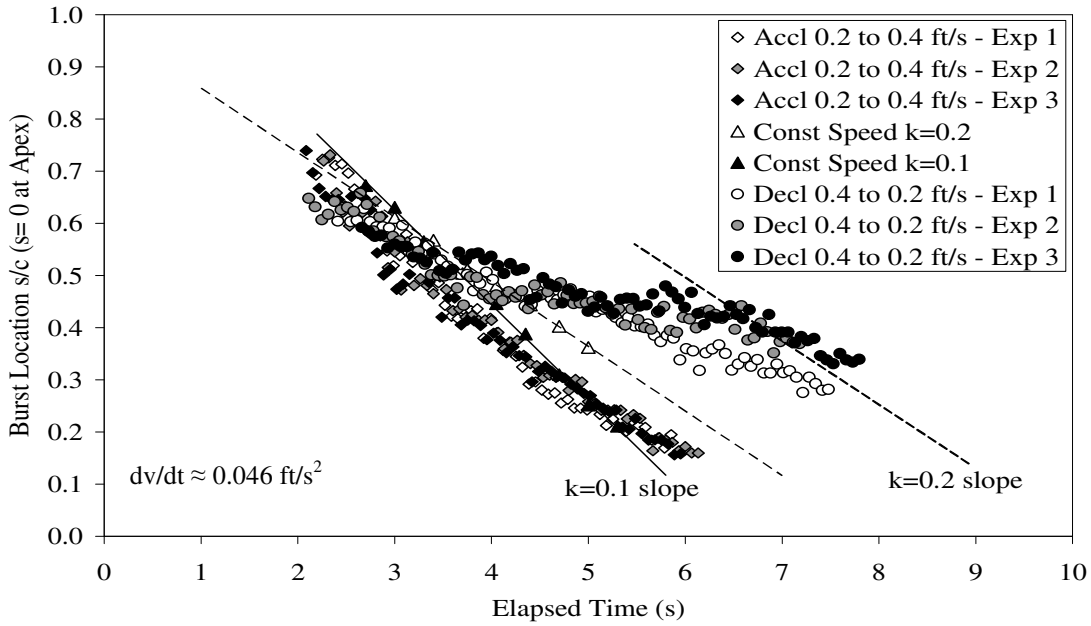

Figure 5.40. Burst Comparison, Pitch Up at κ=0.1,
Acceleration / Deceleration from 0.2 ft/s (30 deg) to 0.4 ft/s (50 deg).

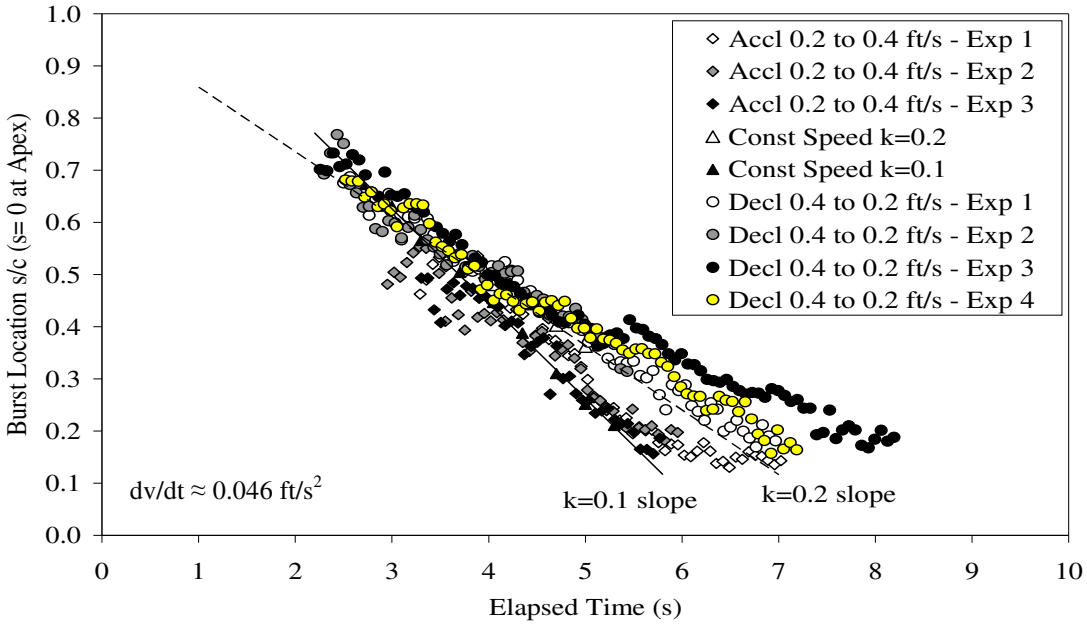

Figure 5.41. Burst Comparison, Pitch Up at κ=0.1,
Acceleration / Deceleration from 0.2 ft/s (45 deg) to 0.4 ft/s (beyond 55 deg).

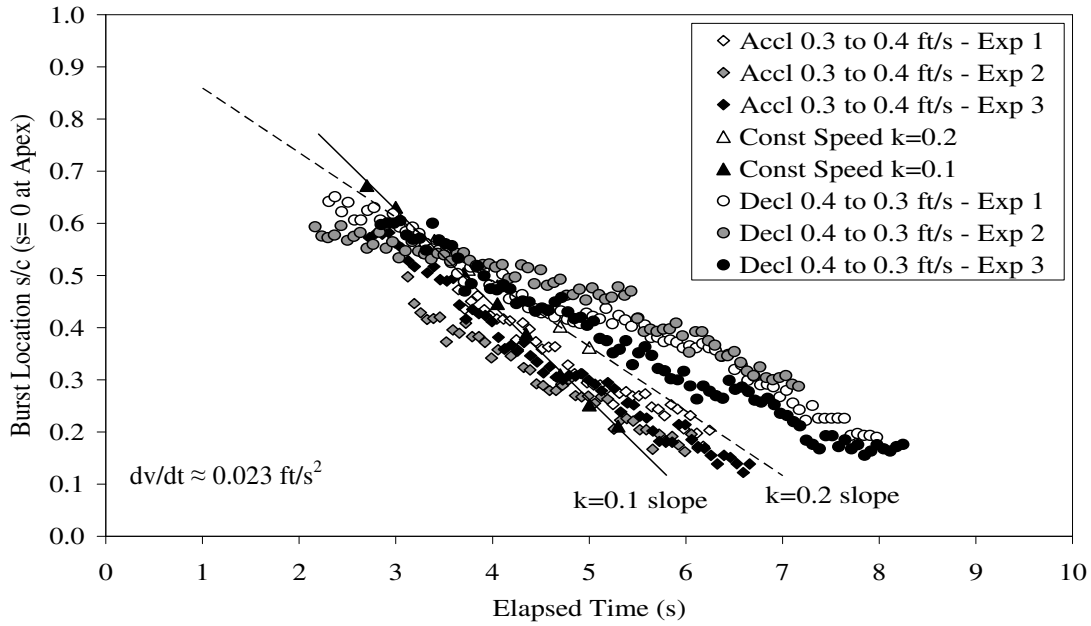

Figure 5.42. Burst Comparison, Pitch Up at κ=0.1,
Acceleration/Deceleration from 0.3 ft/s (30 deg) to 0.4 ft/s (50 deg).

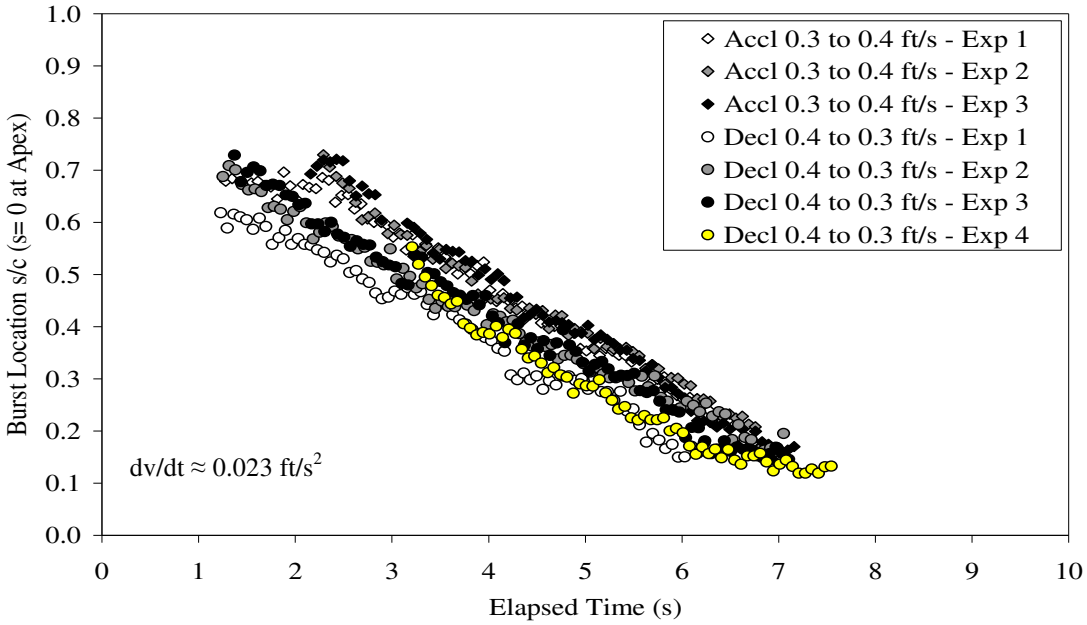

Figure 5.43. Burst Comparison, Pitch Up at κ=0.1,
Acceleration/Deceleration from 0.3 ft/s (45 deg) to 0.4 ft/s (beyond 55 deg).

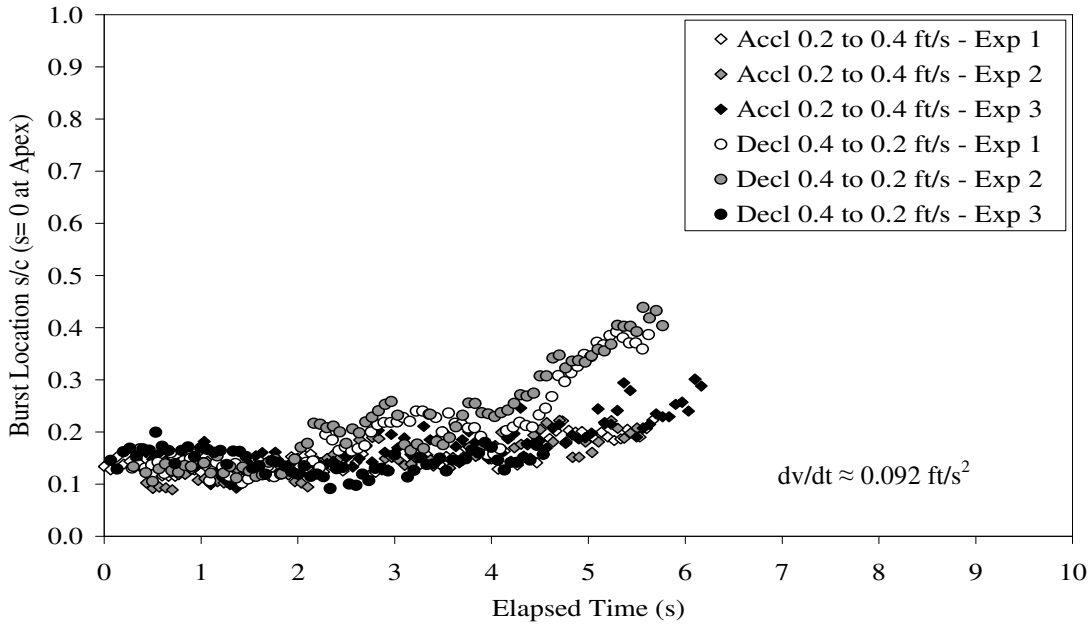

Figure 5.44. Burst Comparison, Pitch Down at κ=0.1,
Acceleration/Deceleration from 0.2 ft/s (50 deg) to 0.4 ft/s (40 deg).

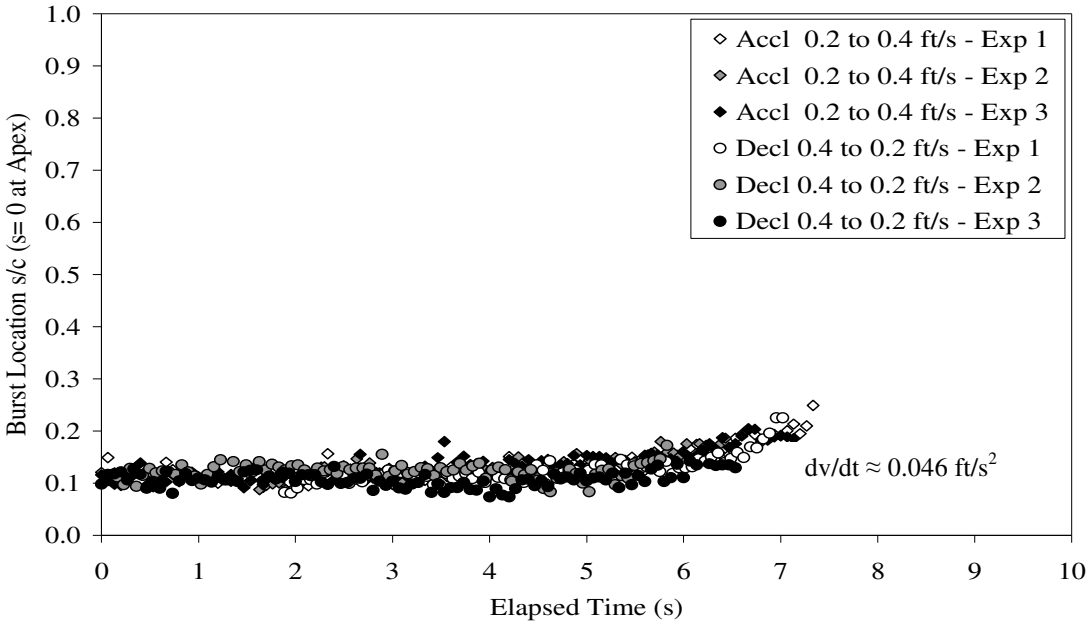

Figure 5.45. Burst Comparison, Pitch Down at κ=0.1, Acceleration/Deceleration from 0.2 ft/s (50 deg) to 0.4 ft/s (30 deg).

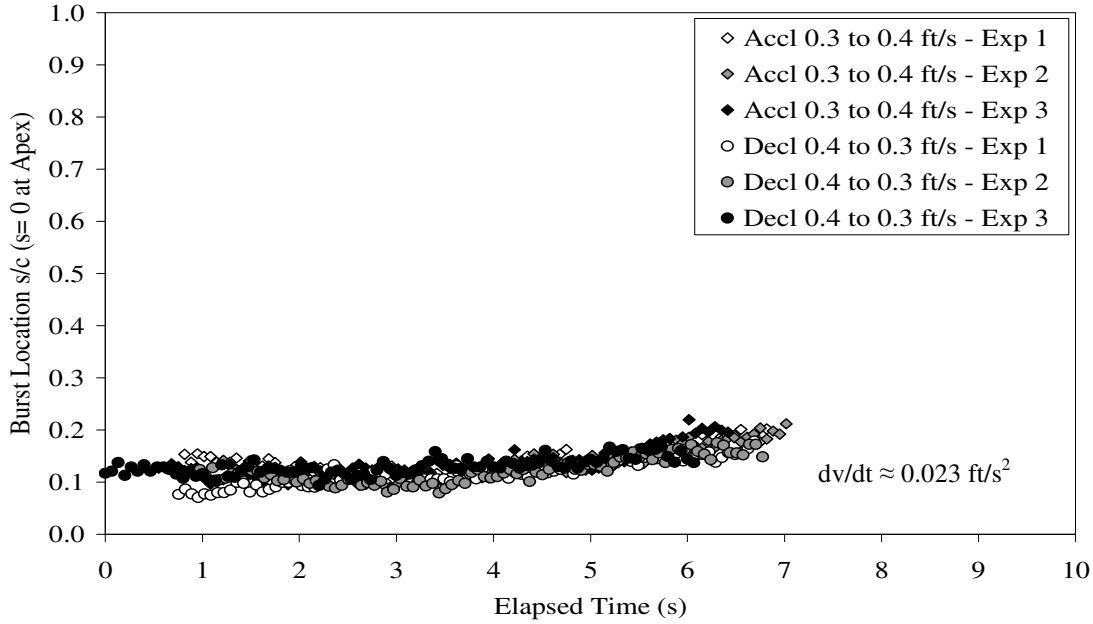

Figure 5.46. Burst Comparison, Pitch Down at κ=0.1, Acceleration/Deceleration from 0.3 ft/s (50 deg) to 0.4 ft/s (30 deg).

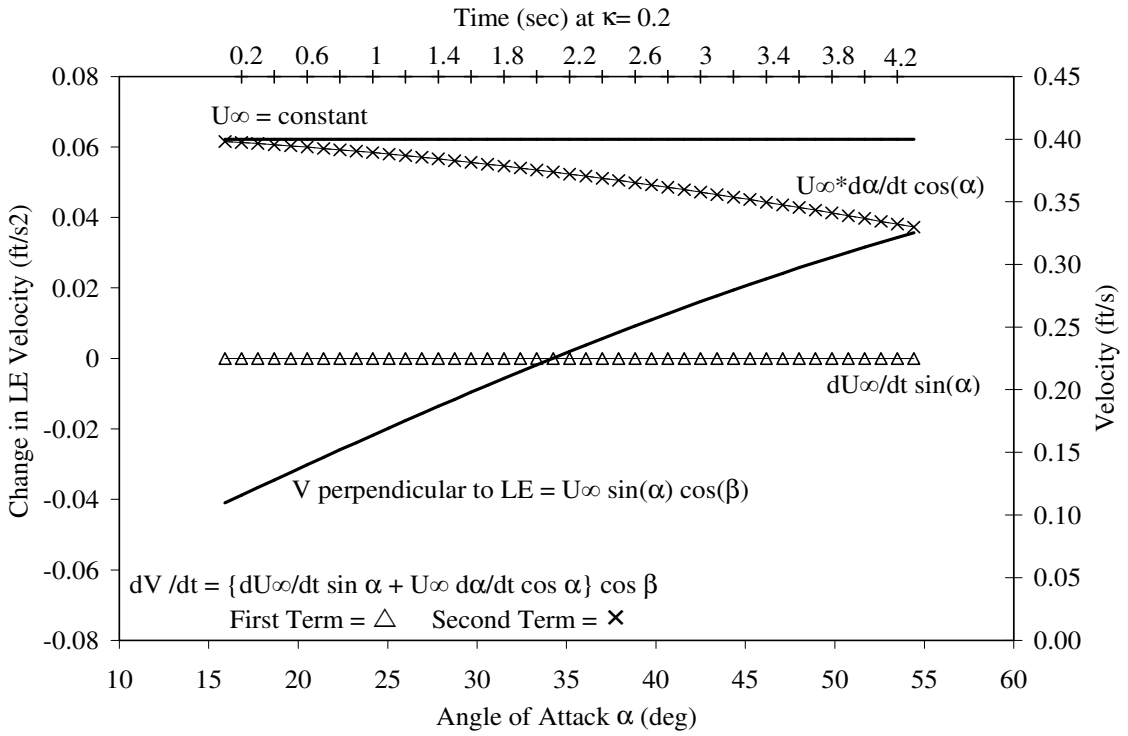

Figure 5.47. Example of Perpendicular Velocity at Leading Edge (Equation (5.2)), Constant Pitch Up Rate, $dU_\infty/dt = 0$ (Ideal Representation of Myose et al [49]).

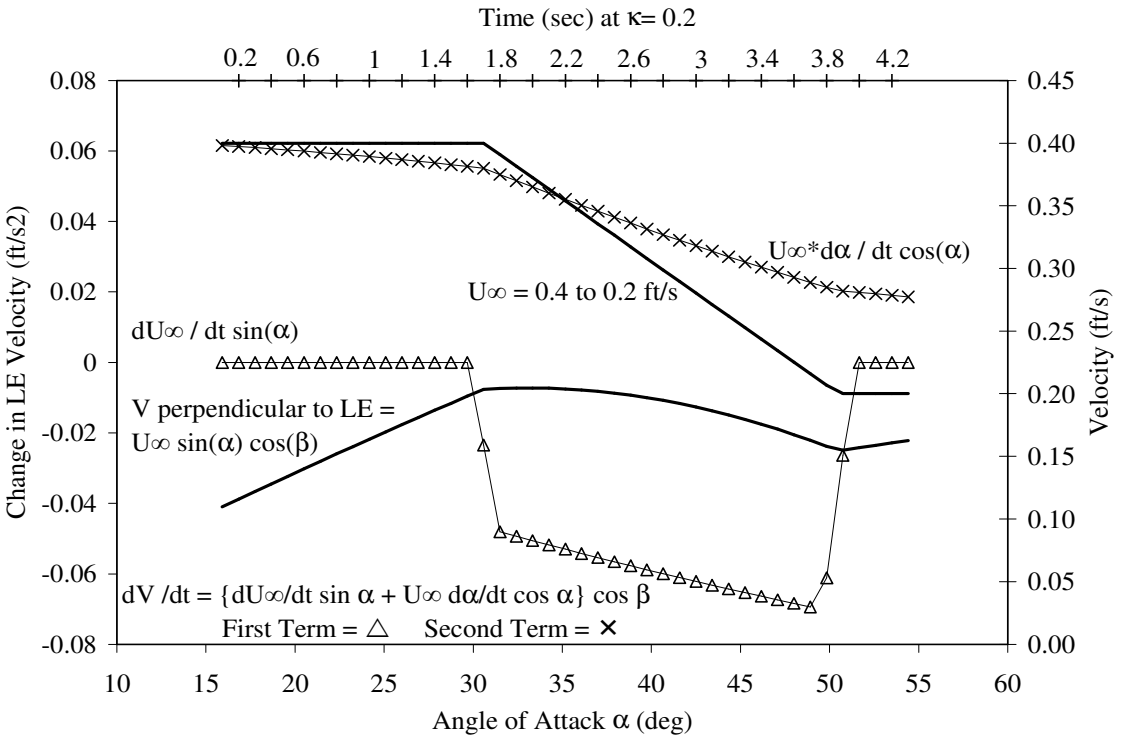

Figure 5.48. Example of Perpendicular Velocity at Leading Edge, Constant Pitch Up Rate and Deceleration (Ideal Representation of Figure 5.35).

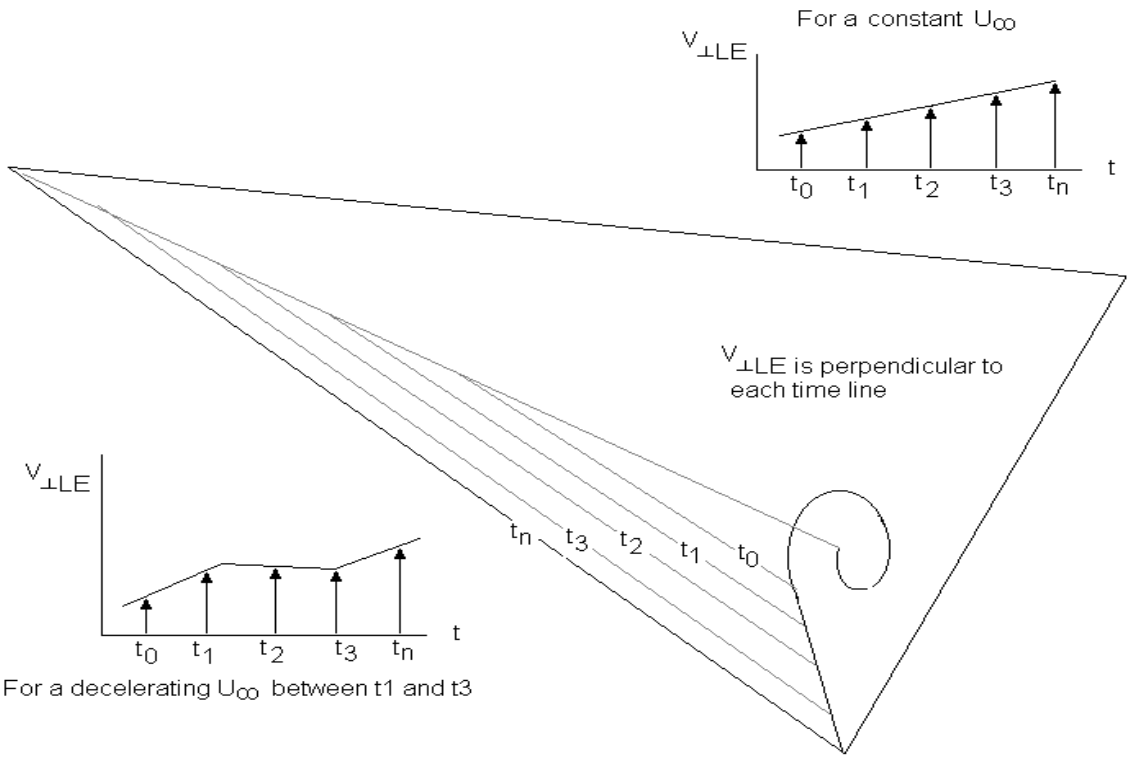

Figure 5.49. Time Progression of Perpendicular Velocity at Leading Edge into the Vortex Core.

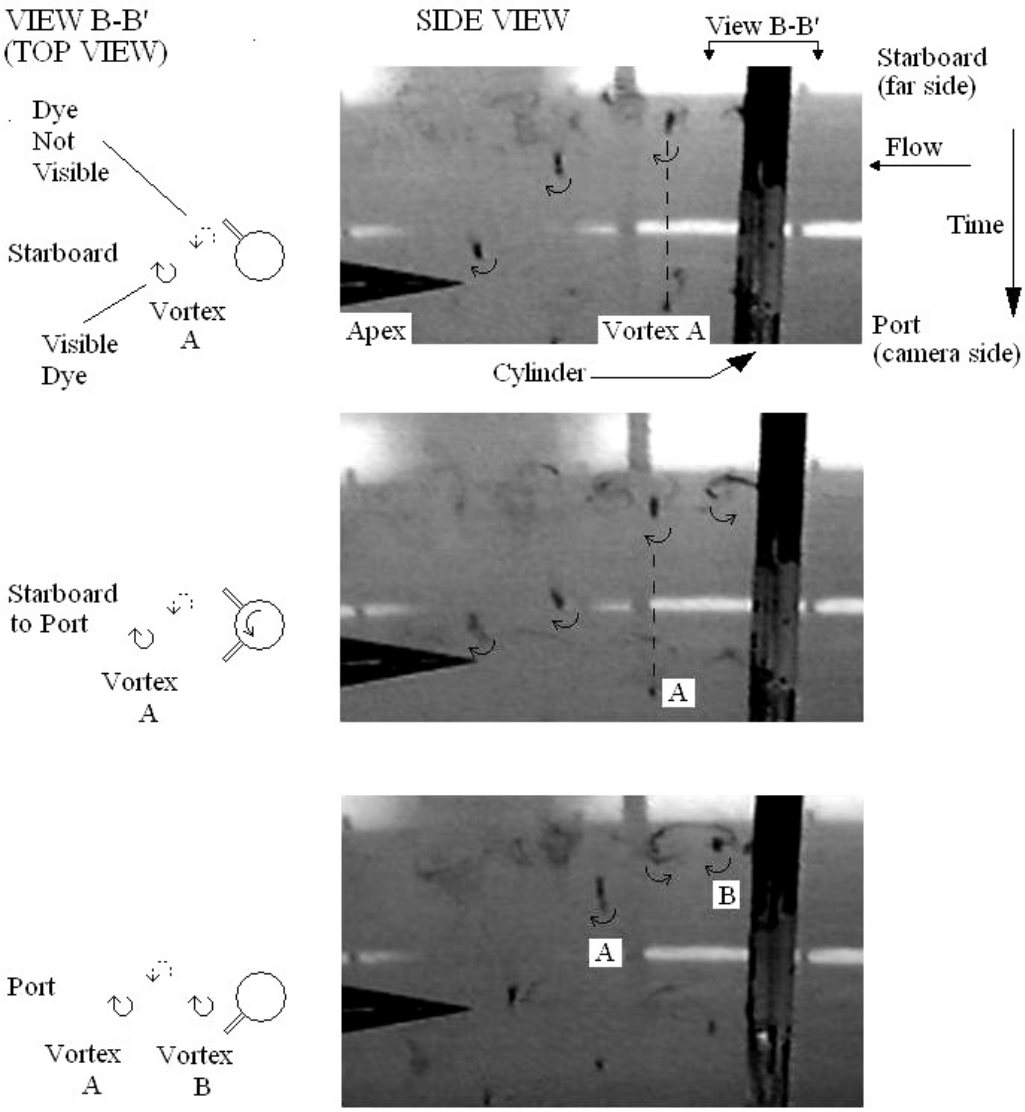

a) Oscillating Cylinder

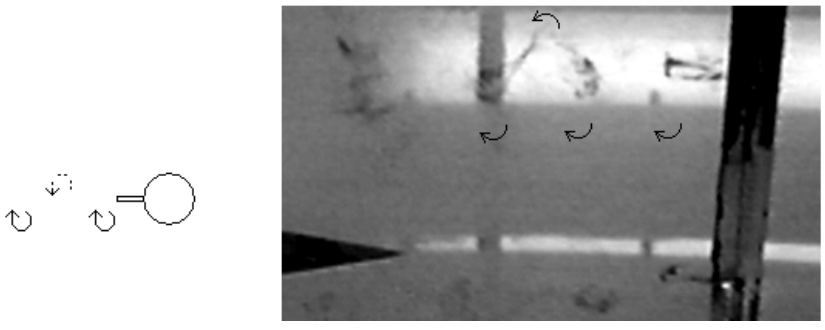

b) Fixed Cylinder

Figure 6.1. von Kàrmàn Wake Locked by Cylinder Oscillation.

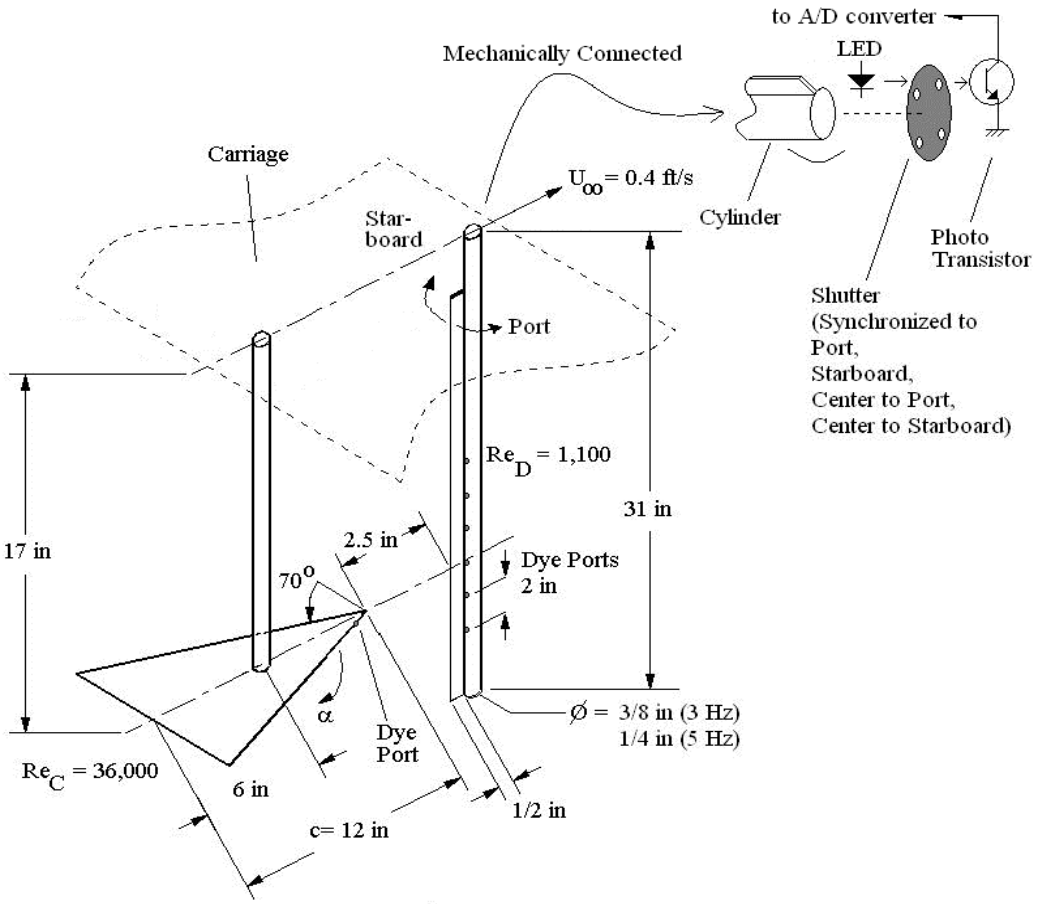

Figure 6.2. Simplified Cylinder Set-Up with Synchronization Circuit.

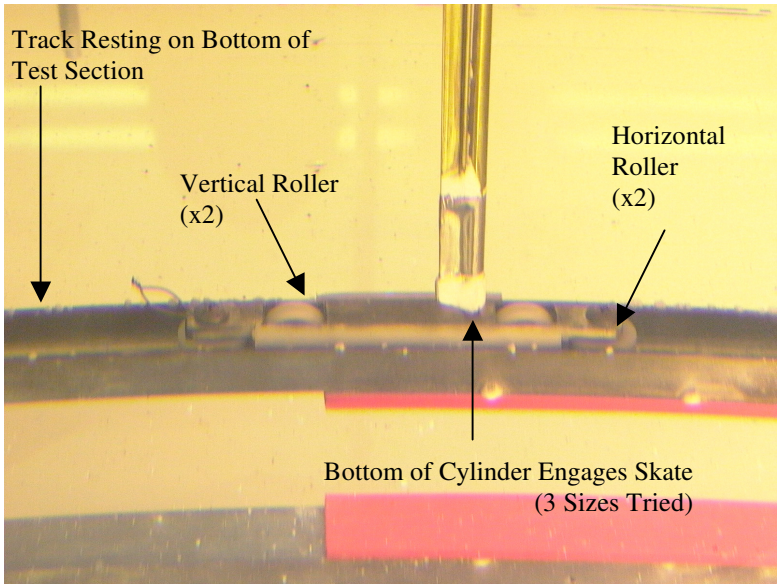

Figure 6.3. Close-Up View of Bottom Cylinder Guide and Skate.

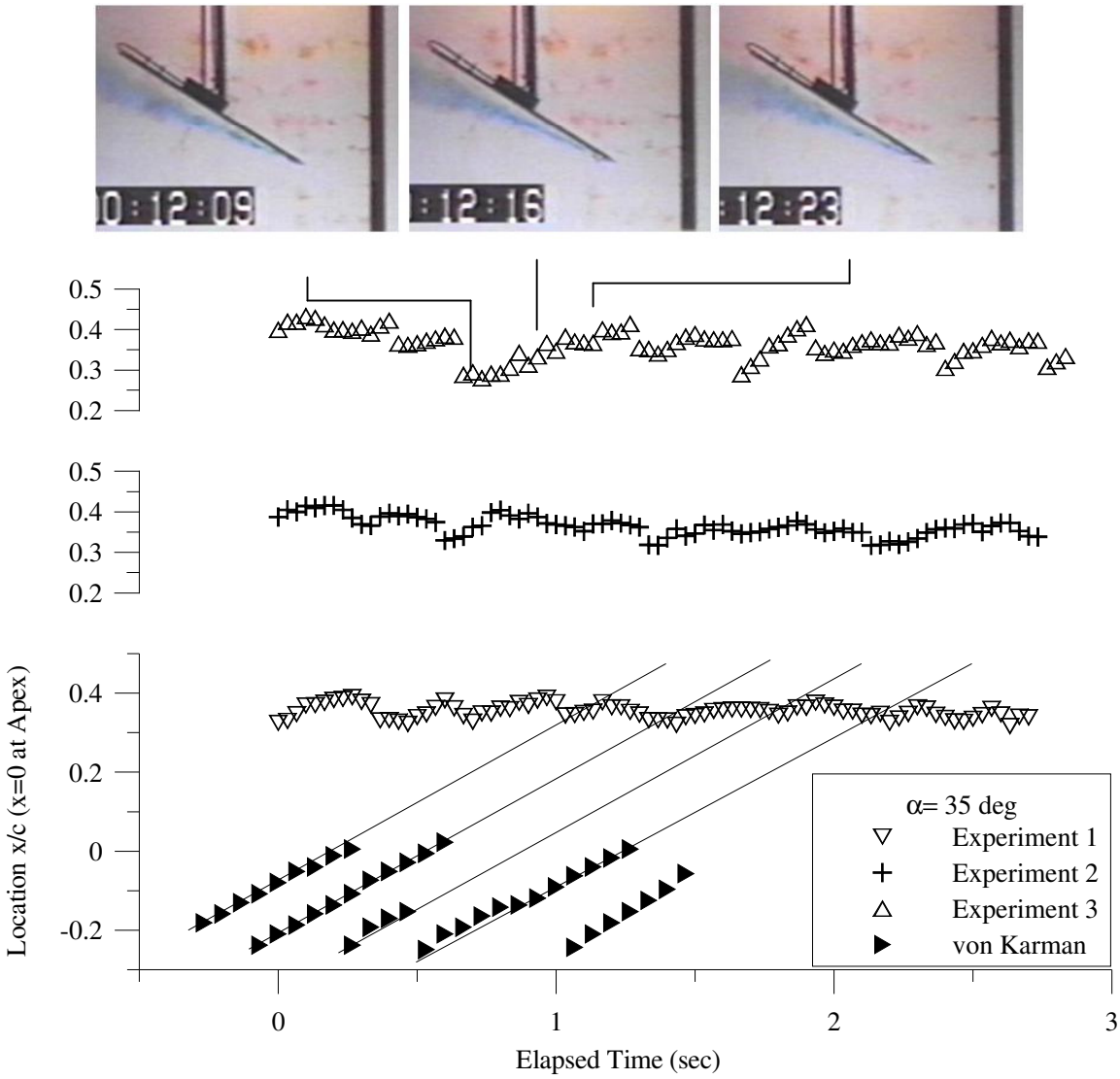

Figure 6.4. Fixed Large Cylinder Vortex Burst Time History, $\alpha = 35$ deg.

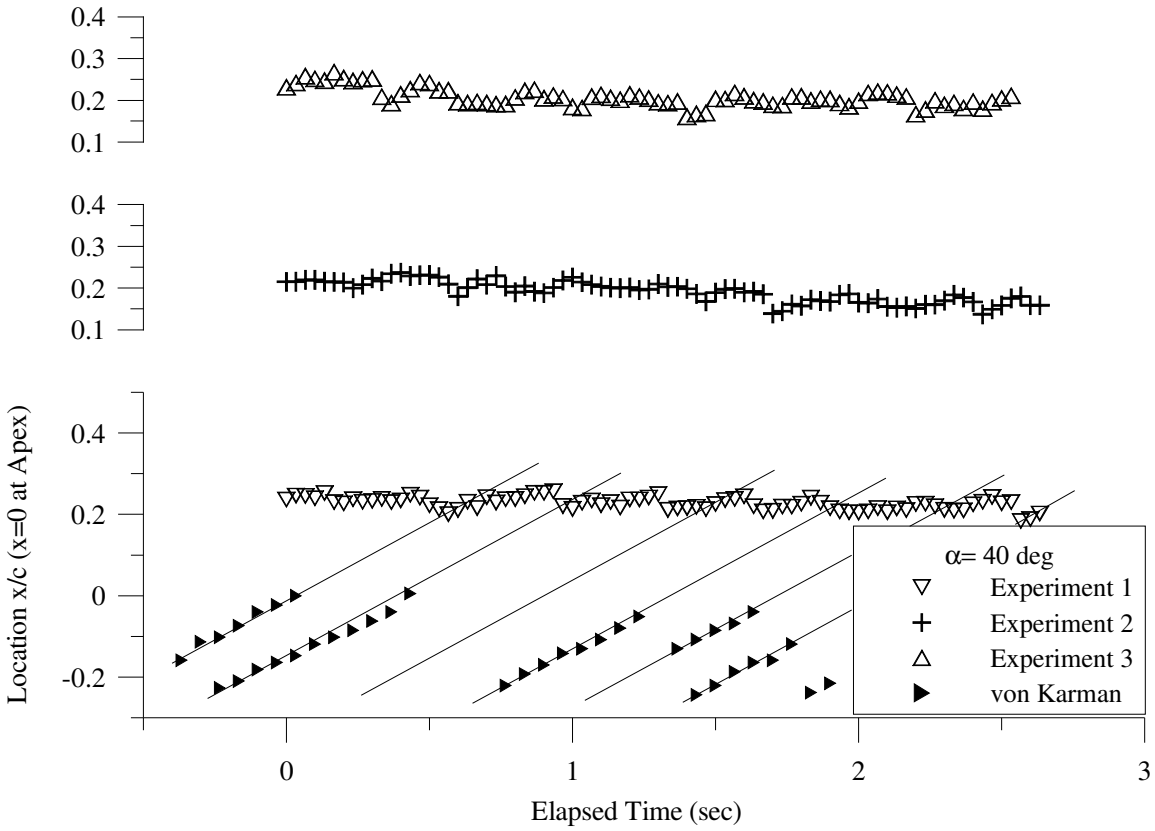

Figure 6.5. Fixed Large Cylinder Vortex Burst Time History, $\alpha = 40$ deg.

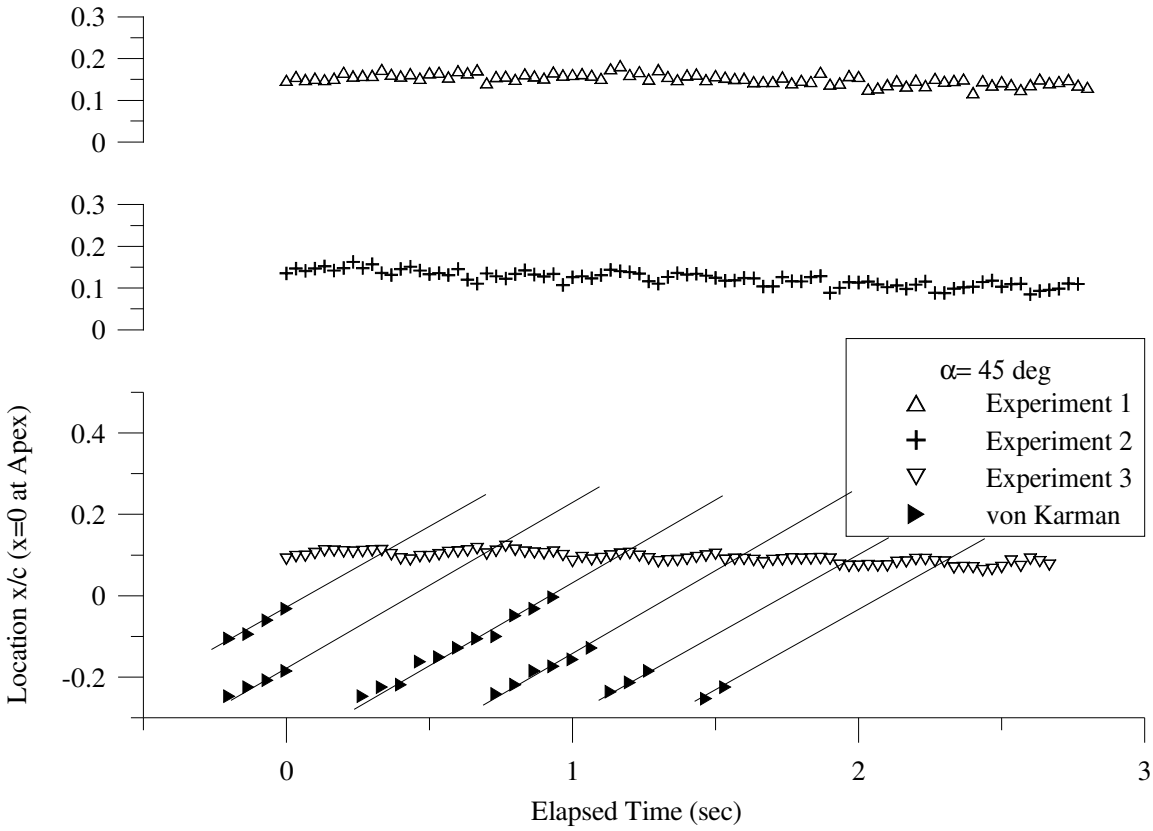

Figure 6.6. Fixed Large Cylinder Vortex Burst Time History, $\alpha = 45$ deg.

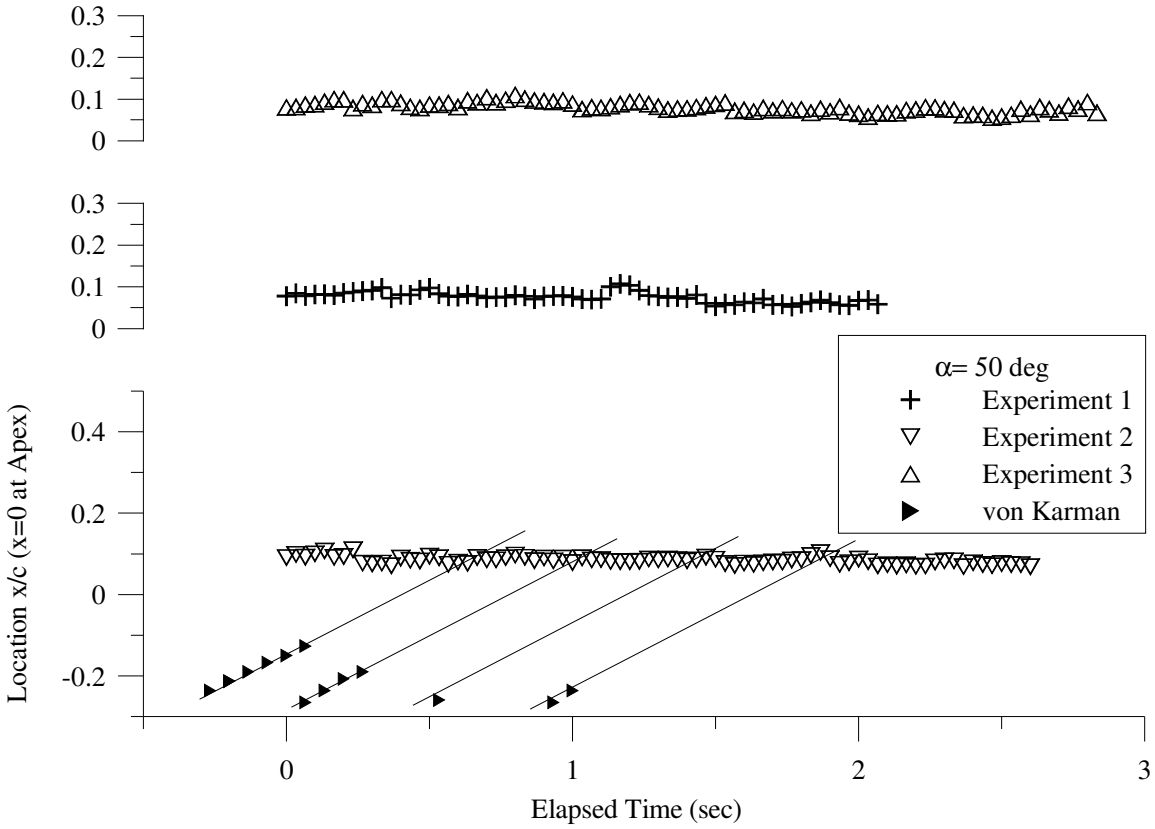

Figure 6.7. Fixed Large Cylinder Vortex Burst Time History, $\alpha = 50$ deg.

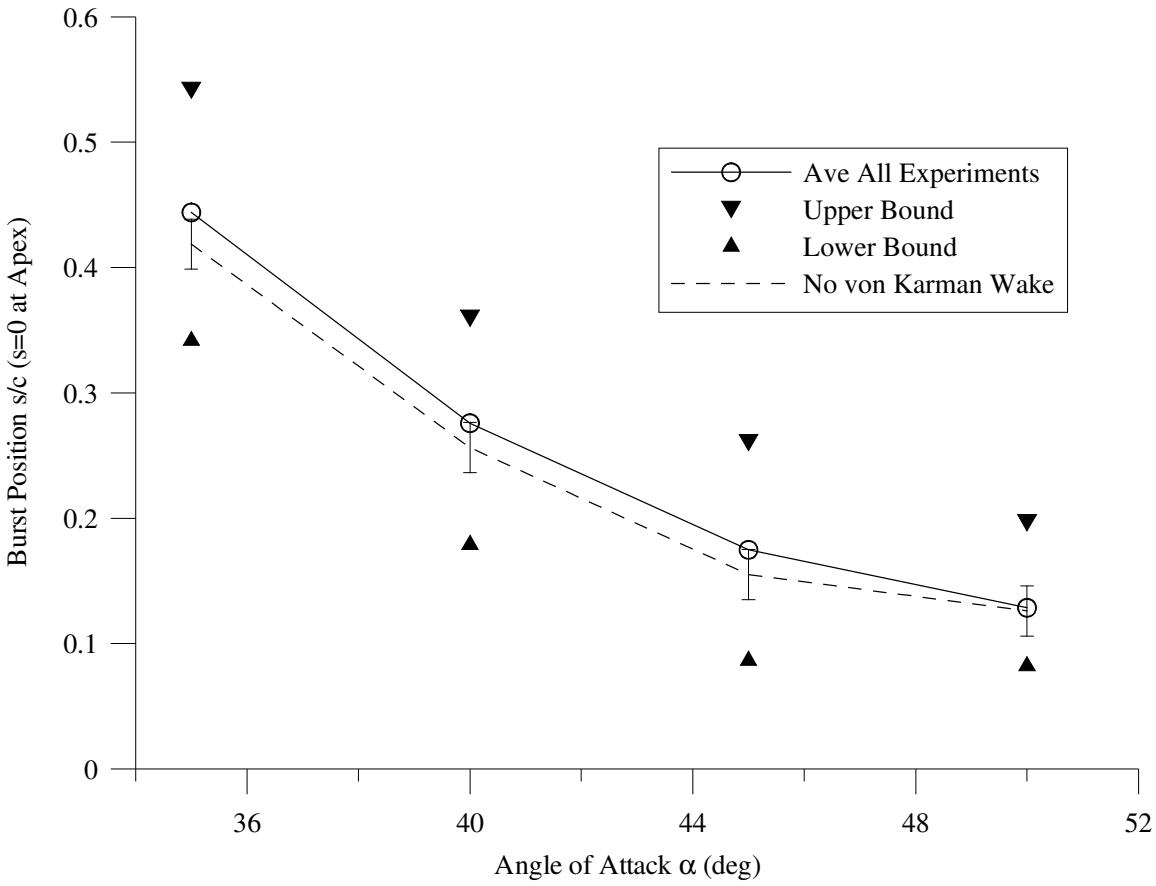

Figure 6.8. Fixed Large Cylinder Angle of Attack Behavior Comparison.

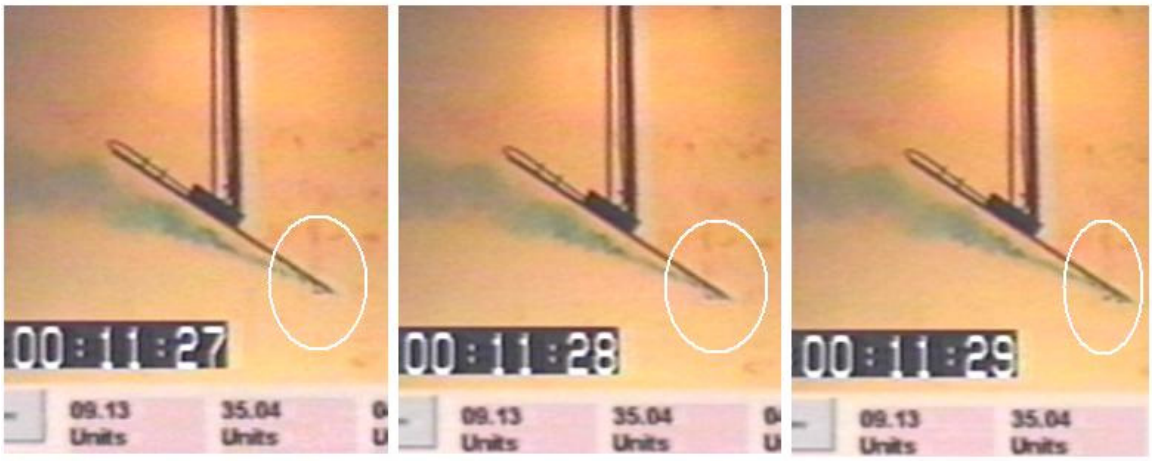

Figure 6.9. Small Amplitude Wave Distortion of LE Vortex Core, α=35 degrees.

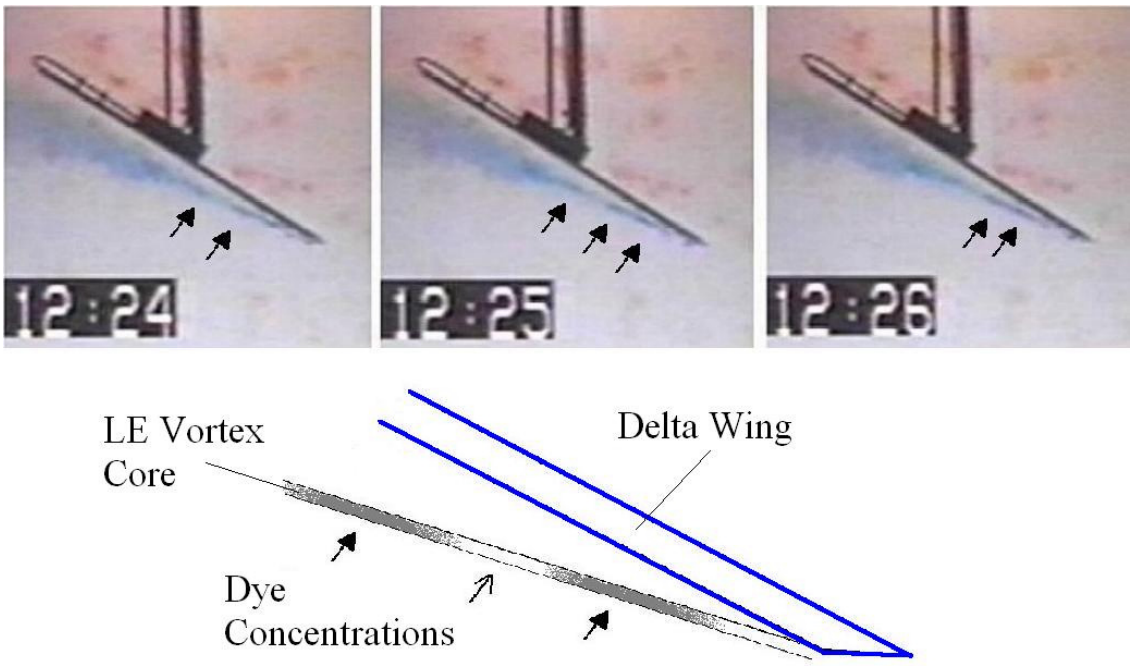

Figure 6.10. Formation of Regular Dye Concentrations on LE vortex core, α=35 degrees.

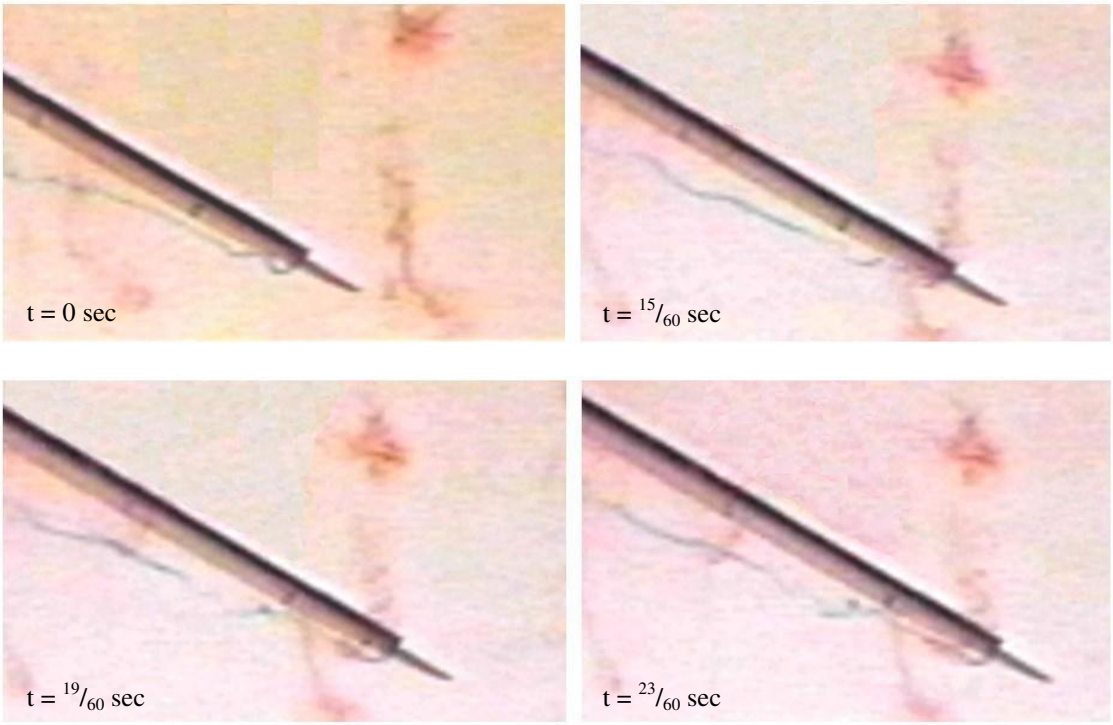

Figure 6.11. Entrainment of von Kàrmàn vortex filament in shear layer, α=35 degrees.

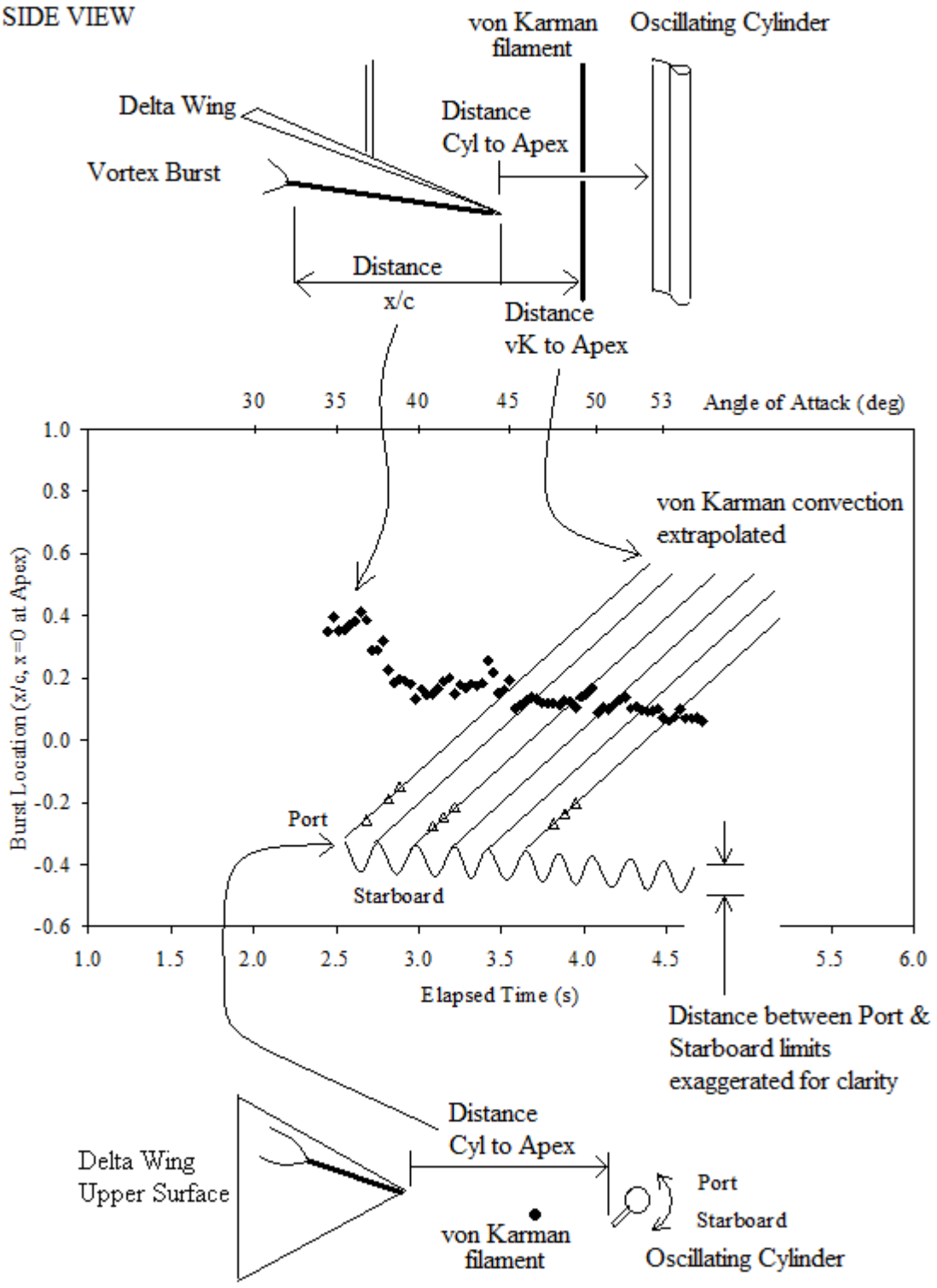

Figure 6.12. Schematic Explanation of Cylinder Plotting Nomenclature for Figures 6.13 to 6.82.

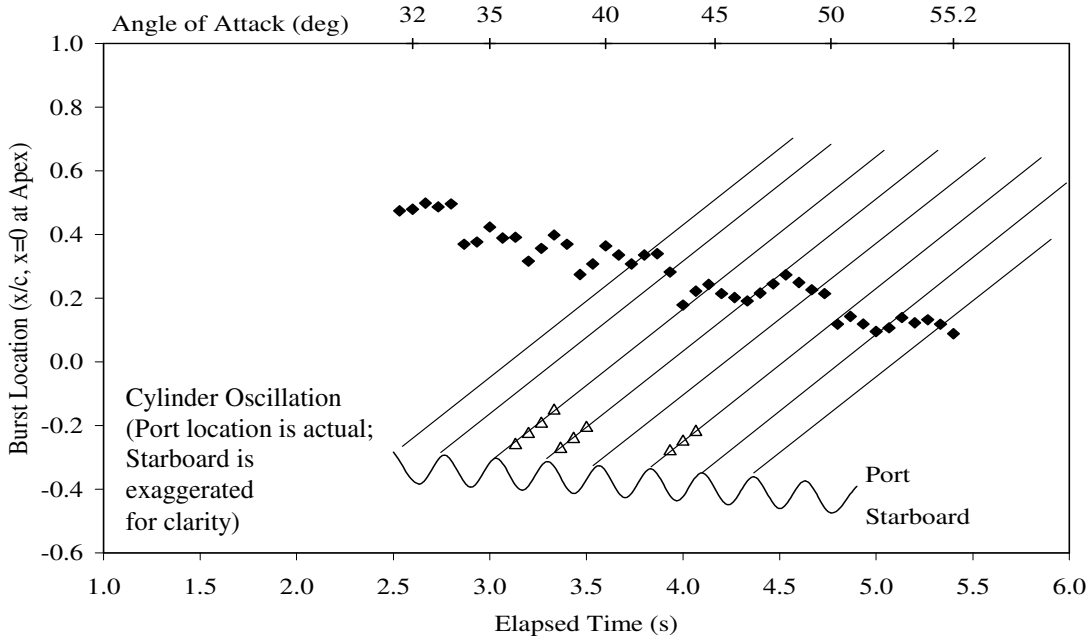

Figure 6.13. Large Cylinder, Pitch-Up Initiation Synchronized to Cylinder's Port Deflection, $15 < \alpha < 55$ degrees, $\kappa = 0.2$ (Experiment 1).

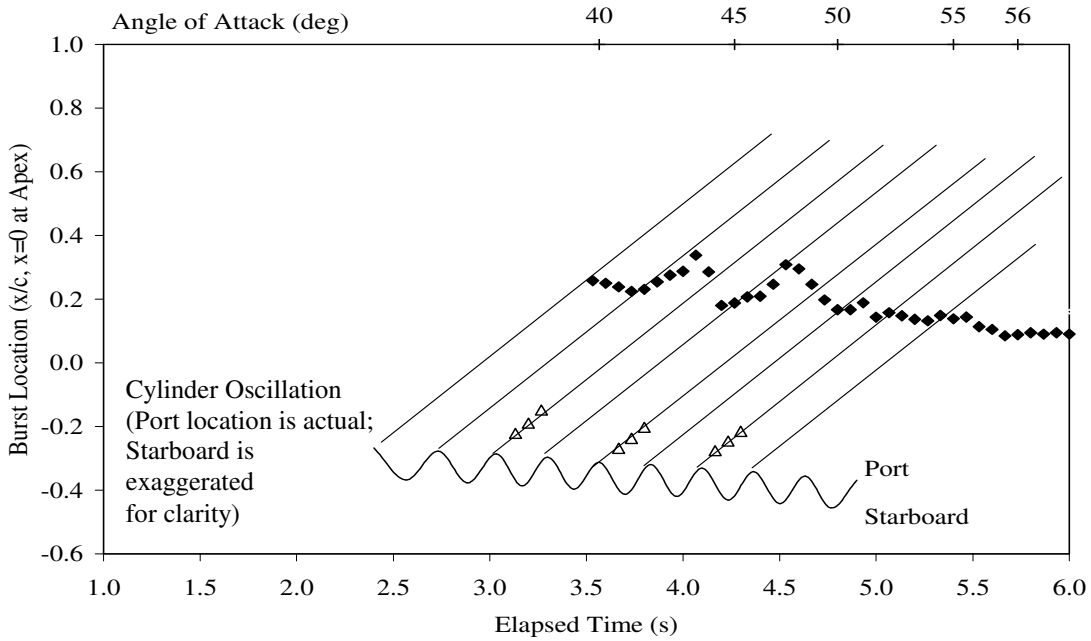

Figure 6.14. Large Cylinder, Pitch-Up Initiation Synchronized to Cylinder's Port Deflection, $15 < \alpha < 55$ degrees, $\kappa = 0.2$ (Experiment 2).

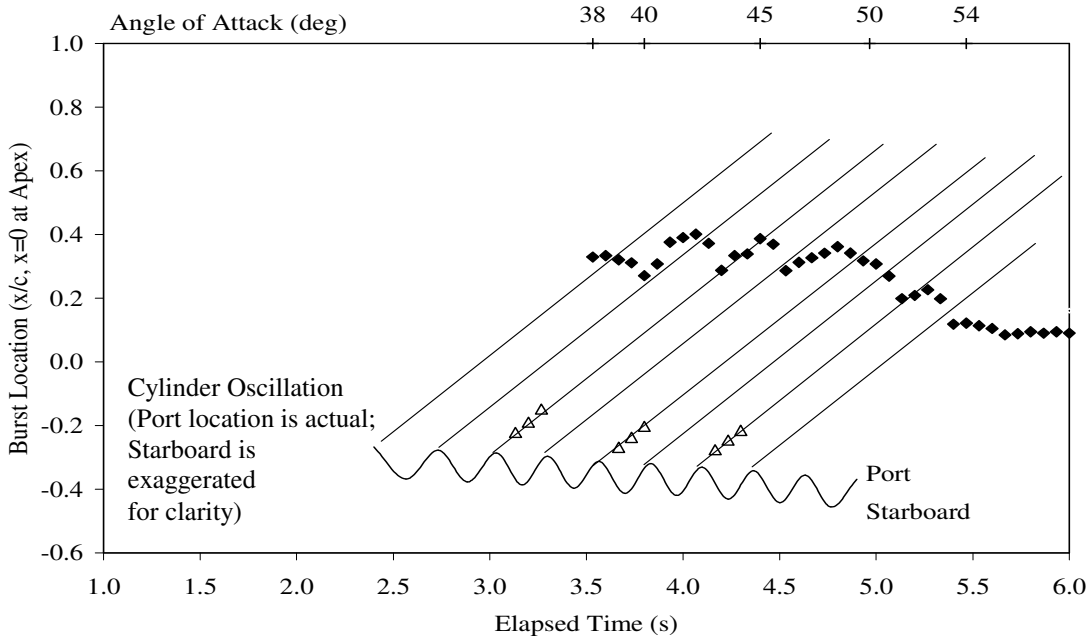

Figure 6.15. Large Cylinder, Pitch-Up Initiation Synchronized to Cylinder's Port Deflection, $15 < \alpha < 55$ degrees, $\kappa = 0.2$ (Experiment 3).

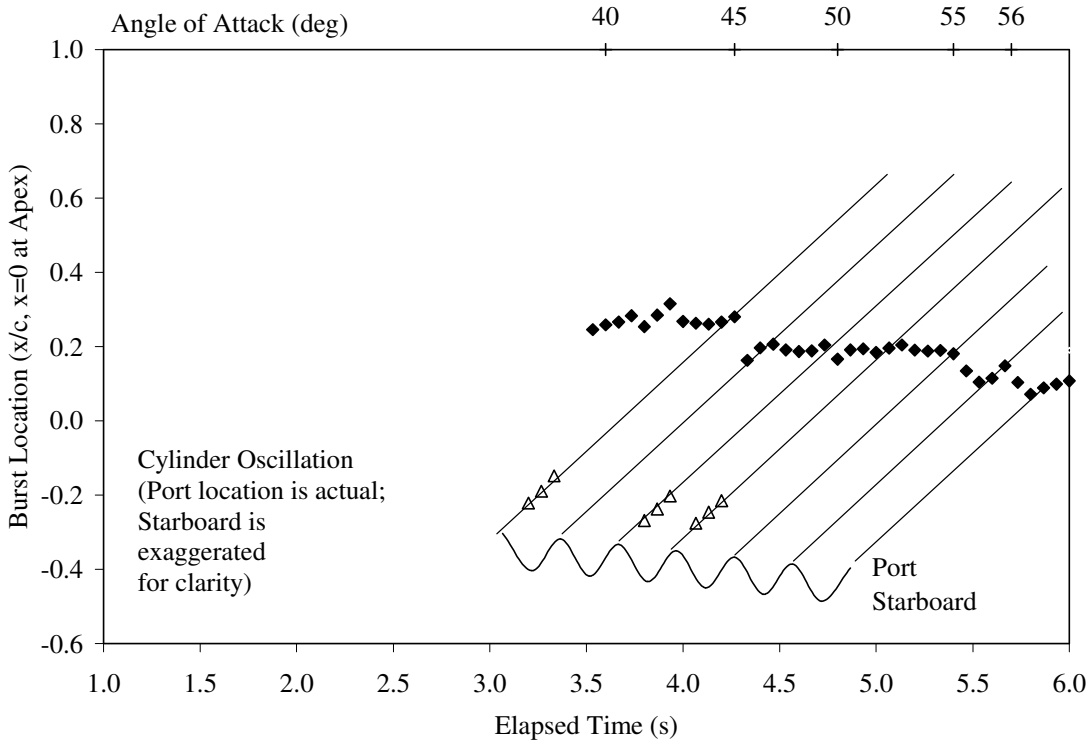

Figure 6.16. Large Cylinder, Pitch-Up Initiation Synchronized to Cylinder's Starboard Deflection, $15 < \alpha < 55$ degrees, $\kappa = 0.2$ (Experiment 1).

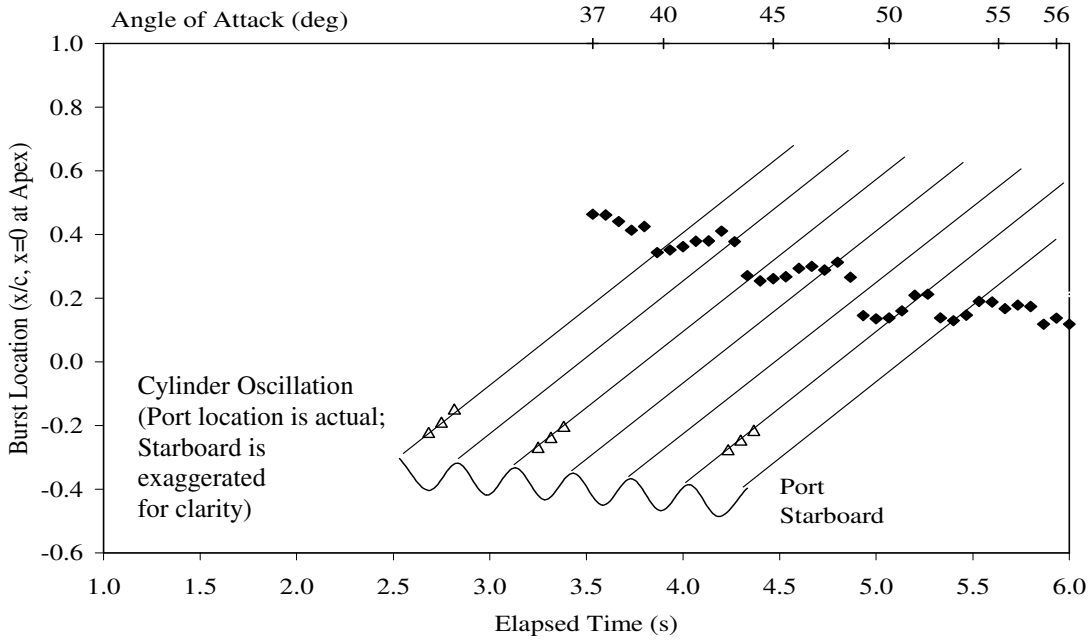

Figure 6.17. Large Cylinder, Pitch-Up Initiation Synchronized to Cylinder's to Starboard Deflection, $15 < \alpha < 55$ degrees, $\kappa = 0.2$ (Experiment 2).

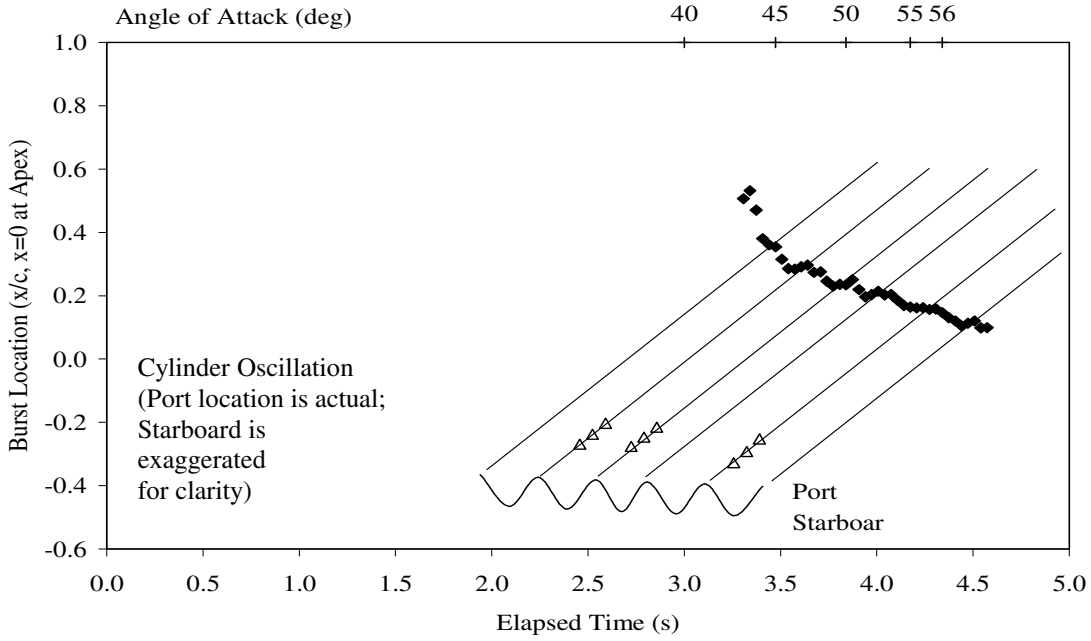

Figure 6.18. Large Cylinder, Pitch-Up Initiation Synchronized to Cylinder's to Starboard Deflection, $15 < \alpha < 55$ degrees, $\kappa = 0.2$ (Experiment 3).

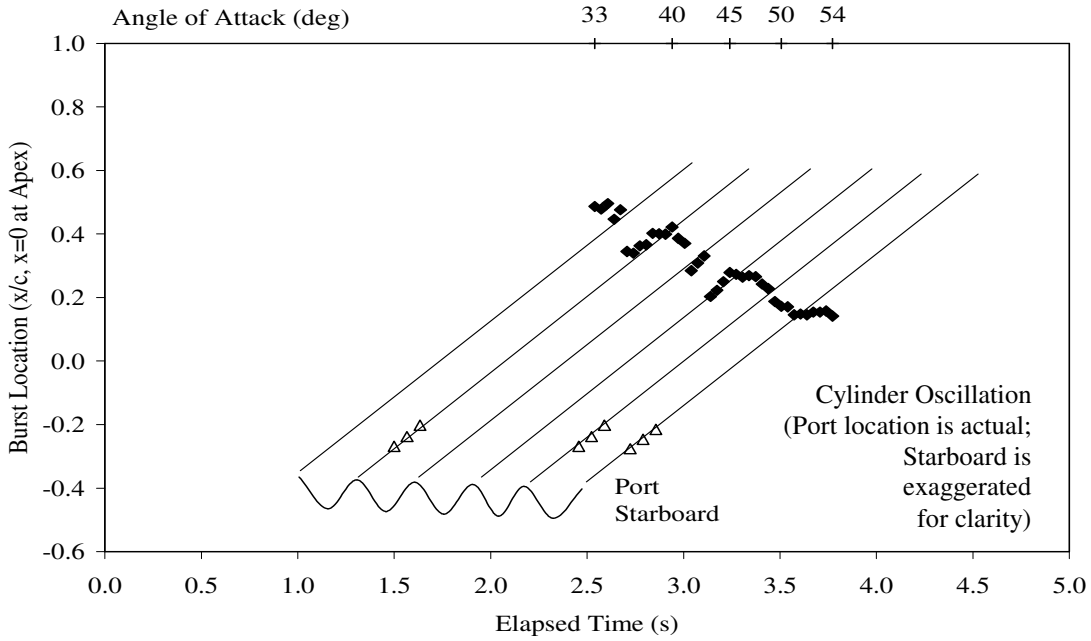

Figure 6.19. Large Cylinder, Pitch-Up Initiation Synchronized to Cylinder's Center to Port Deflection, $15 < \alpha < 55$ degrees, $\kappa = 0.2$ (Experiment 1).

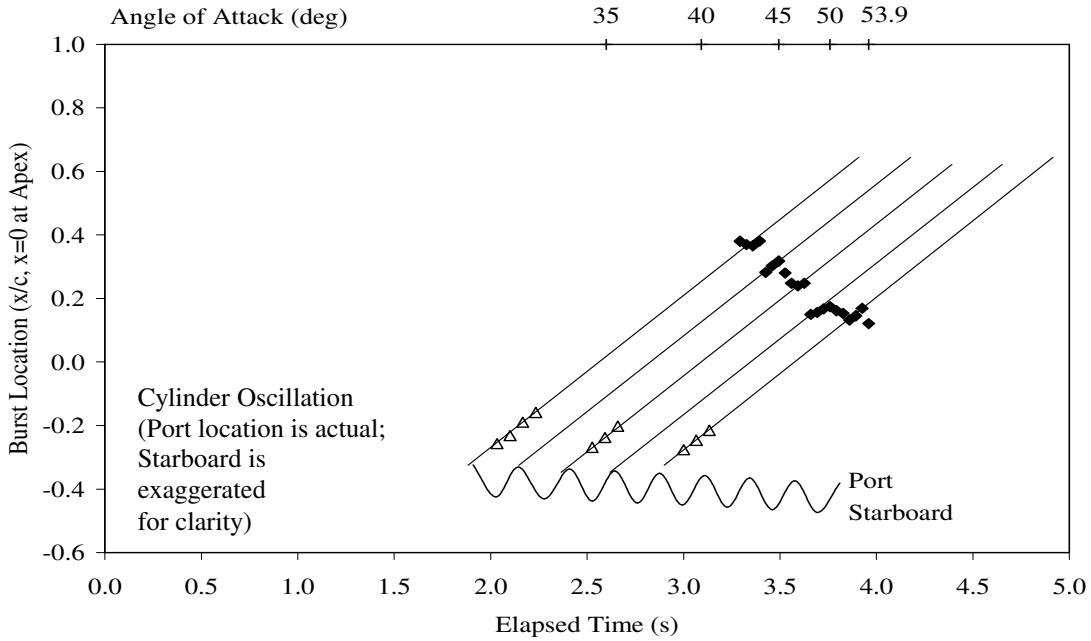

Figure 6.20. Large Cylinder, Pitch-Up Initiation Synchronized to Cylinder's Center to Port Deflection, $15 < \alpha < 55$ degrees, $\kappa = 0.2$ (Experiment 2).

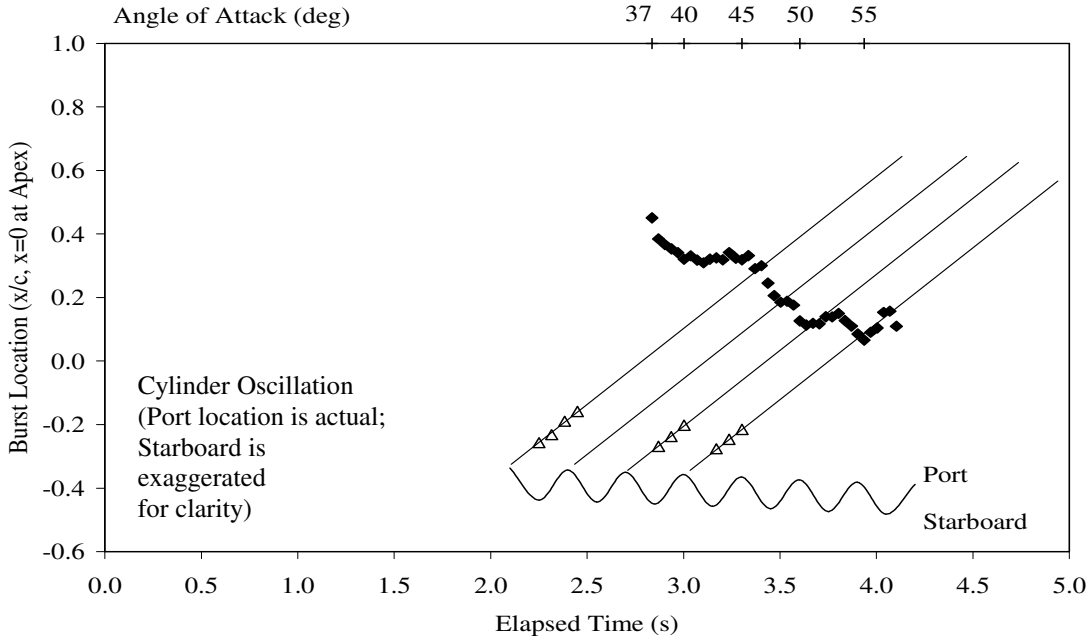

Figure 6.21. Large Cylinder, Pitch-Up Initiation Synchronized to Cylinder's Center to Port Deflection, $15 < \alpha < 55$ degrees, $\kappa = 0.2$ (Experiment 3).

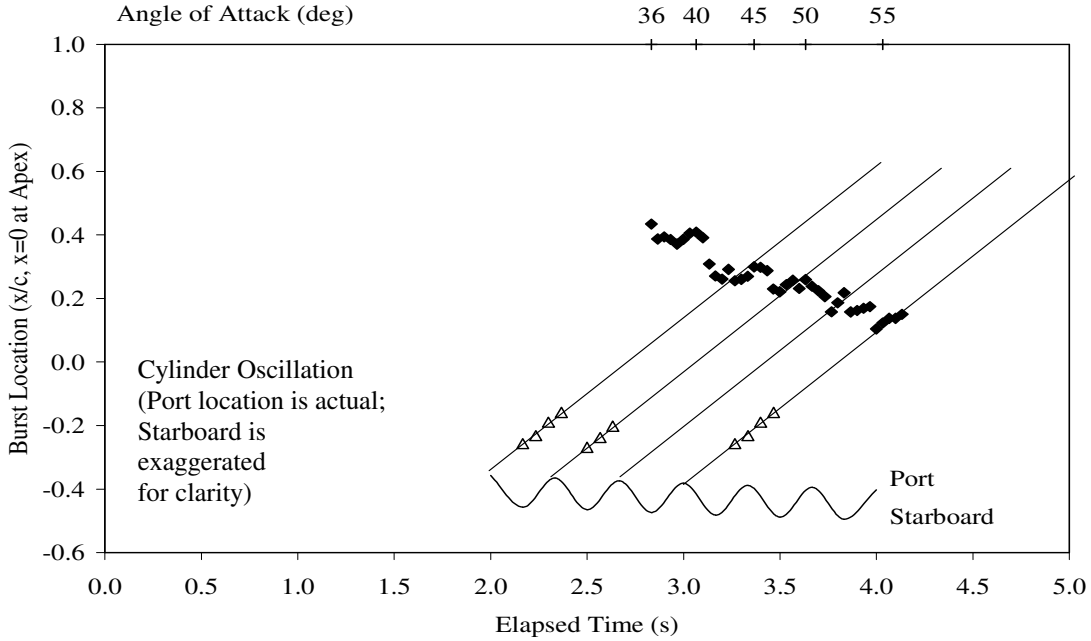

Figure 6.22. Large Cylinder, Pitch-Up Initiation Synchronized to Cylinder's Center to Starboard Deflection, $15 < \alpha < 55$ degrees, $\kappa = 0.2$ (Experiment 1).

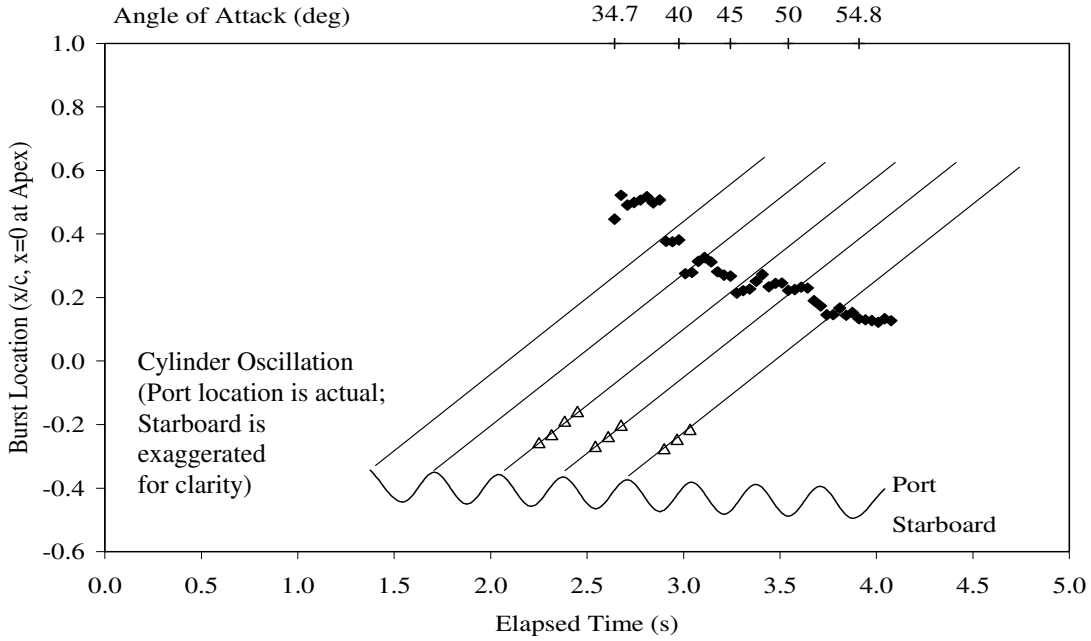

Figure 6.23. Large Cylinder, Pitch-Up Initiation Synchronized to Cylinder's Center to Starboard Deflection, $15 < \alpha < 55$ degrees, $\kappa = 0.2$ (Experiment 2).

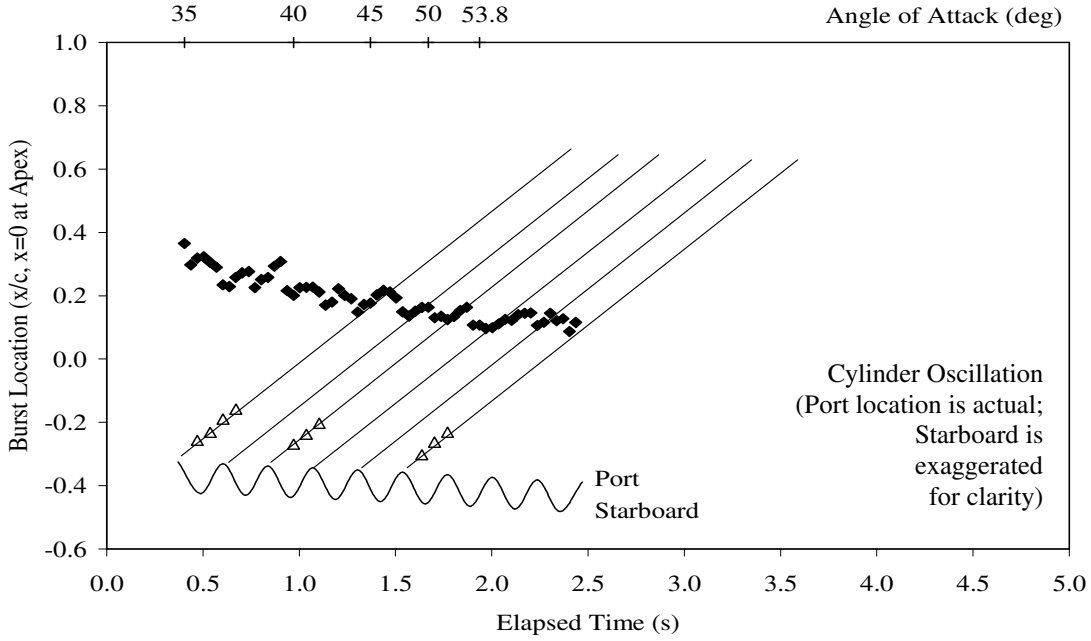

Figure 6.24. Large Cylinder, Pitch-Up Initiation Synchronized to Cylinder's Center to Port Deflection, $35 < \alpha < 55$ degrees, $\kappa = 0.2$ (Experiment 1).

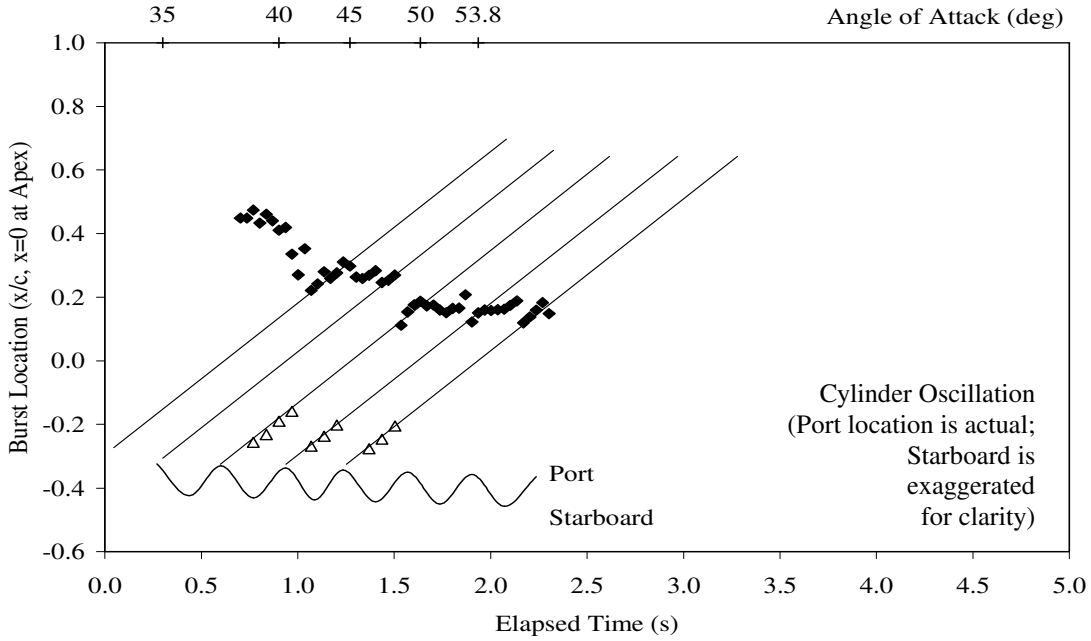

Figure 6.25. Large Cylinder, Pitch-Up Initiation Synchronized to Cylinder's Center to Port Deflection, $35 < \alpha < 55$ degrees, $\kappa = 0.2$ (Experiment 2).

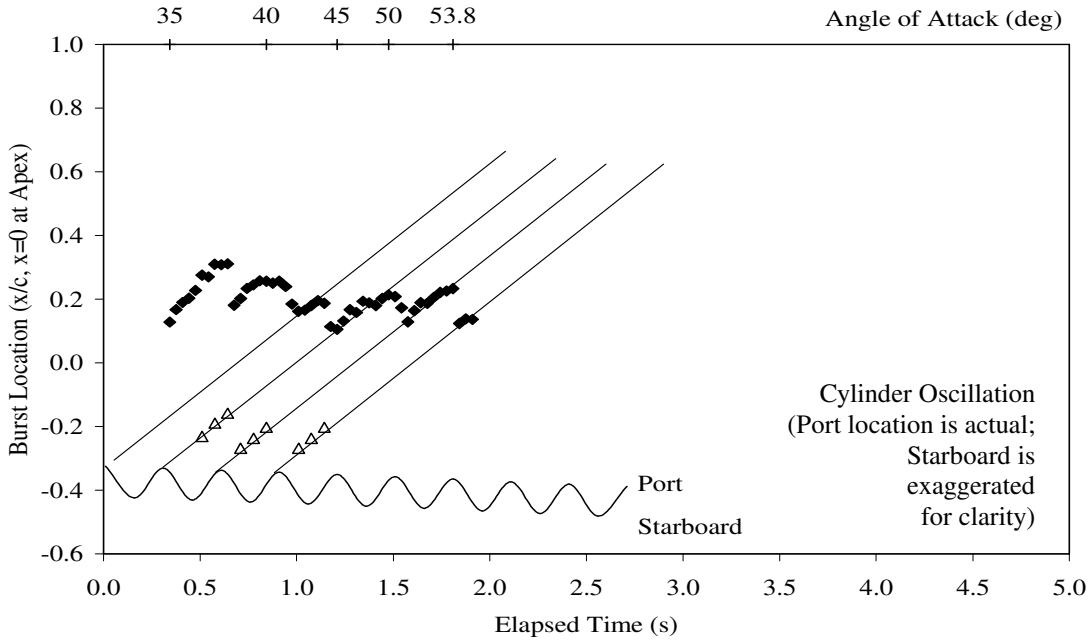

Figure 6.26. Large Cylinder, Pitch-Up Initiation Synchronized to Cylinder's Center to Port Deflection, $35 < \alpha < 55$ degrees, $\kappa = 0.2$ (Experiment 3).

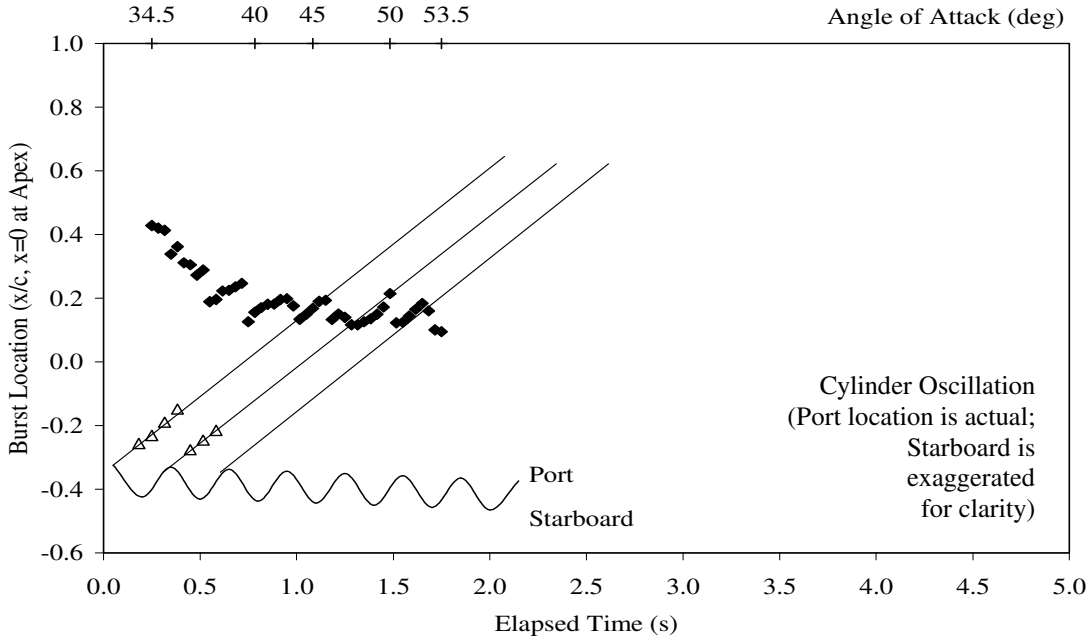

Figure 6.27. Large Cylinder, Pitch-Up Initiation Synchronized to Cylinder's Center to Starboard Deflection, $35 < \alpha < 55$ degrees, $\kappa = 0.2$ (Experiment 1).

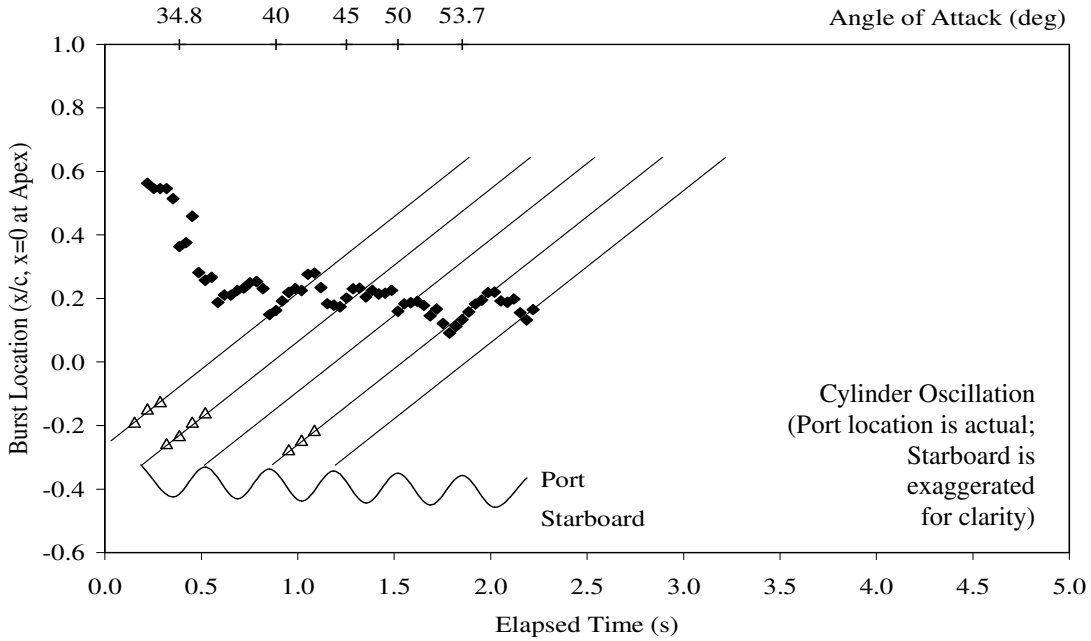

Figure 6.28. Large Cylinder, Pitch-Up Initiation Synchronized to Cylinder's Center to Starboard Deflection, $35 < \alpha < 55$ degrees, $\kappa = 0.2$ (Experiment 2).

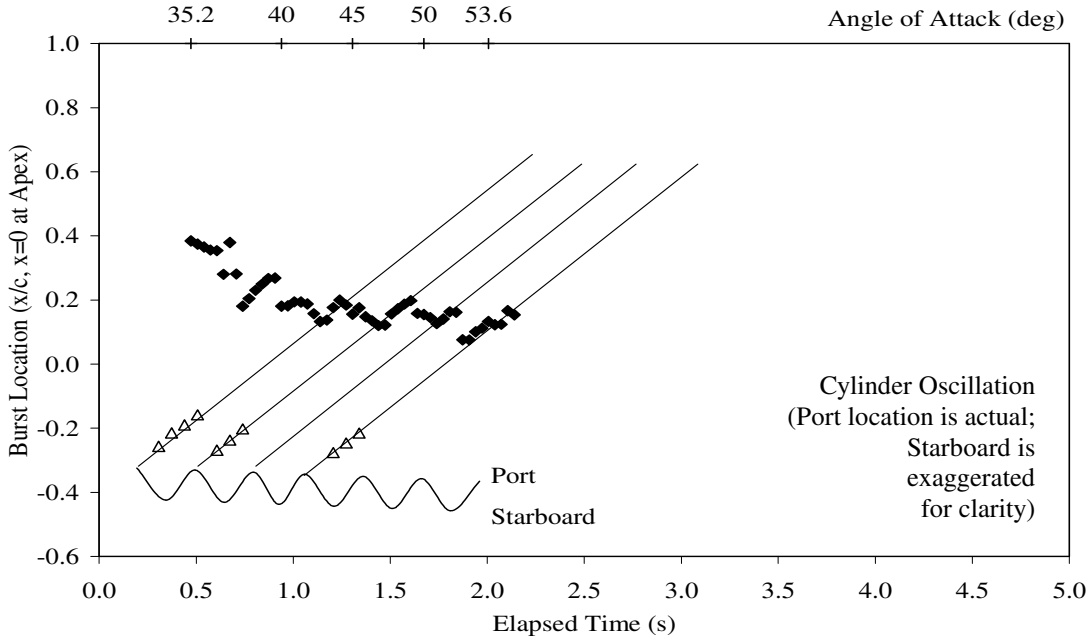

Figure 6.29. Large Cylinder, Pitch-Up Initiation Synchronized to Cylinder's Center to Starboard Deflection, $35 < \alpha < 55$ degrees, $\kappa = 0.2$ (Experiment 3).

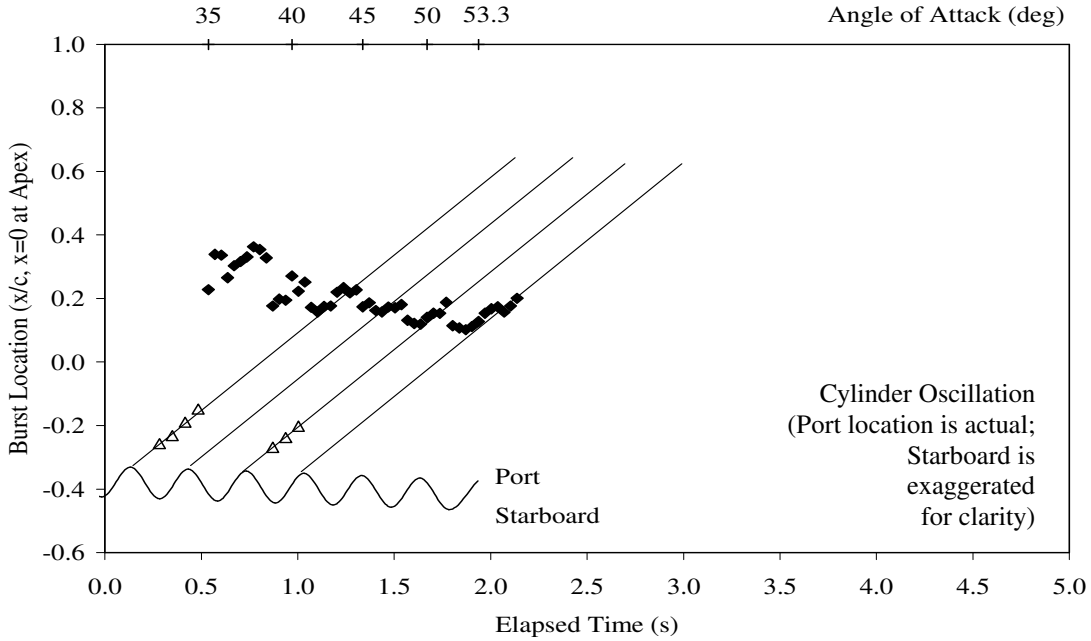

Figure 6.30. Large Cylinder, Pitch-Up Initiation Synchronized to Cylinder's Starboard Deflection, $35 < \alpha < 55$ degrees, $\kappa = 0.2$ (Experiment 1).

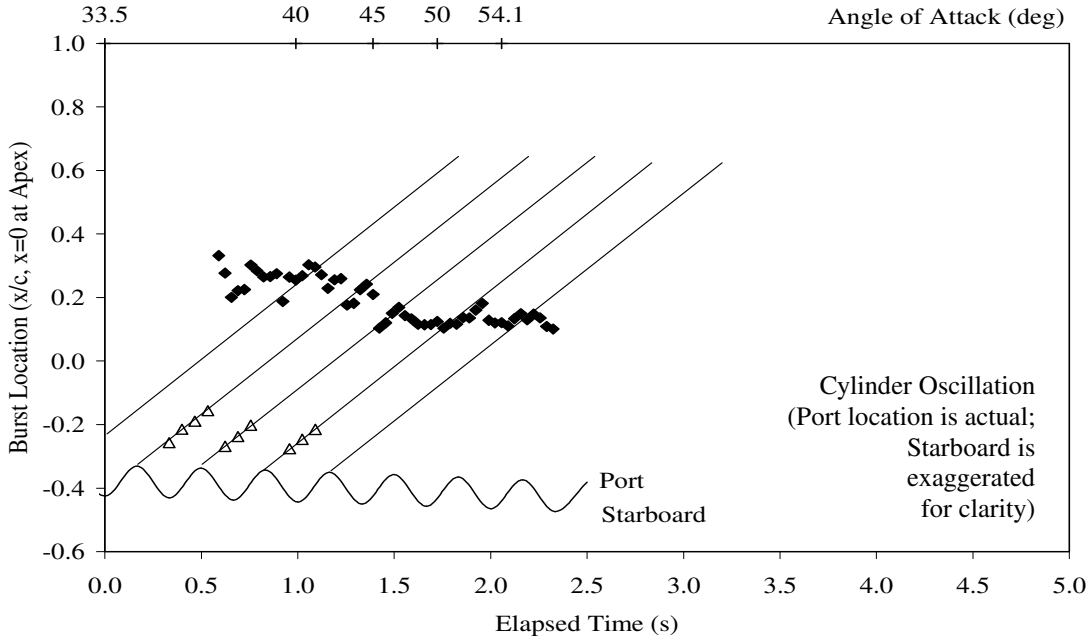

Figure 6.31. Large Cylinder, Pitch-Up Initiation Synchronized to Cylinder's Starboard Deflection, $35 < \alpha < 55$ degrees, $\kappa = 0.2$ (Experiment 2).

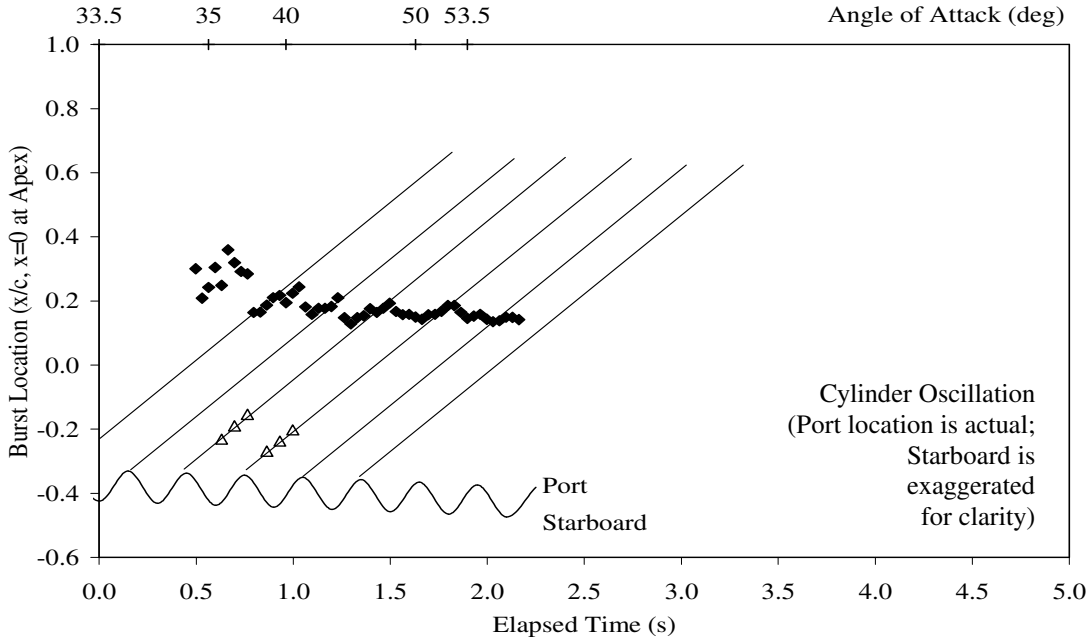

Figure 6.32. Large Cylinder, Pitch-Up Initiation Synchronized to Cylinder's Starboard Deflection, $35 < \alpha < 55$ degrees, $\kappa = 0.2$ (Experiment 3).

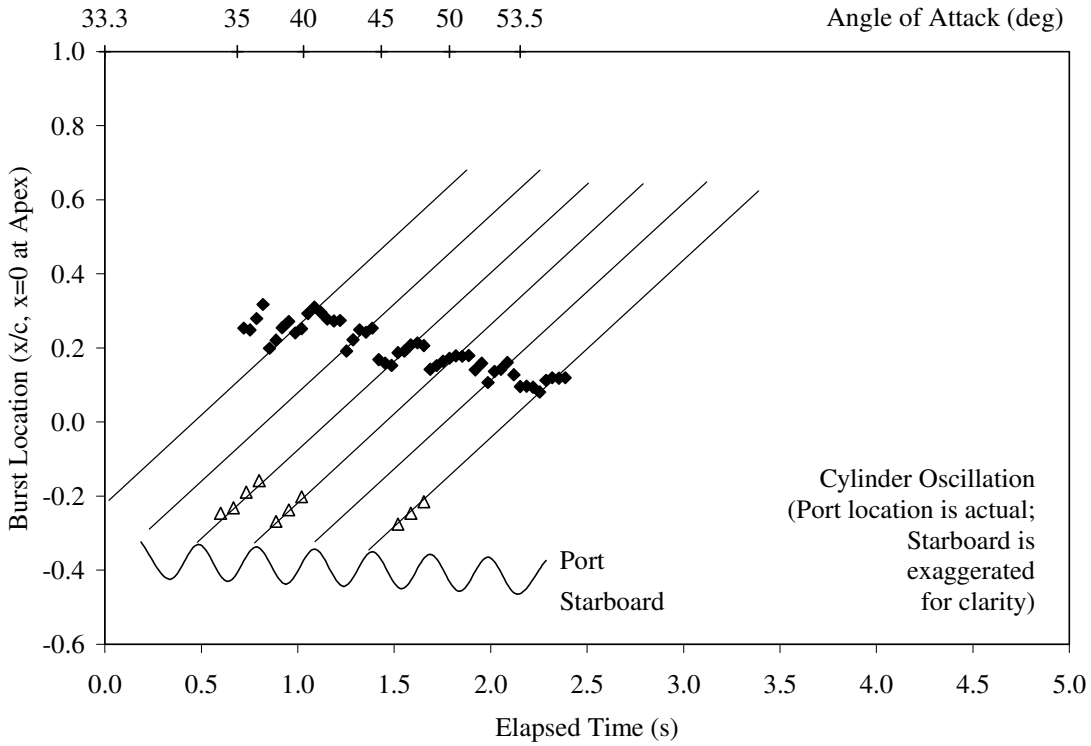

Figure 6.33. Large Cylinder, Pitch-Up Initiation Synchronized to Cylinder's Port Deflection, $35 < \alpha < 55$ degrees, $\kappa = 0.2$ (Experiment 1).

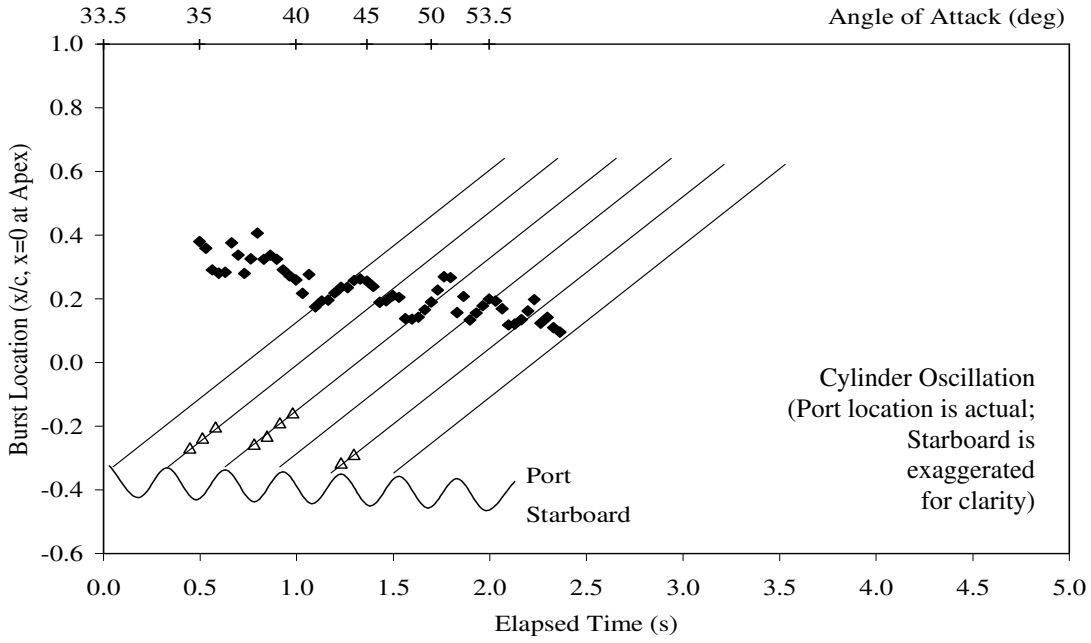

Figure 6.34. Large Cylinder, Pitch-Up Initiation Synchronized to Cylinder's Port Deflection, $35 < \alpha < 55$ degrees, $\kappa = 0.2$ (Experiment 2).

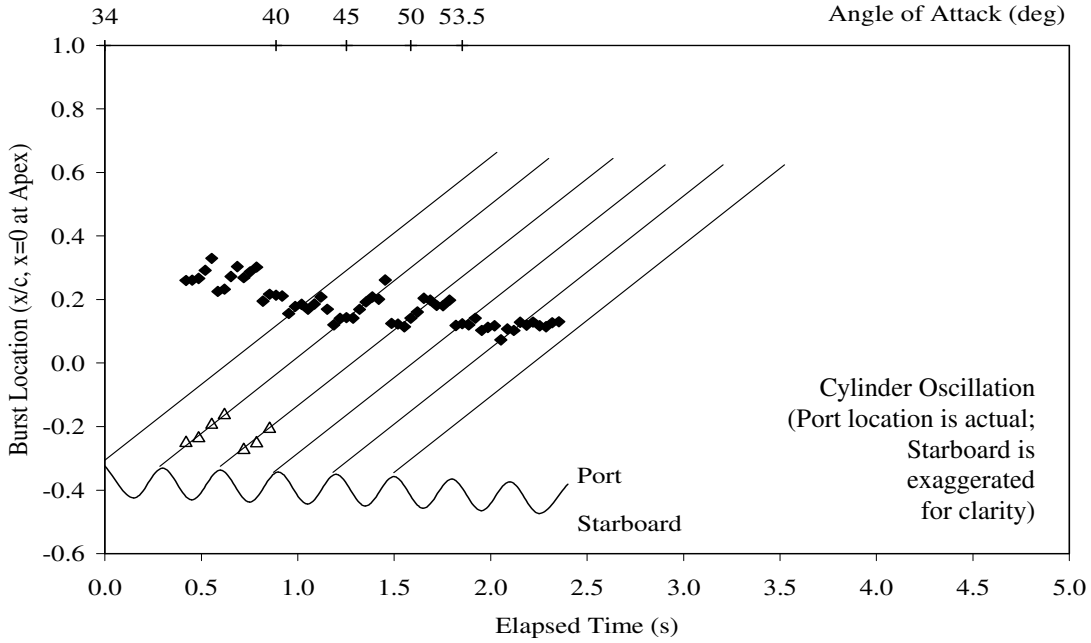

Figure 6.35. Large Cylinder, Pitch-Up Initiation Synchronized to Cylinder's Port Deflection, $35 < \alpha < 55$ degrees, $\kappa = 0.2$ (Experiment 3).

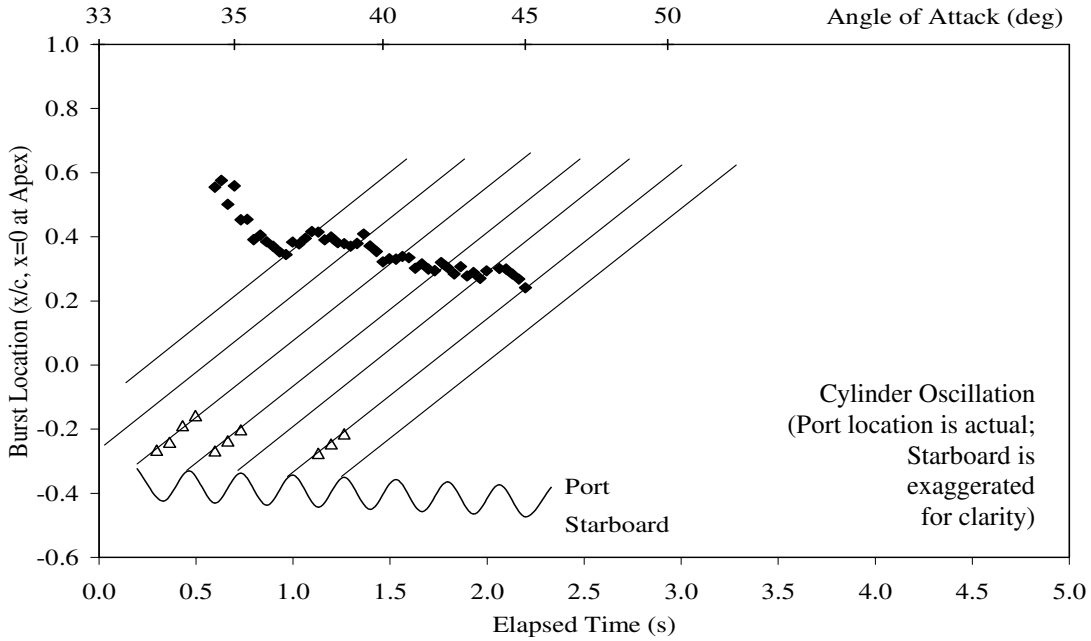

Figure 6.36. Large Cylinder, Pitch-Up Initiation Synchronized to Cylinder's Center to Starboard Deflection, $35 < \alpha < 55$ degrees, $\kappa = 0.1$ (Experiment 1).

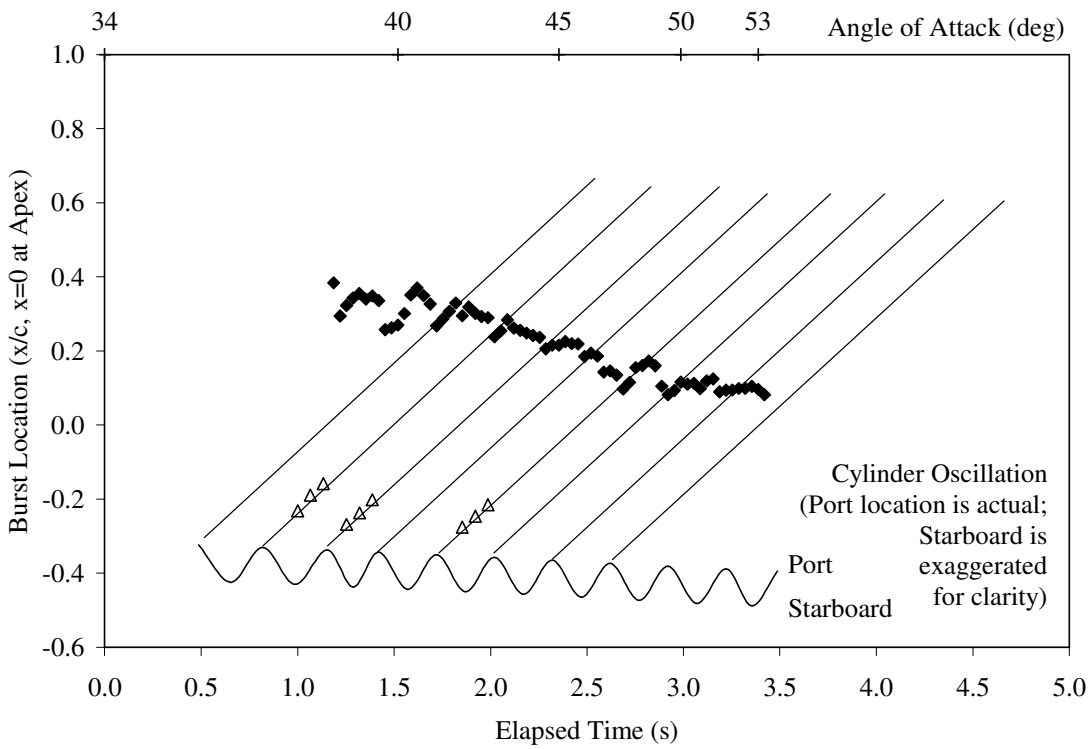

Figure 6.37. Large Cylinder, Pitch-Up Initiation Synchronized to Cylinder's Center to Starboard Deflection, $35 < \alpha < 55$ degrees, $\kappa = 0.1$ (Experiment 2).

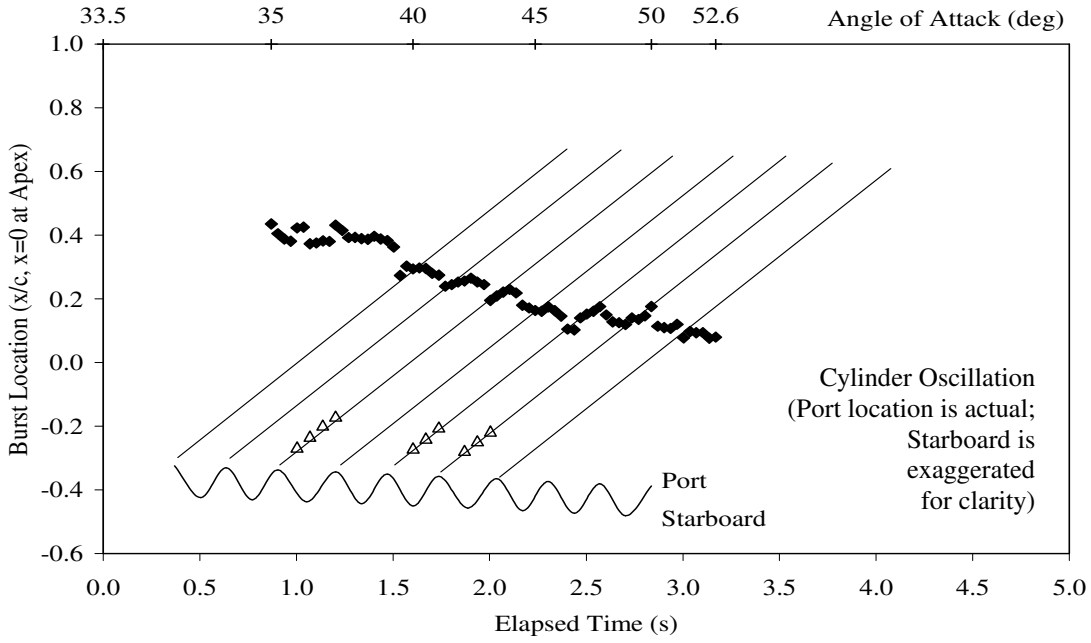

Figure 6.38. Large Cylinder, Pitch-Up Initiation Synchronized to Cylinder's Center to Starboard Deflection, $35 < \alpha < 55$ degrees, $\kappa = 0.1$ (Experiment 3).

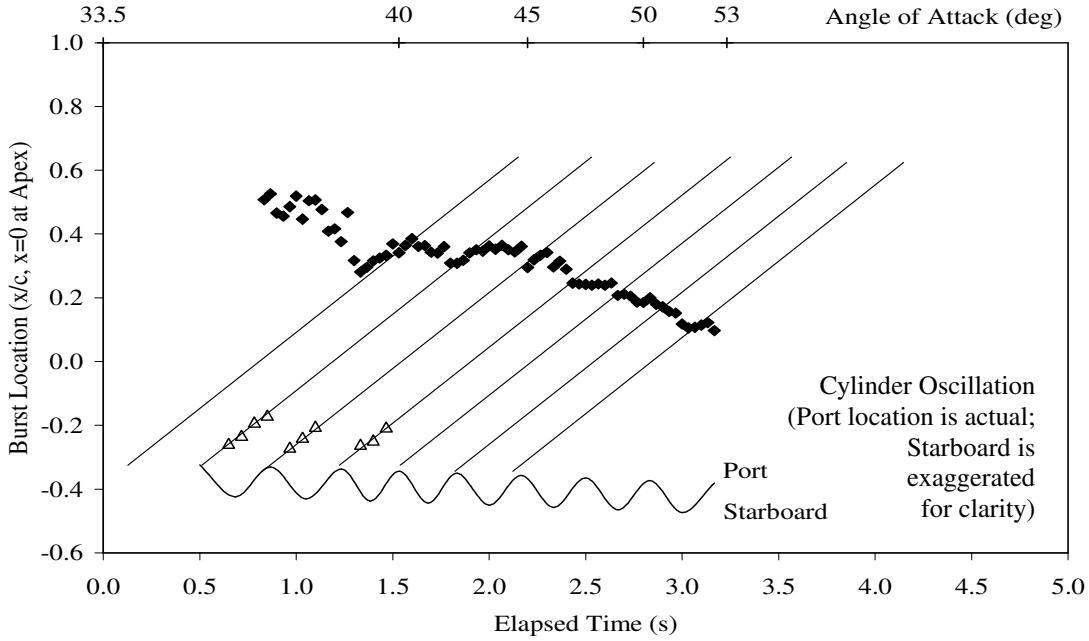

Figure 6.39. Large Cylinder, Pitch-Up Initiation Synchronized to Cylinder's Starboard Deflection, $35 < \alpha < 55$ degrees, $\kappa = 0.1$ (Experiment 1).

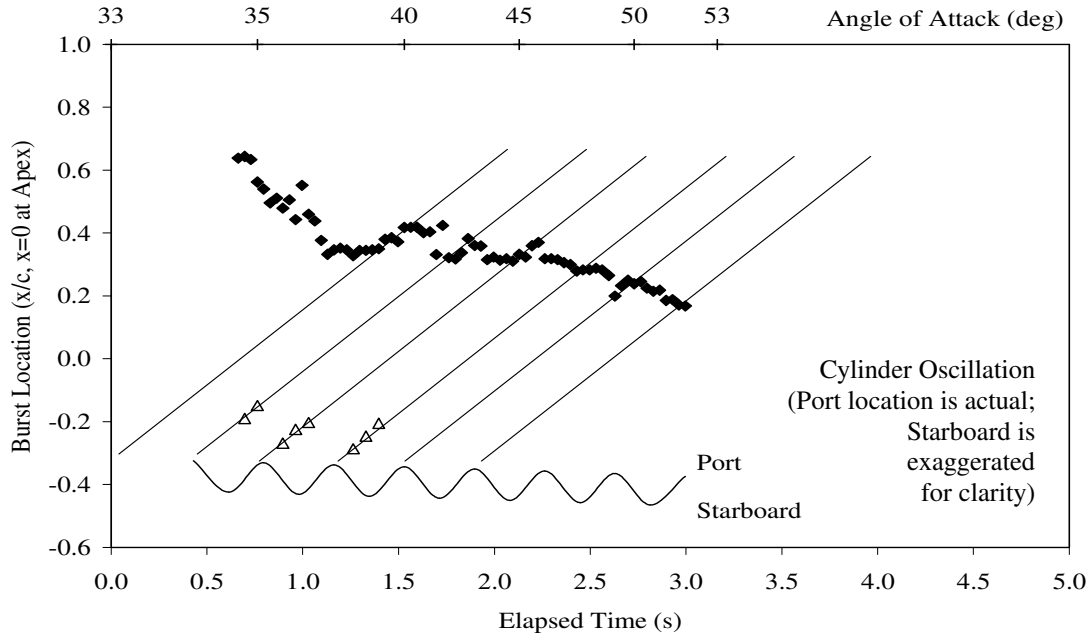

Figure 6.40. Large Cylinder, Pitch-Up Initiation Synchronized to Cylinder's Starboard Deflection, $35 < \alpha < 55$ degrees, $\kappa = 0.1$ (Experiment 2).

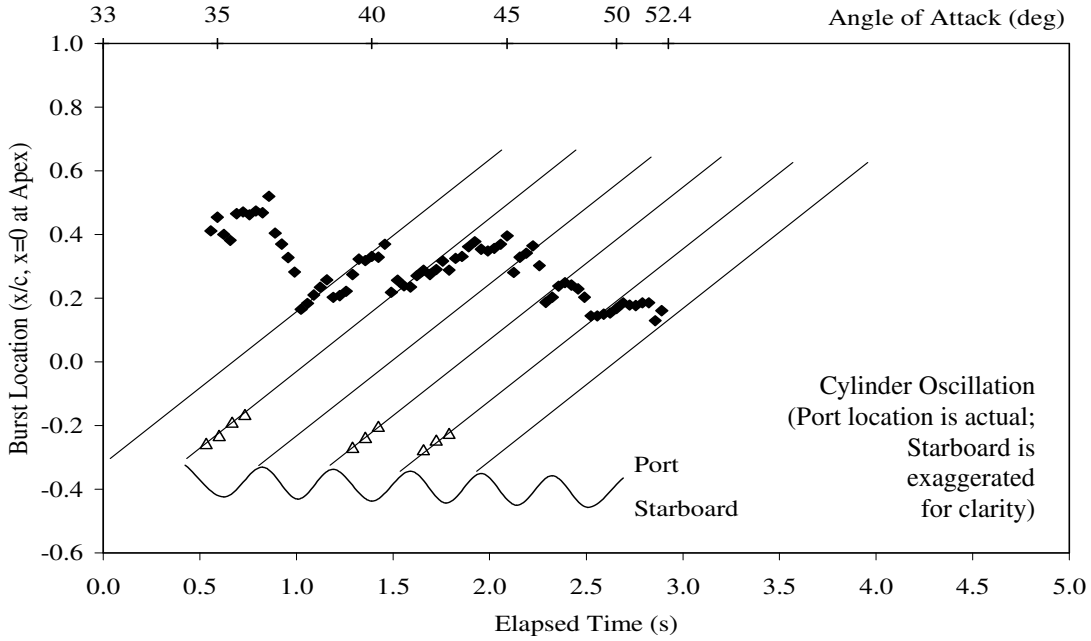

Figure 6.41. Large Cylinder, Pitch-Up Initiation Synchronized to Cylinder's Port Deflection, $35 < \alpha < 55$ degrees, $\kappa = 0.1$ (Experiment 1).

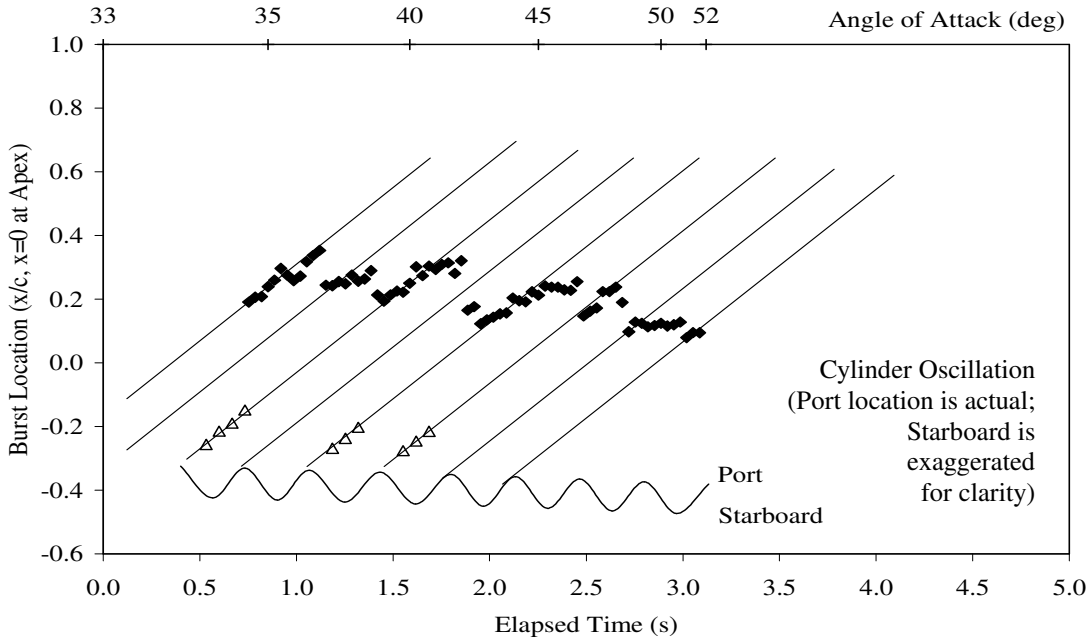

Figure 6.42. Large Cylinder, Pitch-Up Initiation Synchronized to Cylinder's Port Deflection, $35 < \alpha < 55$ degrees, $\kappa = 0.1$ (Experiment 2).

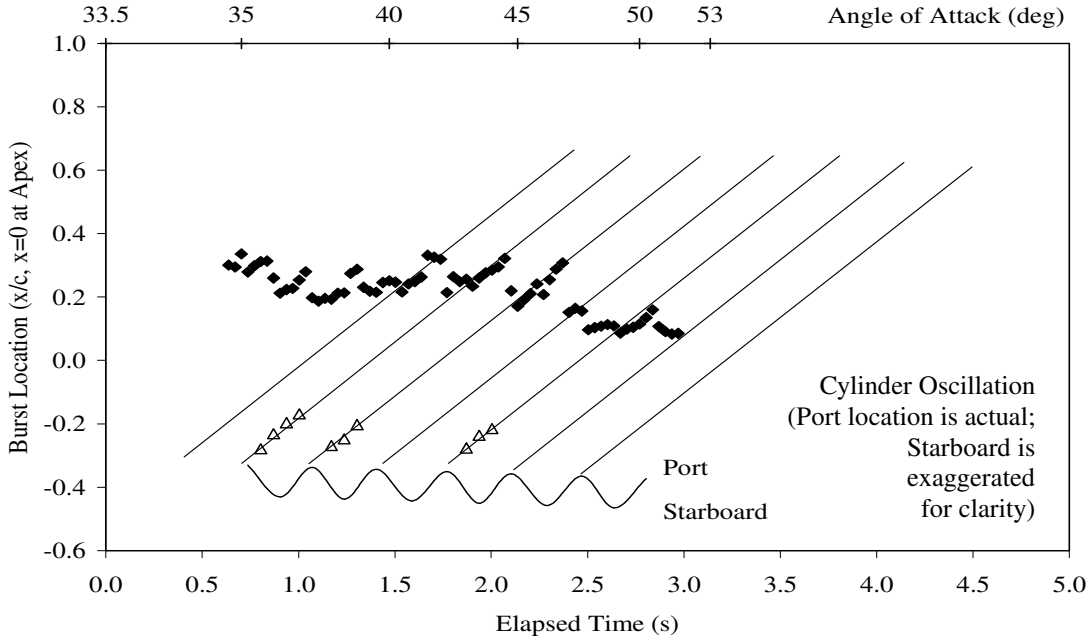

Figure 6.43. Large Cylinder, Pitch-Up Initiation Synchronized to Cylinder's Port Deflection, $35 < \alpha < 55$ degrees, $\kappa = 0.1$ (Experiment 3).

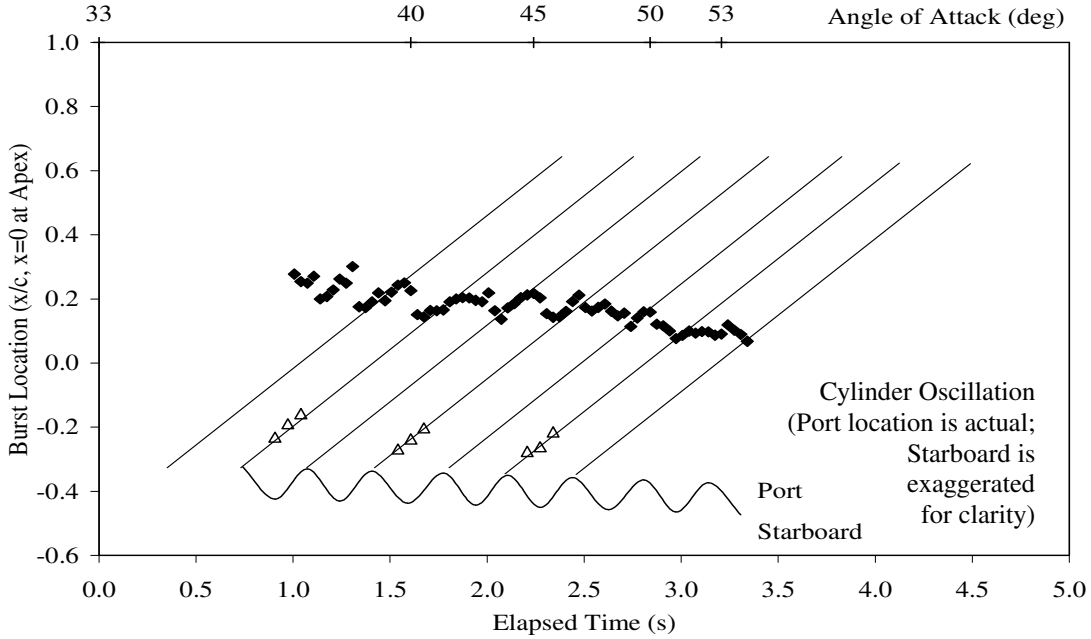

Figure 6.44. Large Cylinder, Pitch-Up Initiation Synchronized to Cylinder's Center to Port Deflection, $35 < \alpha < 55$ degrees, $\kappa = 0.1$ (Experiment 1).

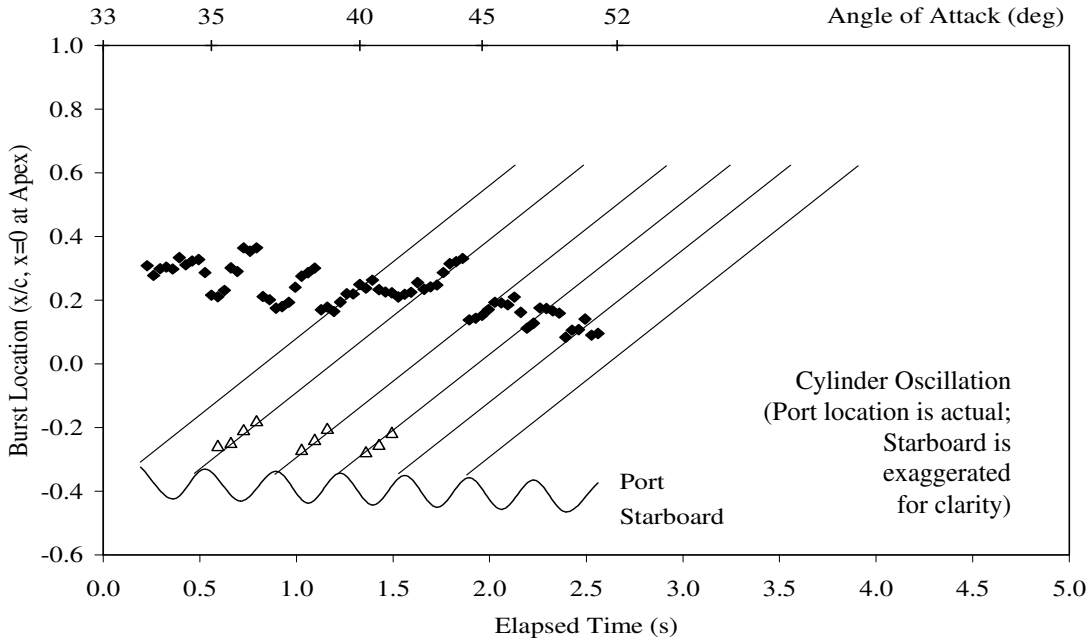

Figure 6.45. Large Cylinder, Pitch-Up Initiation Synchronized to Cylinder's Center to Port Deflection, $35 < \alpha < 55$ degrees, $\kappa = 0.1$ (Experiment 2).

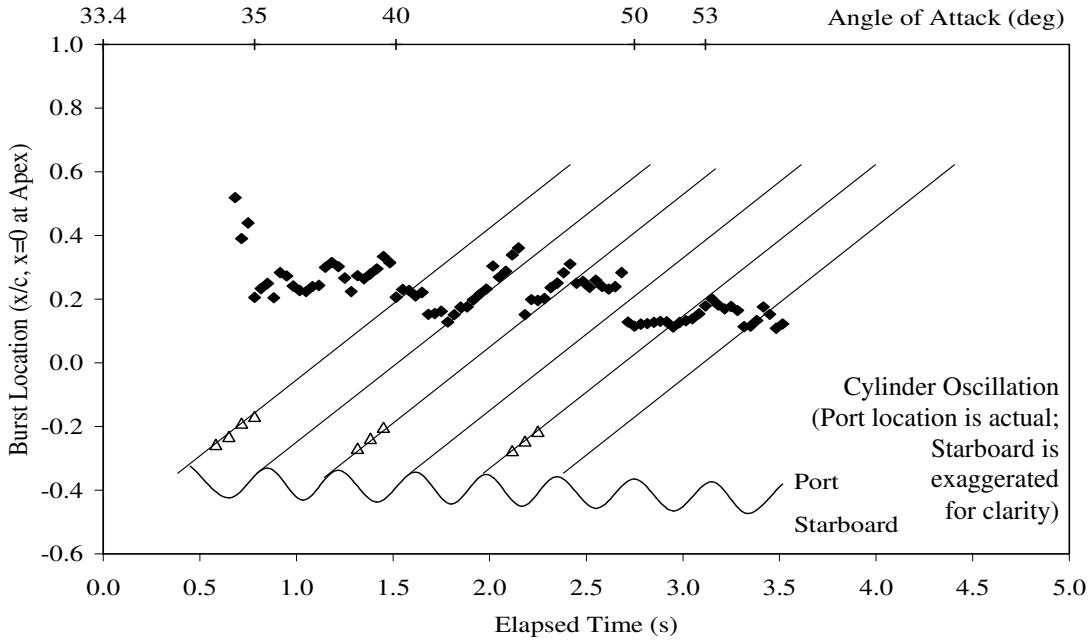

Figure 6.46. Large Cylinder, Pitch-Up Initiation Synchronized to Cylinder's Center to Port Deflection, $35 < \alpha < 55$ degrees, $\kappa = 0.1$ (Experiment 3).

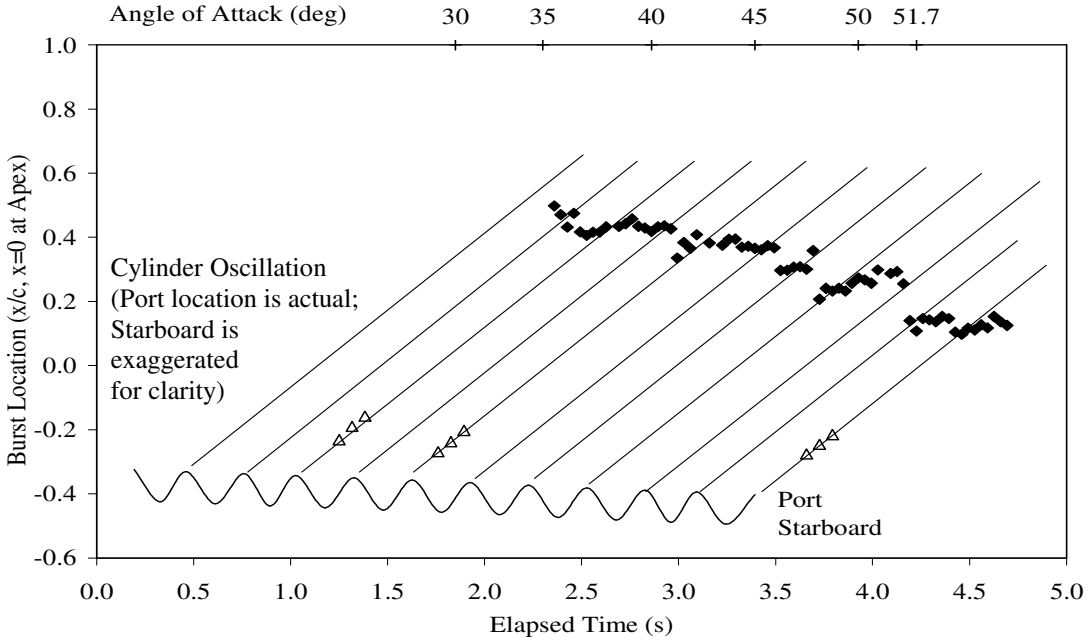

Figure 6.47. Small Cylinder, Pitch-Up Initiation Synchronized to Cylinder's Port Deflection, $15 < \alpha < 55$ degrees, $\kappa = 0.2$ (Experiment 1).

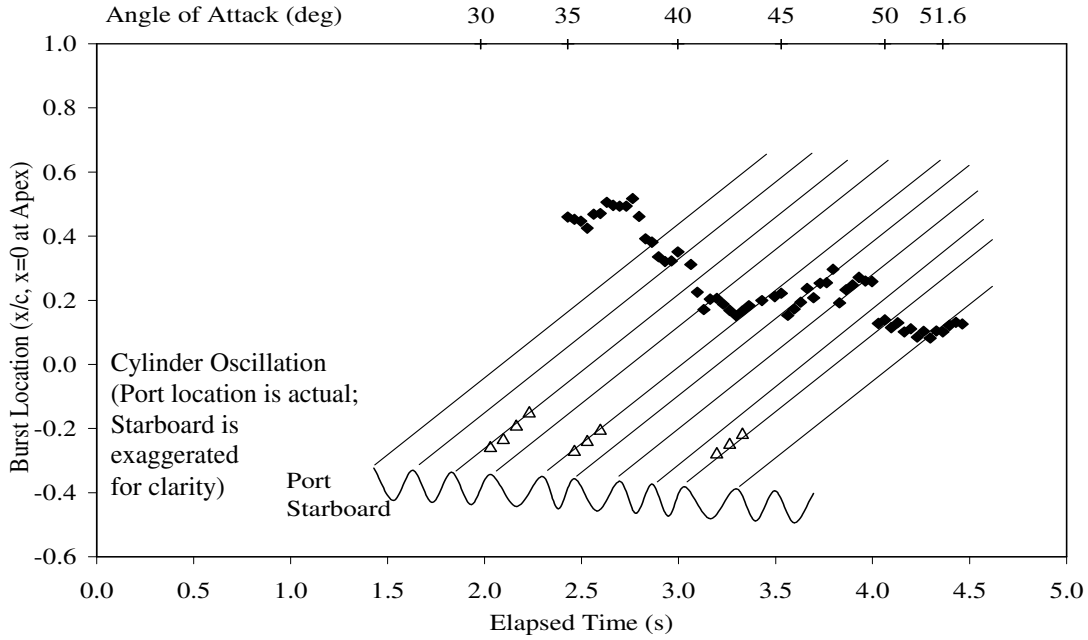

Figure 6.48. Small Cylinder, Pitch-Up Initiation Synchronized to Cylinder's Port Deflection, $15 < \alpha < 55$ degrees, $\kappa = 0.2$ (Experiment 2).

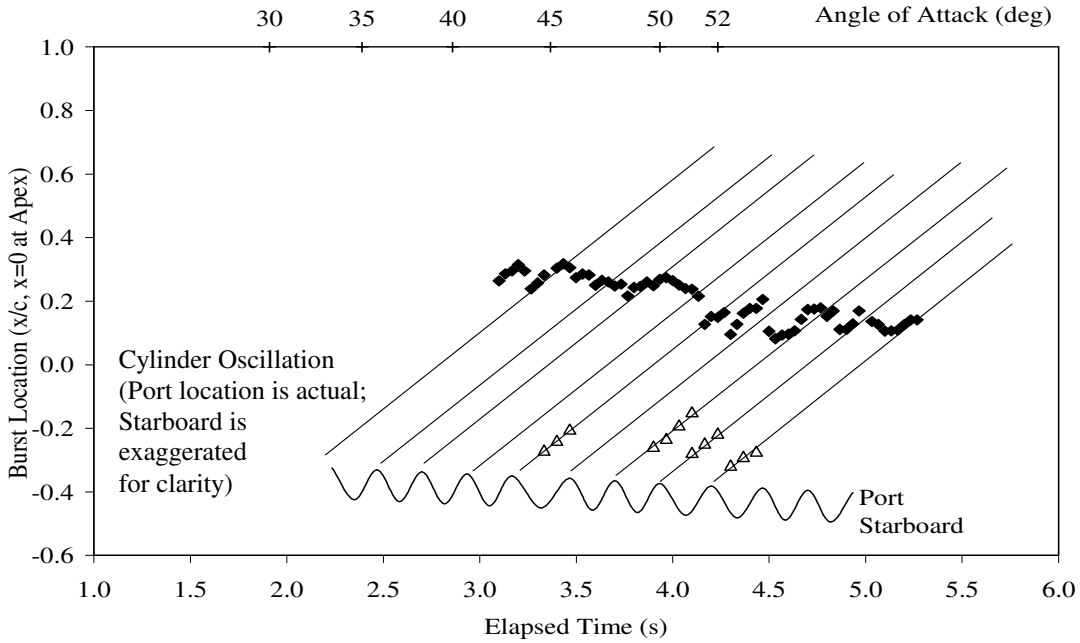

Figure 6.49. Small Cylinder, Pitch-Up Initiation Synchronized to Cylinder's Port Deflection, $15 < \alpha < 55$ degrees, $\kappa = 0.2$ (Experiment 3).

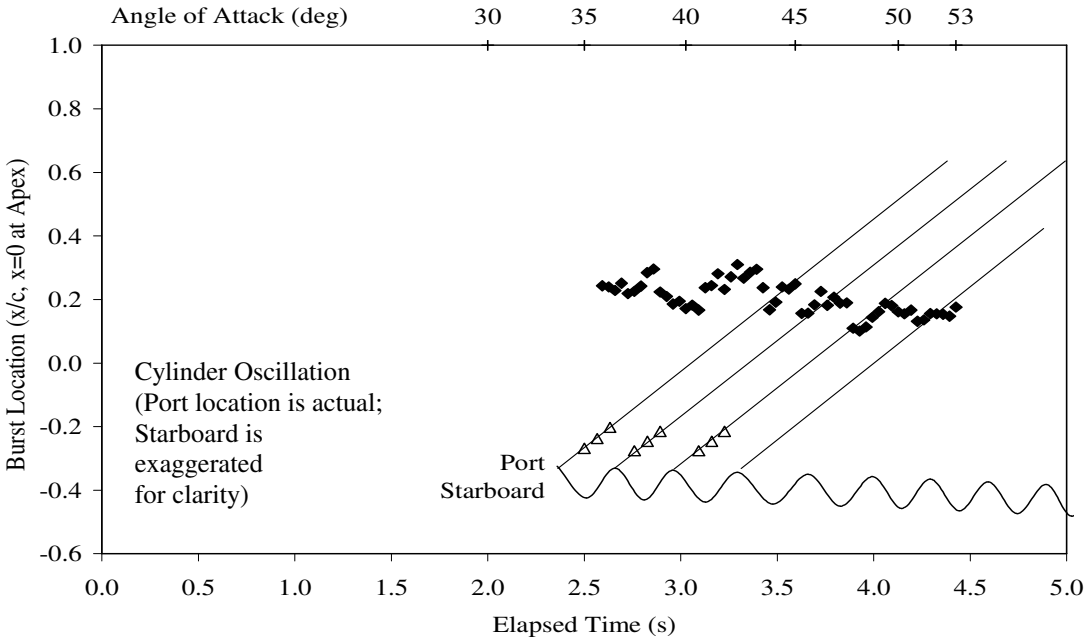

Figure 6.50. Small Cylinder, Pitch-Up Initiation Synchronized to Cylinder's Center to Starboard Deflection, $15 < \alpha < 55$ degrees, $\kappa = 0.2$ (Experiment 1).

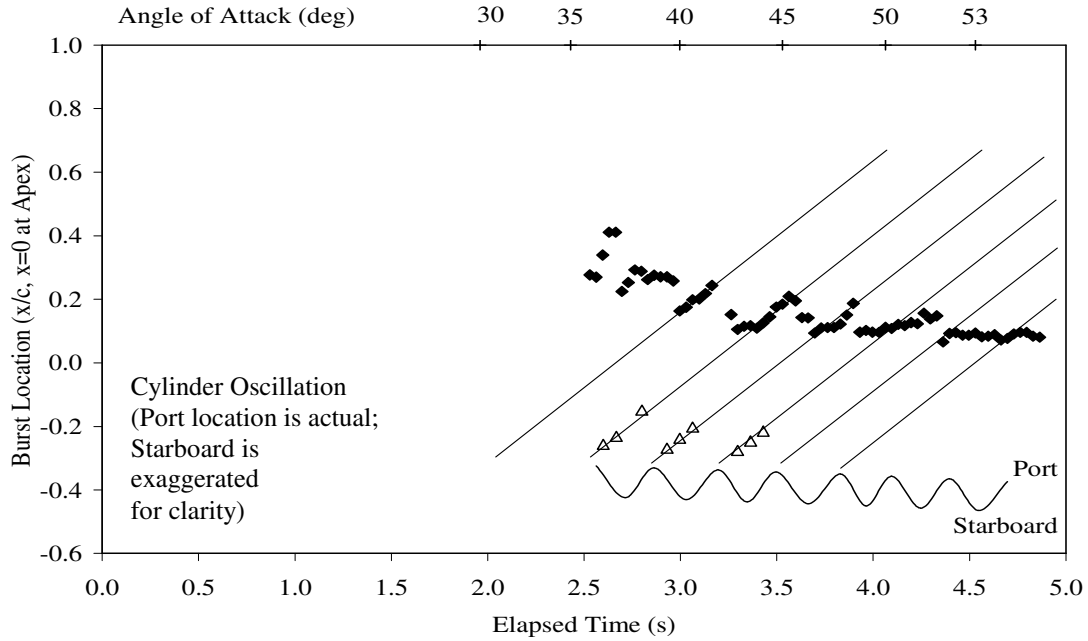

Figure 6.51. Small Cylinder, Pitch-Up Initiation Synchronized to Cylinder's Center to Starboard Deflection, $15 < \alpha < 55$ degrees, $\kappa = 0.2$ (Experiment 2).

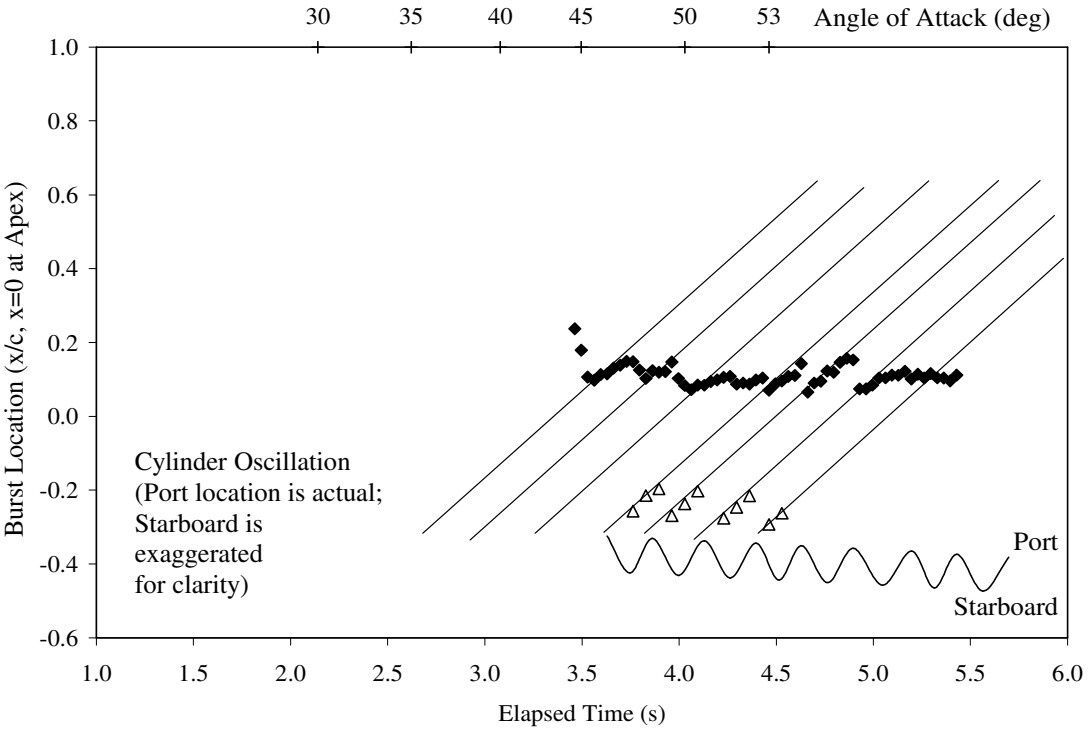

Figure 6.52. Small Cylinder, Pitch-Up Initiation Synchronized to Cylinder's Center to Starboard Deflection, $15 < \alpha < 55$ degrees, $\kappa = 0.2$ (Experiment 3).

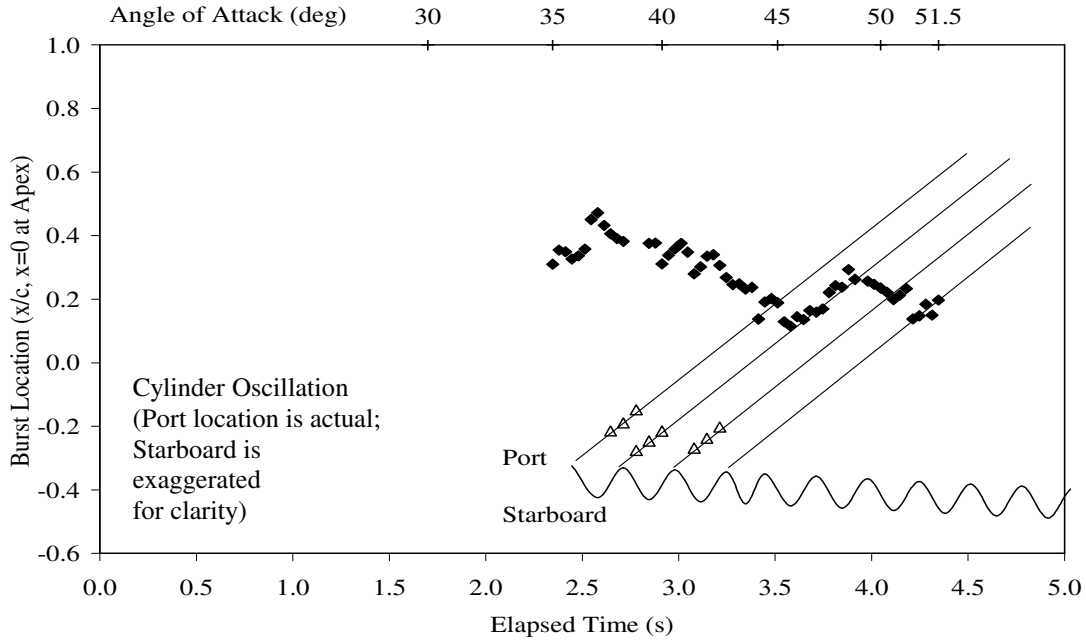

Figure 6.53. Small Cylinder, Pitch-Up Initiation Synchronized to Cylinder's Starboard Deflection, $15 < \alpha < 55$ degrees, $\kappa = 0.2$ (Experiment 1).

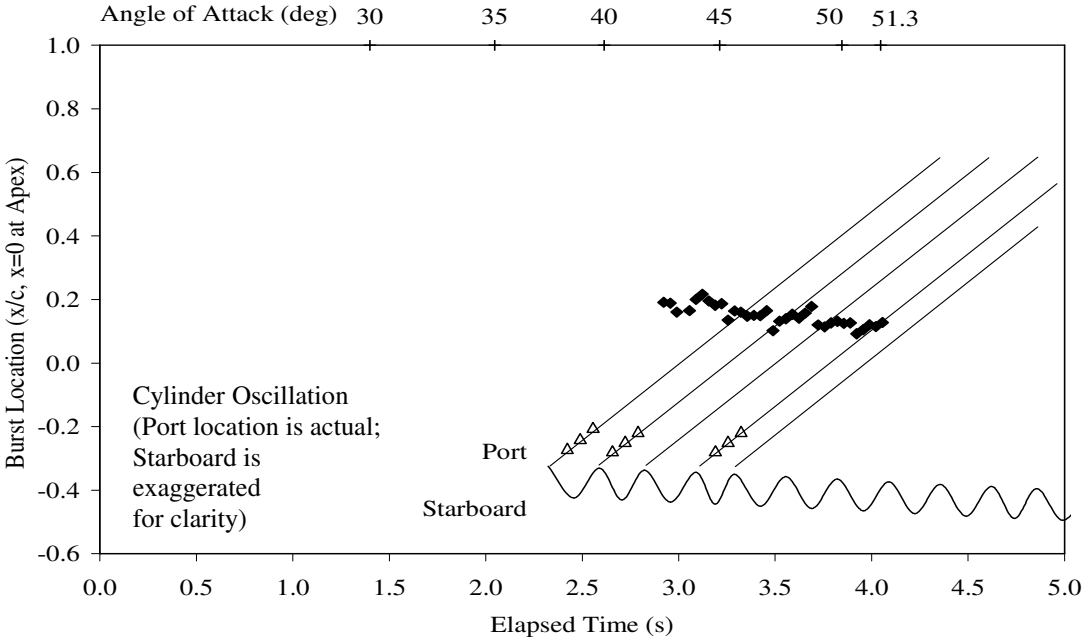

Figure 6.54. Small Cylinder, Pitch-Up Initiation Synchronized to Cylinder's Starboard Deflection, $15 < \alpha < 55$ degrees, $\kappa = 0.2$ (Experiment 2).

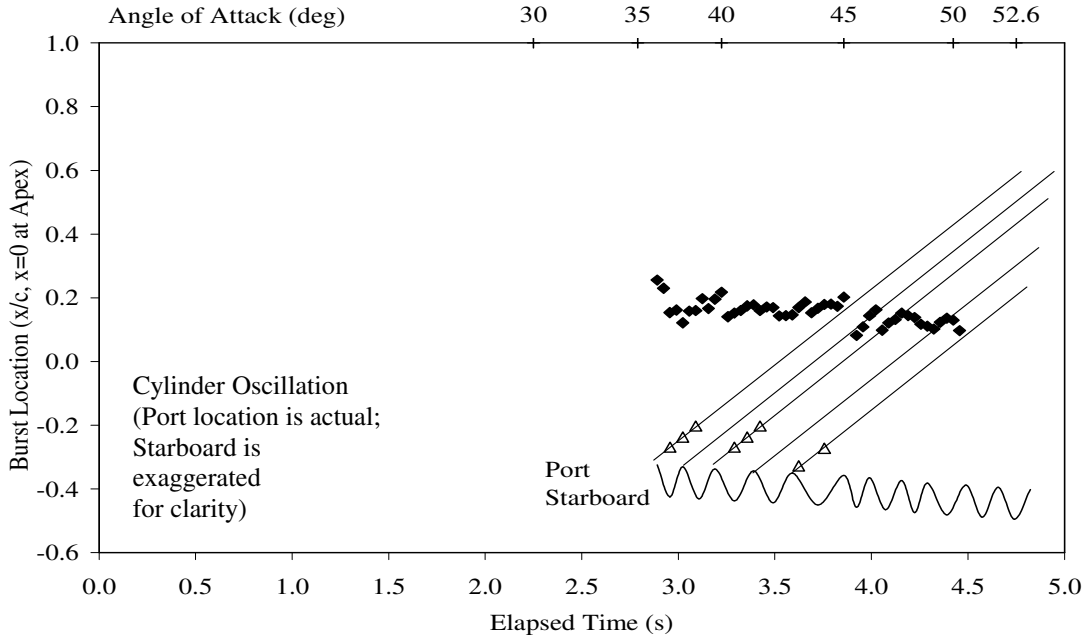

Figure 6.55. Small Cylinder, Pitch-Up Initiation Synchronized to Cylinder's Starboard Deflection, $15 < \alpha < 55$ degrees, $\kappa = 0.2$ (Experiment 3).

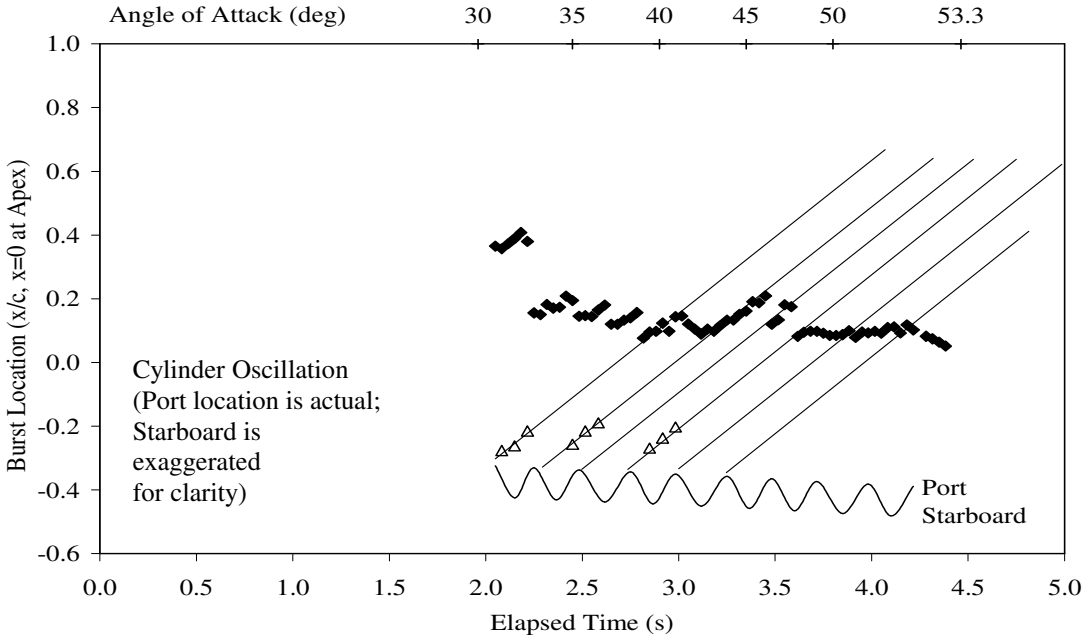

Figure 6.56. Small Cylinder, Pitch-Up Initiation Synchronized to Cylinder's Center to Port Deflection, $15 < \alpha < 55$ degrees, $\kappa = 0.2$ (Experiment 1).

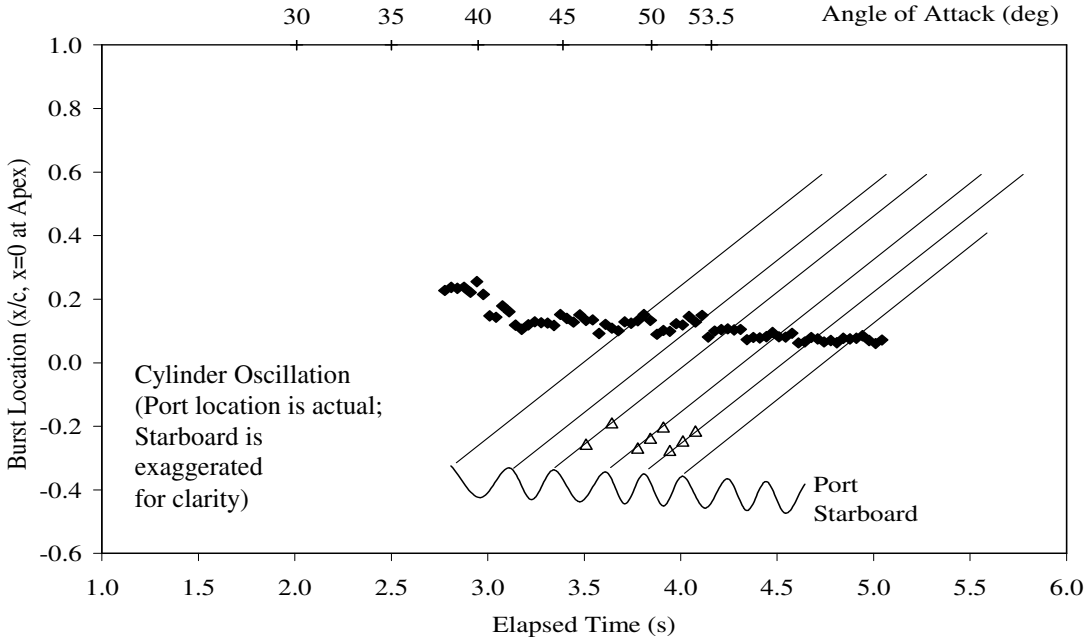

Figure 6.57. Small Cylinder Pitch-Up Initiation Synchronized to Cylinder's Center to Port Deflection, $15 < \alpha < 55$ degrees, $\kappa = 0.2$ (Experiment 2).

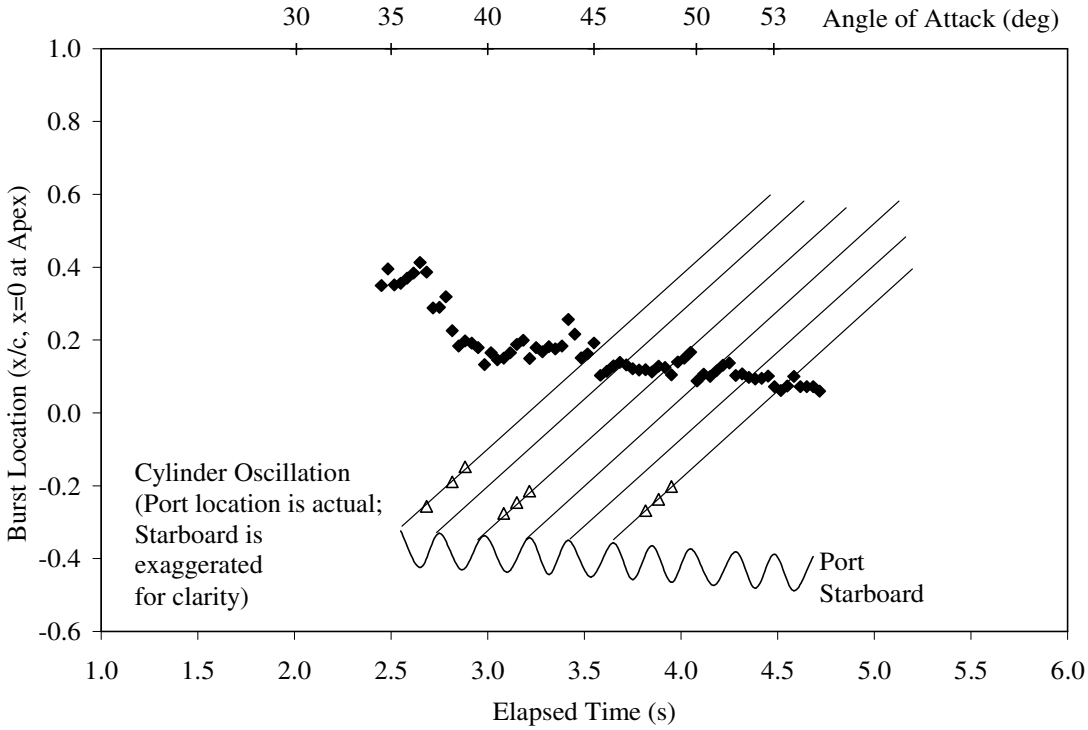

Figure 6.58. Small Cylinder, Pitch-Up Initiation Synchronized to Cylinder's Center to Port Deflection, $15 < \alpha < 55$ degrees, $\kappa = 0.2$ (Experiment 3).

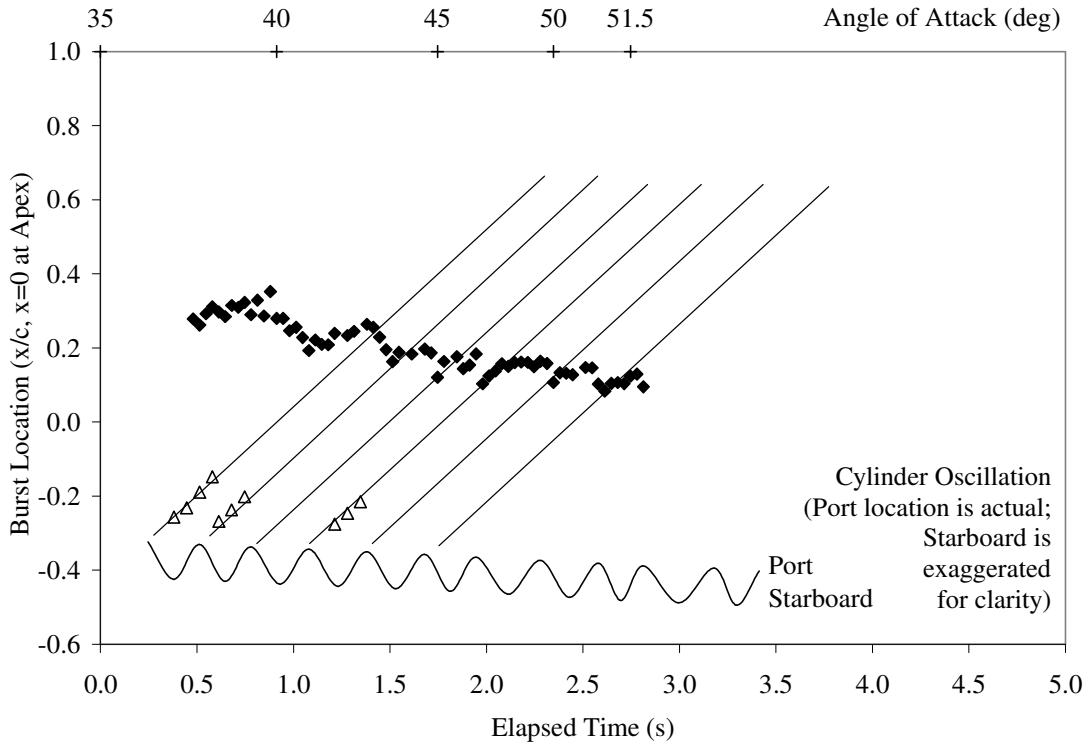

Figure 6.59. Small Cylinder, Pitch-Up Initiation Synchronized to Cylinder's Port Deflection, $35 < \alpha < 55$ degrees, $\kappa = 0.2$ (Experiment 1).

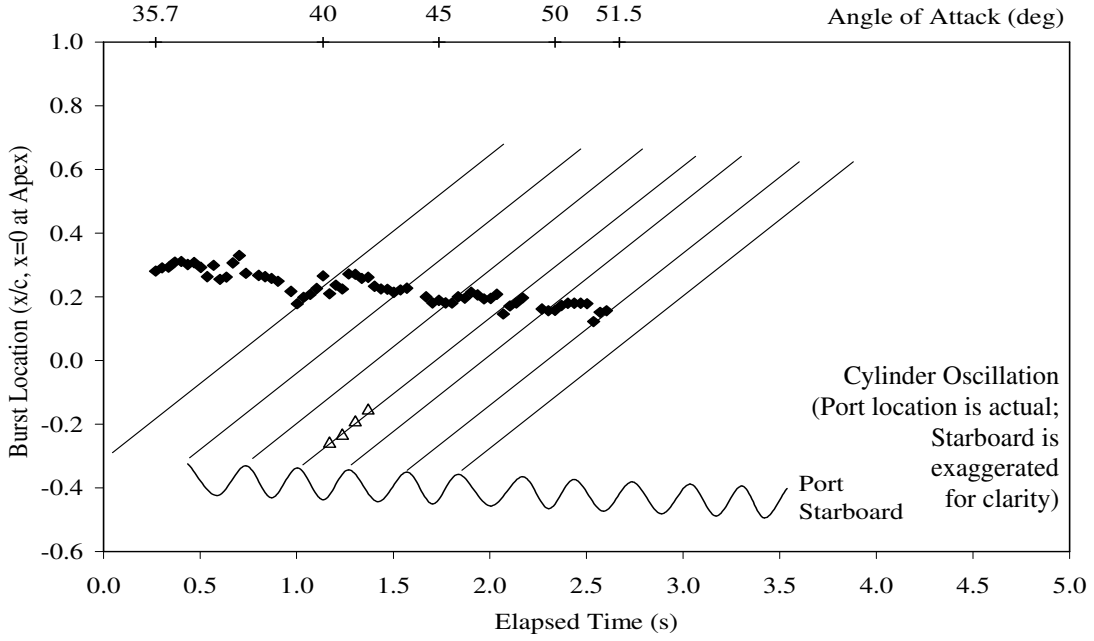

Figure 6.60. Small Cylinder, Pitch-Up Initiation Synchronized to Cylinder's Port Deflection, $35 < \alpha < 55$ degrees, $\kappa = 0.2$ (Experiment 2).

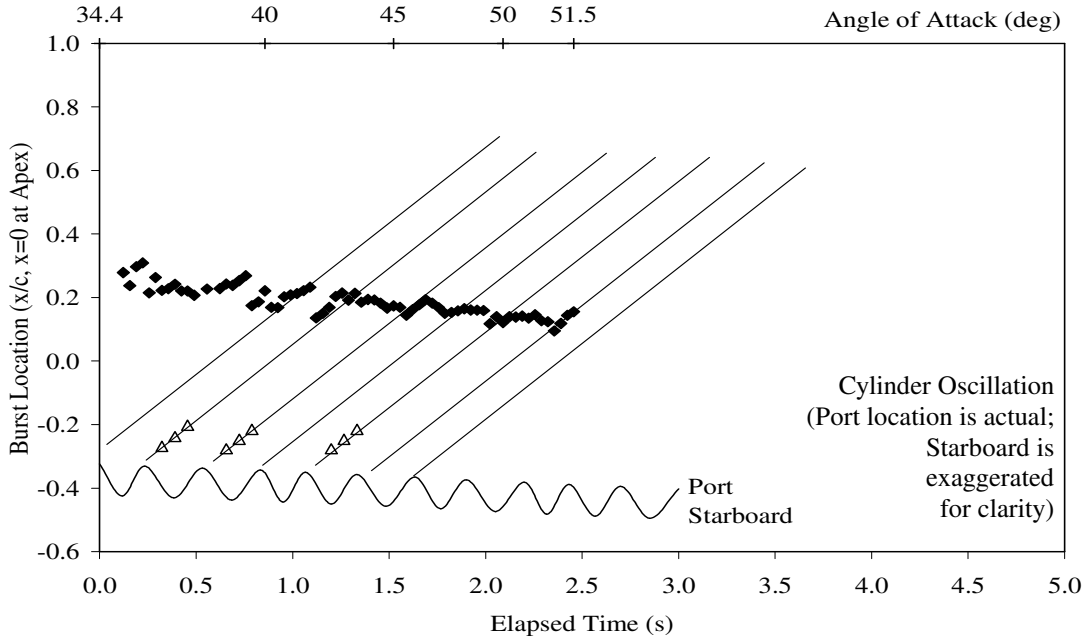

Figure 6.61. Small Cylinder, Pitch-Up Initiation Synchronized to Cylinder's Port Deflection, $35 < \alpha < 55$ degrees, $\kappa = 0.2$ (Experiment 3).

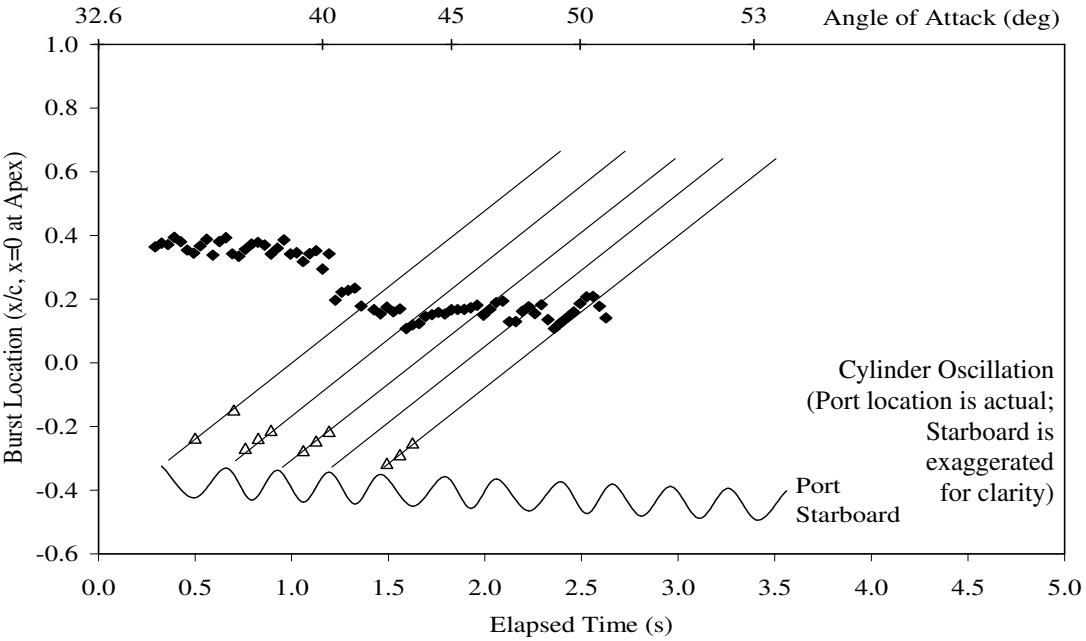

Figure 6.62. Small Cylinder, Pitch-Up Initiation Synchronized to Cylinder's Center to Starboard Deflection, $35 < \alpha < 55$ degrees, $\kappa = 0.2$ (Experiment 1).

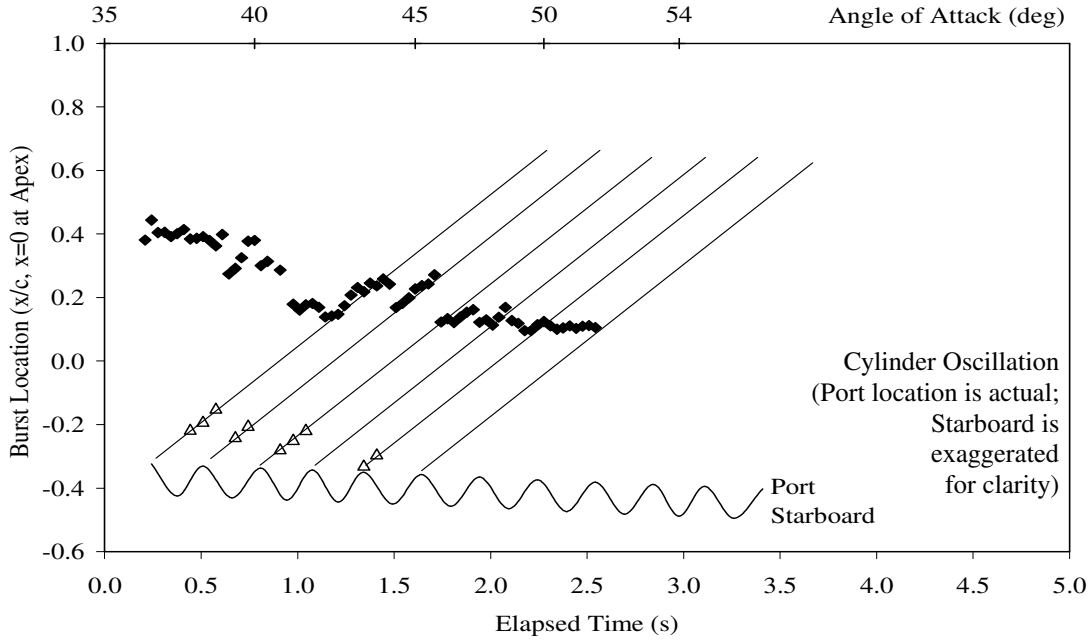

Figure 6.63. Small Cylinder, Pitch-Up Initiation Synchronized to Cylinder's Center to Starboard Deflection, $35 < \alpha < 55$ degrees, $\kappa = 0.2$ (Experiment 2).

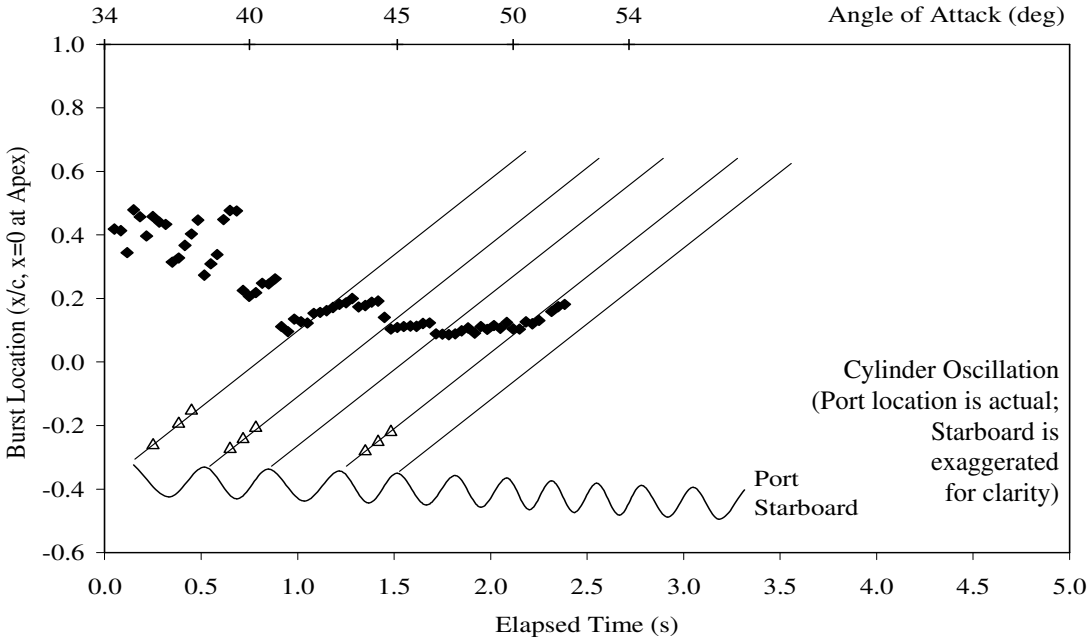

Figure 6.64. Small Cylinder, Pitch-Up Initiation Synchronized to Cylinder's Center to Starboard Deflection, $35 < \alpha < 55$ degrees, $\kappa = 0.2$ (Experiment 3).

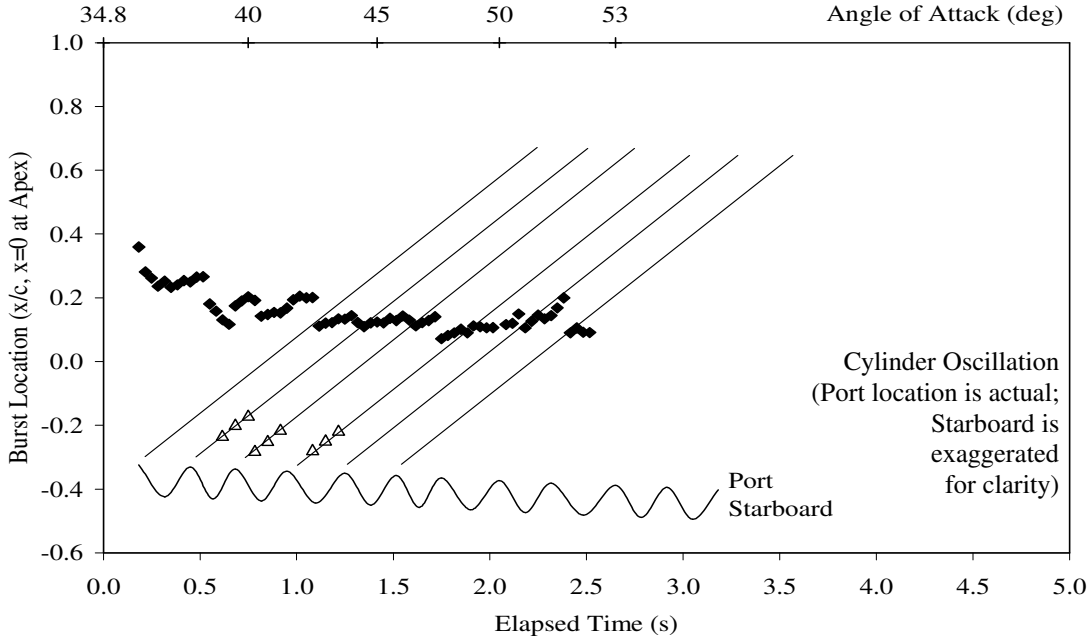

Figure 6.65. Small Cylinder, Pitch-Up Initiation Synchronized to Cylinder's Starboard Deflection, $35 < \alpha < 55$ degrees, $\kappa = 0.2$ (Experiment 1).

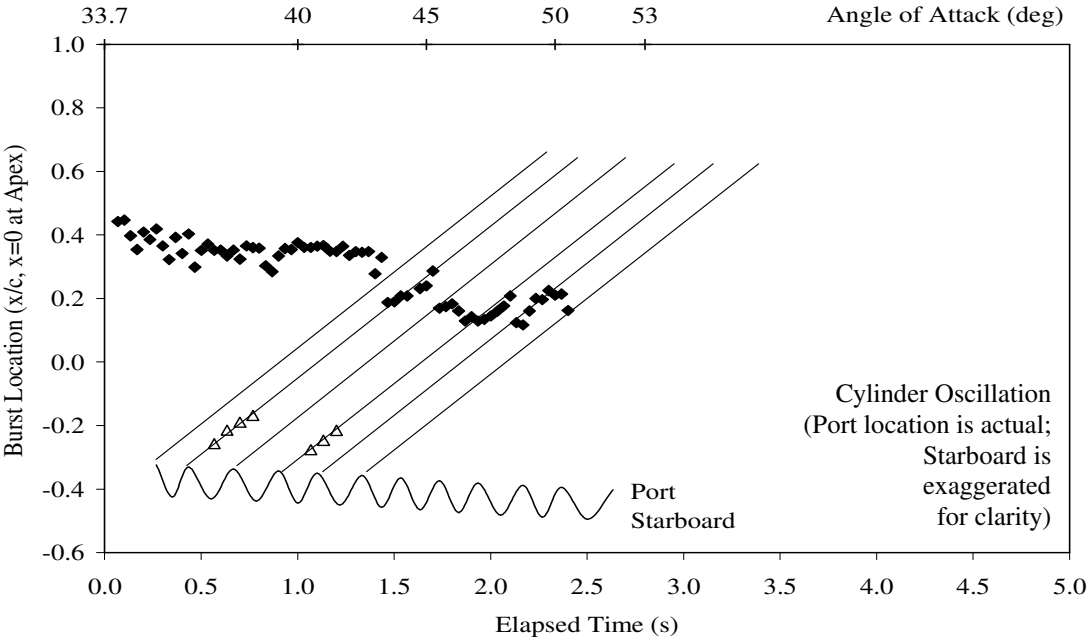

Figure 6.66. Small Cylinder, Pitch-Up Initiation Synchronized to Cylinder's Center to Port Deflection, $35 < \alpha < 55$ degrees, $\kappa = 0.2$ (Experiment 1).

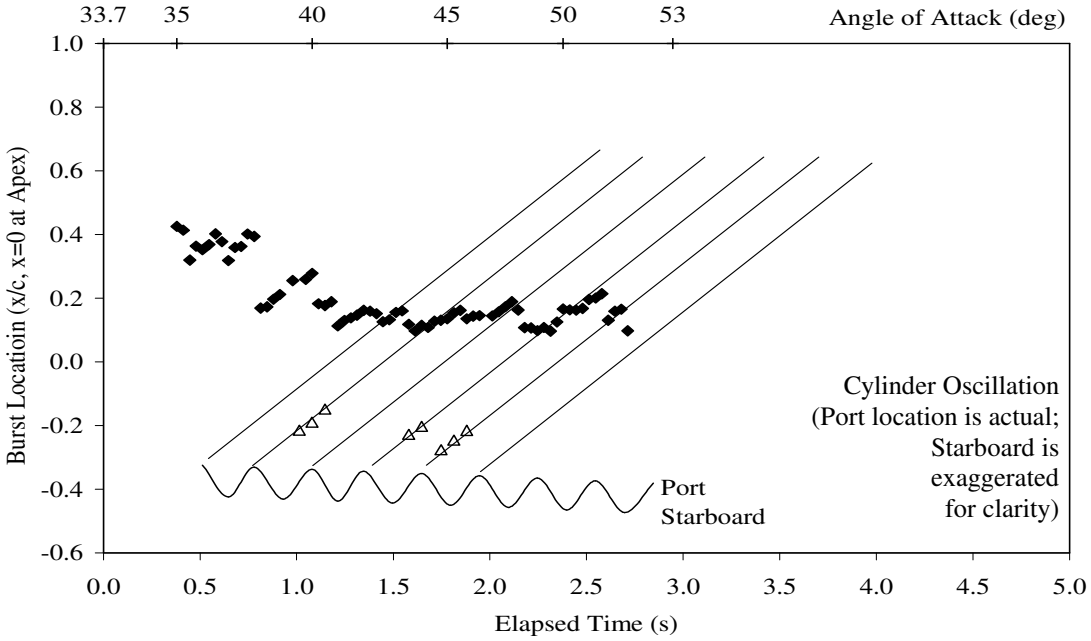

Figure 6.67. Small Cylinder, Pitch-Up Initiation Synchronized to Cylinder's Center to Port Deflection, $35 < \alpha < 55$ degrees, $\kappa = 0.2$ (Experiment 2).

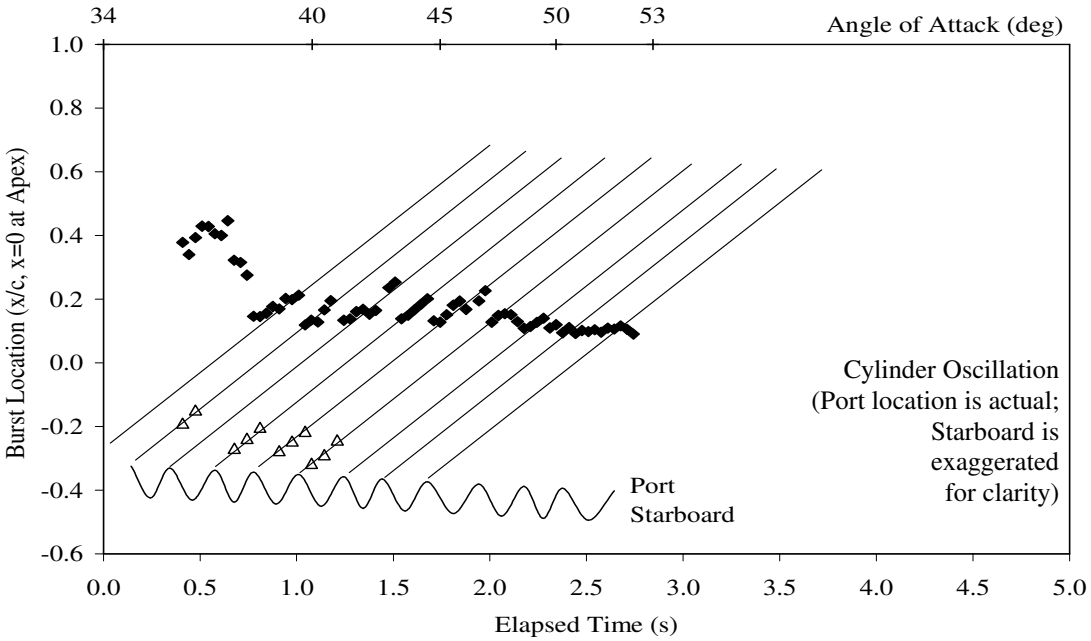

Figure 6.68. Small Cylinder, Pitch-Up Initiation Synchronized to Cylinder's Center to Port Deflection, $35 < \alpha < 55$ degrees, $\kappa = 0.2$ (Experiment 3).

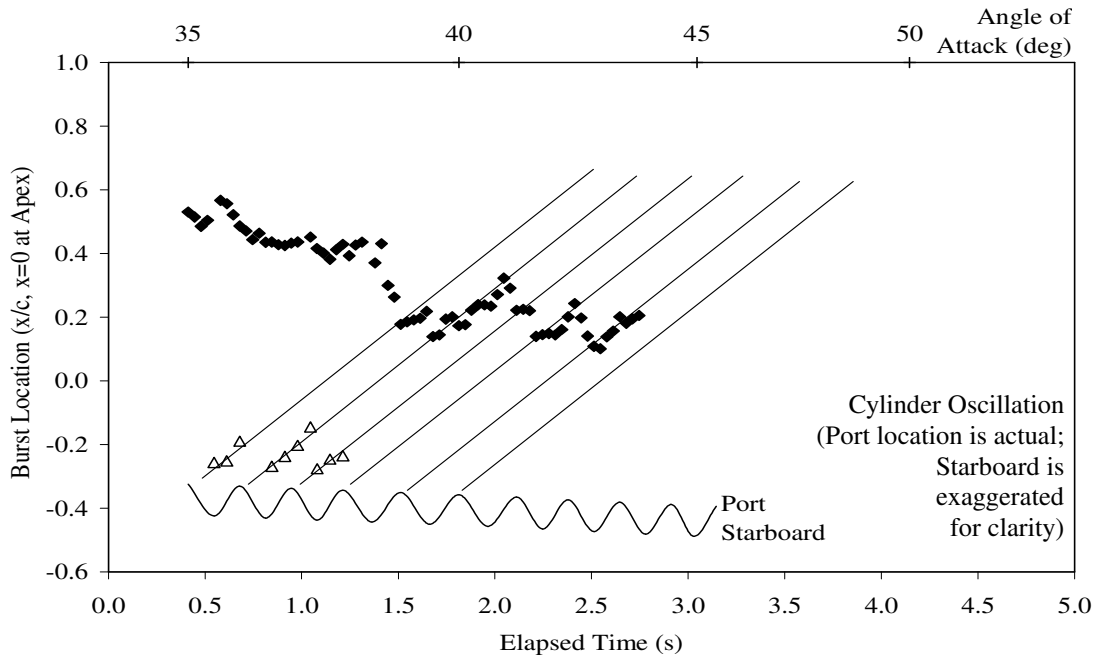

Figure 6.69. Small Cylinder, Pitch-Up Initiation Synchronized to Cylinder's Port Deflection, $35 < \alpha < 55$ degrees, $\kappa = 0.1$ (Experiment1).

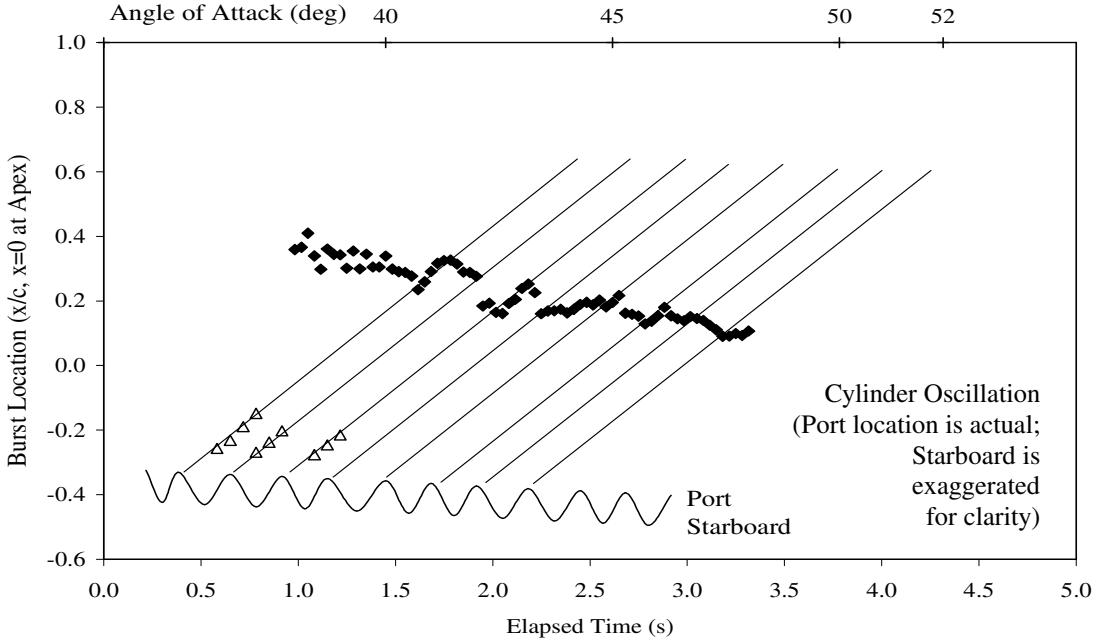

Figure 6.70. Small Cylinder, Pitch-Up Initiation Synchronized to Cylinder's Port Deflection, $35 < \alpha < 55$ degrees, $\kappa = 0.1$ (Experiment 2).

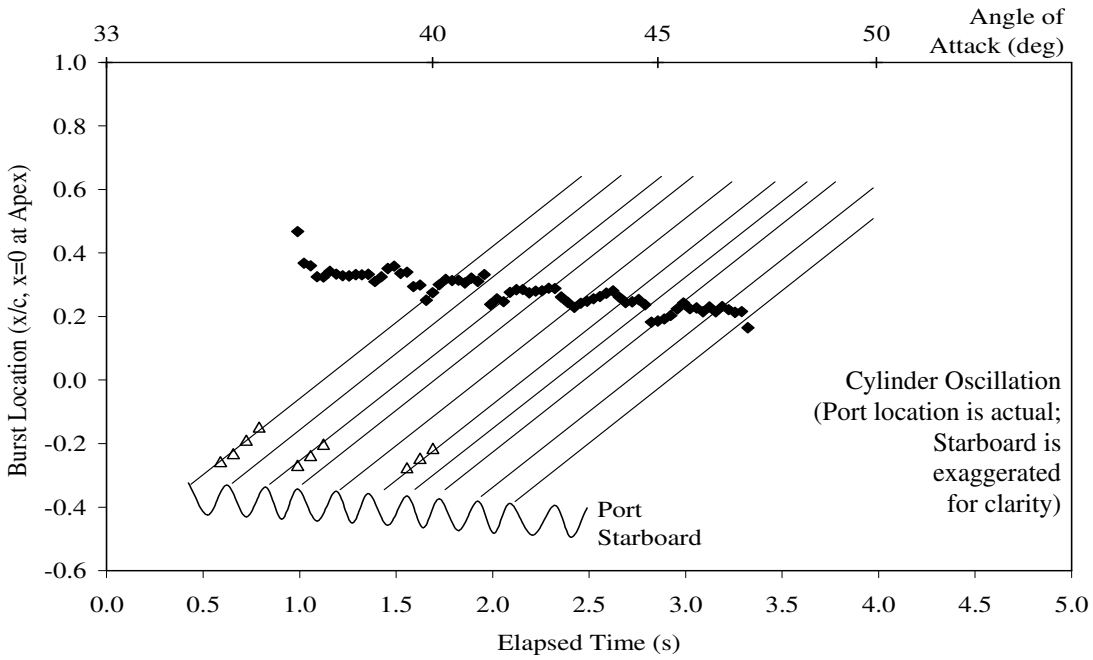

Figure 6.71. Small Cylinder, Pitch-Up Initiation Synchronized to Cylinder's Starboard Deflection, $35 < \alpha < 55$ degrees, $\kappa = 0.1$ (Experiment 1).

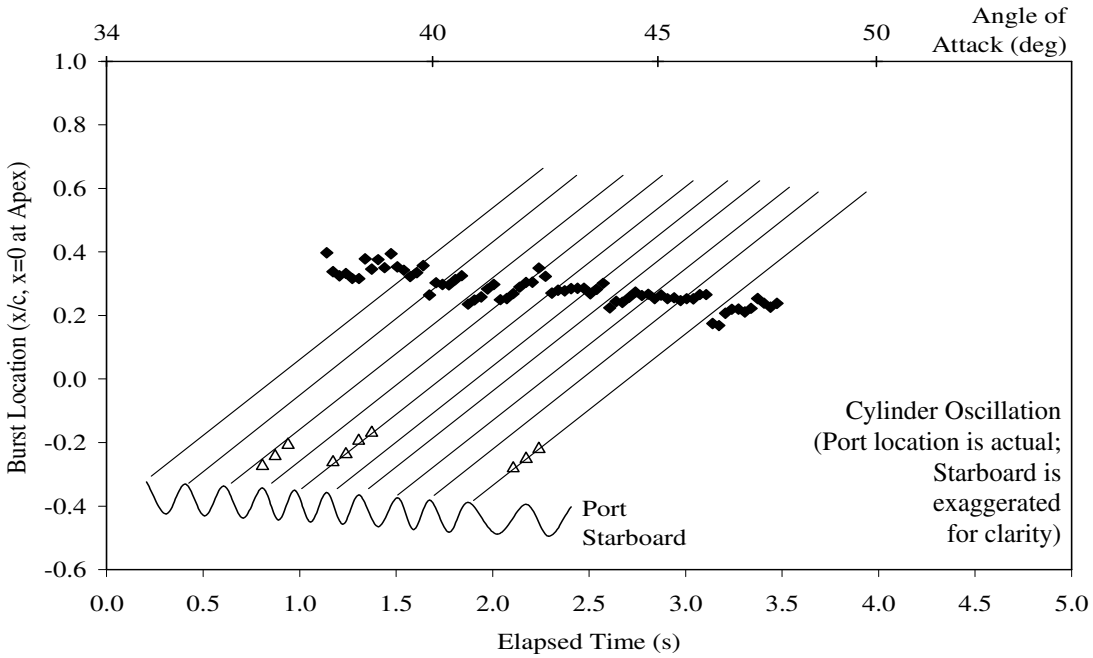

Figure 6.72. Small Cylinder, Pitch-Up Initiation Synchronized to Cylinder's Starboard Deflection, $35 < \alpha < 55$ degrees, $\kappa = 0.1$ (Experiment 2).

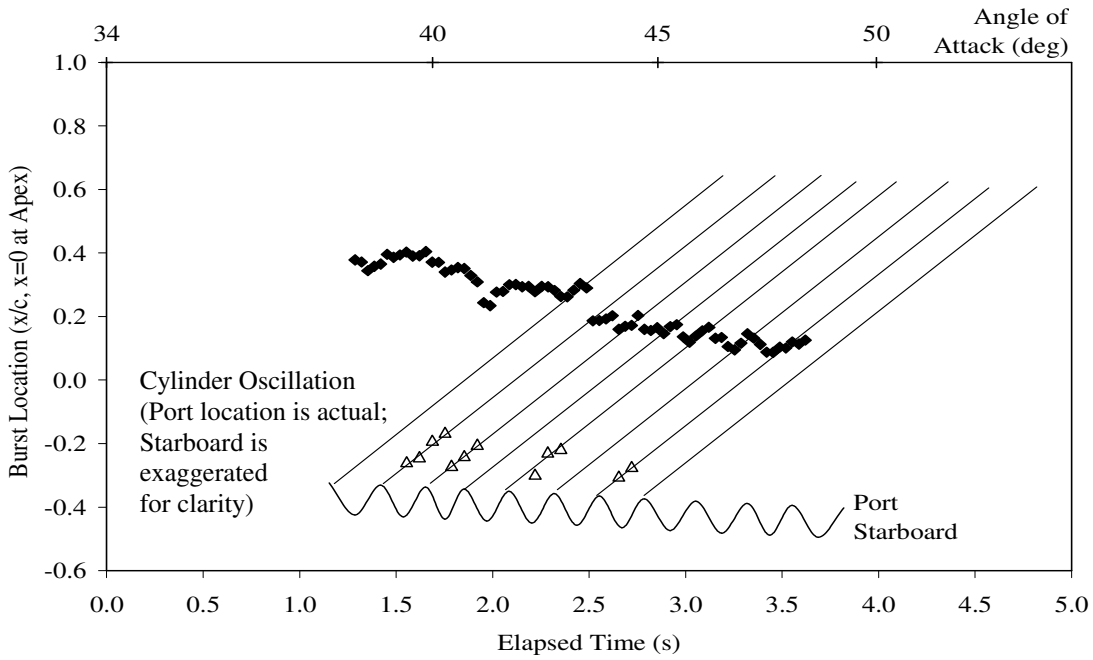

Figure 6.73. Small Cylinder, Pitch-Up Initiation Synchronized to Cylinder's Starboard Deflection, $35 < \alpha < 55$ degrees, $\kappa = 0.1$ (Experiment 3).

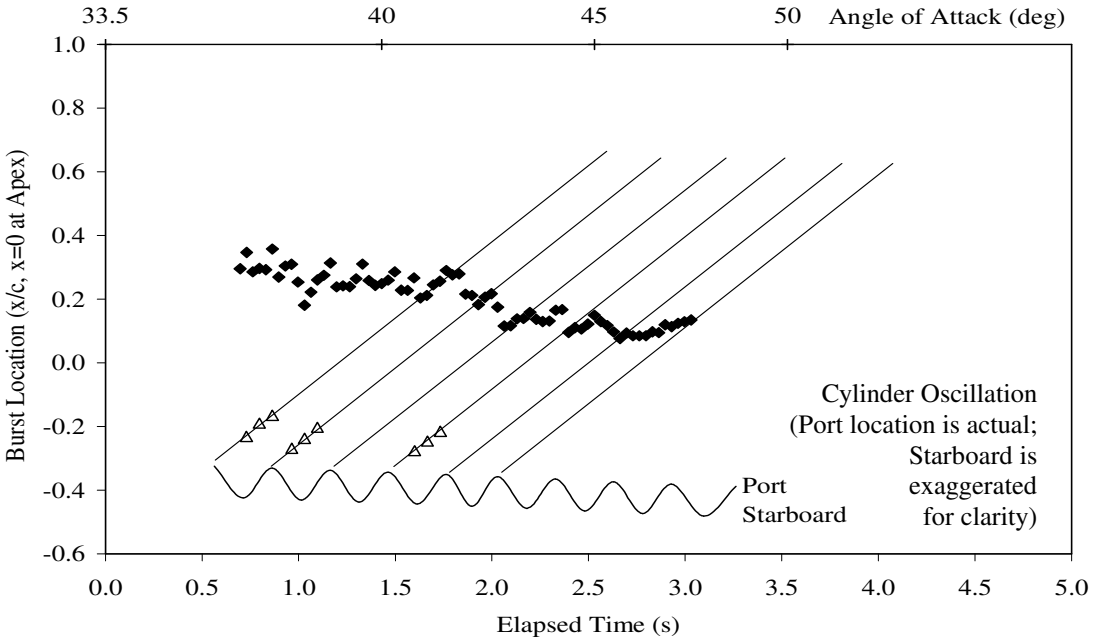

Figure 6.74. Small Cylinder, Pitch-Up Initiation Synchronized to Cylinder's Center to Port Deflection, $35 < \alpha < 55$ degrees, $\kappa = 0.1$ (Experiment 1).

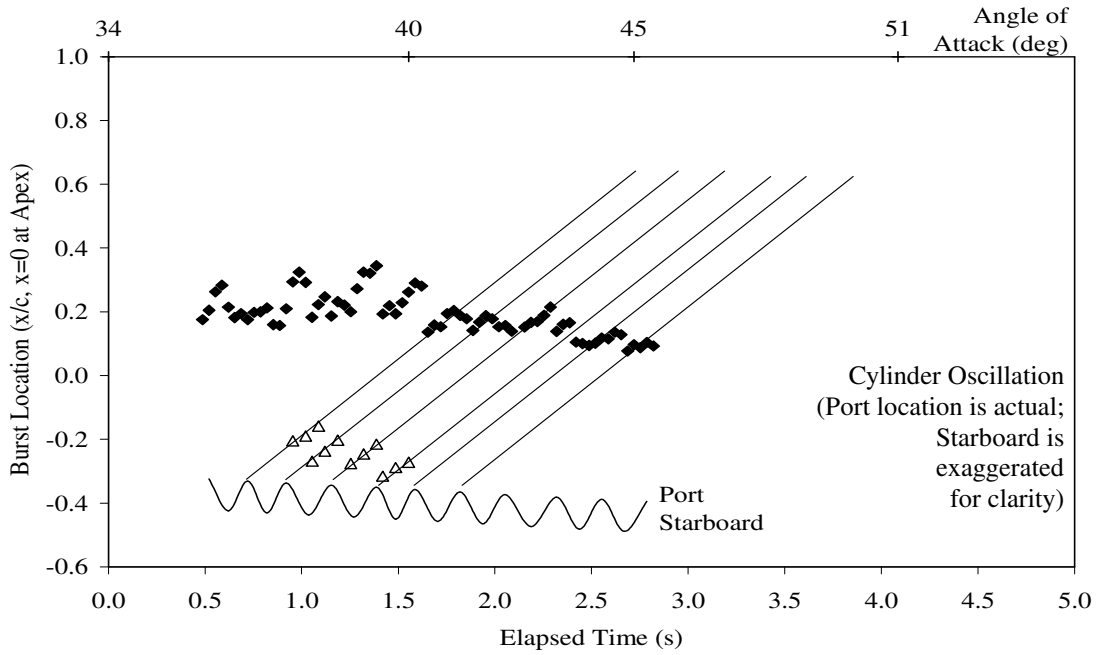

Figure 6.75. Small Cylinder, Pitch-Up Initiation Synchronized to Cylinder's Center to Port Deflection, $35 < \alpha < 55$ degrees, $\kappa = 0.1$ (Experiment 2).

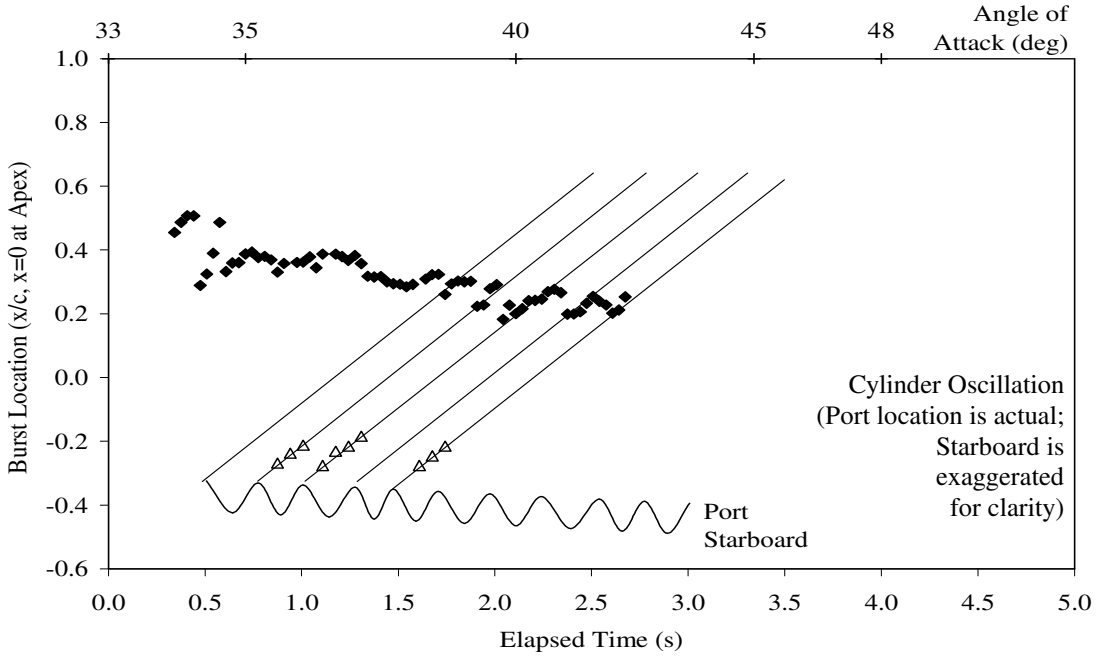

Figure 6.76. Small Cylinder, Pitch-Up Initiation Synchronized to Cylinder's Center to Port Deflection, $35 < \alpha < 55$ degrees, $\kappa = 0.1$ (Experiment 3).

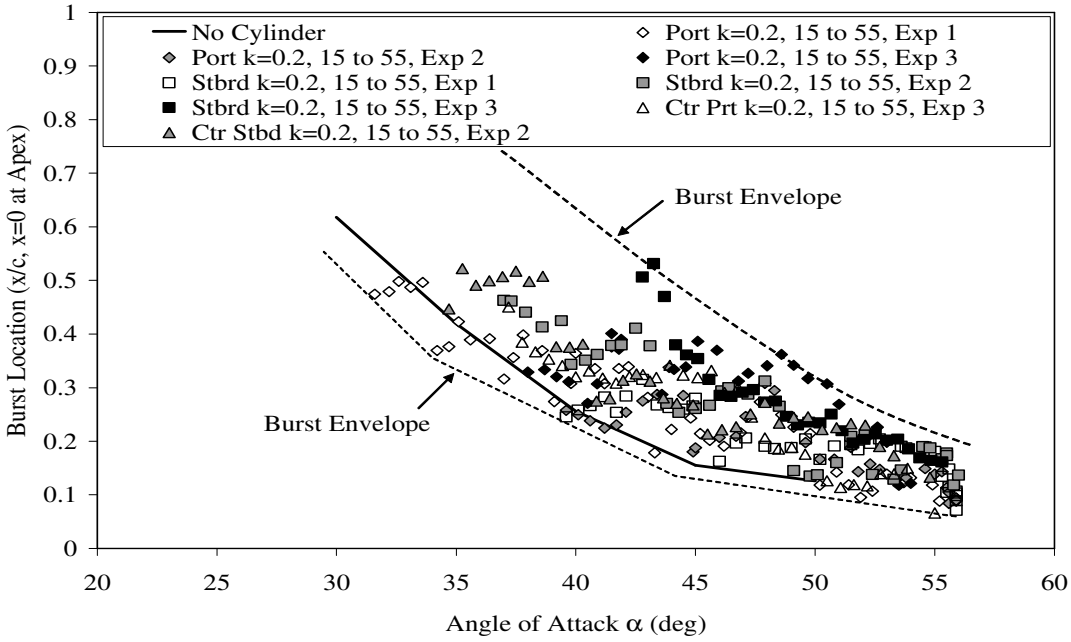

Figure 6.77. Large Cylinder Burst Envelope, Sample Experiments, $\kappa = 0.2$, $15 < \alpha < 55$ deg.

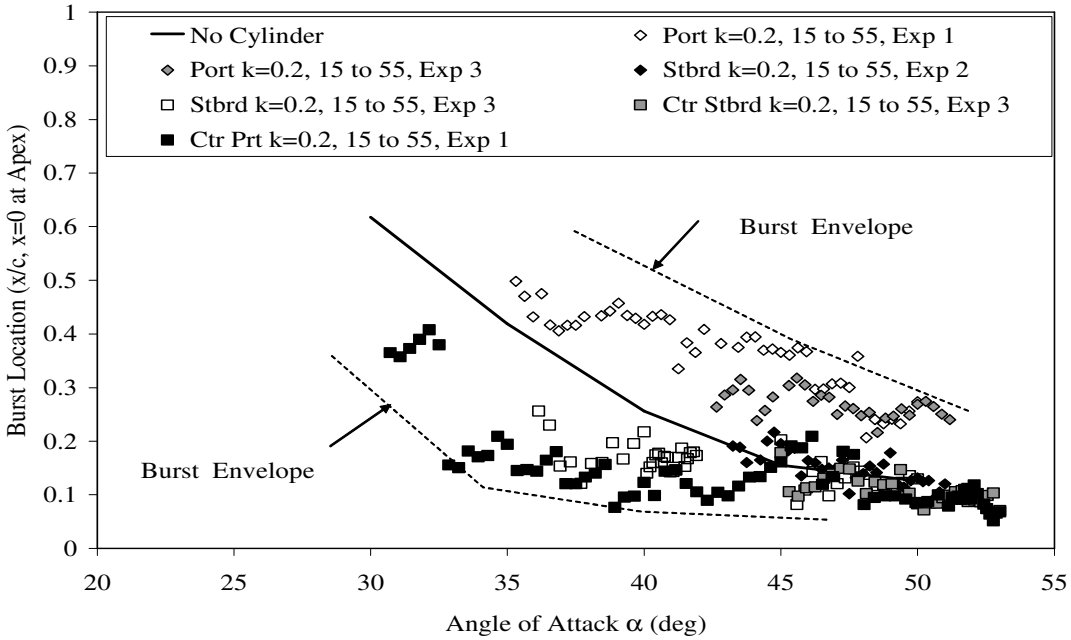

Figure 6.78. Small Cylinder Burst Envelope, Sample Experiments, $\kappa = 0.2$, $15 < \alpha < 55$ deg.

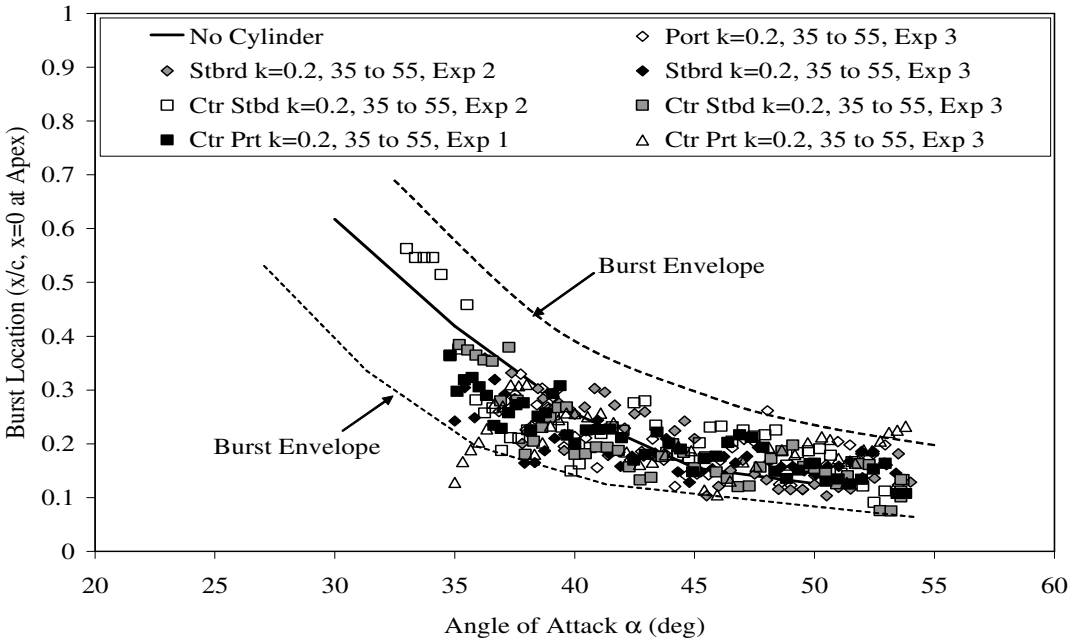

Figure 6.79. Large Cylinder Burst Envelope, Sample Experiments, $\kappa = 0.2$, $35 < \alpha < 55$ deg.

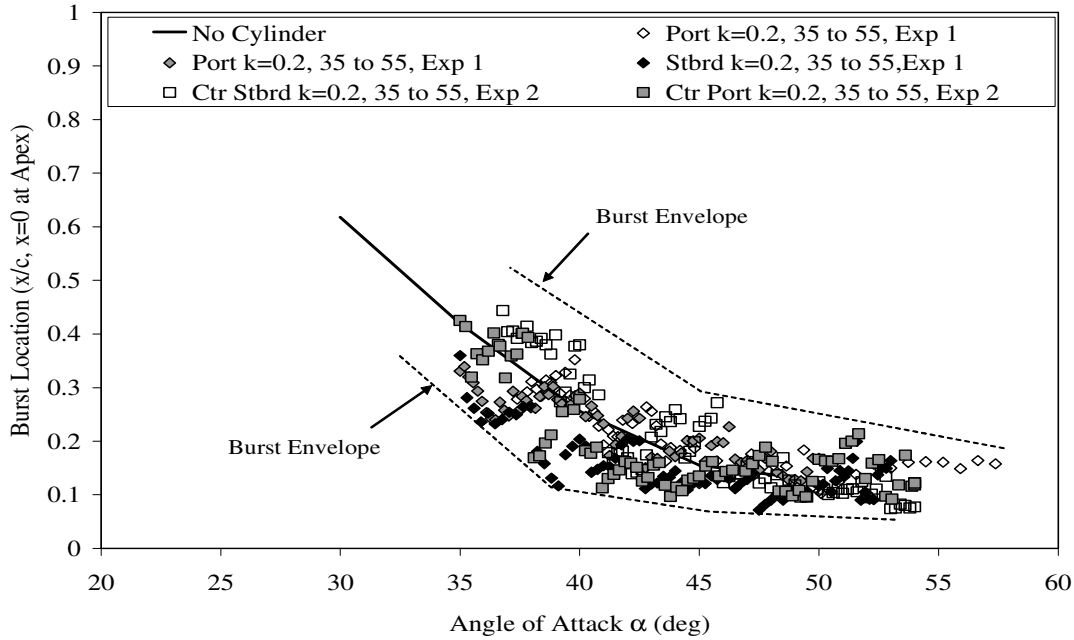

Figure 6.80. Small Cylinder Burst Envelope, Sample Experiments, $\kappa = 0.2$, $35 < \alpha < 55$ deg.

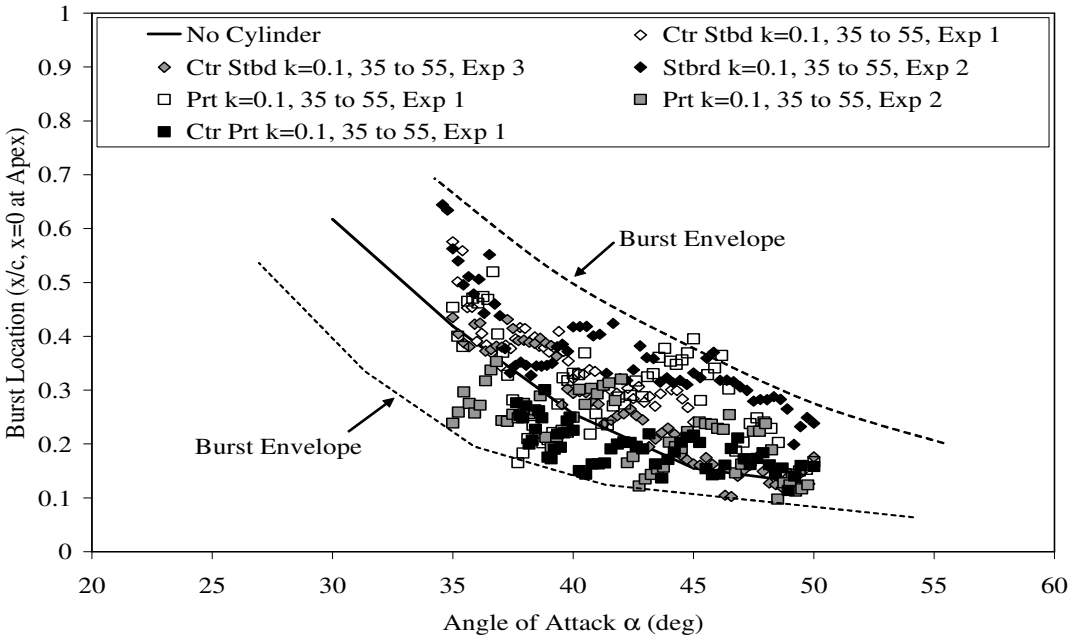

Figure 6.81. Large Cylinder Burst Envelope, Sample Experiments, $\kappa = 0.1$, $35 < \alpha < 55$ deg.

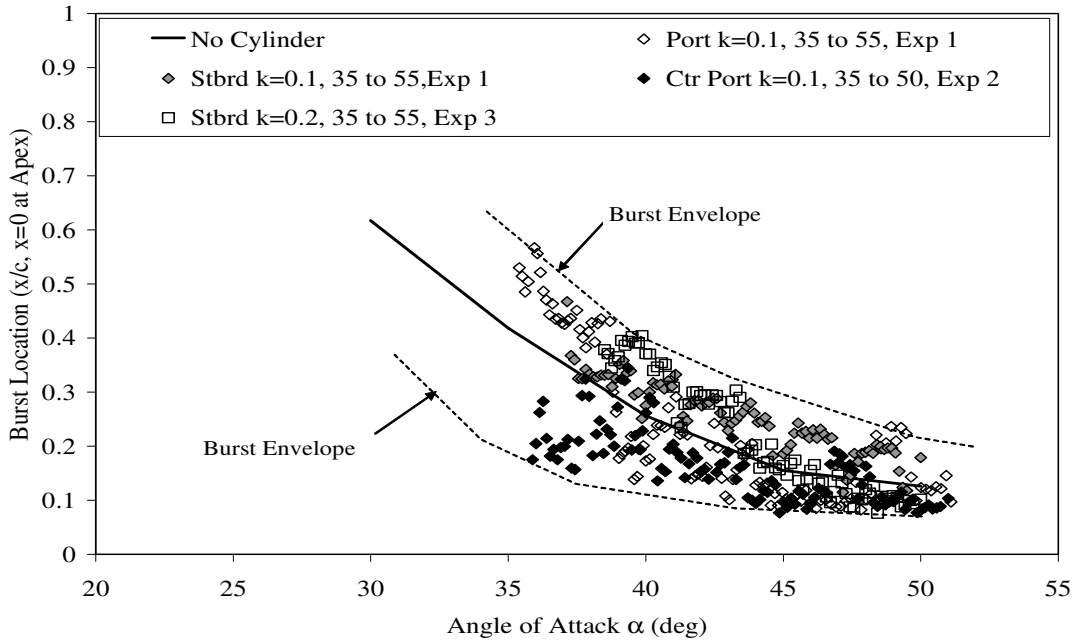

Figure 6.82. Small Cylinder Burst Envelope, Sample Experiments, $\kappa = 0.1$, $35 < \alpha < 55$ deg.

APPENDIX B

TOWING MOUNT CIRCUIT DIAGRAMS

The infrared light from diodes LD1 and LD2 is interrupted periodically by a shutter driven either from the von Kàrmàn motor (LD1), or from the carriage rolling motion (LD2), as shown in Figure B1.

Transistor Q1 (Table B1) conducts when it sees light, and switches on 8.7v to the base of Q2 through the 100kΩ resistor. When Q2 has this voltage applied, it conducts from collector → emitter → collector on Q3, and turns on relays RL1 (which in turn activates the power to the α-pitch motor) and RL2 (which provides via SW1 an alternate path to transistor Q3).

Q3 is turned on when a voltage is available from the control box for the α-pitch motor to work. This voltage is derived from the switched 12vdc to the reverse switch SW4 through the IC1 and opto-coupler LD3-Q4, and is applied at the base of Q3 through the 100kΩ current-limiting resistor. Thus, the circuit to ground can only be completed when Q3 turns on. The α-pitch motor voltage is completely isolated from PCB1.

Switch SW1 provides an alternate path to ground around Q2. When SW1 is turned on, the α-pitch motor synchronizes with the von Kàrman shutter, turns on and stays on. When SW2 is off, the α-pitch motor only turns on when the von Kàrmàn shutter is open and a voltage is available from the motor control box. Thus, SW1 is labeled “latch” for continuous turn-on, or “inter” for intermitted operation of the α-pitch motor.

The carriage velocity tachometer comprised by LD2 and Q5 similarly turns on/off when the shutter attached to the carriage roller opens or closes. For a nominal 0.4 ft/s velocity, the shutter opening/closing frequency is 10 Hz approximately. Thus, a square wave from 0.7v to 8.7v with a frequency proportional to the velocity is available at the ring terminal of the $^1/_8$ inch phones jack.

The 5kΩ linear taper pot works as a voltage divider, and provides a voltage proportional to the crank angle of the linkage that moves the model's pitch up or down. A small ceramic capacitor C1 is included to short to ground any high-frequency noise.

TABLE B1

COMPONENTS USED IN CARRIAGE ELECTRONICS LAYOUT

Component	**Type**	**Used for**	**Radio Shack Cat.**
Q1	NPN Phototransistor, Fairchild AN3005 or equiv.	von Kàrmàn sync	276-145
Q2	NPN Transistor, 2N5088 or other General Purpose	Relay control	276-1617
Q3	NPN Transistor, 2N5088 or other General Purpose	α in motion switch	276-1617
Q4	NPN Phototransistor, Fairchild AN3005 or equiv.	α motor isolation	276-145
Q5	NPN Phototransistor, Fairchild AN3005 or equiv.	Velocity tachometer	276-145
RL1	SPDT Relay, 12 V	α motor control	275-248A
RL2	SPST Relay, 5 V	Latch for relay 1	275-232
D1	Diode	Inductive load protect	276-1114
D2	Diode	Push-off bypass current	276-1114
LD1 - LD3	IR Diode, 1.2 V, 100 mA	Infra-red light source	276-143
IC1	7805 Voltage Regulator **CAUTION:** Gets HOT!!	LD3 voltage source	276-1770
VR1	5 kΩ Pot, Linear Taper	α sensor voltage	271-1714
SW1	SPST, PC mount, rat-tail	von Kàrmàn sync mode: Latch-intermittent	275-645
SW2	SPST, PC mount, rat-tail	Relay 1 bypass	275-645
SW3	Micro-switch	$\alpha = 0$ travel limit switch	275-016
SW4	Micro-switch	$\alpha = \alpha$ max, reverse pitch motion	275-016
C1	Ceramic wafer, 10 pF approx.	α sensor noise control	

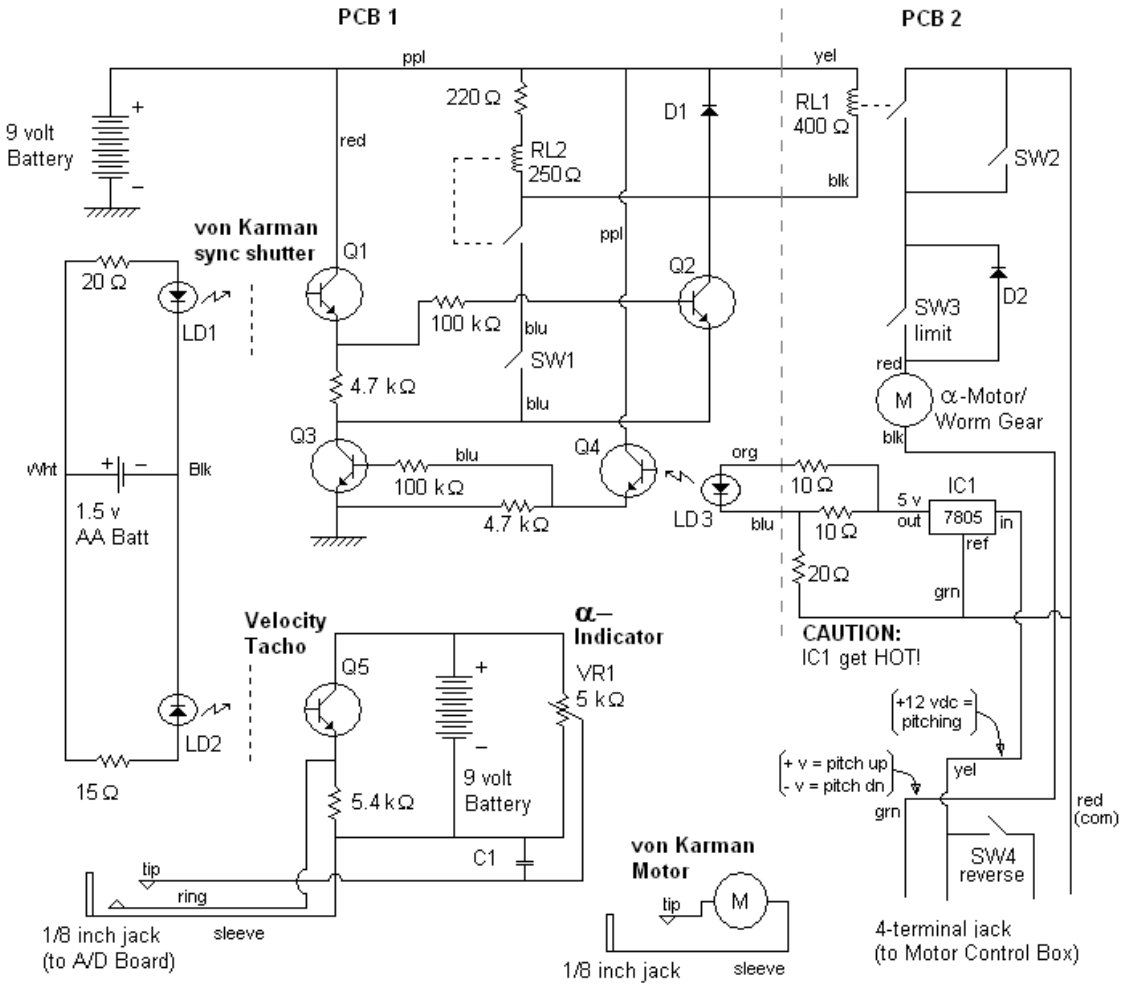

Abbreviation	Color	Abbreviation	Color
blk	Black	red	Red
yel	Yellow	ppl	Purple
grn	Green	org	Orange
blu	Blue	wht	White

Figure B1. Carriage Schematic Diagram.

The Elenco power supply unit has a variable 0 to +12vdc output section, which is connected through switch SW5 (Table B2) to the Toshiba motor that moves the carriage (Figure B2). Switch SW5 serves to control the polarity of the voltage fed to the motor, resulting in the direction of the carriage movement being reversible.

The Elenco power supply also supplies +12 and –12vdc (referenced to a 0v "common" terminal) to the box. The negative branch (-12v) is used exclusively to power the α-pitch motor during pitch down. The positive branch (+12v) is used to pitch up the model. Voltage for the α-pitch motor is derived through 3x 100Ω current limiting resistors and the 25Ω potentiometer wired as a voltage divider. When relay 3 is deactivated, the pitch-up voltage is delivered to the normally closed (NC) terminal of one set of contacts in relay 3 and then to the carriage.

The positive branch also supplies voltage to relay RL3, which switches from the +12v branch to the –12v branch when pitch-down is commanded. This occurs either through switch SW6 being manually moved, or through a voltage being applied to the base of Q6 by the reverse switch SW4 on the carriage. That is, as pitch up occurs, a pawl on the linkage closes SW4 when the maximum α has been attained, and +12v are applied through the 1.2kΩ resistor to Q6, which turns on and activates RL3.

The second set of contacts on RL3 are an alternate ground path. Once RL3 engages, the second set of contacts allow RL3 to latch continuously until the switch SW6 is returned to the "OFF" position, cutting the +12v power to the relay.

TABLE B2

COMPONENTS USED IN CARRIAGE POWER SUPPLY

Component	Type	Used for	Radio Shack Cat.
SW5	DPDT Switch w/Off Position	Forward/Rev Carriage	275-653
SW6	DPDT Switch w/Off Position	Pitch Up/Down	275-653
Q6	NPN Transistor, 2N5088 or other General Purpose	Pitch down relay control	276-1617
VR2	25 Ω, 3W Wire-Wound Pot **CAUTION:** Gets HOT!!	α pitch-up rate adjust	271-265
VR3	25 Ω, 3W Wire-Wound Pot **CAUTION:** Gets HOT!!	α pitch-down rate adjust	271-265
Rt	15 Ω, 3/4 W Carbon, 10%	Optional, used w/heavy Delta wing models	
RL3	DPDT Relay, 12 V	Pitch down relay	
D3	Diode	Inductive load protect	276-1114

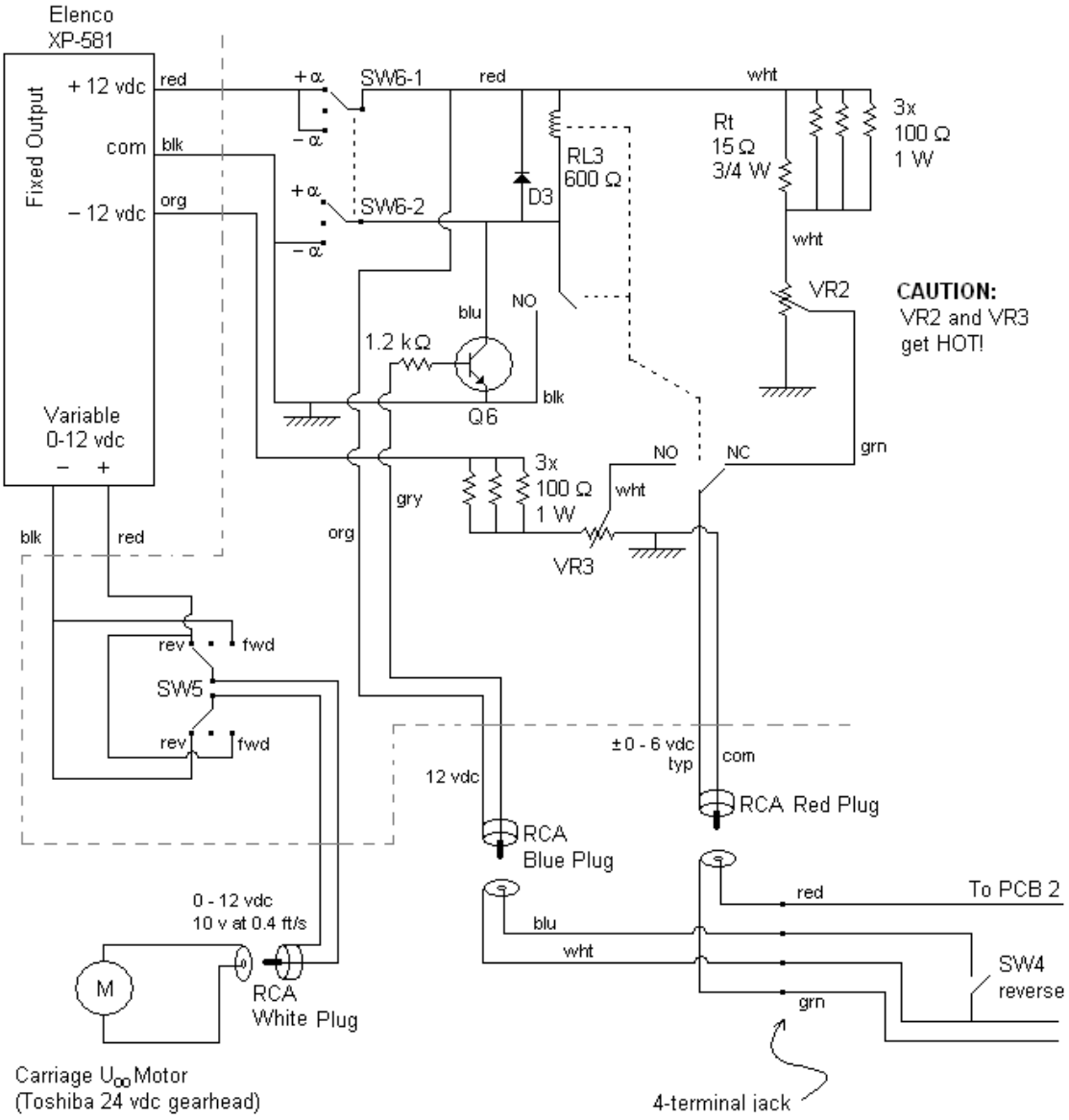

Abbreviation	Color	Abbreviation	Color
blk	Black	red	Red
gry	Gray		
grn	Green	org	Orange
blu	Blue	wht	White

Figure B2. Towing Mount Power Supply Schematic.

The Elenco bench power unit supplies +5vdc through the bridge rectifier. (The polarity of the leads connected to the bench unit is not important.) From here, 5v is supplied to the timer (IC2) and to the motor (Table B3 and Figure B3).

The 555 timer IC can be thought of as two solid-state relays inside. When pin 6 is high (i.e., sees greater than 70% of the 5v supply voltage), the output pin 3 goes low (i.e., ground potential). Conversely, if pin 6 is low, pin 3 goes high (i.e., supplies 5v). Likewise, pin 7 connects to ground when pin 2 detects a falling edge (voltage goes from high to low).

On start-up, capacitor C3 is discharged. Pin 6 is low, thus pin 3 is high, and pin 7 is open. Now, C3 begins to charge through the current provided by the top part of both pots VR4-a and -b. Close examination will reveal that the top part of both pots are connected in parallel to the supply voltage, thus lowering the combined resistance. This increases the speed with which C3 charges.

When the voltage stored in C3 climbs to 3.5v or so, pin 6 is considered "high", pin 3 and pin 7 go to ground. Capacitor C3 discharges through the bottom half of VR4-a only. The 1.2kΩ resistor is there to limit the discharge current when the pot is at its lowest position (and thus out of the discharge sequence).

As soon as the voltage in C3 drops to 30% of the supply, pin 6 goes low, pin 2 sees a falling edge. Pin 3 goes high, and the cycle repeats itself. The 555 timer is connected in a monostable multivibrator mode. Because pin 3 switches from 5v to 0v and back, a square wave is generated. The frequency of the wave is dependent on the value of capacitor C3 and how fast it charges and discharges. In this application, the frequency is not constant, but is centered around 110 Hz or so. The ratio of the wave's "on" period to total period (i.e., "on" + "off" time) is called a duty cycle. The duty cycle varies with the position of the pot VR4 between

50% to about 90% of the period. Thus, the higher the duty cycle, the faster the motor will turn. This square wave is usually called a pulse-width modulated signal (PWM).

Switch SW7 allows the rotation of the motor to be manually reversed, and diode D4 is connected as a "freewheel" diode to absorb the back EMF current that occurs when output pin 3 goes to ground and the magnetic field in the motor's coils collapse. Transistor Q7 is a high-power NPN device that switches the current from the motor to ground in response to the PWM signal from pin 3.

Any brushed dc motor can be connected to this speed control, as long as it can run satisfactorily with 5vdc. In fact, 12vdc motors run at this low voltage usually run slow, and the PWM allows even more control at slow rotational velocities. If the motor is rated at less than 5vdc, then a suitable resistor Ro should be wired in series with the motor.

TABLE B3

COMPONENTS USED IN PWM MOTOR DRIVER

Component	**Type**	**Used for**	**Radio Shack Cat.**
SW7	DPDT Switch w/Off Position	Forward/Rev motor	275-653
Q6	NPN Transistor, TIP 31 or other Power Type	Motor pulse control	276-2017
IC2	555 Timer	Pulse generator	276-1723
VR4	2-Ganged, 100 kΩ Pot	Motor velocity	
C2	0.1μF, Polyester Film	Control voltage	272-1069
C3	0.1μF, Polyester Film	Threshold and trigger	272-1069
BR1	Full Wave Bridge Rectifier	Polarity protection	276-1152
D4	Diode	Inductive load protect	276-1114
D5	Diode	Voltage trim	276-1114

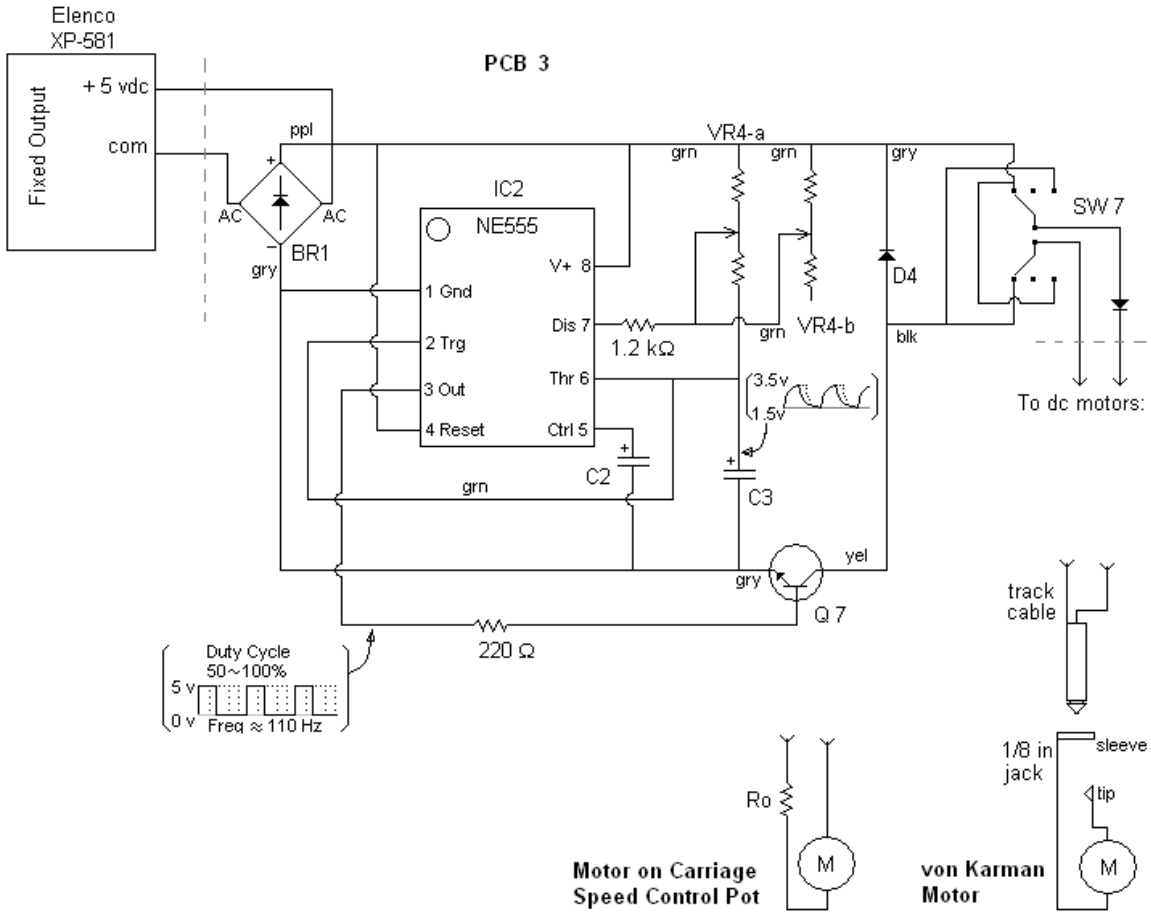

Abbreviation	Color	Abbreviation	Color
blk	Black	wht	White
Gry	Gray	ppl	Purple
grn	Green		

Figure B3. Pulse-Width Modulated von Kàrmàn Motor Speed Control Schematic.

APPENDIX C

VisualBASIC® PROGRAM LISTINGS

Program DELTA2 uses the Snappy© video capture accessory and the OLE libraries included in the installation CD to capture a video input as a Bitmap. The program also uses the coordinates of the mouse pointer, in pixels relative to the upper left hand corner of the screen, to determine the location of the features of the image on-screen, e.g., delta wing apex and VB burst point. The commands are typically self-explanatory, except that upon saving the values, the program quits.

```
' Delta2
' Ismael Heron
' Dec 2002
'
' This program uses function call to the Snappy video capture accessory to
' capture a video input file as a BMP, or the program directly loads a previously
' existing video file (JPG or BMP).  The mouse is then used to get the location of the
' mouse pointer in pixels at the start and the end of a line.
' These coordinates are associated with text input from the keyboard, and then save
' to file at the end of the session.
'
' IMPORTANT: When installing on a new computer, go to Project menu - Components -
' insertable objects, and click on Snappy OLE controls.  This need only be done the
' first time this program is loaded in a new computer system.
'
'
'================================================================================
' SNAPPY OLE CALLS
'
' Snappy1.PrepareToSnap     Signals Snappy to prepare to acquire video
' Snappy1.Snap              Acquire video and store it locally
' Snappy1.CopyToClipboard   Copy the captured video to a Windows memory buffer
'
'================================================================================


' Constants and Variable Declaration
' Variables declared here are shared between all subs and modules (Public)
' Variables not declared here are private within each sub
' A non-declared variable will pass as 0 between subs !!


Public DrivePath, DefaultPath, DefaultFile, FileName, DeltaPix As String
Public X_start, Y_start, X_end, Y_end As Integer
Public i_res As Integer
Public PaintNow, OutSavedFlag  As Boolean
Dim Results(100, 7) As Double
Dim Comments(100) As String

'================================================================================
' This sub assigns to the results array the x,y positions of the vector and the text
' to be associated with it.
```

```
Private Sub cmdRecord_Click()
Comments(i_res) = RemInput.Text             'Text and coords of the vector being
Results(i_res, 0) = X_start                 'described by the mouse are assigned
Results(i_res, 1) = Y_start
Results(i_res, 2) = X_end
Results(i_res, 3) = Y_end

Coords.Caption = "Saved Data pnt " & i_res  'User is notified
i_res = i_res + 1                           'and the index is updated

End Sub

'================================================================================
' This loads the form and establishes the default drive and path
' Then using an input box, the user is asked if the default is correct or needs
' to be modified.
' If the user modifies the drive path, the new one becomes the default

Private Sub Form_Load()

TitleBar = "Working Directory"
DefaultPath = "d:\Ismael\Myose\Dissertation\Results\"
DrivePath = InputBox("What is the working drive path? " & Chr(13) & "(Cancel for local path)",
_
            TitleBar, DefaultPath)

Label1.Caption = DrivePath                  'The user has visual confirmation of the active
                                            'drive path
NotSavedFlag = True                         'Since no files have been saved, the flag is
                                            'initialized
i_res = 0                                   'And the index for the results storage array is set

End Sub

'================================================================================
' The sub asks the user for the name of an existing file (through an input box)
' to be loaded.

Private Sub cmdLoadFile_Click()

' Upon clicking the LOAD BMP button, do following:
' Use InputBox to Obtain file name

FileName = InputBox("Input graphics file name: " & Chr(13) & DrivePath, _
            TitleBar, DefaultFile)

' If user clicks CANCEL, FileName is blank and end subroutine
' Otherwise, DeltaPix has the complete file location
' Load file named in DeltaPix and use FileName as caption to Label1 object
' Also, set FileName as default name for next time this cmd is used

If FileName = "" Then
    MsgBox ("No file loaded...")
    GoTo 299
Else
    DeltaPix = DrivePath & FileName

    Label1.Caption = FileName
    View1.Stretch = True
    View1.Picture = LoadPicture(DeltaPix)
    DefaultFile = FileName

End If

299 End Sub

'================================================================================
' This sub saves the current picture as a BMP file, regardless of its origin!

Private Sub cmdSavePix_Click()
```

```
' When used clicks SAVE BMP do the following:
' Use input box to obtain file name

TitleBar = "Saving Bitmap"

FileName = InputBox("Saving graphics file: " & Chr(13) & DrivePath, _
            TitleBar, DefaultFile)

' If user clicks CANCEL, FileName is blank and end subroutine
' Otherwise, DeltaPix has the complete file location
' Save file named in DeltaPix using SavePicture method

If FileName = "" Then
    MsgBox ("No BMP saved...")
    GoTo 399
Else
    DeltaPix = DrivePath & FileName
    SavePicture View1, DeltaPix
End If

399 End Sub

'================================================================================
' This sub is used to clear the loaded picture of any modifications or vectors drawn
' by the mouse

Private Sub cmdClearPix_Click()

' Upon clicking the CLEAR button, reset Label1 caption to empty
' and clear View1 object of all lines

Coords.Caption = ""
View1.Refresh

End Sub

'================================================================================
' This sub terminates the propgram by calling the FileOutput sub to save the results
' array to file first, then unloads the form

Private Sub cmdQuit_Click()

Call FileOutput

' Upon clicking the QUIT button, unload Delta2.frm

    Unload Form1
    Set Form1 = Nothing

End Sub

'================================================================================
' The View1_MouseDown, _MouseUp, and MouseMove are used to draw a vector, a line
' whose tip and tail coordinates are recorded.  In _MouseDown, the down click of the
' mouse button records the coordinate in terms of pixels

Private Sub View1_MouseDown(Button As Integer, Shift As Integer, X As Single, Y As Single)

'As long as either mouse button is held down, PaintNow is TRUE.  The moment this
'occurs, save the current X,Y coords as starting points of a line to be drawn

PaintNow = True

X_start = X
Y_start = Y

End Sub

'================================================================================
```

```
Private Sub View1_MouseUp(Button As Integer, Shift As Integer, X As Single, Y As Single)

'When the mouse button being held down in View1_MouseDown goes up, signaling the end
'of dragging operation, set PaintNow to FALSE and save coords as end points of the line

PaintNow = False

X_end = X
Y_end = Y

'Display the starting and ending points of the line just drawn

Coords.Caption = "Pixels:" & Chr(13) & "From " & X_start & " , " & Y_start _
                    & Chr(13) & "To " & X_end & " , " & Y_end
End Sub

'================================================================================

Private Sub View1_MouseMove(Button As Integer, Shift As Integer, X As Single, Y As Single)

'As long as PaintNow is true, this functions to draw a line as the mouse is dragged over
'the View1 object

'Set coordinate origin, line width, and coordinate shift

ScaleMode = 0
ScaleLeft = 0
ScaleTop = 0
DrawWidth = 1


'When the mouse buttons are pushed, display current coordinates in Coords label
'When the right mouse button is used, paint the points using PSet method
'When the left button is used, draw a line from initial Position to the
'current pointer position; redraw before next line is painted

If PaintNow Then
    Coords.Caption = "Pixels:" & Chr(13) & "X= " & X & "  Y= " & Y

    If Button = vbLeftButton Then
        ForeColor = vbYellow
        View1.Refresh
        Line (X, Y)-(X_start, Y_start)
    Else
        ForeColor = vbRed
        PSet (X, Y)
    End If

End If


End Sub

'================================================================================
' Signal Snappy to prepare to acquire video frame, then acquire as soon as it signals
' readiness.  The captured picture is located in the Snappy memory buffer

Private Sub cmdSnapPix_Click()

    Snappy1.PrepareToSnap
    Snappy1.Snap

End Sub

'================================================================================
' Once the picture is snapped, it needs to be moved from the Snappy buffer to the View1
' image area.  This is done in two steps.  First, the captured picture is moved from
' Snappy to the Clipboard (Windows memory buffer), then to the View1 object
```

```
Private Sub cmdMovePix_Click()

    Snappy1.CopyToClipboard                     'Copy from Snappy to Clipboard
    View1.Stretch = True
    View1.Picture = Clipboard.GetData(Bitmap)   'Now move to the picture area
    cmdSavePix_Click

End Sub

'=============================================================================
' This sub handles the saving of the results array to an output file.  It requests
' from the user the file name (if name is blank, no file is saved), then opens the
' appropriate file and dumps the data, closes the file.

Private Sub FileOutput()

TitleBar = "Writing Output"                 'This is the default file name
DefaultFile = "out001.txt"

FileName = InputBox("Writing the Output file: " & Chr(13) & DrivePath, _
                    TitleBar, DefaultFile)

'If user clicks CANCEL, FileName is blank and warn Output not saved
'Otherwise, use given name and save the contents of the Results array

If FileName = "" Then
    MsgBox ("Output NOT SAVED! ")
    OutSavedFlag = False
    GoTo 450
Else
    Open DrivePath & FileName For Output As #2
    OutSavedFlag = True
End If

For row = 0 To i_res
    Write #2, Comments(row), Results(row, 0), Results(row, 1), Results(row, 2), _
              Results(row, 3)
Next row

Close #2

450 End Sub
```

Program ASCAN uses the Omega © DAS08 Analog to Digital (A/D) converter and the DLL libraries included in the installation CD to capture the motor voltage, tachometer pulse, and angle of attack voltage values from the carriage. Typically, motor voltage is input to channel 0, angle of attack is on channel 1, and tachometer is on channel 2. When the program runs the top window used for user interface (Figure C1) is displayed. Since the max sampling rate possible by the DAS08 is 24 kHz, and it is divided into whatever number of channels are scanned sequentially, the user inputs how many counts and how many channels to scan, beginning at channel 0 up to channel X. Pressing the "Check Input Values" button calculates the total number of samples as well as the sampling rate.

Pressing the "Zero" button acts as a wind-off zero, and tares whatever voltages are present at the moment of execution. Pressing the "Start" button then executes the sampling, and toggles to a "Stop" button. When finished, the "Save Data" button saves the voltage values in a CSV file.

```
' AScan Program
' Ismael Heron
' Feb 2003
'
'
' This program uses function calls from the Omega AD Universal Library (UL) to control
' the DAS08 board located in the Tangent machine.
' This board does not support software adjustable gain.
' Max Samplign Rate (total all channels) is 24 kHz
'
' Board Set Up: Channels 0 to 7, bipolar +/- 10 volts each, 1 MOhm input impedance ea.
' IRQ dip switch set at 7.  Base address is 340H
'
' DAS08 on background mode will continue on background until EXPLICITLY told to stop!!
'
'================================================================================
' OVERALL FLOW CHART:
'
' Load Form1 => Declare Const and Vars => Read Input Parameter => WOZ* => Start* => Display
'
'* WOZ acquires zero-out voltages as follows:
'  12-bit in Windows Buffer => ADData array => convert to volts => WOZ array
'
'  Start acquires as follows:
'  12-bit in Buffer => ADData array => convert to volts => Volts array => Volts * Factors in
results array
'
'  Display polls the Windows Buffer periodically and updates screen
```

```
'  The Windows buffer ALWAYS retains the last set of data written to it.  The buffer to
'  array function only copies this buffer!
'
'
'=========================================================================================
' UL CALLS:
'
' cbDeclareRevision()            Used to get version number of UL library
' cbGetStatus%()                 On background mode, gets update on AD conversion progress
' cbStopBackground%()            Stops AD in background mode
' cbErrHandling%()               Specifies how to handle errors
' cbAInScan()                    Scans AD conversion in sequencial order
' cbWinBufFree()                 Releases Windows memory buffer
' cbWinBufAlloc()                Allocates memory space in Windows as a data buffer
' cdWinBufToArray()              Transfers data from Windows buffer to a VBasic array
'
'=========================================================================================
' VARIABLES:
'
' MemHandle&     Long Int        Pointer to Windows buffer memory location where the AD dumps
data
' Counts&        Long Int        Number of Total data counts (channels scanned * counts ea)
' Fs&            Long Int        Sampling Frequency per channel
' ETA&           Long Int        Estimated Time to Acquire data
' CurIndex&      Long Int        Location in WinBuffer where latest complete scan is stored
'
' BoardNum%      Short Int       Board number 1 for DAS08, Board 0 for UL emulator
' LoChan%,HiChan%                Lowest and highest channels to scan
' CDown%         Short Int       Elapsed time since cmdStart
' ADData%        Short Int       VBasic array where the Windows buffer dumps 12-bit data
'
' Factors        Variant Array   Contains conversion factors read from file (e.g. volts to
degree)
' VOLTS          Variant Array   Voltages per channel
' WOZ            Variant Array   Wind-off zero: used to zero out each channel prior to data
acq.
' Results        Variant Array   Contains the results in user-units (12-bit => VOLTS => user-
units)
'
'=========================================================================================


' Constants and Variable Declaration
' Variables declared Here are shared between Subs
' Variables Not declared here are private within each Sub
' A non-declared variable will pass as 0 between Subs!!

Const Gain = BIP10VOLTS                         ' Gain adjusted to 10 V bipolar
Const Range& = 20                               ' Voltage Range (-10 to +10 = 20 V)
Const DefFactorsFile = "Factors.txt"            ' Location of file w/conversion factors
Const NumPoints& = 10000                        ' Max Number of data points to collect
Const NumChnls% = 8                             ' Max Number of channels for this board
Const Options = BACKGROUND + CONVERTDATA        ' AD Options: Background collect, convert 16 to
12 bits

Dim MemHandle&, Counts&, Fs&, ETA&, CurIndex&
Dim BoardNum%, LoChan%, HiChan%, CDown%
Dim ADData%(NumPoints&)
Dim Factors(NumChnls%), VOLTS(NumChnls%), WOZ(NumChnls%), Results(NumPoints&, NumChnls%)

'=========================================================================================
' This Sub calculates the total number of counts, the total sampling rate, and the estimated
time
' the board will take to finish the job given the input parameters

Private Sub cmdCalculate_Click()

'Read In Values from User Input

BoardNum% = Val(txtBoard.Text)          'Board 0 is a UL emulator that behaves like a board
```

```
                                        'Board 1 is the DAS08 board

LoChan% = 0                             'Channel where scan starts
HiChan% = Val(txtChannel.Text)          'Channel where scan ends, as entered in txtChannel

Counts& = Val(txtCounts.Text) * (HiChan% + 1)
                                        'Number of total samples all channels
Fs& = Val(txtRate.Text)                 'Sampling frequency per channel as entered in txtRate

'Advise user on time to completion

Stotal = (Fs& * (HiChan% + 1))
ETA& = Counts& / Stotal                 'Estimated time to acquire

If (Stotal >= 24000) Or (Counts& >= 10000) Then
    ADLimits.ForeColor = vbRed
    ADLimits.Caption = " CHECK INPUTS!!!" & Chr(13) & Stotal & " Hz" _
                       & Chr(13) & Counts& & " Counts"

Else
    ADLimits.ForeColor = vbBlack
    ADLimits.Caption = "Total Fs (Hz) = " & Stotal & Chr(13) & _
                       "Total Counts = " & Counts& & _
                       Chr(13) & Chr(13) & _
                       "Est. Time to Finish (secs) = " & ETA&
End If


End Sub


'=============================================================================================
' This Sub is used to Reset all input values to initial start-up mode

Private Sub cmdClear_Click()

' Initial Values for Input Parameters

txtBoard.Text = "1"                     'Board 0 is a UL demo program that behaves like a board
                                        'Board 1 is the DAS08 board

txtChannel.Text = "2"                   'Channel where scan stops
txtRate.Text = "100"                    'Sample rate per channel
txtCounts.Text = "2000"                 'number of samples per channel

'Show Limits

Call cmdShowLimits_Click

' Stop background AD Conversion if in process

ULStat% = cbStopBackground(BoardNum%)
If ULStat% <> 0 Then
    Faults.Caption = "Stopped! Background Err =" & ULStat%
    Stop
End If

' Indicates program has been reset

Faults.Caption = "Program Cleared"
End Sub

'=============================================================================================
' To quit the porgram, free Windows buffer and exit

Private Sub cmdQuit_Click()

' Free Windows memory buffer

ULStat% = cbWinBufFree(MemHandle&)
```

```
If ULStat% <> 0 Then
    Faults.Caption = "Stopped! Buffer Free Err =" & ULStat%
    Stop
End If

' Unload and terminate all forms

Unload Form1
Set Form1 = Nothing

End Sub

'=============================================================================================
' This sub copies the Windows Buffer after data acq. has been completed and arranges it
' in columns (each column is a channel), and rows.  It then writes the data to a file
' called output.txt in the local directory

Private Sub cmdSave_Click()

' Copy the buffer to the ADData array

ULStat% = cbWinBufToArray(MemHandle&, ADData%(0), 0, CurIndex&)

' The ADData array now contains all the counts in sequential order, i.e.,
' ch0, 1, 2...6, 7, 0, 1, 2...6, 7, 0, 1, 2, etc
' This needs to be parsed into columns, each column represents a channel


k = 0                               ' k is the ADData index from 0 to (Counts)*(channels)

jmax& = (Counts& / (HiChan% + 1))   ' jmax is the number of counts per channel

For j = 0 To jmax& + 1              ' j counts the rows in the output file
    For i = 0 To HiChan%            ' i counts the columns

            Results(j, i) = (((ADData%(k) / 204.8) - 10) - WOZ(jcol))
            Results(j, i) = Results(j, i) * Factors(i)
            k = k + 1
    Next i
Next j

' Now write the output file

Open "output.txt" For Output As #2

Write #2, "WOZ Info:"

Write #2, Format$(WOZ(0), "00.000"), Format$(WOZ(1), "00.000"), _
            Format$(WOZ(2), "00.000"), Format$(WOZ(3), "00.000"), _
            Format$(WOZ(4), "00.000"), Format$(WOZ(5), "00.000"), _
            Format$(WOZ(6), "00.000"), Format$(WOZ(7), "00.000")


Write #2, "Results: "

For i = 0 To jmax& + 1

        Write #2, Format$(Results(i, 0), "00.000"), Format$(Results(i, 1), "00.000"), _
                    Format$(Results(i, 2), "00.000"), Format$(Results(i, 3), "00.000"), _
                    Format$(Results(i, 4), "00.000"), Format$(Results(i, 5), "00.000"), _
                    Format$(Results(i, 6), "00.000"), Format$(Results(i, 7), "00.000")

Next i

Close #2
Faults.Caption = "OUTPUT.TXT complete!"
End Sub

Private Sub cmdShowLimits_Click()
```

```
' Display Limits of DAS08 To the User
ADLimits.ForeColor = vbBlack
ADLimits.Caption = "LIMITS: " & Chr(13) & Chr(13) & _
                   "Hi Channel = 7" & Chr(13) & _
                   "(Sample Rate)(# Channels) < 24 kHz" & Chr(13) & _
                   "(Counts)(# Channels) < 10000" & Chr(13) & Chr(13) & _
                   "-10 to +10 Volts per channel"
End Sub

'=========================================================================================
' This Sub is initiated by the start button, which then calculates parameters needed to
' pass into the DAS08, executes a check of two critical values, and initiates background
' conversion.  Timer1 is used to update the on-screen display without affecting conversion
' progress.

Private Sub cmdStart_Click()

' Button Control

cmdStart.Visible = False: cmdStart.Enabled = False
cmdStop.Visible = True: cmdStop.Enabled = True
cmdQuit.Enabled = False: cmdWOZ.Enabled = False

' Get Input values for sample rate Fs and Number of Counts per Channel

Call cmdCalculate_Click


' Check for input errors

If Fs& < 1 Then Stop
If HiChan% > 7 Then HiChan% = 7
If (Fs& * (HiChan% + 1)) > 24000 Then Stop

' Establish Timer1 to periodically ask for updates to write to screen.  Every so many msec)
' as specified in Interval the buffer is dumped and displayed WHILE data collection CONTINUES
' in background mode

Timer1.Interval = (1 / Fs&) * 1000

' Initiate Data Collection

ULStat% = cbAInScan(BoardNum%, LoChan%, HiChan%, Counts&, Fs&, Gain, MemHandle&, Options)
If ULStat% <> 0 Then
    Faults.Caption = "Stopped! AinScan Err =" & ULStat%
    Stop
End If

' Start the countdown timer and Timer1 to update screen

CDown% = 0
ETF.Enabled = True
Timer1.Enabled = True

End Sub

'=========================================================================================
'Stops Background Data Collection

Private Sub cmdStop_Click()

'Stop all timers

ETF.Enabled = False
Timer1.Enabled = False

'Now stop all AD activity

ULStat% = cbStopBackground(BoardNum%)
If ULStat% <> 0 Then
```

```
    Faults.Caption = "Stopped! Background Err =" & ULStat%
    Stop
End If

'Button Control

cmdStart.Visible = True
cmdStart.Enabled = True
cmdStop.Visible = False
cmdStop.Enabled = False
cmdQuit.Enabled = True
cmdWOZ.Enabled = True


End Sub

'=============================================================================================
' This Sub is used to zero any existing voltages prior to data acq.
' E.g. At Angle of attack = 0, voltage present in ch. 0 is 3.  Use WOZ to zero
' this voltage out

Private Sub cmdWOZ_Click()

' Button Control

cmdStart.Enabled = False
cmdStop.Enabled = False
cmdQuit.Enabled = False
cmdWOZ.Enabled = False

' Get board info

Call cmdCalculate_Click

' Initiate Data Collection, one sweep all channels

ULStat% = cbAInScan(BoardNum%, 0, 7, 10, 1000, Gain, MemHandle&, Options)
If ULStat% <> 0 Then
    Faults.Caption = "Stopped! WOZ Err =" & ULStat%
    Stop
End If

' Copy from WinBuff to ADData array, convert to volts, and assign to WOZ array

ULStat% = cbWinBufToArray(MemHandle&, ADData%(0), 0, 8)

        For icol = 0 To 7
            WOZ(icol) = (ADData%(icol) / 204.8) - 10        'Convert 12-bit to volts: 2^12=4096
                                                            'So -10 to +10 volts = 4096 thus 1
volt = 204.8
                                                            'And 0 volts is halfway between 0
and 4096 = 2048
                                                            'Thus Volts = (ADData - 2048)/204.8

            ADOut(icol).Caption = Format$(WOZ(icol), "000.00") & Chr(13) & " Volts"

        Next icol

' Stop further AD action and resets, ready for further instructions

ULStat% = cbStopBackground(BoardNum%)
If ULStat% <> 0 Then
    Faults.Caption = "Stopped! Background Err =" & ULStat%
    Stop
End If

' Button Control

cmdStart.Visible = True
cmdStart.Enabled = True
```

```
cmdStop.Visible = False
cmdStop.Enabled = False
cmdQuit.Enabled = True
cmdWOZ.Enabled = True

End Sub

'=============================================================================================
' This timer is used to get 1000 msec intervals to update the ETF (est. time to finish)
' counter.

Private Sub ETF_Timer()

' Every 1000 msec, the timer executes the following:

CDown% = CDown% + 1
ETA& = CLng(CDown%)
End Sub


'=============================================================================================
' This Loads the Form, reads in conversion factors, and declares error handling routines
' of the AD Board
' This is the FIRST SUB to be performed when LAUNCHING THE PROGRAM

Private Sub Form_Load()

' Button Controls are initialized, Timer is initialized

cmdStart.Visible = True: cmdStart.Enabled = True
cmdStop.Visible = False: cmdStop.Enabled = False
cmdQuit.Enabled = True: cmdWOZ.Enabled = True

Timer1.Enabled = False

' Reset Inputs to Start Up Values

Call cmdClear_Click
Call ReadInFactors

' Declare revision level of Universal Library

ULStat% = cbDeclareRevision(CURRENTREVNUM)

' Initiate error handling
' activating error handling will trap errors like
' bad channel numbers and non-configured conditions.
' Parameters:
'  PRINTALL    :all warnings and errors encountered will be printed
'  DONTSTOP    :if an error is encountered, the program will not stop,
'               errors must be handled locally

ULStat% = cbErrHandling(PRINTALL, DONTSTOP)
If ULStat% <> 0 Then
    Faults.Caption = "Stopped! cbAErrHandling Err =" & ULStat%
    Stop
End If

' If cbErrHandling% is set for STOPALL or STOPFATAL during the program
' design stage, Visual Basic will be unloaded when an error is encountered.
' Trapping errors locally until the program is ready for compiling
' to avoid losing unsaved data during program design.  This can be done by
' setting cbErrHandling options as above and checking the value of ULStat%
' after a call to the library. If it is not equal to 0, an error has occurred.

' Allocate Windows buffer and obtain a Pointer (called handle) where data is to be stored
' If the MemHandle = 0 then we have an error

MemHandle& = cbWinBufAlloc(NumPoints&)
If MemHandle& = 0 Then
```

```
    Faults.Caption = "Stopped! No Memory Handle Err =" & MemHandle&
    Stop
End If


End Sub

'=========================================================================================
' Timer 1 is used to ask the AD board while it converts AD in badkground mode for regular
' updates on the progress.  This is done with the GetStatus and the cbWinBuffToArray
' functions.  12-bit data is stored in ADData%() array, which is then converted to useful
' units by dividing by a factor stored in the Factors() array.

Private Sub Timer1_Timer()

' Get status of the AD conversion in the background.  If running, dump latest scan from
' Windows buffer into ADData array

ULStat% = cbGetStatus(BoardNum%, Status%, CurCount&, CurIndex&)

If Status% = RUNNING Then
    Faults.Caption = "Running" & Chr(13) & _
                     "Time (secs): " & ETA& & " Count: " & CurIndex&   'Display running

    If CurIndex& > HiChan% Then
        FirstPoint& = CurIndex&    'start of latest channel scan in MemHandle buffer
        ULStat% = cbWinBufToArray(MemHandle&, ADData%(0), FirstPoint&, 8)


'Display in each area specific to each channel and save in Results array

        For icol = 0 To HiChan%         'display for active channels
            VOLTS(icol) = ((ADData%(icol) / 204.8) - 10) - WOZ(icol)
                                                        'Convert 12-bit to volts: 2^12=4096
                                                        'So -10 to +10 volts = 4096 thus 1
volt = 204.8
                                                        'And 0 volts is halfway between 0
and 4096 = 2048
                                                        'Thus Volts = (ADData - 2048)/204.8

            ADOut(icol).Caption = Format$(VOLTS(icol) * Factors(icol), "00.00") & Chr(13) & "
Units"

        Next icol

        For icol = HiChan% + 1 To 7     'display --- for inactive channels
            ADOut(icol).Caption = "---"
        Next icol

    End If
End If

If Status% <> RUNNING Then
    Faults.Caption = "Finished - Idle"
    cmdStop_Click
End If


End Sub

'=========================================================================================
'This Sub opens a file, reads in the conversion factors, and passes the resulting array
'back to the main Sub.

Private Sub ReadInFactors()

TitleBar = "Conversion Factors"
DrivePath = InputBox("Conversion Factors to use: ", TitleBar, DefFactorsFile)

Open DrivePath For Input As #3
```

```
    For i = 0 To 7
        Input #3, Factors(i)
    Next i

Close #3

End Sub
```

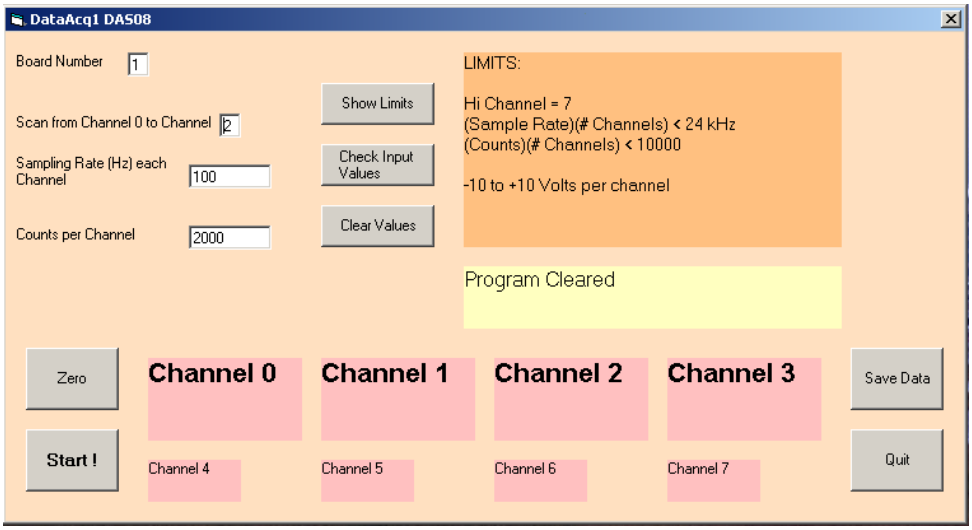

Figure C1. User Interface for ASCAN Program.

APPENDIX D

LAB NOTES ON VON KARMAN EXPERIMENTS

Table D1 presents a summary of the hand-written lab notes and observations taken during the analysis of the von Kàrmàn video tapes. It expands on the information presented in Table 5.3. Note that not every run was scrutinized for VB type or other features.

TABLE D1

VORTEX BURST DETAILS ON VON KARMAN EXPERIMENTS

Fig. No.	Run No.	Pitch-Up (UP) or Down (DN)		Cyl. Size	Vortex Burst Type or Other Comments
		Rate (κ)	Start / End α (deg)		
6.4	36 ~ 38	Static	35 deg	Large	Spiral all.
6.5	32 ~ 34	Static	40 deg	Large	Spiral all.
6.6	28 ~ 30	Static	45 deg	Large	2 runs were bubble; run 28 possible spiral.
6.7	25 ~ 27	Static	50 deg	Large	Bubble all.
6.13	103	0.2	15 to 55	Large	Spiral to $\alpha <$ 51 deg.
6.14	104	0.2	15 to 55	Large	Spiral to $\alpha <$ 40 deg.
6.15	106	0.2	15 to 55	Large	Spiral to $\alpha <$ 50 deg.
6.16	109	0.2	15 to 55	Large	
6.17	112	0.2	15 to 55	Large	Spiral to $\alpha <$ 48 deg.
6.18	114	0.2	15 to 55	Large	
6.19	115	0.2	15 to 55	Large	Spiral to $\alpha <$ 45 deg.
6.20	117	0.2	15 to 55	Large	
6.21	119	0.2	15 to 55	Large	Spiral to $\alpha <$ 48 deg.
6.22	120	0.2	15 to 55	Large	
6.23	122	0.2	15 to 55	Large	Spiral to $\alpha <$ 47 deg.

TABLE D1

(CONTINUED)

Fig. No.	Run No.	Pitch-Up (UP) or Down (DN)		Cyl. Size	Vortex Burst Type or Other Comments
		Rate (κ)	Start / End α (deg)		
6.24	146	0.2	35 to 55	Large	Bubble all.
6.25	148	0.2	35 to 55	Large	Spiral to $\alpha <$ 45 deg.
6.26	150	0.2	35 to 55	Large	
6.27	151	0.2	35 to 55	Large	Spiral to $\alpha <$ 50 deg.
6.28	152	0.2	35 to 55	Large	Spiral to $\alpha <$ 40 deg.
6.29	153	0.2	35 to 55	Large	Bubble all.
6.30	156	0.2	35 to 55	Large	Spiral to $\alpha <$ 43 deg.
6.31	158	0.2	35 to 55	Large	Bubble all.
6.32	160	0.2	35 to 55	Large	Spiral to $\alpha <$ 52 deg.
6.33	161	0.2	35 to 55	Large	
6.34	162	0.2	35 to 55	Large	
6.35	164	0.2	35 to 55	Large	Spiral all.
6.36	125	0.1	35 to 55	Large	Spiral to $\alpha <$ 44 deg.
6.37	126	0.1	35 to 55	Large	Spiral to $\alpha <$ 42 deg.
6.38	127	0.1	35 to 55	Large	Spiral to $\alpha <$ 40 deg.
6.39	131	0.1	35 to 55	Large	
6.40	132	0.1	35 to 55	Large	Spiral to $\alpha <$ 48 deg.
6.41	136	0.1	35 to 55	Large	
6.42	137	0.1	35 to 55	Large	Spiral to $\alpha <$ 40 deg.
6.43	139	0.1	35 to 55	Large	Spiral to $\alpha <$ 46 deg.
6.44	141	0.1	35 to 55	Large	Bubble all.
6.45	142	0.1	35 to 55	Large	Spiral to $\alpha <$ 42 deg.
6.46	144	0.1	35 to 55	Large	Bubble all.

TABLE D1

(CONTINUED)

Fig. No.	Run No.	Pitch-Up (UP) or Down (DN)		Cyl. Size	Vortex Burst Type or Other Comments
		Rate (κ)	Start / End α (deg)		
6.47	205	0.2	15 to 55	Small	Spiral to $\alpha <$ 48 deg.
6.48	207	0.2	15 to 55	Small	Bubble all.
6.49	208	0.2	15 to 55	Small	Bubble all.
6.50	235	0.2	15 to 55	Small	Spiral to $\alpha <$ 49 deg.
6.51	240	0.2	15 to 55	Small	Bubble all. Kinks apparent, easily distinguishable.
6.52	241	0.2	15 to 55	Small	Bubble all.
6.53	217	0.2	15 to 55	Small	Spiral to $\alpha <$ 48 deg.
6.54	218	0.2	15 to 55	Small	Bubble all.
6.55	223	0.2	15 to 55	Small	
6.56	244	0.2	15 to 55	Small	
6.57	245	0.2	15 to 55	Small	Bubble all.
6.58	247	0.2	15 to 55	Small	Bubble all.
6.59	210	0.2	35 to 55	Small	Bubble all.
6.60	212	0.2	35 to 55	Small	
6.61	213	0.2	35 to 55	Small	Bubble all.
6.62	231	0.2	35 to 55	Small	Spiral to $\alpha <$ 50 deg.
6.63	232	0.2	35 to 55	Small	Spiral to $\alpha <$ 48 deg.
6.64	233	0.2	35 to 55	Small	
6.65	230	0.2	35 to 55	Small	Bubble all.
6.66	248	0.2	35 to 55	Small	Spiral to $\alpha <$ 46 deg.
6.67	249	0.2	35 to 55	Small	Spiral to $\alpha <$ 50 deg.
6.68	250	0.2	35 to 55	Small	

TABLE D1

(CONCLUDED)

Fig. No.	Run No.	Pitch-Up (UP) or Down (DN)		Cyl. Size	Vortex Burst Type or Other Comments
		Rate (κ)	Start / End α (deg)		
6.69	258	0.1	35 to 55	Small	Spiral to $\alpha <$ 40 deg.
6.70	259	0.1	35 to 55	Small	
6.71	262	0.1	35 to 55	Small	Spiral to $\alpha <$ 44 deg. Kinks apparent.
6.72	263	0.1	35 to 55	Small	
6.73	265	0.1	35 to 55	Small	Spiral to $\alpha <$ 40 deg.
6.74	252	0.1	35 to 55	Small	Bubble all.
6.75	253	0.1	35 to 55	Small	
6.76	254	0.1	35 to 55	Small	Spiral to $\alpha <$ 40 deg.